

Fluid Structure Interaction analysis considering the structural behavior

Von der Fakultät für Maschinenbau, Elektro- und Energiesysteme der Brandenburgischen
Technischen Universität Cottbus - Senftenberg zur Erlangung des akademischen Grades
Doktor der Ingenieurwissenschaften habilitatus (Dr.-Ing. habil.)

genehmigte Habilitationsschrift

von

Dr.-Ing. Robert Roszak

Vorsitzender der Habilitationskommission: Prof. Dr.-Ing. Ralf Woll

Gutachter: apl. Prof. Dr.-Ing. habil. Bernd Beirow

Gutachterin: Prof. Dr.-Ing. habil. Sabine Weiß

Gutachter: Prof. Dr. hab. inz. Mieczyslaw Kuczma

Weiteres Mitglied: Prof. Dr.-Ing. Matthias Ziegenhorn

Eröffnung des Habilitationsverfahrens: 09.02.2022

Fakultätsratsbeschluss über Zuerkennung der Lehrbefähigung: 17.01.2024

Ich bedanke mich bei Professor Dr.-Ing. Matthias Ziegenhorn und dem gesamten Team für die Hilfe und die Zeit, die sie bei der Erstellung dieser Habilitationsschrift aufgewendet haben. Ich danke auch meiner Familie für ihre Unterstützung und ihr Verständnis.

Contents

1	Introduction	8
1.1	Theoretical background of FSI coupling	8
1.2	Numerical methods of flutter modeling	12
2	Tools used in flutter analysis	16
2.1	Computational Fluid Dynamics - FOI EDGE	16
2.1.1	Introduction	16
2.1.2	Main equations solved during simulation	17
2.1.3	Turbulence models used in the CFD FOI EDGE code	17
2.1.4	Discretization in space and integration in time	19
2.2	Computational Fluid Dynamics - DLR TAU-code	20
2.2.1	Introduction	20
2.2.2	Decomposition of flow grid into computational domains	21
2.2.3	Preparation of data for simulation	22
2.2.4	Calculation solver	22
2.2.5	Flow grid adaptation	22
2.2.6	Moving grid method – CHIMERA	22
2.2.7	Models of turbulence	23
2.3	Numerical structural modeling	23
2.3.1	Modal analysis	23
2.3.2	FEM method – MF3 solver	26
2.4	Coupling tools	27
2.4.1	Introduction	27
2.4.2	Closest proximity search	27
2.4.3	Data interpolation	28
2.4.4	Available aeroelastic tools	31
2.5	Grid deformation tools	32
2.5.1	Introduction	32
2.5.2	Deformation module used by TAU-code	34
2.5.3	Deformation module AE_DEFVOL	35
2.6	Visualisation of calculation results	37
2.6.1	Introduction	37
2.6.2	TecPlot 360/Focus	38
2.6.3	ParaView	42
3	Development of numerical models	44
3.1	Introduction	44
3.2	Selection of tools and model	44
3.3	Creation of 3D geometrical model of the aircraft based on 3D scanning technique	48

3.4	Creation of the reduced structural model	54
3.5	Flow grid generation process	58
3.6	Boundary conditions of the structural model	64
3.7	Modification of the model	77
3.8	Preparation of the calculation	82
4	Results	85
4.1	Numerical analysis - initial calculation	85
4.2	Numerical analysis - final calculation	98
5	Non-linear aeroelasticity	111
5.1	Introduction	111
5.2	Computational aeroelasticity	112
5.3	The non-linear structural problem	112
5.3.1	Non-linear elastic material models used in simulations	113
5.4	The Fluid Structure Interaction Algorithm	114
5.4.1	The description of the FSI algorithm for structures with non-linear behavior	114
5.5	FSI analysis for a chosen non-linear problem	116
5.5.1	The validity of the algorithm for the experiment of the Naca0012 airfoil [70]	116
5.5.2	Experiment data	117
5.5.3	Numerical simulation of the Naca0012 profile	124
5.5.4	Summary	129
5.5.5	A numerical simulation for non-linear material model exemplified by the flexible delta profile	129
5.5.6	Conclusions	133
6	Material behavior analysis	135
6.1	Introduction	135
6.2	Experiments	138
6.2.1	Cyclic tests	138
6.2.2	Temperature measurements	139
6.2.3	Isothermal and non-isothermal tensile tests	139
6.3	Microstructure of material	140
6.3.1	Scanning electron microscopy	140
6.3.2	X-ray refraction	141
6.3.3	Computed tomography	144
6.4	Results	145
6.4.1	Material behavior	145
6.4.2	Isothermal tensile test	147
6.4.3	Non-isothermal tensile test	148
6.5	Numerical simulations	148
6.5.1	Material model by Chaboche	148
6.5.2	Damage model by Gurson-Tvergaard-Needleman (GTN)	151
6.6	Application of models	153
6.6.1	Cyclic test	153
6.6.2	Isothermal tests	154
6.6.3	Non-isothermal tests	155
6.7	Concluding remarks	155
7	Summary	157

Abstract

The development of computer technologies allows using numerical simulations in the early stages of aircraft design more and more often. The role of both wind tunnels and initial test flights used to validate of solutions seems to be diminishing. Big systems for three-dimensional simulations of Fluid-Structure Interactions (FSI) constitute highly specialized and costly software. Most of the codes are based on many simplifications. One of them is the assumption of linearity of the structural model being in contradiction with real-life situations. What is meant by the non-linearity of structure is:

- geometrical non-linearity, in which case large deformations of the system cause the lack of proportionality between the load and the displacement; the influence of the displacement on static quantities;
- material non-linearity stemming from a constitutive equation.

The postdoctoral dissertation presents the results of simulations for complex, multi-scale objects and non-linear structure models and extended structure testing in relation to damage in macro-scale analysis. What is crucial for carrying out the assumed analyses is to extend a numerical tool comprising a flow and a structural program and a space grid deformation model for a system allowing to take into consideration the non-linearity of the structure. Thesis contains the following items:

- joining independent programs: flow, structural, interpolation and three-dimensional CFD grid deformation tools into one integrated system,
- adapting a structural code to a non-linear analysis and modifying FSI control script,
- carrying out tests,
- analyzing FSI on certain examples,
- visualizing the results,
- extension of data and description of the structural model in the field of research carried out at BTU Cottbus-Senftenberg (BTU) and Poznan University and Technology,
- insightful mechanical analysis of material behavior under the influence of a cyclic load.

The point of reference for testing the suggested approaches are the existing solutions of the aeroelastic linear problems. Developing the presented postdoctoral dissertation is devoted to FSI impact studies for selected cases of structural models. Results of the recent research might be applied for the construction of increasingly common unmanned aerial vehicle (UAV). Modern structure is a key element that affects the basic parameters as mass or range of these vehicles. Until now the research and development of the aeroelastic calculation algorithm for commonly used materials in the framework of linear geometry and linear-elastic material behavior was used. The current developments of materials for light-weight design common use of 3D printing technology causes the increasingly widespread use of new alternative materials in the aviation industry. This is particularly true for the design and construction of UAV, where the basic requirements are the lightness of the structure and the maximum range. Unfortunately, the fulfillment of the above criteria means that the materials used are often loaded not only in a elastic range but also more often above this limit. In case of analyzing aeroelastic phenomena for a loaded structure we should take a closer look at the behavior of the material outside the elastic range in which the damage occurs. The process of destroying in the face of such dangerous phenomena as flutter in aircraft constructions requires a deeper analysis of the mechanics of materials, in particular for new materials and their manufacturing techniques. For this purpose, the author started collaborating with the BTU in a

team that studies the description of the behavior of materials that are produced using modern 3D printing techniques. As part of joint experiments and numerical simulations, detailed research was carried out to describe the behavior of printed materials, which will be increasingly used in the design of aircraft structures. Extending the postdoctoral dissertation with the research carried out at BTU will allow further development of the existing FSI algorithm, taking into account the structural behavior more accurately and the possibility of predicting damage processes as a result of the cyclic load.

Scope of habilitation thesis

This thesis consists of eight chapters. Chapter 1 is an introduction to the subject of the work and discusses the purpose and scope of the research undertaken and an overview of the current state of knowledge. Chapter 2 describes the tools used in the field of numerical aeroelastic algorithms. Chapter 3 presents the development of numerical models used in simulations. The chapter contains the theoretical basis and description of the methods used in this work. Chapter 4 presents the obtained results of the FSI simulation for a selected case of an aircraft structure. Chapter 5 covers the problem of structure-flow coupling for the case of non-linear structure properties. It describes the principles of data exchange. The problem of deformation of three-dimensional flow grids is also presented. This chapter discusses the aeroelastic algorithm for static and dynamic analyses. Chapter 6 introduces the issues related to the behavior of the material under cyclic loading. The description includes the study of the behavior of the structure of the materials and the development process of the damaged section. Chapters 7 and 8 contain a summary and conclusions from the conducted research and the references used.

Symbols

ALE - Arbitrary Lagrangian-Eulerian
AM - Additive Manufacturing material
 \mathbf{b} - vector of the mass forces - chapter 1
 \hat{C} - operator describing the conditions determining convection
 $C_1, C_2, \gamma_1, \gamma_2$ - hardening parameters
 C_{01}, C_{10} - parameters of the Mooney Rivlin hyperelastic material model
 \hat{D} - operator describing the conditions determining viscosity
D - damping ratio - chapter 5.5.6
 D_{ij} - turbulence model diffusion part
DMD - Dynamic Mode Decomposition
E - Young's Modulus
 \mathbf{f}^{int} - vector of the internal structural forces
 \mathbf{f}^{ae} - vector of aerodynamic forces applied to the wet surface of the structure
 \mathbf{f} - vector of the forces – chapter 2.3
f - frequency – chapter 3.1, 5.5.6
 f_c - critical porosity
 f_0 - initial porosity
 f_N - nucleation porosity
 f_F - failure porosity
FSI - fluid-structure interaction
 \mathbf{F}^c - vector of ALE convective fluxes
 $F_c(q)$ - convection part
 $F_d(q)$ - diffusion part
GTN - Gurson-Tvergaard-Needleman damage model
 \mathbf{H} - transformation matrix
i - imaginary unit
 \mathbf{I} - identity matrix
 \tilde{k} - kinetic energy of turbulence
 $\tilde{\mathbf{K}}_c$ - an exchange matrix describing dependencies resulting from the structure movement, interpolated on the exchange surface of a moving flow grid
l - characteristic dimension
LCO - Limit-Cycle Oscillations
 M_a - Mach number
 $\mathbf{M}, \mathbf{C}, \mathbf{K}$ - matrices of the mass (inertia), damping and stiffness of the structural model
 $\tilde{\mathbf{M}}, \tilde{\mathbf{C}}, \tilde{\mathbf{K}}$ - fictitious matrices of mass, damping and stiffness assigned to a moving flow grid
n - viscosity exponent
 \mathbf{p} - pressure vector
 \mathbf{P}_{ij} - turbulence initiation part
POD - Proper Orthogonal Decomposition
 $q_k(t)$ - generalized Lagrange co-ordinates
 \mathbf{q} - solution vector – chapter 2.1.2
 \mathbf{q} - vector of generalized displacements – section 5.3
 q_1, q_2 - Tvergaard-Needleman constants
 \mathbf{Q}_k - vectors of generalized modal forces
r - the correlation coefficient – chapter 6
 \mathbf{R} - vector of the diffusion streams
ROM - Reduced Order Modelling

- R_{kin} - static recovery
 s - the standard deviation chapter – chapter 6
 S - operator describing the source of the flowb
 S_N^σ - stress standard deviation
 St - Strouhal's number
 \mathbf{T} - stress tensor as $\mathbf{T} = -p\mathbf{I} + \mu(\nabla\mathbf{v} + (\nabla\mathbf{v})^T)$
 t - time
 \mathbf{u}^* - "friction velocity", defined as: $\mathbf{u}^* = \sqrt{\frac{\tau_w}{\rho}}$
 V - discretization solutions for flow equations (Euler or Navier-Stokes) using the finite element or finite volume method
 V_0 - volume
 \mathbf{v} - fluid velocity vector
 \mathbf{v}_{grid} - grid velocity vector
 \mathbf{w}_t - fluid state vector
 W - work expanded
 \mathbf{x} - displacement or position, depending on the representation of points in the flow domain
 \mathbf{x}_0 - vector of initial values
 \mathbf{x}_Γ - the restriction of \mathbf{x} to $\Gamma(t)$ - which is the same as the position of the wet surface of the structure
 $\bar{\mathbf{x}}$ - eigenvalue vector
 y - the thickness of the first layer
- α - decay rate - chapter 4.2
 δ - relative error - section 3.4
 Δt_0 - local time step
 Γ_t - moving fluid/structure interface boundary
 ϵ_{ij} - dissipation level - chapter 2
 ϵ_{ij} - strain sensor - chapter 6
 ζ_k - modal variable damping k
 λ_0 - integrated convection part
 μ - dynamic viscosity
 $\tilde{\mu}_{0k}$ - sum of dynamic and turbulent viscosity in turbulent flow
 ν - kinematic viscosity
 ν_T - turbulent viscosity
 Π_{ij} - relationship between pressure and deformation
 ρ - fluid density
 σ_N - mean stress
 σ_y - yield stress
 τ_w - static shear stress on wall
 $\phi_{\infty,1}, \phi_{\infty,2}$ - saturation factors
 Ω - arbitrary control range for the boundary S
 ω - modal frequency
 ω_1, ω_2 - decay constants

Chapter 1

Introduction

1.1 Theoretical background of FSI coupling

The engineer's task is to model real systems. The difficulty of modeling is, on the one hand, to take into account various interactions, and on the other hand, be as simple and easy (to apply) as possible. Computer simulation plays a special role in modeling. With the development of the capabilities of modern processors, both the discrete model and the mathematical model of real phenomena could be extended. Discrete models with a large number of degrees of freedom describe the continuum more accurately. Along with increasing computational possibilities, mathematical description allows for joint considerations of various physical phenomena. Since all interactions of the real world result from the simultaneous influence of many physical phenomena, modeling of the "multiphysics" is a challenge for modern engineering. An example of such phenomena of interaction in mechanics is the fluid structure interaction (FSI) which involves the displacements of the structure under the influence of normal and tangential forces occurring in the surrounding fluid. There are issues in which these impacts are decisive for the functioning of the system or devices and their neglect may lead to serious consequences, including failure. An example of an area where the fluid structure interaction is important are the structures of various biological systems (e.g. blood flow). Although aeroelastic phenomena constituting a special range of interactions and their description has been known for a long time, there is a significant problem. Even, if the most known aeroelastic modeling solutions in aviation applications are not considered, it can be concluded that progress in this field is insufficient. An example is the failure of the Tahoma Bridge in 1940 (Fig. 1.1a) [129], but an almost identical scenario is the beginning of the disaster in the case of the Dubrovnik Bridge in 2005 (Fig. 1.1b) [130].

With the increasing possibilities of computer techniques, the numerical simulation is increasingly used in the initial stages of design. Large systems that enable three-dimensional simulations of FSI are highly specialized and expensive (software), and there are only few codes of this type. Most of them are based on some simplifications. One of such simplifications is the assumption that the structural model is linear, which in certain cases makes it impossible to obtain correct solutions. The structure nonlinearity is understood as: a) geometric nonlinearity, where large deformations of the system cause a lack of proportionality between the load and the displacements; the influence of displacements on static quantities is significant; b) non-linear material behavior - linear constitutive equations are not correct. The non-linear approach to problem solving allows the inclusion accurate material data above the proportionality limit.

Computational Aeroelasticity (CAE) [53] studies the effect of a fluid flow on a deformable body. The field combines the methods used in Computational Fluid Dynamics and the area of Computational Structural Mechanics [55]. Elastic aeroelasticity is a field of science that deals with the effects of aerodynamic forces on elastic bodies. A scheme showing aeroelasticity (Figure

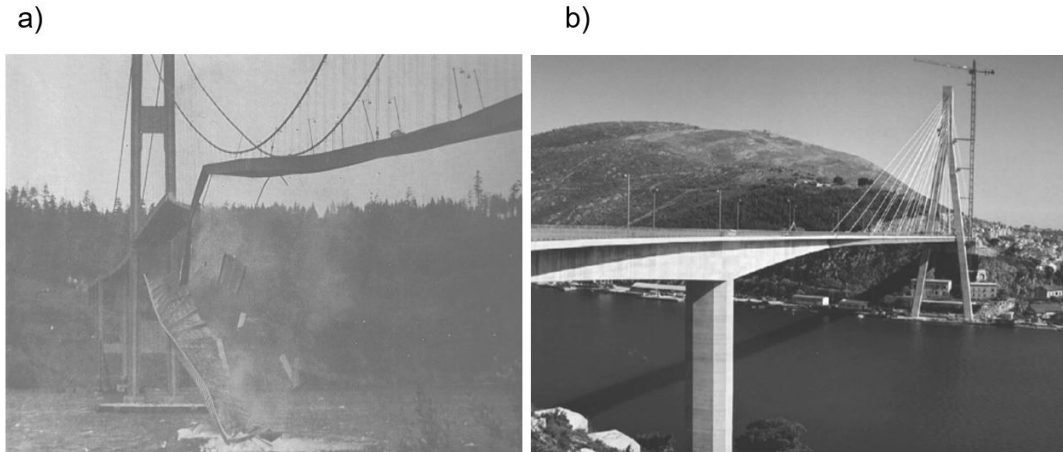


Figure 1.1: Failure to take into account the impact of the wind caused: a) the Tacoma Bridge disaster in 1940 [47], b) significant deformation of the bridge in Dubrovnik in 2005 [130].

1.2) as a multiphysics phenomenon was proposed by Arthur Collar [26]; it is a triangle, whose corners correspond with the types of forces acting on the object in question, and the sides - the phenomena caused by these forces.

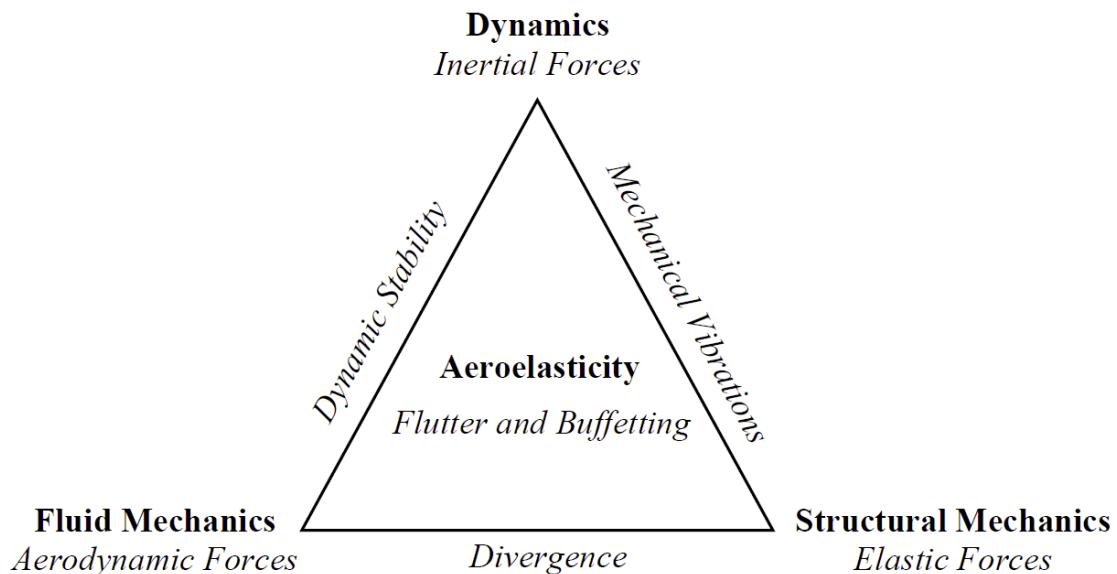


Figure 1.2: Collar's Triangle - a scheme showing aeroelasticity as a multiphysics phenomenon [26]

The flutter phenomenon belongs to the area of the dynamic aeroelasticity, which is the interaction of the structural, aerodynamic and inertia forces. This phenomenon will be described in more detail later in this chapter. Numerical FSI analyses found in the literature [21, 53, 55, 58, 59, 92, 100, 101] usually do not take into account the non-linearity found in structural models. This limits the possibility of simulating such cases like airplane maneuvers, in which large deformations or material non-linearities have a major impact.

There are large deformations of the structure and cases in which there is a non-linear behavior of the structure material. The following is a literature review on the theoretical basis of FSI coupling (Section 2.1), and the computational aspect of aeroelasticity in relation to aerospace applications (Section 2.2).

The basic criterion in modelling the structure-flow coupling is the type of flow. It can be internal flow (e.g. flow in blood vessels (Fig. 1.3a)) and external flow (e.g. streamlining of an aircraft, ship, structure (Fig. 1.3b)).

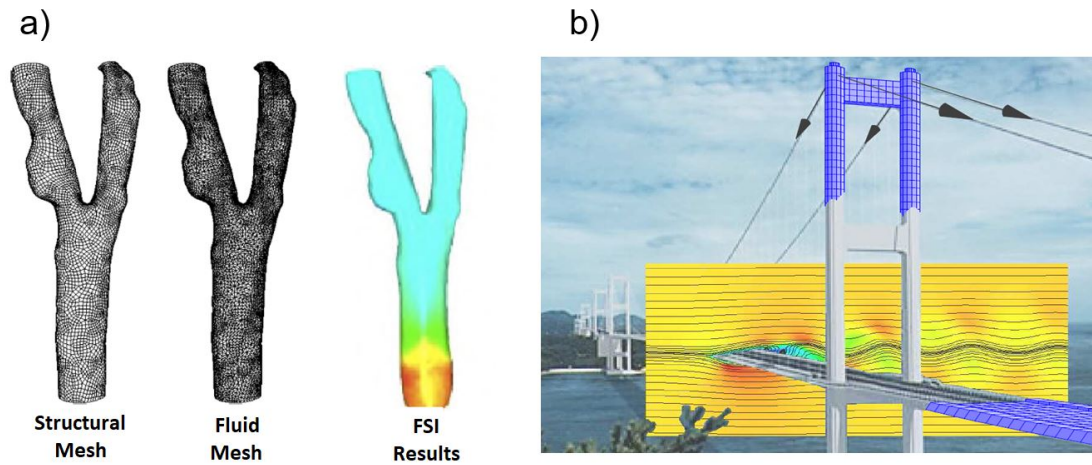


Figure 1.3: Example of FSI coupling modelling: a) for a blood vessel slice [74], b) for a bridge structure [132].

Each of the above-mentioned issues is the subject of numerous studies [129–131]. Increasing development is observed in the area of confined flows in relation to biological tissues. Studies of blood flow in blood vessels have received particular attention [56, 74, 132].

Due to a wide range of topics related to the issues of structure-fluid coupling, the work focuses only on the area related to aviation problems. A review of existing numerical solutions of structure-fluid coupling with respect to aeronautical applications is presented below. Aeroelasticity, understood as the phenomenon of the interaction between aerodynamic and inertia forces resulting from the structural analysis of an elastic body, has been of interest [3] since WWI, when rapid oscillation of the wings of a bomber plane caused by design errors was experienced (Fig. 1.4).



Figure 1.4: The problem of aeroelastic phenomena for the plane (1916) - caused by the lack of stiffening of outer section of the wing [58].

The first definition of FSI as a phenomenon of the interaction of aerodynamic forces on an elastic structure was given in 1955 by Bisplinghoff [55]. According to the author, this phenomenon

is mainly due to the elastic properties of the structure subjected to dynamic loading.

Considering the three domains of mechanics that are taken into account during design works in the aviation industry [129], two types of aeroelastic analyses can be distinguished. **The static aeroelastic analysis**, combining the issues of elasticity with aerodynamics, is an interaction with the omission of the inertia forces of the flowing body, where the quantities resulting from the structural analysis effect the fluid domain. An example of such analyses are stationary wing profile calculations in which the structure deflects due to the forces resulting from the pressure of the flowing fluid. Additionally, the consideration of the quantities resulting from dynamic structural analyses leads to a **dynamic aeroelastic analysis**. In this case, we have to take into account not only the influence of the fluid on the flowing structure, but also the influence of these inertial forces resulting from the displacement of the structure on the disturbance and change of the flow energy. Dynamic aeroelasticity includes many phenomena important for safety in air transport, such as: flutter, buffeting and dynamic response. Flutter is a type of aeroelastic self-excited vibrations of wings, ailerons (in a fixed-wing aircraft) or main rotor blades (in a rotorcraft). The flutter phenomenon occurs when a certain speed, known as the critical speed is exceeded. Even modern aircrafts crash due to flutter. Figure 1.5 shows the occurrence of the flutter phenomenon for a modern F117 fighter.

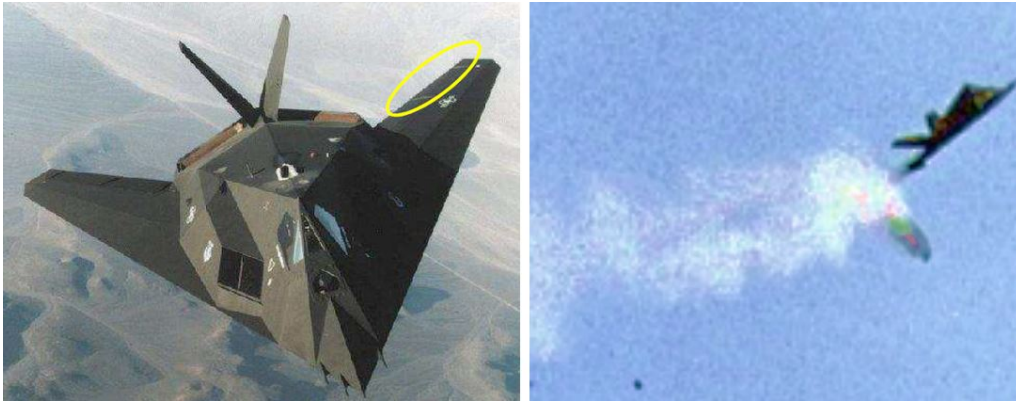


Figure 1.5: F117 aircraft - disintegration of the aircraft structure due to the flutter phenomenon [58].

Buffeting is the phenomenon of vibration of individual components of the aircraft during flight as a result of the flow separation behind the wing or the formation of a vortex path. A dynamic response occurs when a structure is subjected to a dynamic force caused by an aircraft landing or passing through a shock wave after exceeding the speed of sound.

Studying the interaction between the analyzed areas of fluid and structure requires combining programs for flow and structural calculations into one integral system of structural-flow coupling. This combination involves the solution of a number of physical and numerical problems. The physical problems are fluid mechanics and dynamics of an elastic body. The numerical problems include the exchange of information between the flow and the structural code as well as tools for deformation of the flow mesh resulting from the elastic properties of the structure [102]. Every flying object is subjected to aeroelastic phenomena. The possibility of catastrophic phenomena such as flutter must be thoroughly investigated and eliminated before any object is put into use. The research on these phenomena is based on the use of test flights and wind tunnels. These are costly methods and can be carried out in the final stages design. Hence, computer simulations are more and more often used of instead of an aircraft design to investigate the behavior of designed aircraft structures under the influence of flow.

Computer methods allow the study of various aspects of aeroelastic responses and are still the subject of scientific research. For example, many aspects of in computational FSI are related to

the search for common relationships between flow aerodynamics and the dynamics of the structure [21, 53, 55, 59, 61, 100, 101]. This approach has complications due to the interaction between two independent numeric codes. A separate problem to be solved is the way of data exchange between CFD - Computational Fluid Dynamics and CSM - Computational Structural Mechanics codes (Fig. 1.6, the different scale of area discretization and use of different calculation methods for FEM - Finite Element Method and FVM - Finite Volume Method).

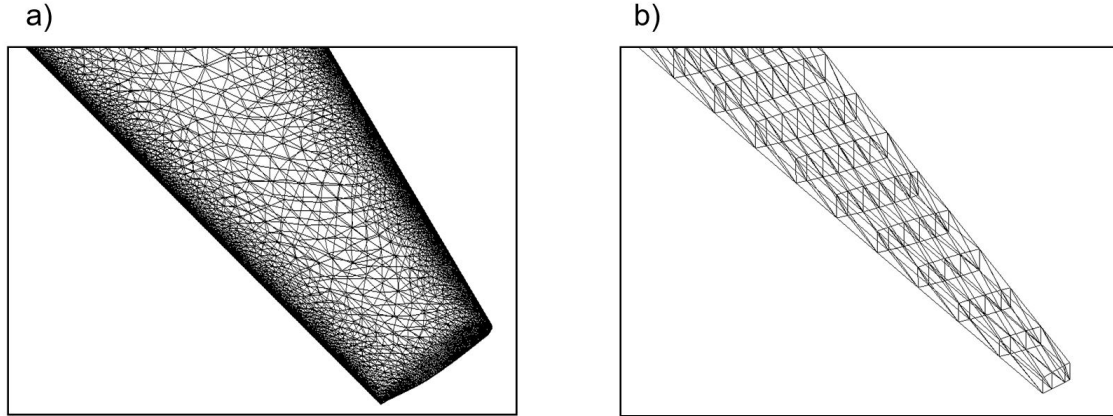


Figure 1.6: Example of discretization differences for a NACA 0012 wing profile: a) flow mesh - "tetra" type elements, b) structural mesh - surface type elements.

An important problem in the analysis of kinematics of the fluid-structure coupling is the description of individual states in relation to two different systems of variables. It is common [53] to use Euler's method - stationary system (CFD) or Lagrange's method - moving system (Computational Structural Dynamics - CSD). Hence the need to develop appropriate data exchange techniques between these systems is appear. It is also a problem to adopt an appropriate time step in the computation which may be different for the flow code and the structure code. It is especially important when conducting a dynamic analysis of the FSI coupling.

1.2 Numerical methods of flutter modeling

Over the years, a number of calculation methods have been developed to enable flutter prediction. Reviews can be found, for example, in the books [26] and [27]. By investigating the development of these methods, it can be stated that depending on the knowledge of aerodynamics and structural calculations and the possibilities of computational methods, the complexity of the models increased, and thus the accuracy of flutter calculations too. Currently, the industry standard is full modeling of both the structure and aerodynamics of the aircraft and interaction analysis as one non-stationary computational process. This study omits historical or simplified flutter models used in aviation and focuses on the latest methods of virtual flutter analysis of the entire aircraft. The numerical description of the interaction between aerodynamic forces, elastic forces and inertia forces was proposed by Farhat [20]. It describes aeroelasticity as a three-domain problem: flow analysis (Eq. 1.1), structural analysis (Eq. 1.2) and flow grid moving (Eq. 1.3). It is defined by the following equations which reflect the essence of aeroelasticity. Additionally denote $\Gamma(t)$ as moving fluid/structure interface boundary:

$$\frac{d}{dt} (\mathbf{V}(\mathbf{x}(t)), \mathbf{w}(t)) + \mathbf{F}^c(\mathbf{w}(t), \mathbf{x}(t), \ddot{\mathbf{x}}(t)) = \mathbf{R}(\mathbf{w}(t), \mathbf{x}(t)) + \mathbf{S}(\mathbf{w}(t), \mathbf{x}(t)) \quad (1.1)$$

$$M\ddot{q}(t) + \mathbf{f}^{int}(q(t), \dot{q}(t)) = \mathbf{f}^{ae}(p(w(t)), \mathbf{x}_\Gamma(t)) \quad (1.2)$$

$$\widetilde{M}\ddot{x}(t) + \widetilde{C}\dot{x}(t) + \widetilde{K}x = \widetilde{K}_c q. \quad (1.3)$$

The symbols reflect the following (physical) entities:

x	displacement or position, depending on the representation of the points in the flow domain,
x_Γ	denotes the restriction of x to $\Gamma(t)$ - which is the same as the position of the wet surface of the structure,
p	represents the pressure field at the interface boundary $\Gamma(t)$,
w	the conservative fluid state vector,
V	discretization solutions for flow equations (Euler or Navier-Stokes) using the finite volume method,
F^c	the vector of Arbitrary Lagrangian-Eulerian (ALE) convective fluxes,
R	the vector ALE diffusive fluxes,
S	the source terms defining the external body forces e.q. gravity and pressure gradient is include as well
q	the generalized displacement vector,
\mathbf{f}^{int}	vector of internal structural forces,
\mathbf{f}^{ae}	the vector of aerodynamic forces applied to the wet surface of the structure,
M	mass matrix of structural model,
$\widetilde{M}, \widetilde{C}, \widetilde{K}$	fictitious matrices of mass, damping and stiffness assigned to a moving flow grid, to prevent undesired interactions between the fluid and its mesh or structure and the moving flow grid,
\widetilde{K}_c	an exchange matrix describing dependencies resulting from the structure movement, interpolated on the exchange surface of a moving flow grid.

The first equation (Eq. 1.1) defines the area of the CFD. The second equation (Eq. 1.2) describes the CSM area of the flowing geometry. And the third equation (Eq. 1.3) is related to the moving of the flow grid. These equations are sufficient to fully describe the FSI phenomena including the flutter. Equations 1.1, 1.2 and 1.3 define the problems of aerodynamic and structural analysis taking into account the dynamics of the flow grid. For example, a linear structural model can be combined with a three-dimensional non-stationary flow model RANS (Reynolds Averaged Navier Stokes) or URANS (Unsteady Reynolds Averaged Navier Stokes) [55]. It is also possible to include a non-linear structural model in equation 1.2. An example of such a solution is the subject of this dissertation and is presented in chapter 5.5.6. The degrees of coupling of computational domains for such specific research problems are divided into [32]:

- fully coupled analysis,
- closely coupled analysis and
- loosely coupled analysis.

A primary polyphysical phenomenon is said to occur when the interaction takes place in an explicitly defined set of phenomena and for the described by (limiting) condition (e.g. aeroelasticity). The same situation occurs in the case of the analysis of the phenomenon of two domains with different degrees of discretization (e.g. the influence of one solid body on the other). The second class includes all those phenomena whose domains overlap, and the combination of phenomena occurs at the level of differential equation considering the full multiphysical approach (e.g. thermal-flow

coupling) [51]. In the fundamental description of the aeroelastic problem (equations 1.1, 1.2, 1.3), the equation combining flow and structural problems is a generalized equation of the flow grid motion (1.3), specifically the right-hand side of this equation [20, 32]. It is a generalized force vector that takes the inertia of the body and its aerodynamics into account. The adopted method of considering this vector implies the degree of coupling of the whole system. An integral system is a set of equations that explicitly describes the completeness of the coupled phenomena. For flutter, the binding equation would have to take two completely different equations (Navier-Stokes equation for the flow and the material law for the structure), other reference systems for each part (Lagrange for the structure, Euler for the flow) and the resulting different stiffness matrices of each system (for the structure the stiffness is larger by one order of magnitude) into account. The finite element mesh in structural calculations is deformed at each time step. The technique that allows bringing two systems to a single reference system is the ALE description, which links the velocity of the flow with the velocity of the deformed mesh [13]. Using this technique, the problem of different reference systems is eliminated, but it is still not possible to create a unified numerical scheme [32]. Integral systems for the aeroelastic analysis are therefore only applicable to small two-dimensional problems with a small number of degrees of freedom. Therefore, the aeroelastic system is decomposed into separate modules, which are solved separately, and the results of one analysis are transferred to the next time step with the use of a time stepping pattern. In this way, the equations describing the flow and structural parts are solved using independent numerical schemes. Data transfer takes place via special information exchange modules. The advantage of this method is the possibility of using different types of computational flow grids (structural, unstructured), overlapping on the border between two domains.

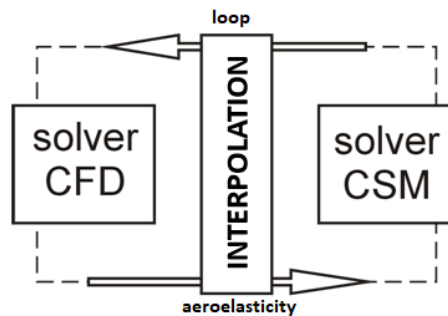


Figure 1.7: Schematic diagram of a freely connected aeroelastic system

Loosely connected systems are built on the principle of independent, cooperating programs connected by the external exchange interface. Data are transferred after the separate convergence of the solution in each program. An example of an external interlinking system is the MpCCI (*Mesh-based parallel Code Coupling Interface*) program, in which the interface is divided into two groups: the first one is used to search for interacting areas of two computational grids, and the other - to ensure convergence of the solution [32]. After the structural calculations are performed, the displacements are interpolated from the structural grid to the flow grid, which undergoes modification under the influence of these displacements. In such a coupled solution of the aeroelastic problem there is no total convergence required (in each program), and the exchange can be performed several times before the solution is determined in a given time step. Then, the bidirectional coupling calculation process is repeated in the aeroelastic loop. The modified flow grid introduced at the beginning of each iteration affects the simulation conditions in the next step. The grid motion included in the flow equation using the ALE description is introduced into the convective Euler flow equation (or Navier-Stokes - equation 1.4 for the viscous flows). Thus the convection velocity changes [13].

$$\rho \left(\frac{\partial \mathbf{v}}{\partial t} + ((\mathbf{v} - \mathbf{v}_{grid}) \cdot \nabla) \mathbf{v} \right) = \nabla \mathbf{T} + \rho \mathbf{b} \quad (1.4)$$

where:

ρ	fluid density,
\mathbf{v}	fluid velocity vector,
\mathbf{v}_{grid}	grid velocity vector,
\mathbf{b}	vector of mass forces,
\mathbf{T}	stress tensor: $\mathbf{T} = -p\mathbf{I} + \mu \left(\nabla \mathbf{v} + (\nabla \mathbf{v})^T \right)$,
p	pressure vector,
μ	dynamic viscosity,
\mathbf{I}	identity matrix.

Using the program for flow calculations taking into account the grid velocity in subsequent time steps, a pressure distribution or a distribution of force vectors in the nodes on the surface of the tested object is obtained. With the help of interpolation tools, solutions are transferred to the exchange surface and then to the structure grid nodes. The interpolated values are interpreted as boundary conditions applied in the structural analysis. The set of nodal displacement of the interface surface modifies the flow grid (in the vicinity of the structural object).

Chapter 2

Tools used in flutter analysis

2.1 Computational Fluid Dynamics - FOI EDGE

2.1.1 Introduction

One of the fundamental parts of FSI calculations is the CFD analysis. This analysis determines loads in the form of pressure and force distribution resulting from the aerodynamics of the investigated object. Based on the example of selected programs adapted to FSI calculations, the basics of flow calculations are discussed. This description is based on CFD codes known by the author, such as FOI EDGE and TAU-Code from the DLR. The latter will be discussed later in section 2.2. However, the described phenomena can be related to the general description of the CFD problem.

FOI EDGE is a computational solver designed to simulate unstructured flow grids. Developed by the Swedish FOI Defense Agency since 1997, it provides solutions to Euler or Navier-Stokes equations for stationary and non-stationary flows [16]. It is used to solve a wide range of CFD problems from subsonic to hypersonic flows. The turbulent flow can be modeled by introducing different models of turbulence including Reynolds stresses models. The partial differential equations used for numerical solution of FOI EDGE system by finite volume method (FVM), which consists of generating non-overlapping control volumes around nodes created by a multi-grid method based on dual grids (called *dual grid*) [28] (based on the original flow model). Thanks to this, the required convergence of calculations is improved. This process is based on the agglomeration of dense volume mesh (primary mesh) elements in order to obtain flow models with sparse discretization (Fig. 2.1).

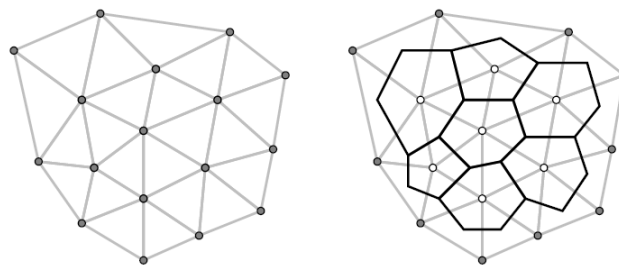


Figure 2.1: Creation of a double flow grid (on the right) as a result of the agglomeration process based on the primary grid (left) [19]

The coordinates of the three-dimensional input (primary) grid are obtained for each node, and the connectivity matrix is determined by the corresponding information of neighboring nodes. In addition, the control surface nS for each edge is attached to the node number when n as the normal vector, and S as the surface area. The control surfaces of all the edges surrounding the node create

a control volume. The surface vector is directed to the center node of volume element. The sum of all the control surfaces form a corresponding volume:

$$\sum_{i=1}^k n_i S_i = 0 \quad (2.1)$$

Equation (2.1) validating the correct element generation is applied to all created dual grid control volumes. In the case of three-dimensional elements, the construction of the control volumes takes place as follows:

- from the center of gravity (centroid), the segments connect the given point with the centers of the walls and edges of the building element
- the control walls that are created in the vicinity of the node create a closed surface.

Each control wall assigned to the edge consists of several control surfaces is described by three points: the geometric center, the center of the wall and the center of the edge.

2.1.2 Governig equations for the flow simulation

Main equations solved in system can be described as:

$$\frac{\partial q}{\partial t} + \hat{C}(q) + \hat{D}(q) = S, \quad (2.2)$$

where the conditions defining the convection and viscosity are described respectively by the operators \hat{C} and \hat{D} , and S describes the flow source. The solution vector q contains the state variables $q = (\rho, \rho u, \rho v, \rho w, \rho E, \rho \phi)^T$ for the density ρ , three velocity components (u, v, w), the total energy E and values describing the turbulence ϕ . The symbol ϕ represents one or more variables defining the turbulence of flow. For example, for a turbulence model with two equations k - ω the variable ϕ describes the kinetic energy of turbulence k and the level of its dissipation ω .

The EDGE flow calculation system can be used for any type of volume element. The main equation comprising the system expressed symbolically in the equation (2.2), integrated over the arbitrary control volume Ω for edge S , is presented as follows:

$$\frac{\partial}{\partial t} \int_{\Omega} q d\Omega + \oint_S [F_c(q) - F_d(q)] \vec{n} \cdot d(\vec{S}) = \int_{\Omega} S(q) d\Omega, \quad (2.3)$$

where $F_c(q)$ and $F_d(q)$ describe the convection and diffusion terms.

Moreover, the viscous flow is estimated by splitting the viscosity operator into the normal derivatives. And is approximated at the edges, and the tangent derivatives using discretization.

2.1.3 Turbulence models used in the CFD FOI EDGE code

In order to analyse turbulent flows in FOI EDGE, the methods of the flow turbulence modeling can be divided into three groups: RANS method (Reynolds averaged Navier-Stokes equation), LES method (large eddy simulation method) and hybrid RANS + LES and DES method (*Detached Eddy Simulation*) [18].

Single-equation Spalart-Allmaras model This model is used to solve only one energy transport equation for the ϵ_T , which is a eddy viscosity. Since the turbulence is characterized by two quantities: the velocity and the Reynolds length. Only one of them is calculated according to this model, therefore an additional parameter y^+ is introduced.

Models based on the definition of the turbulent viscosity with two equations In the following turbulence models, two equations transferring the kinetic energy of turbulence k and some additional quantities (ϵ , ω or τ) are solved. The turbulent description in question is:

- turbulence model $k - \epsilon$ is a two-equation model suitable only for fully turbulent flows. Extensive and quite accurate despite many limitations. The most widely used turbulence model for industrial applications, includes submodels to consider compressibility, resilience, combustion;
- turbulence model $k - \omega$ (**Wilcox**), in which turbulent viscosity is described as

$$v_T = \rho \frac{k}{\omega}; \quad (2.4)$$

- turbulence model $k - \omega$ **for small values of Reynolds number** (LRN), used to explain the effects of damping at the surface of the object in the flow;
- turbulence model $k - \omega$ **Kok TNT**, introduced to limit the non-physical behavior of the undisturbed fluid;
- turbulence model $k - \omega$ **Menter BSL and SST** also used to limit the non-physical behavior of undisturbed fluid; it is a combination of the standard model $k - \epsilon$ (for the areas outside the wall layer) and $k - \omega$ (for the areas inside it). The Menter BSL model is almost identical to the Menter SST model. Only one constant ($\sigma_{k1} - k - \omega$ closure) and the expression for turbulent eddy viscosity are different.

Models EARSM (Explicit Algebraic Reynolds Stress Models) These models are presented as an approximation of total Reynolds stresses (anisotropic Reynolds stress is treated as constant in time and space) and described in the tensor form determining a velocity gradient and the turbulence:

$$\overline{\rho v_i v_j} = \rho k \left(a_{ij} + \frac{2}{3} \delta_{ij} \right), \quad (2.5)$$

where $\overline{\rho v_i v_j} = \overline{c_{ij}}$ – is (defined as the *Reynolds Stress Tensor*) – turbulent stress tensor (Reynolds) in EARSM model, a_{ij} is a dimensionless anisotropy tensor, k is the turbulent kinetic energy and δ_{ij} is the Kronecker delta.

Differential Reynolds Stress Model (DRSM) The energy transfer equation described by the Reynolds stress tensor deriving from the Navier-Stokes equation takes the form of:

$$\frac{D\overline{v_i v_j}}{Dt} = P_{ij} - \epsilon_{ij} + \Pi_{ij} + D_{ij}, \quad (2.6)$$

where P_{ij} – part initiating turbulence, ϵ_{ij} – dissipation level, Π_{ij} – relationship between the pressure and the distortion and D_{ij} – the diffusion part. The initiating part is described by the Reynolds stresses:

$$P_{ij} = -\overline{v_i v_k} \frac{\partial U_j}{\partial x_k} - \overline{v_j v_k} \frac{\partial U_i}{\partial x_k}, \quad (2.7)$$

while the other flow conditions must be defined. In the case of the Reynolds differential stress models (2.6), the energy transport equations are evaluated separately for each Reynolds stress component. In the general case of the three-dimensional average flow, six equations are introduced, taking the symmetry of the Reynolds stress tensor into account. The dissipation coefficient ϵ_{ij} is decomposed into to the isotropic and anisotropic part – $\epsilon_{ij} = \epsilon(e_{ij} + 2\delta_{ij}/3)$, where the total dissipation level ϵ is modeled by the transport equation, similar to model $k - \epsilon$.

DES models and RANS+LES hybrid models This group of flow turbulence modeling methods has been developed for the purpose of the aeronautical simulations, where we deal with the turbulent flows characterized by unsteady stream and vortex motions. In order to avoid the distribution of a large number of elements close to the geometry of the structure occurring in the case of LES (Large Eddy Simulation) simulations for large Reynolds numbers, modeling using the RANS method for boundary layers in combination with the LES method in the remaining area is used. DES and RANS + LES models often turn out to be a good compromise in terms of computational efficiency (RANS) and accuracy (LES).

2.1.4 Discretization in space and integration in time in the EDGE system

The finite volume discretization is obtained by applying the integral formulation of the governing equation. [16]. It is necessary for the control volume surrounding the unknown $U_0\nu_0$ at the node n_0

$$\frac{\partial}{\partial t} (U_0\nu_0) + \sum_{k=1}^{m_0} F_{I_{0k}} S_{0k} + \sum_{k=1}^{m_0} F_{V_{0k}} S_{0k} = S_{t0}\nu_0, \quad (2.8)$$

where m_0 is the number of neighbors to node n_0 . The surfaces S_{0k} enclose control volumes for node n_0 and form the dual grid illustrated in figure 2.2 in 2D.

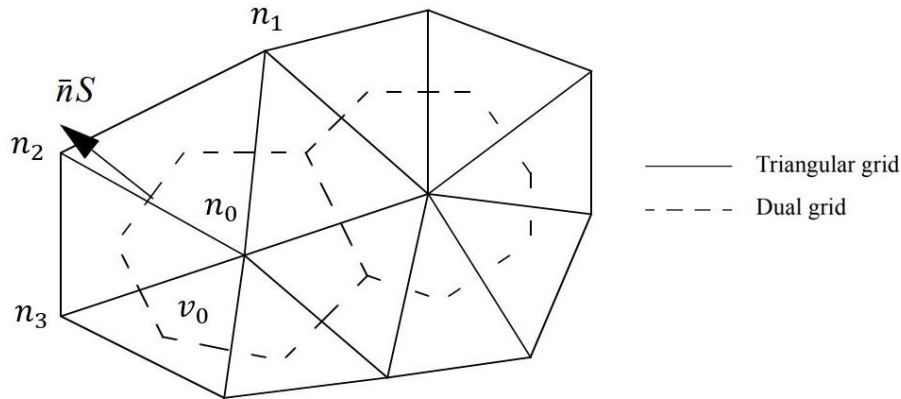


Figure 2.2: The input grid (triangular grid) and its dual grid forming the control volumes for a given triangulation [18].

The flux vectors $F_{I_{0k}}$ and $F_{V_{0k}}$ are computed on the edge consisting of nodes n_0 and n_k where S_{0k} is given. The source n_{t0} is computed directly at the node.

In the case of inviscid flows, a central discretization scheme is applied, taking into account the dissipation conditions. For this purpose, a central scheme is used by means of an artificial dissipation component or the so-called "upwind" scheme. The central scheme is approximated by using the second order central scheme for the Navier-Stokes equations and the "upwind" differential Roe's flow division [16] diagram is used for the turbulence transport equation. Due to the similarity of Martinelli's [126] scaling of the original mesh values, the EDGE procedure describes the dissipation as a value proportional to the local spectral radius in the direction in which the stretching of the grid elements takes place.

In the case of viscous flows, the discretization of space is based on a thin-layer approximation or on the determination of turbulence conditions. The first type contains only the normal derivatives of turbulent parts: $n = (n_1, n_2, n_3)$. The viscosity interactions for momentum equations can be described as follows:

$$\tau_{ij}n_j = (\tau_{ij}n_j)_{tl} + (\tau_{ij}n_j)_{tan}, \quad (2.9)$$

where $(\tau_{ij}n_j)_{tl}$ contains only normal derivatives and leads to a thin-layer discretization in case when this part is included. The total approximation of viscosity conditions will be present if the remaining part, i.e. $(\tau_{ij}n_j)_{tan}$ is added.

Convergence of stationary analysis using the EDGE system is ensured by the use of the 3-stage explicit Runge-Kutta scheme, in which the diffusion part is solved in the first order (step I). To ensure the stability of calculations and to obtain the desired convergence, the local time step is used. This scheme is presented in the form of the equation:

$$\frac{dU}{dt} = F(U), \quad U = (u^1, u^2, \dots) \quad (2.10)$$

where the vectors of unknowns are defined:

$$\begin{aligned} u^1 &= u^n + \alpha_1 \Delta t F(u^n), \\ u^2 &= u^n + \alpha_2 \Delta t F(u^1), \\ &\dots \\ u^q &= u^n + \Delta t F(u^{q-1}), \\ u^{n+1} &= u^q. \end{aligned} \quad (2.11)$$

The coefficients α_i determine stability and order of the Runge-Kutta scheme, which is selected depending on the complexity of the problem.

The local time step calculated for each node n_0 is determined by the formula:

$$\Delta t_0 = \min \left(CFL \frac{V_0}{\lambda_{n_0}} \right), \quad (2.12)$$

where V_0 is the volume and CFL is a condition for the stability of unstable numerical methods modeling convection or wave phenomena, and λ_{n_0} is the integrated convection part described by the following equation:

$$\lambda_{n_0} = \sum_{k=1}^{m_0} \tilde{\mu}_{0k} 2^{n_{\dim}} \frac{S_k^2}{\rho_{0k}}. \quad (2.13)$$

On the edges between nodes n_0 and n_k , the sum of dynamic and turbulent viscosity in turbulent flow is represented by $\tilde{\mu}_{0k}$ [16]. In order to increase the maximum time step, implicit residual smoothing is applied for every residuum and carried out for each solution independently. Smoothing for the residuum of node n_0 can be determined with the use of the equation [16, 18]

$$\hat{R}_0 = R_0 + \epsilon \nabla^2 \hat{R}_0, \quad (2.14)$$

where ϵ is a constant, ∇^2 is a Laplacian, and \hat{R}_0 is a new, smoothed residuum. In order to accelerate the convergence of the solution to a given flow problem, the multigrid agglomeration method is used.

2.2 Computational Fluid Dynamics - DLR TAU-code

2.2.1 Introduction

This chapter describes the most important functions of the DLR TAU-Code software. The previously discussed methods of solving CFD equations for EDGE FOI and models of turbulence are also implemented in the DLR software. DLR TAU-code as a flow-based computational system

has been developed since the late 1990s by the DLR (Deutsches Zentrum für Luft- und Raumfahrt - German Aerospace Center) in cooperation with research and development institutions during many projects (EU Framework Programme FASTFLO, MEGAFLOW, TAURUS). It is a tool used in flow calculations, both static and dynamic, for compressible and in-compressible flows. The computational algorithm is based on the finite volume method and was used to solve the average Navier-Stokes equations. With the use of complex geometries on the basis of unstructured hybrid grids, simulations of subsonic flow and supersonic flows can be performed. Additionally, the system integrates the main solver of flow calculations contains other modules and libraries. Individual subroutines can be started independently using input/output files. One of the most important aspects of the TAU-code system is the high efficiency of parallel computations based on the decomposition of the computing domain and the flow of information using the MPI communication protocol. In spite of the lack of tools allowing the generation of flow grids, the program includes modules enabling their modification, adaptation and deformation. The system uses hybrid nonstructural grids built of elements such as:

- HEXA (hexagonal, used in structural grids),
- PRISM (pentagonal prisms, used in boundary layer modeling),
- TETRA (tetragonal, used in modeling of flow domain without boundary layer),
- PYRA (pentagonal pyramids, used for modeling the transition area between rectangular and triangular elements).

2.2.2 Decomposition of flow grid into computational domains

In order to perform parallel calculations, the flow grids are decomposed into a defined number of computational domains at the beginning of the simulation (Fig. 2.3). It uses a technique of data dispersion between multiple processors - even loading of computer cluster nodes. When determining which part (domain) of the grid will be calculated by a given processor, arrays are created to ensure the data transfer. They contain all the information necessary to update data at the domain boundaries.

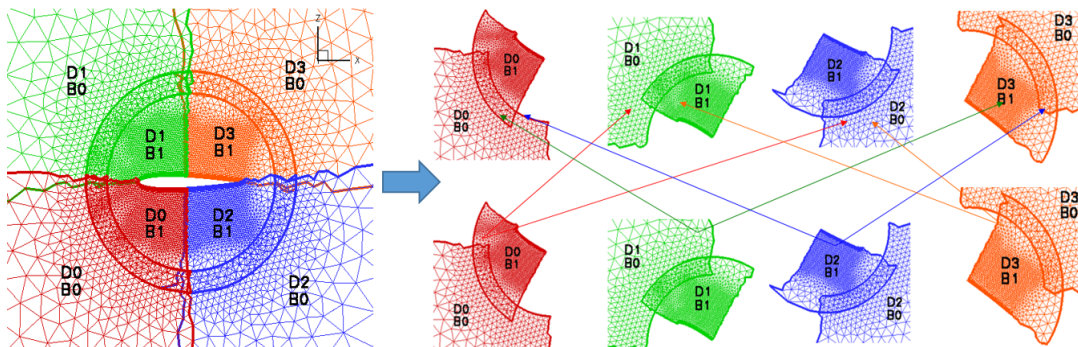


Figure 2.3: Example of division of the flow grid into individual domains based on DLR TAU-Code partitioning [37]

In the case of adaptation, the hierarchy of the grid, which contains information on the density of elements, is entered on all domains. After the mesh division process, the remaining TAU-code modules (described below) are initiated and they calculate the variables in each of the computational domains.

2.2.3 Data preparation (DLR TAU Code pre-processing)

TAU pre-processing is a module that is run only once for the input flow grid (primary) and is based on the multigrid method generating dual grids [chapter 2.1].

The module also generates all element metrics (normal vectors representing the size and orientation of the surface, geometric coordinates of the nodes and control volumes in the case of dual grids). The grid is tested for correctness of elements and negative volumes that can occur in the process of grid deformation are detected. In case of detection of invalid elements in the grid, the calculation process will be stopped. A small negative volume may appear in this process, which will be fixed in the calculations. If the same metrics are retained in the newly created mesh, it can be recalculated according to the same approach of the dense mesh. All information regarding the transfer of data between flow models with different discretization is generated in the agglomeration process.

2.2.4 Calculation solver

The target flow calculation module is based on edge-based dual-cell approach, e.g. on the vertex-centred scheme. Non-viscous flows are calculated using the second order central scheme or the so-called "upwind" schemes - with the use of linear reconstruction for the second order accuracy. In turn, compressible flow calculations use only the second-order central scheme.

Integration over time follows the use of various explicit Runge-Kutta schemes. However, the explicit approach leads to limitations in the Courant-Friedrichs-Lewy (CFL) number range. This results in the necessity of solving a large number of iterations in order to achieve the desired accuracy of calculations, especially in the case of large-scale problems. To avoid these problems, the implicit L-USGS (*Lower-Upper Symmetric Gauss-Seidel*) scheme or the Krylov's subspace method is used. In order to speed up the convergence of the solution, a multigrid algorithm has been implemented.

2.2.5 Flow grid adaptation

Automatic adaptation of the flow grid is an important stage in Computational Fluid Dynamics. The adaptation process consists of two parts: determining the method of refinement of flow grids and searching for areas, where adaptation occurs and determining the degree of their refinement. The operation of the module consists of determining the list of edges of the grid elements and then marking those to be refined depending on the density parameters. In the next step, the iterative procedure marks additional edges. The required refinement cases taking in order to obtain a conformal grid into account. The algorithm included in the DLR TAU-Code system allows to increase the number of unstructured hybrid mesh elements.

2.2.6 Moving grid method – CHIMERA

The method of overlapping flow grids is based on the decomposition of the flow domain into subdomains, with at least one subdomain as a moving subdomain. In this way, the modeling of a given flow problem is simplified. This procedure does not require the existence of a common border between subboundary. A full overlapping ensures the transfer of information and simulation results (Fig. 2.4).

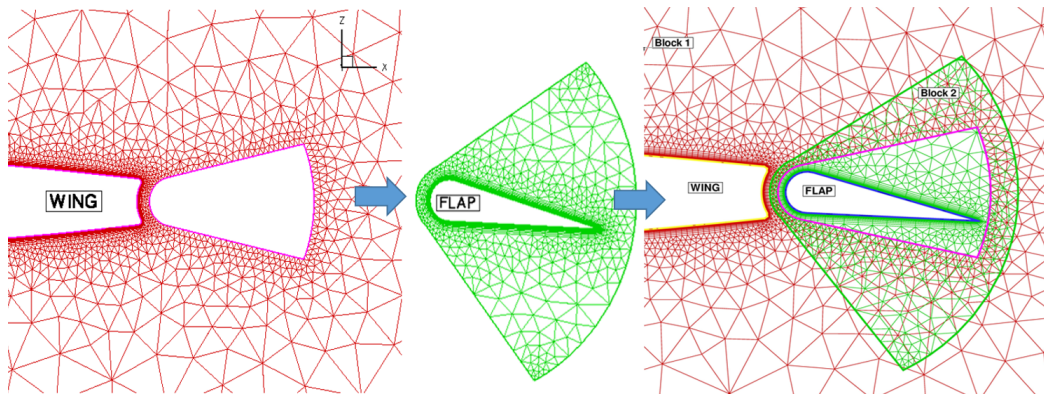


Figure 2.4: Hybrid CHIMERA mesh for the wing with a movable flap [46]

In this way, it is possible to simulate aircraft maneuvers or the flow past the control surface. In order to update the results and edges of moving grids for TETRA type elements, the linear interpolation based on finite element theory is introduced. In the case of other elements (PRISM, PYRA, HEXA), the linear interpolation is used after the remesing of elements into the TETRA elements.

2.2.7 Models of turbulence

The turbulence models implemented in the DLR TAU-Code are based on a linear and a nonlinear approach, described by a one- and two-equation definition of turbulent flows. The standard model of turbulence is the single-equation Spalart-Allmaras model, which provides satisfactory results for a wide range of issues and model SST (Shear Stress Transport) Menter models or $k - \omega$: Wilcox or Kok-TNT. In addition, the nonlinear explicit algebraic Reynolds stress model (EARSM) and the linearized LEA model are also implemented in the DLR TAU-Code system. An additional model is the *Detached Eddy Simulations* (DES) model of turbulence. It is based on the Spalart-Allmaras or SST Menter models and the (*Extra-Large Eddy Simulation*) (XLES) model derived from the large eddy method. It is assumed that the DES model can in principle be applied to any viscous fluid modeling for the turbulent flows.

In order to extend the functionality of the DLR TAU-Code with regard to supersonic and highly dissipative flows, modifications among others stabilization of the solver for large Mach numbers were introduced. Thermochemical equilibrium flows were also implemented.

2.3 Numerical structural modeling

2.3.1 Modal analysis

The natural vibrations in the construction occur when, after its initial excitation, no additional forces are applied. In this sense, each structure with a specific stiffness and mass distribution is characterised by its natural frequencies and corresponding shapes. The equation of motion is as follows [34]:

$$M\ddot{x} + C\dot{x} + Kx = f, \quad (2.15)$$

For the case when no external forces act on the structure, the equation will take the form:

$$M\ddot{x} + C\dot{x} + Kx = 0, \quad (2.16)$$

where:

M – mass matrix,
 C – damping matrix,
 K – stiffness matrix,
 x – displacement vector,
 f – external force vector.

All mentioned matrices are symmetric. In the case of natural vibration $C = 0$, the equation (2.16) takes form of:

$$M\ddot{x} + Kx = 0. \quad (2.17)$$

The general solution of the equation (2.17) can be shown as:

$$x = \bar{x}e^{i\omega t}, \quad (2.18)$$

where:

\bar{x} – vector of normal modes form,
 ω – natural frequency,
 t – time,
 i – imaginary unit ($i^2 = -1$).

After substituting the equation (2.18) to (2.17) we get:

$$(K - M\omega^2)\bar{x} = 0. \quad (2.19)$$

Equation (2.19) describes generalized the eigenvalue problem and has a nontrivial solution if the determinant is equal to zero:

$$|K - M\omega^2| = 0. \quad (2.20)$$

If matrices K and M have dimensions $n \times n$, then equation (2.20) will produce n solutions. Equation (2.19) can be presented in the simplified form as the standard problem describing normal modes. For this purpose, the mass M matrix is triangulated:

$$M = LL^T, \quad (2.21)$$

where matrix L is the upper triangular matrix of the mass matrix M . In addition, it is defined that:

$$L\bar{x} = q \quad (2.22)$$

and

$$H = L^{-T}KL^{-1}. \quad (2.23)$$

Hence the equation:

$$(H - I\omega^2)q = 0, \quad (2.24)$$

describes the problem of the modal analysis.

In numerical tasks, the problem is solved by means of various algorithms, which can be divided into two groups: those finding all eigenvectors and those assuming their range. The first group includes, for example, the method *Tridiagonal QL Implicit* (TQLI) [44], and the other includes such methods as: subspace iteration, iterative Lanczos algorithm [10] as well as Arnolis iterations [2]. In a freely coupled system of calculations of aeroelastic problems such as flutter, the solution to the structural analysis part consists of solving the so-called modal approach [49]. With this formulation of the problem, the vector of initial values $x(t)$ of the structure's grid (here: the

structured model grid or the exchange surface) is represented as a linear combination of constant base mode vectors ϕ_k .

$$\mathbf{x}(t) = \mathbf{x}_0 + \sum_{k=1}^{N_m} q_k(t) \phi_k. \quad (2.25)$$

The $\mathbf{x}(t)$ represents a column vector containing grid displacements of nodes, and \mathbf{x}_0 is a vector of initial values (for $t = 0$). The scalar variables $q_k(t)$ are generalized Lagrange coordinates (modal coordinates). Using the equation (2.25), equation of motion of the structural model (2.15), indispensable in aerodynamic analysis and orthogonality of vectors ϕ_k , we come to a generalized equation of motion:

$$a_k \ddot{\mathbf{q}}_k + 2\zeta_k a_k \omega_k \dot{\mathbf{q}}_k + a_k \omega_k^2 \mathbf{q}_k = \mathbf{Q}_k, \quad k \in [1, N_m], \quad (2.26)$$

where ζ_k is modal damping ratio dedicated to the k -th mode, while

$$\mathbf{Q}_k = \phi_k^T \mathbf{f} \quad (2.27)$$

corresponds to generalized forces. It is assumed that the damping matrix of the structural model \mathbf{C} , which is a linear combination of the inertia \mathbf{M} and stiffness matrix \mathbf{K} , is referred to as Rayleigh damping (proportional damping). The equation (2.26) is a simplification of the diagonal system and, unlike the equation (2.15), it can be integrated without operations performed on matrices. This requires calculating in each step the values of the generalized modal forces Q_k , which together with the modal vectors are defined in the whole structure grid. In contrast, the forces resulting from the flow simulation performed in the DLR TAU-Code are determined only on the exchange surface and these are usually separate groups of nodes. For this purpose, the models are coupled through the transformation matrix \mathbf{H} , which maps the displacements from the structure's grid to the exchange surface and then to the flow grid according to the formula:

$$\phi_k^W = \mathbf{H} \phi_k^S, \quad (2.28)$$

where indexes W and S refer to the contact surfaces of the flow (CFD) and structural (CSM) domains, respectively. According to the principle of energy conservation while maintaining the transformation matrix \mathbf{H} you can formulate the equation:

$$\delta W = (\delta \mathbf{x}^S)^T \mathbf{f}^S = (\delta \mathbf{x}^W)^T \mathbf{f}^W, \quad (2.29)$$

where δW is commonly used for virtual inner work. It means that for each linear displacement the transformation matrix \mathbf{H} has a unique value resulting from the mapping of forces from the CFD grid to the CSM

$$\mathbf{H}^T \mathbf{f}^W = \mathbf{f}^S \quad (2.30)$$

Therefore, the equation (2.27) shows that the magnitude of modal forces Q_k is dimensionally the work integral invariant for the transformations given in equations (2.28) and (2.30). For each modal system it is necessary to find the appropriate linear transformation and to calculate the set of modes of modal vibrations transformed into the exchange surface. This is possible using information about the forces contained in the name Q_k . The programs, which implement the structural calculations using the modal method in the aerodynamic testing system, are the AE_SMS and AE_UMS (AErcoupling Steady/Unsteady Modal Solution modules). They were made available by a partner of the Poznan University of Technology team, EADS Germany (European Aeronautic Defense and Space Company) during the TAURUS project. The module AE_SMS is used to solve stationary problems and AE_UMS is applied for non-stationary problems.

2.3.2 FEM method – MF3 solver

MF3 is a program used to calculate the problems of solid state mechanics, belonging to a broader package of numerical solution using the finite element method (FEM). It was developed by the team of the Poznan University of Technology within the scope of the TAURUS project. In addition, interfaces connecting this program with numeric information exchange tools have been developed. The MF3 package is used for scientific research in areas such as:

- flow stability,
- flow problems modeled by Navier-Stokes equation,
- POD analysis (*Proper Orthogonal Decomposition*).

The solver uses its own data storage format – finite element meshes and a description of the problem. In order to facilitate the exchange of models from or to available commercial environments, such as Femap/Nastran or Abaqus, dedicated codes have been developed. Other aerodynamics systems:

- NLR FI,
- MpCCI,
- AErocoupling modules.

are integrated in data exchange process.

The MF3 program is a non-linear, non-stationary FEM solver. The input data is read from a file with information about geometry, boundary conditions as well as material and geometrical properties. On this basis, the element matrix is built. The description of the geometry is a set of information. The coordinates of nodes in space and the mutual relationship between them in the form of a matrix, define each of the finite elements. Material and geometric properties are grouped, to which the element number is then assigned.

MF3 supports the following types of elements:

- mass,
- rod,
- beam,
- plate (first order quadrilateral, first order triangular),
- three-dimensional tetrahedral (first order, 4-node, second order, 10-node),
- RBE (*Rigid Body Element*) – without mass, with infinite stiffness.

Additional files are used to provide settings into the solver and manage it during simulation.

All files (control and finite element meshes) are written in text form.

Control files allow modifications to:

- the default level of convergence of calculations,
- number of timesteps, initial and final time as well as timestep,
- calculation type (stationary/nonstationary/explicit problem),
- coefficients of numerical models – Newmark's scheme, Rayleigh's model [48],
- number of calculated eigenvectors and eigenvalues.

In non-stationary calculations initial conditions are required. These are defined by introducing to the solver information on initial displacements and the time of simulation in which they were made. Another option is to initiate calculations by defining initial conditions in the form of force. The MF3 solver uses an incremental algorithm for solving nonlinear equations. The solution of linear equations (static and dynamic theory of elasticity) is obtained in one step. The basic technique to solve this problem is the Newton-Raphson method. However, in the case of solutions of linear equations, it is solved iteratively until the required accuracy is achieved. The nonlinear equation is solved using the Lanczos method. For hyperbolic or dynamic problems over time, a second order derivative over time is also used. Parabolic problems are solved by the methods of progression in time. In the case of hyperbolic equations, like the generalized equation of motion (1.3), the standard method of time integration applied - the Newmark approach.

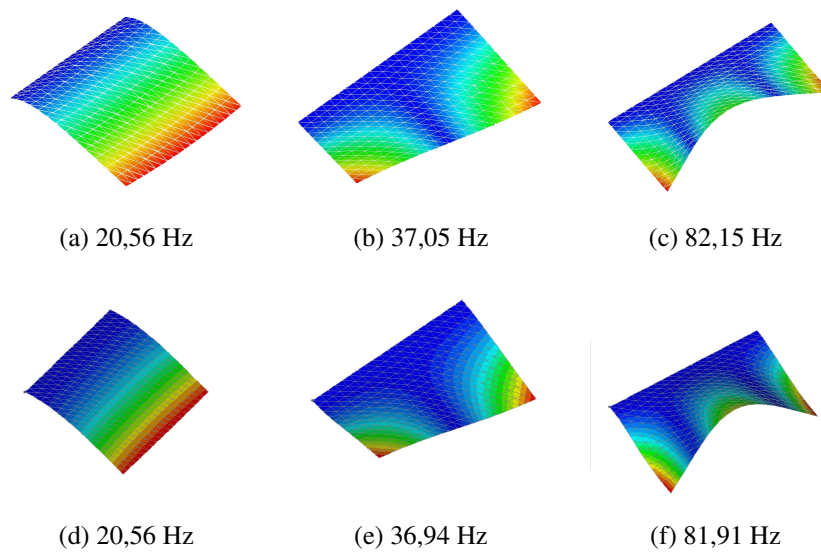


Figure 2.5: Comparison of the results of the natural vibration analysis (form and frequency) obtained using the MF3 program (a – c) with the results obtained from MSC / Nastran (d – f) for steel [43].

In the Fig. 2.5 an example of the explicit problem for the cantilevered plate elements (CTRIA) is presented. As demonstrated in [42], the solver results of structural problems are consistent with the results obtained using commercial programs. Flat elements of the shell type were used.

2.4 Coupling tools

2.4.1 Introduction

Data exchange between the flow grid and the structure grid (and vice versa) is not a trivial process. Each domain is solved at the level of differential equations using different techniques: the finite element method for the structure of the studied object and the finite volume method for the flow around it. The resulting differences in the discretization of each model cause that data for exchange are assigned to various, often inappropriate areas. In order to correctly carry out the data transfer between the two grids, it should be indicated in which regions the models work together. Using programs or coupling modules, you first need to search for corresponding pairs of domains on each mesh, and then interpolate values between these domains. The first issue is solved using algorithms to search for the closest neighborhood/proximity. Both models must be located in the same global coordinate system. The second task, data interpolation, is performed using conservative or non-conservative methods – depending on the type and direction of the interpolated physical quantity. In order to improve these two processes, some approaches use the (so-called) exchange area [23, 43, 48].

2.4.2 Closest proximity search

Searching for the closest neighborhood is the process of assigning a group of nodes (or elements) of one area to a group of nodes (or elements) of another area. This is an indispensable procedure for two grids with different degree of discretization (defining the data exchange). Different cases of interpolation problems require different types of interpolation schemes (Fig. 2.6). There are three possible dependencies [23]:

- node–element – in case of standard interpolation method,
- element–element – in the case of interpolation involving the overlapping of two areas,

- node–node – for overlapping meshes or interpolation based on search for the nearest neighbor.

In order to use a standard conservative or non-conservative interpolation method, nearest elements to each node of the first domain have to be established. Next, the nearest elements belonging to the second domain should be determined. Then the nodes is projected onto the designated area of the elements. The node can be projected inside the element or outside the element. Therefore, it is necessary to take into account the set of criteria according to which a given node will be included in or excluded from the interpolation process or take into account its impact in a different way.

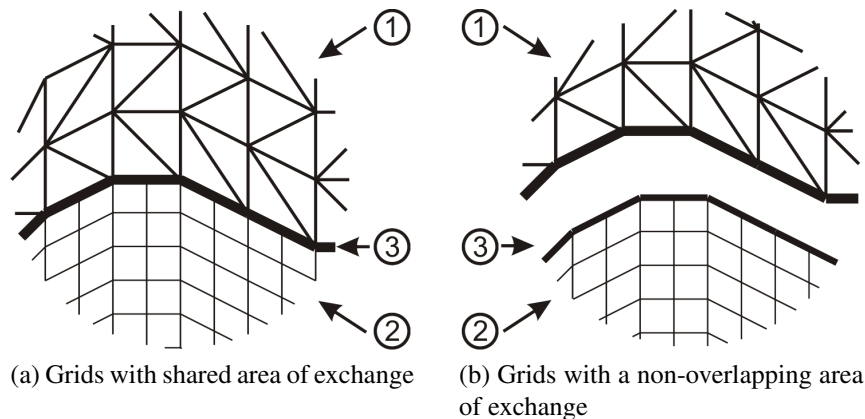


Figure 2.6: Locations of cooperating areas (on the example of two-dimensional meshes): a) shared and b) independent areas; 1 – first grid, for example non-structural, 2 – second grid, for example structural, 3 – area (line) of exchange [43]

The second group includes the exchange based on the element definition. The areas of cooperating elements of the two models are searched. One element of the grid corresponds to several elements of the second grid. Also in this case, it is necessary to project this element to the cooperation area and apply criteria for the selection of elements for interpolation (or distribution of values from the element by weights). The third dependency applies to models with a common contact surface. For a node from one grid, the closest one from the second grid is searched and the interpolated physical entities is passed directly to it. The problem of finding the nearest proximity is solved by means of different algorithms. One of the simplest is line search. As shown in [23], the working time of such an algorithm grows rapidly proportional as the amount of data increases. Algorithms based on the division of the searched area into smaller ones, like *kd-tree* [24] or *octree* (or *quadtrees* for a two-dimensional problem [39]) belong to the logarithmic class. This means that the program works slightly slower as the size of the grids increases. As shown in [8], the *kd-tree* algorithm for two directions is more efficient than the *quadtrees* algorithm considered to be currently the fastest. The disadvantage of the *quadtrees/octrees* algorithm is the ability to search only in two/three dimensions, while the *kd-tree* algorithm, is suitable for multidimensional sets.

2.4.3 Data interpolation

After determining the domains, in which the data exchange between the grids of the aerodynamic calculation system takes place, the interpolation procedure is called. This process is more complex when a relative movement of the models is present. Then one of the following dependencies occurs:

- area deformation – the grids are modified as a result of changing their position from one to the other,

- slipping of two contact surfaces – the meshes move relative to each other, but they do not deform,
- secondary discretization – one of the meshes (or both) are fully or partially are generated.

In order to apply the correct interpolation method, it is necessary to define the type of data exchange. In the structural-flow coupling, a pressure distribution on the surface needs to be transferred from the flow side to the structure. From the structural side, displacements field are determined based on aerodynamic loads on the flow side. In addition, the important is a type of element (beam, plate e.q.), in the data exchange which the interpolation will be performed at the space in which the element is defined (two- or three-dimensional) should be taken into account:

- conservative (e.g. standard, Shephard), used when the rules of conservation of momentum, energy and flow continuity are valid or when some initial value needs to be distributed by preserving the sum of the partial values;
- non-conservative (e.g. standard), used when the behavior of the output variables is not a priority or when values from a certain area should be transferred to one discrete element, e.g. temperature distribution.
- closest proximity - interpolated values take the value of the nearest node.

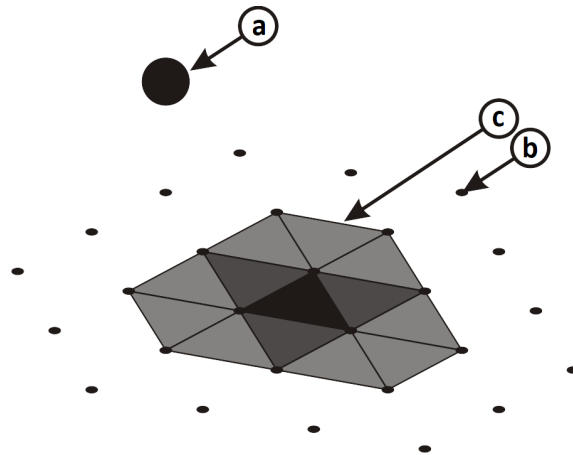


Figure 2.7: Shephard interpolation method: a – node from first grid (e.g. CFD), b – node from second grid (e.g. exchange surface), c – closest proximity of elements from second grid for the node from the first grid, with weights taken into account (darker color means higher weight – element of closer proximity) [43]

All methods based on the node-element dependency are called standard. In the standard conservative interpolation method, the node is projected to the target element, and then the source value is passed to the nodes of this element taking weights into account. The Shephard interpolation method (inverted weighted distances, figure 2.7) is based on the distribution of the initial value into several nodes including weights (2.31); the sum of these values is equal to unity (2.32) [9, 23, 39]. The weight value is determined after solving the (so-called) weighting function N_i [23], whose arguments are usually the distance s_i between the output node and the target node. Distances between the elements (nodes) for which interpolation is performed and the number of these elements (nodes) are determined during the operation of the search module of corresponding pairs (Fig. 2.8).

$$P_i = \sum_{i=1}^N Q \cdot w_i \quad (2.31)$$

$$\sum w_i = \sum_{i=1}^n N_i(s_1 \dots s_n) = 1 \quad (2.32)$$

where:

P_i – target value on node

Q – input value,

N_i – weight function,

w_i – (value) weight,

s_i – distance between the flow grid node and the exchange surface element,

n – the number of elements in the proximity where interpolation takes place.

The weight w_i in Shephard method is defined as follows [9]:

$$w_i = \left(\frac{1}{\sum_{i=1}^n s_i^k} \right) \cdot s_i^k \quad (2.33)$$

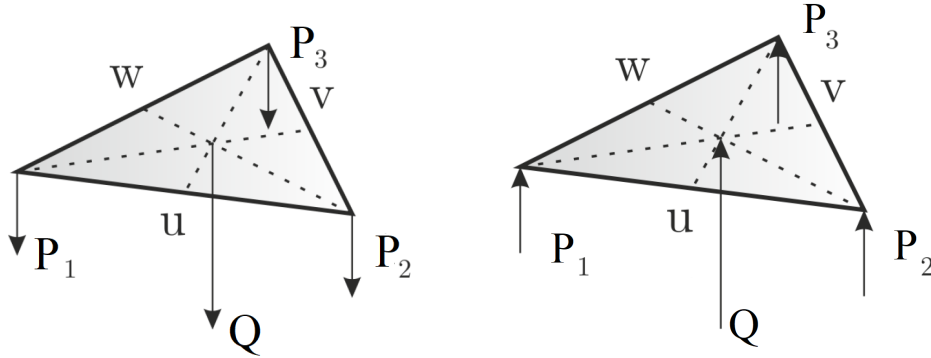
where:

n – the number of elements in close proximity where interpolation takes place,

s_i – distance between CFD grid node and exchange surface element,

k – exponent determining the influence of the nearest environment elements; the higher its value, the greater is the weight of the proximal elements compared to the more distant ones.

The value of the weight coefficient decreases as the distance between two nodes increases, and increases with the increase of the coefficient k .



(a) Conservative method: source data Q is interpolated into target data P_i

(b) Non-conservative method: source data P_i is interpolated into target data Q

Figure 2.8: An example of a standard interpolation based on the definition of a four-sided element [23]

The standard non-conservative method of interpolation, consists from many output values, located in the element's nodes, are referenced to one value located at a point inside in this element. [23]. This point is the node of the target grid, previously projected the element.

$$Q = \sum P_i \cdot w_i \quad (2.34)$$

$$\sum w_i = \sum N_i(u, v, w) \neq 1 \quad (2.35)$$

where:

P_i – input values,

Q – target values,

N_i – weight function,

u, v, w – local coordinates,
 w_i – variable weight.

When using non-conservative interpolation methods, the sum of weights is not equal to one.

2.4.4 Available aeroelastic tools

The Chair of Virtual Engineering in Poznan University of Technology has several tools for data exchange in a closely coupled aerodynamic system. Modules and programs have been made available by partners of the Poznan University of Technology team during the TAURUS project. The main task was to develop a MF3 structural calculation program and an interface connecting this program with the entire aeroelastic system. In this way, unique tools used in the system for flutter calculations were obtained. Available tools are:

- NLR FI,
- MpCCI,
- Modules f2s_pp, s2f_pp,
- *AErocoupling modules*.

The FI program developed by the NLR (Dutch National Laboratory for Space Research), interpolating aerodynamic forces and structure displacements, was based on the *spline* curve method. Exchange between flow and structural programs is carried out using text files. The structural program is started directly from the FI program. The compatibility of the FI module with the TAU-code system is also done through files, however, it is not necessary to join these two programs into one. As shown during TAURUS project [42], the FI program returns reliable results in aeroelastic analysis. The geometric method of data exchange is correct for finite element meshes with a non-overlapping contact area. The disadvantage of this approach is the long exchange process.

The MpCCI (*Multi-Physics Code Coupling Interface*) program, developed by the Fraunhofer Institute in Germany, serves to exchange information using the mesh topology. The program allows interpolation of data between grids with a matched or unmatched exchange area. The exchange process consists of searching for cooperating pairs of areas (implemented algorithms are *octree* and *kd-tree*) and interpolations (standard methods) [22, 23]. MpCCI is able to work without creating additional files (directly in the computer's memory), which greatly speeds up the process of data exchange. This is possible because systems for structural and flow calculations are run directly from the MpCCI program. It is also possible to choose a set of commercial applications to perform multidisciplinary simulations, but the use of any program is complex. Software developers can adapt their own source code to work with the exchange module. As a result of the cooperation of the Poznan University of Technology team with the DLR team, the TAU-code flow calculation program was adapted to work with the MF3 structural calculation program using MpCCI. According to the research carried out as part of the TAURUS project [42], MpCCI is very good in exchanging data between models with a corresponding area of influence. However, in the case of grids without a shared contact surface, this module generates incorrect data for the deformation module, therefore, this aeroelastic simulation cannot be considered correct.

The modules f2s_pp and s2f_pp were developed at Poznan University of Technology [41]. The developed interpolation method is included in the group of algebraic methods and the process itself has been applied only to triangular elements. In order to apply the principles of general mechanics, the finite element mesh is assumed to be a rigid body. The tests show that this method works well in cases with small displacements. The disadvantage of these modules is the long search time of cooperating areas.

The modules ae_f2s and ae_s2f were provided by EADS Germany (*European Aeronautic Defense and Space Company*). These solutions are based on non-deformed meshes and the use of so-called *exchange surface*, defined as a fragment of the structural model closest to the fluid-solid

boundary surface. The contact surface of the flow model is determined at each iteration. The modules enable interpolation of data between grids with a matched and unmatched area of exchange for flat and one-dimensional elements. The data is transferred using files containing results obtained from other components of the aeroelastic dynamic calculation system. Without the need to access sources-codes of every program solving the structural or flow-related problem. In the *ae_f2s (AErocoupling Fluid to Structure)* module, aerodynamic forces are interpolated using the Shephard method on the exchange surface elements. The pairs of cooperating areas (CFD node - elements of the exchange surface) are determined during the *ae_init (AErocoupling Initialization)* module using the method of searching the closest proximity with the use of a linear algorithm. Then, the forces from the exchange surface element are interpolated to each of the nodes. The value of force in the exchange surface node is the vector sum over all elements belonging to it. Displacement interpolation is carried out using the *ae_s2f (AErocoupling Structure to Fluid)* module). In order to accelerate the interpolation process, the surface grid is projected onto the target grid and then displacements for a given surface replacement element are interpolated using a standard, non-conservative method on the flow grid node. As shown in [48], the aerodynamic system using these tools works well during numerical simulations. The values of forces and displacements are correctly interpolated and (thus) the mesh is properly deformed.

2.5 Grid deformation tools

2.5.1 Introduction

In modern flow simulations, the problem of dynamics of the grids plays a significant role in the case of free surface flows, forced vibrations or multidisciplinary problems (fluid-structure interaction). The key step in the calculation is the deformation of the flow grid during time-integration throughout the non-stationary simulation. In this process, the coordinates of the internal nodes are updated as functions of surface displacements including grid quality control. A correctly deformed mesh consists of displaced and modified elements that maintain the connectivity (matrix) and are within certain bends (no overlap, flatness, zero volume). There are many methods of deforming grids, which can be used to solve the above problem correctly; most of them can be divided into two main groups [33]:

- methods used in the case of meshes with variable link matrices, based on a simple interpolation of the flow of the entire domain by refinement or unfolding of the flow grid; the change in the number of elements ensures an appropriate level of quality, that is the appropriate density of the distribution of nodes, necessary to carry out the simulation of a specific physical phenomenon;
- methods used for meshes with fixed link matrices, based on very complicated interpolating algorithms; with their use, the required correctness of the grids during the interpolation process is ensured with the number of grid elements remaining constant.

Fig. 2.9 shows an example of flow grid deformation for the wing example. On the right, a cross-section and grid before and after deformation are shown. The deformation is based on the displacements of the CSM model provided by the interpolation tools.

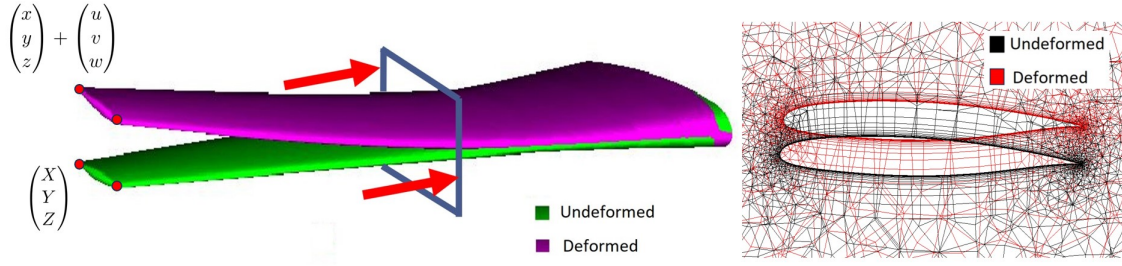


Figure 2.9: Example of mesh deformation for wing. The initial configuration - undeformed and a final configuration after modification - deformed). [12]

The general approach to the deformation of the flow domain can be presented in the form of:

$$\begin{pmatrix} X \\ Y \\ Z \end{pmatrix} = \begin{pmatrix} x \\ y \\ z \end{pmatrix} + \begin{pmatrix} u \\ v \\ w \end{pmatrix}, \quad (2.36)$$

where $(X, Y, Z)^T$ – coordinates of the nodes of the undeformed mesh, $(x, y, z)^T$ – coordinates of the deformed mesh.

The dependency (2.36) is used for each node with the displacements in the flow grid $(u, v, w)^T$. The distribution of displacements can be determined using the least square method. In this way, correct angles between the edges of the elements forming the mesh are ensured. Such a distribution pattern, however, corresponds to the orthogonal mapping. In the case of the space $(X, Y)^T$ and $(x, y)^T$ of the initial and deformed grids a conformal mapping occurs between them and to this end the Cauchy–Riemann equation is used.

$$\frac{\partial x}{\partial X} - \frac{\partial y}{\partial Y} = 0, \quad \frac{\partial x}{\partial Y} + \frac{\partial y}{\partial X} = 0. \quad (2.37)$$

For least squares method it will not be possible to determine the correct boundary conditions, if the deformation of the grid is presented in a generalized way (equation 2.36), which makes it impossible to find the correct solution. Therefore, a function is created using the least-squares method, which must be minimized (in order) to obtain a grid that meets the condition:

$$I = \int ((u_X - v_Y)^2 + (u_Y + v_X)^2) dX dY. \quad (2.38)$$

Another method of deforming flow grids is the elastic analogy of the solid body presented by Lynch and O'Neill [40]. It considers the flow grid as a solid body with elastic properties. The deformation of the grid is then described by the function defining the energy of the deformation.

$$I = \int (u_X^2 + (u_Y + v_X)^2 + v_Y^2) dX dY \quad (2.39)$$

In the case of a spring analogy, the current most popular method is treating the connection as a system of springs. Each edge forming an element, is represented as an elastic element with a certain stiffness. The energy of straining the mesh is determined by each spring, and the function describing the deformation is

$$I = \sum K_{ij} ((u_i - u_j)^2 + (v_i - v_j)^2), \quad (2.40)$$

with K_{ij} as the spring stiffness.

This shows that the shorter the edge, the stiffer the spring element. The dependency between the stiffness K_{ij} and the distance L_{ij} combining two points i,j can be generalized to the form:

$$K_{ij} = L_{ij}^M, M < 0. \quad (2.41)$$

According to Batina [5], the exponent M should be -1 . However, if the deformation is so large that it can cause elements to intermingle, then the value of M should be reduced to prevent intersections of edges that generate incorrect grid cells. An extension of this procedure enrich the model with torsional springs, which also allows to control angles between the edges. In the case of non-structured meshes, the deformation methods are most often based on the analogy of springs (linear or torsional) or on a linear elastic analogy.

2.5.2 Deformation module used by DLR TAU-code

In order to correctly deform the flow mesh resulting from changing the position of the structural mesh of the structure to aerodynamic loads in the FSI analysis, the DLR TAU-Code deformation module is used. The input data for the mesh modification process is the unstructured hybrid mesh and the geometry point displacement vectors. For the remaining grid points, it is required to provide input parameters in order to define the behavior of its boundary. The nodes can be fixed, they can move freely or can be projected onto surfaces (e.g. on the plane of symmetry) after calculating their displacements. The resulting information from the deformation is a new flow grid with the new coordinates of all nodes taken into account and maintains the unchanged of element connectivity matrix. In the first stage, the algebraic method was used to avoid time-consuming iterative solutions of many equations used in the spring analogy method or in a linear elastic analysis. The process consists of the following steps:

- sorting all nodes of the grid, taking the distance from the moving (deforming) surface into account;
- loop over all nodes, where the new displacement of each node is the average displacement of the neighboring points that have already been deformed; the average offset D regarding points i and j is described by the weights of the length of the intersecting edges L :

$$D_i = \sum_j \frac{1}{L_j} D_j \quad (2.42)$$

The scale is a function of the ratio between the local displacement and the cell sizes around the grid point. It is used to reduce the displacements by a fraction of the local cell sizes in order to decrease the mesh deformation with increasing distance from the deformed surfaces. Therefore for each grid point a minimum height of the surrounding elements is computed and stored as length scale. If the local point displacement D is smaller than a fraction (e.g. $K = 0.1$) of this length L the local displacement is reduced by $D = D * D / (K * L)$, where $*$ denotes the element wise multiplication respectively. In the case of parallel flow analysis, individual deformation steps are counted on each calculation domain; each of these domains contain one layer of overlapping elements. Displacements are calculated inside each domain, and variables in shared areas are updated as a result of data transfer with the neighboring domain corresponding to the given shared points. The algorithm is repeated until the displacement values of points in shared areas in two successive iterations are unchanged. On average, one loop takes 20 to 50 iterations, depending on the complexity of the problem. In order to increase the efficiency of implementation of this method, the algorithm **calculates** the distance between grid nodes and the nearest point lying on the contact surface with the structural model used.

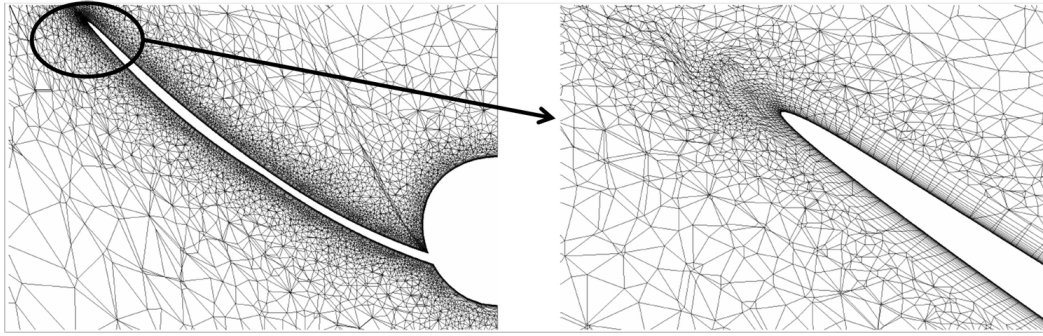


Figure 2.10: Example of mesh deformation in the TAU-Code system module at the maximum wing deflection (left) and a detailed flow mesh at wing tip after modification (right) [12]

The second stage of the deformation in the DLR TAU-Code software is the repair of the deformed mesh. The algorithm searches for areas consisting of defective elements and their properly defined elements surrounding them. In the properly defined space the initial and deformed mesh, the volume interpolation method is used, which allows the reconstruction of degenerated cells to the original form (before deformation). This process requires a short calculation time, only if there are small areas containing degenerate elements. Otherwise, the computational cost of improving the grid increases quadratically with the number of nodes included in the area to be improved. Then, the areas are divided into smaller ones, numbering about one thousand elements and interpolation with the spline functions is used in each of them separately, which allows to reduce the computing expenses. There are cases where the described method is insufficient to create the correct mesh; then, before repetition of interpolation, the regions under repair are extended with an additional layer of neighboring cells. This process continues until all elements are repaired.

2.5.3 Deformation module AE_DEFVOL

AE_DEFVOL delivered as part of the TAURUS project by EADS Germany is a module enabling deformation of the flow grid in accordance with the movement of the structure. The method is based on a spring model and relies on efficiently moving the flow grid elements without creating negative volumes. However, these procedures are very complicated in terms of computation. They are mainly used in the case of deformation of unstructured meshes, in which structural three-dimensional interpolation methods cannot be used. Input data in the process of modifying the mesh using the AE_DEFVOL module is a file concerning displacements of boundary nodes (located only on the changing surface) and the primary flow grid on which the numerical simulation was carried out. In the first stage of the module's operation, the quality of the primary mesh is checked. Creating correct quality metrics is an important stage in the deformation process of flow meshes for which the discrete Jacobi the matrix J_m is calculated for each element m . The element quality G_m , is defined as:

$$G_m = J_m^T J_m. \quad (2.43)$$

The next stage of the deformation process is the determination of new coordinates of the mesh nodes. There are two cases: the deformation of the non-adhesive mesh (only TETRA type elements) and the deformation of the viscous (hybrid) mesh in which the loop over the elements and nodes takes place from the nearest moved geometry to the furthest ones. The process consists of the following steps:

- defining the number of nodes for which the displacement is known (given in the input file or calculated earlier on another element);

- running a subroutine to estimate the initial displacements and coordinates of the nodes to be moved; for this purpose, mean coordinates and displacements (translations and rotations) of already moved nodes are determined;
- calculation of target displacements and coordinates using a spring analogy; this step is based on the iterative equation

$$x_i^{new} = x_i^{old} + \delta_i, \quad (2.44)$$

where x^{new} and x^{old} are the coordinates of the mesh nodes before and after the i element displacement and δ_i is a displacement, calculated using the following formula:

$$\delta_i = \delta'_i - \bar{\delta}_i, \quad (2.45)$$

where $\bar{\delta}_i$ is the mentioned average displacement and the variable δ'_i is described by:

$$\delta'_i = \frac{\sum_{j=1}^{v_i} \alpha_{ij} \delta_j}{\sum_{j=1}^{v_i} \alpha_{ij}}. \quad (2.46)$$

Equation (2.46) describes the displacement with the use of a modified spring analogy method, because i the number of the modified node δ_j – known displacement of j -th node. The α_{ij} – spring elements stiffness **are** inserted between nodes i and j :

$$\alpha_{ij} = \frac{1}{\sqrt{(x_i - x_j)^2 + (y_i - y_j)^2 + (z_i - z_j)^2}}. \quad (2.47)$$

In this way, the coordinates of the new grid are obtained.

In the second case, when we deal with hybrid grids, deformations must occur on all elements. Due to the variety of elements in the grid, the PRISM type elements are on the surfaces of to the geometry elements that are deformed and the deformation process starts from there. Then, the PYRA type elements are moved, and finally the TETRA elements. The algorithm works according to the scheme:

- searching the elements of the wall layer directly on the surface of the deformed geometry and determining the number of nodes for which the displacement is known (given in the input file or calculated earlier on another element),
- determining the distance between triangular faces in PRISM elements,
- calculation of target displacements and coordinates using the spring analogy discussed above (analogously to the first case),
- searching for TETRA type elements and determining the number of nodes for which the displacement is known (given in the input file or calculated earlier on separate element),
- starting a subroutine forecasting the probable displacements and coordinates of nodes to be shifted,
- calculation of target displacements and coordinates using a spring analogy (analogously to the first one).

The final stage of the AE_DEFVOL module is to check and possibly improve the deformed mesh. The main criterion is the previously described condition of non-negative and non-zero volumes. Each element, regardless of the type, is evaluated and checked. Damaged elements are subjected to relaxation by determining the weights of displacements of nodes forming a given cell. If this procedure is not successful, the element remains undeformed and the average distances resulting from the movement and changes of neighboring elements are moved – the procedure will lead to **element stiffening**.

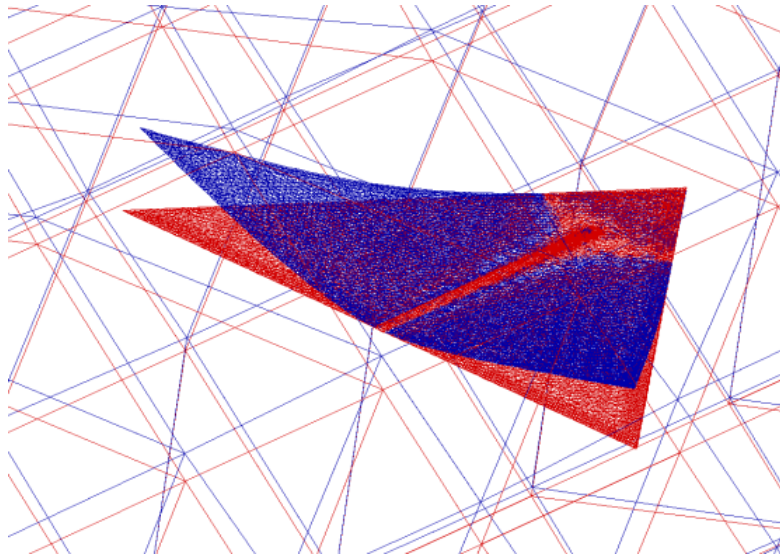


Figure 2.11: Example of grid deflection in AE_DEFVOL module, based on structural displacements [47]

Therefore, the deformation process carried out by different modules should be [47]:

- effective for complex hybrid grids,
- accurate, i.e. should ensure the creation of meshes with acceptable quality in the flow analysis process,
- easy to use, meaning invisible to the user with minimized required information,
- efficient, because in a closely-coupled analysis both the flow and structure meshes move with each iteration, so the grid deformation pattern is used in each time step,
- parallelizable, i.e. must be able to operate in a parallel environment and cannot cause increased communication loads or extend the time of numerical analyzes.

2.6 Visualisation of calculation results

2.6.1 Introduction

Data visualisation is the presentation of a certain abstract information in the form of an ordered pattern. Tables, line charts, contour charts or even concise charts description are used to find a relationship, to facilitate understanding of a phenomenon or to prove a (given) hypothesis. In order to understand the message, the issue should be presented in a simple and functional way. R. W. Hamming in paper [30] states that "the purpose of (scientific) calculations is to look at the phenomenon being studied, not the number". The visualisation of scientific data is the presentation of the obtained results, using computer graphics in three-dimensional form in order to understand the geometry and mutual relations in the physical phenomenon under observation [43]. It is important that the given phenomenon is presented in an unambiguous way, i.e. that the provided information could not be interpreted depending on the individual perception of the recipient. Visualization of scientific data is the last step in the simulation and analysis of the obtained calculation results. A proper presentation of data may result in a change in the methodology of scientific research and solving engineering problems. The process of presenting results consists of two steps:

- discovery – understanding of the studied or observed phenomenon or test results,
- presenting – transfer of information.

The simulation results of the flutter phenomenon can be divided into three groups - including two areas that are combined and a common reaction of the whole system:

- CFD – distributions of pressure, velocity, density, kinetic energy of turbulence and others [15],
- CSM – distributions of stresses, displacements, deformations,
- CSM – exceeding the allowable stresses and the elastic limit,
- FSI – the aeroelastic response of the tested system.

In addition, it is possible to obtain aeroacoustic response in the form of a generated sound, but currently this type of calculations are not made in the Flutter Laboratory. The laboratory has several tools to visualize the results in a loosely-coupled aerodynamic system. Available data visualization tools are:

- Tecplot 360 and Focus
- Paraview.

2.6.2 TecPlot 360/Focus

Tecplot 360 is a specialized visualization system for numerical calculations, such as CFD data. It enables obtaining and presenting results important in engineering and scientific issues. The program allows to load complex two- and three-dimensional data as a their static display creation of animations. The data is stored in the memory of a single workstation. However, the process of rendering and data processing itself takes place as a parallel process on the processors available in the given architecture. The procedure of presenting the results is shown in the Figure 2.12 [50]. The presentation of flow results starts with their processing and preparation for reading the data into the visualization system. The area containing continuous distribution of a certain value (e.g. pressure, temperature) should be discretized by a finite number of smaller one is. Then, the scalar value should be assigned to the vertices of each area element according to the interpolation rules. The interpolated data is saved to a file in the appropriate format.

This step is performed automatically in the TAU-Code flow calculation system. The finite element mesh is used, to which the calculated nodal values are assigned. In practice, the aim is to standardize the formats of information exchange. In programs solving flow or structural issues, the possibility of writing to formats supported by programs for visualization or vice versa is implemented. In addition, visualization programs allow to import data from many different formats. The calculation results file contains:

- the coordinates of each of the finite element mesh nodes - most often in the Cartesian coordinate system,
- the connectivity matrix,
- results as scalar or vector values assigned to nodes or elements.

An example of a standardized format containing information about the finite element mesh and results is CGNS (*CFD General Notation System*). The TecPlot format is also considered as a standard for data exchange for visualization purposes. The next important stage of data visualization is its processing. It is desired that the abstract image created at this stage is:

- easy to understand,
- clearly presenting the phenomenon of interest,
- the removing any unnecessary elements hindering the message.

Tasks to be carried out include:

- presentation of the structure of the phenomenon,
- search for the influence of relations between variables,
- emphasizing the influence of the most important parameters of the model.

Files with results of numerical simulation are loaded into the program. The data is then displayed on the screen as a three-dimensional abstract image in space –AVO (*abstract visualization object*). On the basis of the information gathered in the finite element grid, it is possible to display surface elements of the structure and directly related values in the nodes, i.e., pressures, stresses, strains,

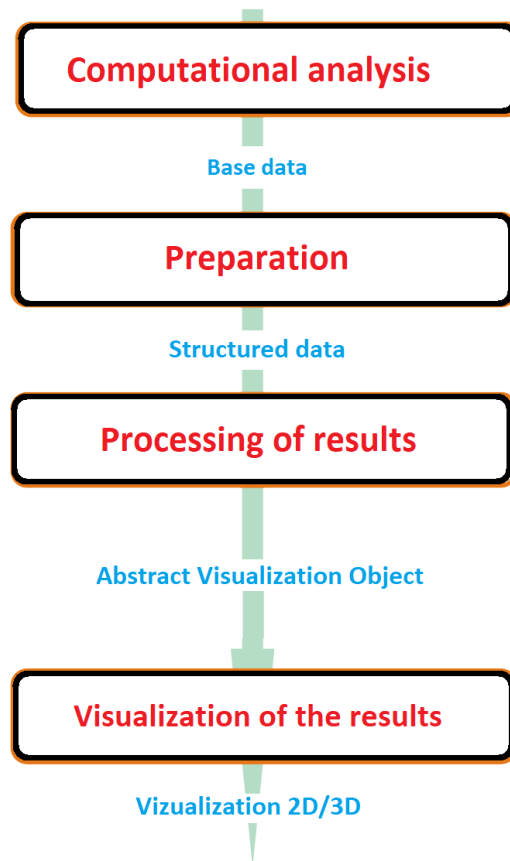


Figure 2.12: A general scheme for creating an image showing the studied physical phenomenon based on data from computer simulation [50].

etc. The scalar values in the nodes of the surface grid are interpolated to any of its points using the finite element shape function. In this way, a continuous distribution of values is created and the thresholds between successive levels are highlighted by means of color maps. This procedure is used to intuitively present data values - the minimum and maximum values are assigned to the extreme colors of the palette (ordered color set). Usually the distribution of the values on the surface is sufficient to analyze the engineering problem (e.g. the distribution of force vectors, needed to determine the resistance coefficient or the bearing force). However, in the case of analysis of more complex problems, it is important to recognize and present phenomena occurring inside the material (for numerical problems of solid mechanics – *CSM*, *Computational Structure Mechanics*) or inside the fluid (for numerical fluid mechanics – *CFD*, *Computational Fluid Dynamics*). Visualization of the results collected for volume elements of the grid is in practice impossible (due to the hardware capabilities and the pointlessness of such a procedure). Therefore the aim is to present the most important information. The selected range of the results is best presented on the surface, which can be obtained as a simple cross-section or as a three-dimensional surface representing a given group of values (so-called isosurfaces). The tools of the TecPlot 360 or Focus system enable the use of the following spatial visualizations:

- cross-section - a flat surface created by the plane intersection of the volume; it is the simplest method of visualizing three-dimensional data, reducing the problem of the visualization to two dimensions;
- contour - the area boundary showing the values as a color map assigned from the color palette; this procedure can be used in relation to flat or three-dimensional surfaces;

- isolines - a function of several variables that creates a line connecting points of the same value (Fig 2.13d, 2.13e);
- isosurface - a surface created by a connection in the space of fixed points (or subsequent isolines). In order to determine such a surface, the Marching Cubes technique is used, according to which the total volume is divided into a series of smaller ones. The Marching Cubes algorithm proceeds through the scalar field, taking eight neighbor locations at a time (thus forming an imaginary cube), then determining the polygon(s) needed to represent the part of the isosurface that passes through this cube. The individual polygons are then fused into the desired surface [38] (Fig 2.13c). Another technique for determining the iso-surface is Marching Tetrahedra. It is a method similar to the one described before, but is based on the definition of tetrahedral elements [7];
- streamline - a line tangent at each point to the velocity direction of the fluid particle. The streamlines connects starting point with the next ones, shifted relative to each other by the vector $[dx, dy, dz]$ (Fig. 2.13a, 2.13b):

$$\frac{dx}{u_x} = \frac{dy}{u_y} = \frac{dz}{u_z} \quad (2.48)$$

where: $\vec{u} = (u_x, u_y, u_z)$ – velocity vector;

the new segments of a line are calculated, as long as one of the following criteria is met:

- reaching the maximum calculation time,
 - reaching the maximum length of the current line,
 - reaching the boundary of the calculation domain,
 - reaching the velocity of 0 - stopping the flow (e.g. stagnation point on the edge of the wing profile),
 - the intersection of a streamline - the flow becomes circular, the streamline is infinitely long in this direction.
- current path (trajectory) - a line in space tangent at any point to velocity vectors at the right moment; in steady flows the path of the fluid element coincides with the streamline:

$$\frac{d\mathbf{x}}{dt} = \mathbf{u}(\mathbf{x}, t) \quad (2.49)$$

where: $\mathbf{x}(t_0) = \mathbf{x}_0$ – the initial conditions;

visualization of the current path is a more complicated issue than the visualization of the current line; it is caused by the fact that the analyzed fluid molecule is related to time; therefore, the presentation of movement variation takes place by means of animation;

- volume rendering – (also: rendering the maximum intensity) – a technique allowing the presentation of data from the entire volume by projecting it on the plane of the control volume, which has the highest value in this projection direction; usually this technique is used in medical imaging;
- glyphs – for each point on arrow (cone, line fragment, etc.), is assigned to represent a vector field. It can additionally be represented by the color of the corresponding amplitude value; this procedure can be applied to a flat or three-dimensional surface, to a line or to the entire volume; in the case of a volume. It is stated that the information presented by means of glyphs is an explanation in the form of small symbols (arrows, lines, etc.); thanks to this technique, it is possible to present clearly the direction of fluid movement in the computational domain, e.g. air in the room (Fig 2.13f).

Finally, the three-dimensional abstract image of the physical phenomenon is presented in a flat image (rendering) or three-dimensions (in virtual reality systems - VR, *virtual reality*). This stage is carried out automatically by the TecPlot 360/Focus program using the so-called rendering

techniques. It is a technique of data rasterization, which means a data transformation into a bitmap. The following operations are used for this purpose:

- transforming an orthogonal image into a perspective view,
- use of textures,
- lighting of the created object,
- removing invisible edges and surfaces.

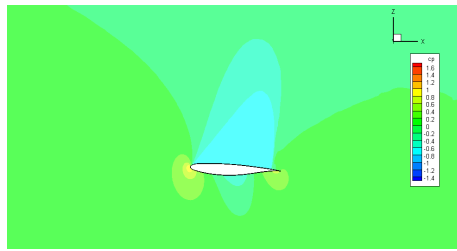
The processed abstract image is displayed on a separate screen or three-dimensional projector or is saved to a file. The TecPlot 360/Focus program was created mainly for the purposes of visualization of fluid mechanics simulations, therefore it contains a package of tools facilitating the analysis of this data and enabling:

- the grid quality analysis – aspect ratio, skewness, orthogonality and stretch factor,
- the calculation of pressure coefficients C_p , speed values in the turbulent field and others,
- the recognition and isolation of shockwave surface, vortex cores or separation lines,
- the displaying the current line, current paths, trajectory of movement,
- the integration of mass and momentum coefficients to confirm convergence.

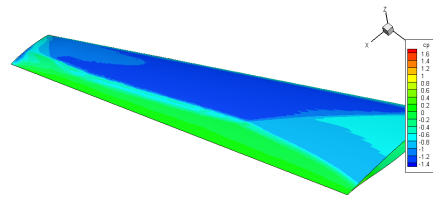
The TecPlot 360/Focus program also allows you to analyze the results of structural calculations. The following operations are available:

- the movement animation,
- the distinction of von Mises stresses or strains and principle stresses or strains,
- displaying the geometry with the deformation applied (scaling optic to facilitate observation included).

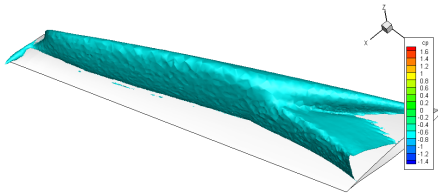
In addition, all available activities can be automated using macros.



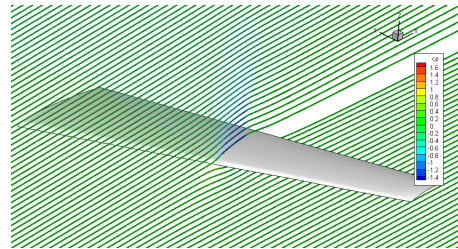
(a) contour of the cross-section



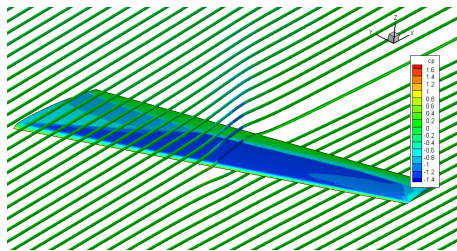
(b) contour of a three-dimensional surface



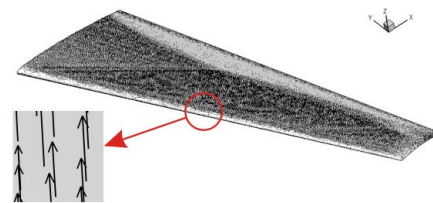
(c) isosurfaces



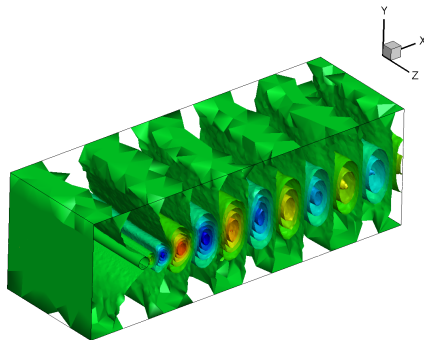
(d) stream lines; The values of the pressure coefficient were distinguished in color C_p



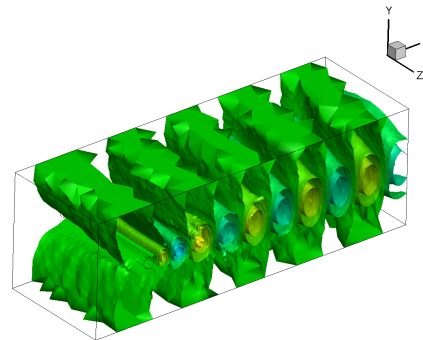
(e) contour of the wing surface with stream lines



(f) field of force vectors (glyphs) on the surface of the wing



(g) spatial visualization of DMD (Dynamic Mode Decomposition) flow modes as isosurfaces – 5. mode



(h) spatial visualization of DMD flow modes as isosurfaces – 3. mode

Figure 2.13: Example of the presentation techniques in the TecPlot 360 program - the distribution of the pressure coefficient for the LANN wing, configuration CT9 [43]

2.6.3 ParaView

The ParaView software is a specialized system for analyzing numerical results. Its most important feature is the ability to generate data in a parallel environment. This program was based on an

architecture that enables communication between a workstation and a computer cluster server. The process of generation of AVO space, presented in the previous section does not take place in real time. It only consists of sending commands to the server – a data processing requests. The result is returned and displayed on the client’s screen. In addition, it is possible to work on a single station – in processing of small data. The following operations are available in ParaView [43]:

- displaying structural meshes (also with a curvilinear definition of the border) and unstructured, set of photos and others,
- visualization of vector data using glyphs - in the form of small symbols (arrows, lines, etc.); Glyphs can be subjected to scaling operations using scalars, vector components, or vector values, and can be oriented using a vector field,
- displaying contour areas, areas, current lines, current paths,
- refining data to be processed with cutting surfaces or volume;
- the determination of data to be processed by applying value thresholds;
- the full automation with macros.

The greatest advantage of ParaView is the a ability to define the processing and visualization pipeline using a variety of filters (including programmable ones), which gives full control over the displayed image.

Figure 2.14 shows a number of data visualization methods in ParaView software.

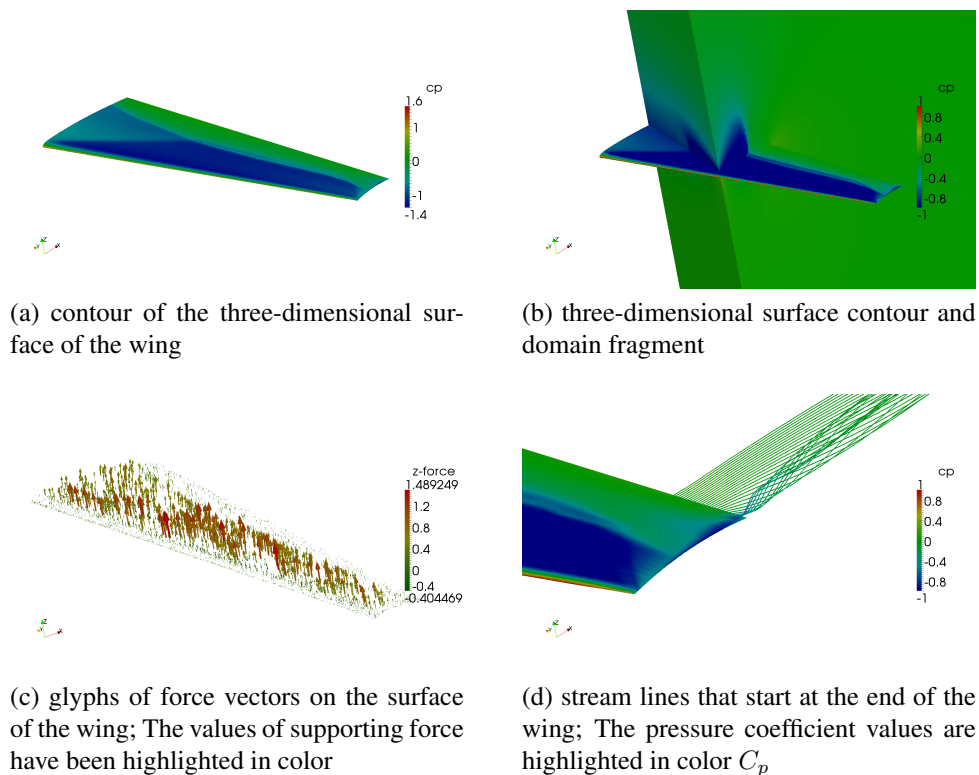


Figure 2.14: Example of a technique for presenting results in the ParaView program - distribution of the pressure coefficient (C_p) for LANN wing, configuration CT9 [43]

Chapter 3

Development of numerical models

3.1 Introduction

In order to perform numerical flutter studies, it was necessary to develop a numerical model for method validation. The object of research, on the basis of which the numerical models were created, was the PZL I-22 Iryda aircraft. Due to the access to a complete aircraft documentation provided by the Institute of Aviation in Warsaw, this model was chosen as a test case for the validation of numerical tools.

3.2 Selection of tools and model

In the first stage of the work, analysis and selection of tools needed to carry out numerical simulations of the flutter phenomenon were performed. In addition, the actual aircraft was chosen as a numerical model of the method demonstrator. The available documentation was analyzed and measurements were made to obtain missing data.

Chapter 2 presents available tools used in the Flutter Laboratory at the Poznan University of Technology and included a description of their principles. The aeroelastic analysis system was built on the principle of the loosely coupled programs [32]. This means that each part of the system is a separate program and the information is exchanged using special modules. The schematic diagram of the system is shown in figure 3.1.

First, procedures are performed to search for cooperating pairs of areas (set of elements) of the flow and structural grid. The methods used for this purpose are described in section 2.4. The result of this operation is an exchange file containing information about the location of the cooperating pairs of both system models. This stage is performed only once, at the beginning of the entire system operation. It was assumed that the exchange will take place only on undeformed meshes. Therefore, there is no need to repeat this process in each aeroelastic iteration.

Then, the main procedure begins. The program for solving flow problems is started, which determines the distribution of pressure or forces on the surface of the (method) demonstrator. Using information about cooperating pairs, the data are interpolated into the structural model or the information exchange surface. Then the structural model is calculated. The displacements determined during the analysis are interpolated into a deformed flow grid. Then the next aeroelastic iteration starts with the calculation of the flow model determined by the previous step. The calculations last until the assumed level of convergence in the CFD and CSM calculation programs is reached and the response of the aeroelastic system is constant.

In the case of a stationary analysis, the calculations are completed after the first iteration cycle. In the case of non-stationary simulation, the presented process describes a solution for only one time step. After achieving the assumed convergence for a single time step, the next iteration begins.

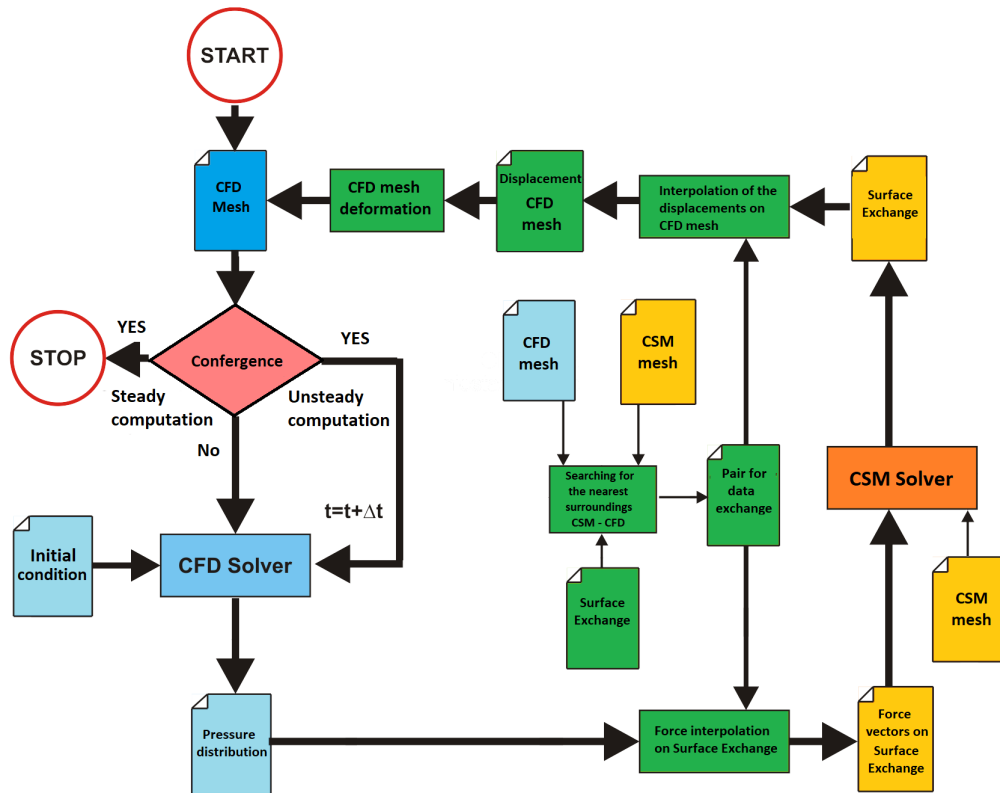


Figure 3.1: Scheme of the aeroelastic system used in Flutter Laboratory (own study) [43]

In this type of simulation, it is important to combine the motion information and the velocity of the deformed flow grid with the structural mesh using the ALE technique presented in section 1.2. Another important step in dynamic computation is the impact load. It consists of introducing a force impulse in a short time and analysing the response of the structure in time [43].

According to the scheme shown above (Fig. 3.1) the study of aeroelastic phenomena, no moving parts are taken into account (ailerons and flaps). The DLR TAU-code allows flow simulation with respect to moving parts, but the remaining tools (deformation, interpolation) are not adapted to such aeroelastic analysis. This determines the methods of developing flow models and structural models that are presented in the next stages of work. Flow calculations are performed using the DLR TAU-code system presented in the section 2.1. From the available data exchange software in the aeroelastic system (section 2.4), the *AErocoupling* modules were selected to have all necessary features for the analysis of the flutter phenomenon. Tools using interpolation methods on the so-called exchange surfaces are very effective and provide an accurate solution even with large displacements. This is especially important for flutter analysis, when the displacements of the structure increase rapidly. The accuracy of the interpolated values and the correctness of the deformed flow grid plays a key role. From the available flow grid deformation software (section 2.5), the *AE_DEFVOL* tool was selected and applied. The choice was dictated by its high functionality. It is possible to modify hybrid meshes (unstructured with a boundary layer) for very large displacements. In addition, this module has been enriched with the ability to check the modified mesh. The criteria for verifying the correctness of the first order grid are positive values of the Jacobians and the element size. If elements are incorrect, the repair procedure (discussed in the section 2.5) be performed.

In order to accelerate the structural calculations, the frequency domain was used (section 2.3). Here, low-dimensional models are applied which are characterized by the same mechanical prop-

erties (or very similar) as large or exact models, and at the same time consisting of several hundred nodes. Using this technique for structural calculations a single processor is highly efficient even on. In this case, the entire structure model is required to as set of eigenmodes and eigenvalues. An important advantage of this approach is the possibility of using flutter data provided by the client - based on natural vibration data [43].

The next stage is the selection of appropriate FSI calculation methods, in which numerical analyzes were carried out. The selection of models was done. Three models are needed in the aerospace system:

- the CAD surface model, necessary for flow grid generation and used as data exchange surface,
- the structural model in form of mode shapes and natural vibration,
- the flow grid.

The numerical model for aerodynamic simulation can be provided by a partner or a calculation client. The Institute of Aviation in Warsaw has its dynamically similar model for flutter analysis. The main factors determining the choice of this facility were:

- the availability of real models,
- the full identification of flutter phenomena for the aircraft and its model,
- the extensive experience of the Institute of Aviation in flutter research (especially concerning the PZL I22 Iryda aircraft),
- the availability of documentation.

These aspects were decisive when choosing an object that fullfield the function of the method demonstrator. The aircraft was developed in the years 1976-1992. Computer methods were not widespread in this period, so there is no digital model of the aircraft that could be used in numerical calculations.

The Non-uniform rational basis spline (NURBS) geometric surface model was developed from a physical aerodynamic model and flow meshes were then created from the geometry. The basis for the numerical structure model was the flutter model. Both real models were made with appropriate scales. The geometry of the model was scaled down four times (Eq. 3.1) due to the dimensional constraints of the wind tunnel (diameter 5m). The model dimensions are given in Tab. 3.1.

Table 3.1: Dimensions of the method demonstrator [43]

Size	Value [m]
Length	3,1
Wingspan	2,2
Height	1,0

The wind tunnel for low speeds at the Institute of Aviation enables the study of objects with a span of up to 5 m at a flow velocity up to 57 m/s. Due to the construction of the tunnel, an appropriate velocity scale (Eq. 3.2) and air density (Eq. 3.3) were adopted. The remaining scales result from the conversion of the scales K_l, K_v, K_ρ previously adopted (Eq. 3.4, 3.5).

Linear scale:

$$K_l = 1 : 4 \quad (3.1)$$

Velocity scale:

$$K_v = 1 : 10 \quad (3.2)$$

Density scale:

$$K_\rho = 1 : 1 \quad (3.3)$$

Mass scale:

$$K_m = K_\rho \cdot K_l^3 = 1 \cdot 0,25^3 = 1 : 64 \quad (3.4)$$

Frequency scale:

$$K_f = \frac{K_v}{K_l} = \frac{0,1}{0,25} = 1 : 2,5 \quad (3.5)$$

In the analysis of phenomena related to natural vibrations (e.g. flutter), the criterion determining the dynamic similarity of the model to the real object is the Strouhal number. Ensuring the compliance of the Strouhal number allows the model to reproduce the same physical phenomena that occur on the real object. From the accepted scales and from the equation 3.6 it follows that they are equal and, thus the similarity of scaled model has been preserved:

$$Sr_o = \frac{l_o \cdot f_o}{v_o} = \frac{4l_m \cdot 2,5f_m}{10v_m} = Sr_m \quad (3.6)$$

where:

- Sr – Strouhal number,
- v – characteristic fluid velocity,
- l – characteristic dimension,
- f – characteristic frequency.

The index *o* refers to the size associated with the real object and the index *m* to the size associated with the model.

Based on the model documentation, the data on the mass distribution and the centers of gravity of the wings, the horizontal and vertical (rudder) stabilizers were obtained. This information was necessary to build a numerical structure model. Received them based on measurements is a complex task. Missing data from the documentation regarding to the geometry of the internal components of the structural model were collected using standard measurement tools (Fig. 3.2) at the Institute of Aviation in Warsaw. Information about the geometry of the external surface of the model was not documented and could not be measured using traditional methods. Therefore, it was decided to mimic the geometry of the external object using a three-dimensional scanner and using the reverse engineering technique to create the NURBS surface model. Correct and accurate mapping is of particular importance at a later stage of the work, i.e. in flow calculations.



Figure 3.2: Measurements of the flutter model to correct the missing data in the documentation

3.3 Creation of 3D geometrical model of the aircraft based on 3D scanning technique

The next stage of the work was the preparation of a three-dimensional model of a NURBS type surface (compatible with CAD systems) created on the basis of a real object (used for research) in the wind tunnel. For this purpose, a three-dimensional structured light scanner was used, which was installed in the Laboratory of Virtual Engineering at the Poznan University of Technology.

The ScanBright scanner made by Smartech was used for measurements (Fig. 3.3). The measurement consist in analyzing the deformation of light stripes on the object's surface. The measured surfaces are illuminated by a structural white light and at the same time observed by the detector module. A result of the analysis of collected stripped images is a cloud of surface points with a resolution of 0.05 mm. Each point is determined by the XYZ coordinates and the RGB color values. As a result of measurement from one site, information about the full geometry is obtained. To obtain a full representation of a geometric object, many clouds taken from different directions are combined. The measuring volume of the scanner is $450 \times 450 \times 120$ mm.



Figure 3.3: Optical scanner ScanBright during the measurement of the method demonstrator – Laboratory of Virtual Engineering [78]

In order to obtain a high quality 3D model, a number of test measurements and analyzes of various algorithms were made. Taking into account the measuring volume of the scanner, it was estimated that to get a full data set, about fifteen measurements should be done along the body length and five measurements along the height. Performing a significant number of measurements while maintaining the accuracy of the model mapping (e.g. maintaining a simple aircraft axis) requires the use of special measurement procedures. An additional difficulty in the 3D scanning process were the trailing edges for the wings, tails and rudder. Due to the small distances between the upper and lower surfaces for the wing and the horizontal stabilizer, comparable with the distances between individual points in the part clouds, it was not possible to use the standard process of combining results from consecutive measurements.

In order to eliminate the aforementioned problems, the system of dividing the object into equal areas was used, creating a grid of quadrants of equal width and length (Fig. 3.4). For this purpose, horizontal and vertical lines were determined using optical instruments (laser level, laser with a

collimator). In order to check the correctness of the prepared grid and perpendicularity of the lines, an optical projector was used.



Figure 3.4: Division of the object (fuselage) into the measurement areas [78]

In order to obtain a 3D scan of the entire aircraft, a method was developed: providing each measurement with a letter denoting a measurement session and a number denoting the measurement sector (Fig. 3.5). As part of the measurement, the following was distinguished:

- the measurement steps - scanning of models along their axes at a fixed height, from a given direction (entering zones A to H - Fig. 3.5b); due to the scanning range of the scanner, the data acquisition included two columns with an offset;
- the measurement sectors listing the elements of the measurement session at column height, labeled 1 to 14 beak to tail;
- the assembly of measuring sectors on the entire length of the model.

Due to the symmetry of the object, all measurements were made on one side only. The next step was to cover the object with a special matting agent (Fig. 3.6) to avoid excessive brightening and to ensure good quality measurements. It reduces by a high color gradients, causing errors in reading the depth of the image, depending on the reflected wave length recorded by the scanner's camera.

In the laboratory intended for scanning models, the test stand had to be adapted. To this end, the room was darkened to obtain the right measurement conditions. In addition, the object scanned was precisely positioned relative to the scanner. This is important because the wrong positioning of the device may lead to measurement errors or complete prevent the data acquisition. It requires both manual efforts and well experience. Before proceeding with the scan, the instrument is calibrated by adjusting the detector's iris settings to minimize underexposed and overexposed areas of the object. The next step was the processing of the point clouds (Fig. 3.7a). This is necessary to ensure the continuity of the surface. It is requires for the proper functioning of the algorithm during cloud assembly. The data processing included:

- removing excessive information, i.e. 'cutting' the cloud to the desired size of the measuring section element; all erroneous points on the border of the cloud (discontinuities) and surfaces parallel to the direction of light emitted by the projection modules are have to be remove, as these data may be distorted;
- the elimination of incorrect points ("jumps" of single points, breaking out a scan object); the measurement noise is, constituting a small part of the overall data; these are single points

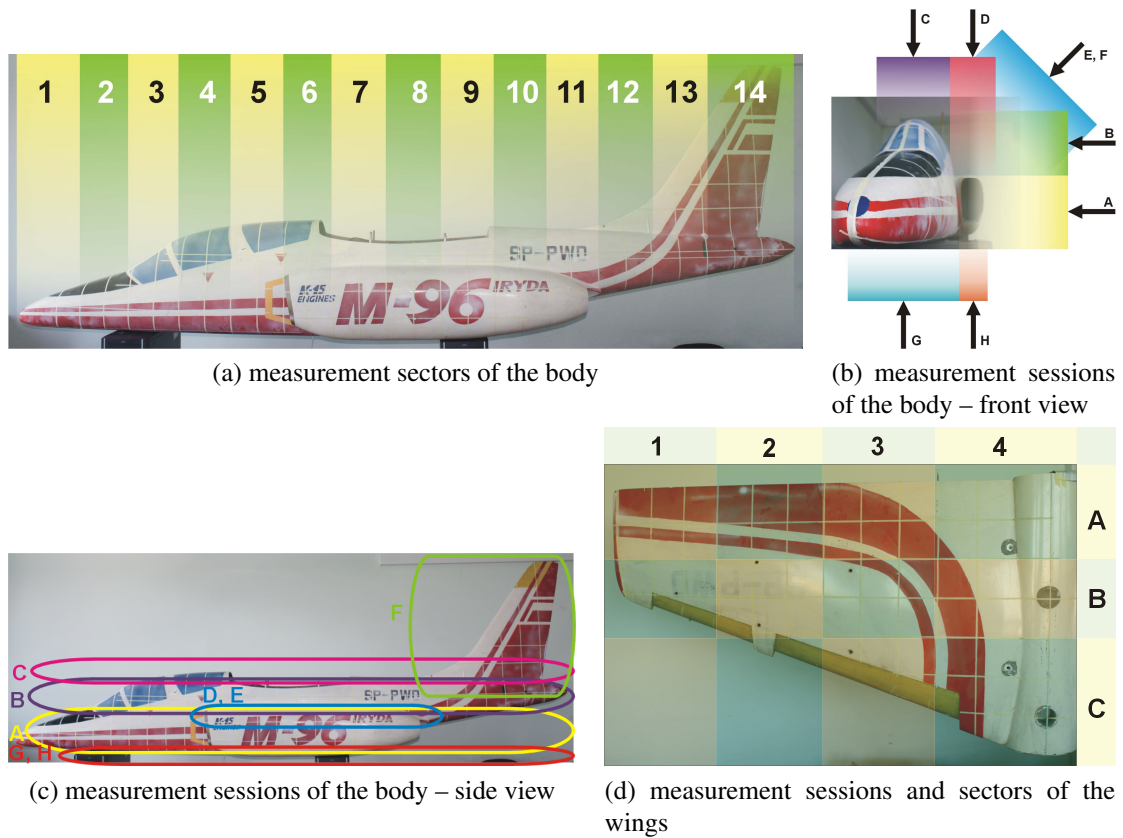


Figure 3.5: Method of dividing the object for the measurement – fuselage, wing [64]

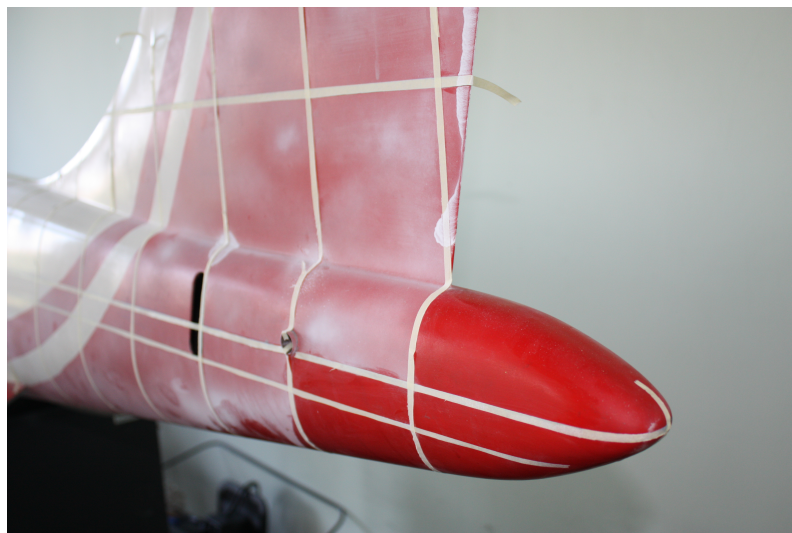


Figure 3.6: The process of applying a matting agent to the tail part of the body of a measured object [78]

- randomly scattered around the main cloud;
- the reduction of the number of points registered during the scanning to reduce the amount of data and facilitate processing. A resolution of 1 mm was adopted.

Figure 3.7 shows the process of removing points that are collected outside the measured section. The combining of point clouds is one of the most important and time-consuming processes of recreating the geometry of real objects. The model has been compared between three measure-

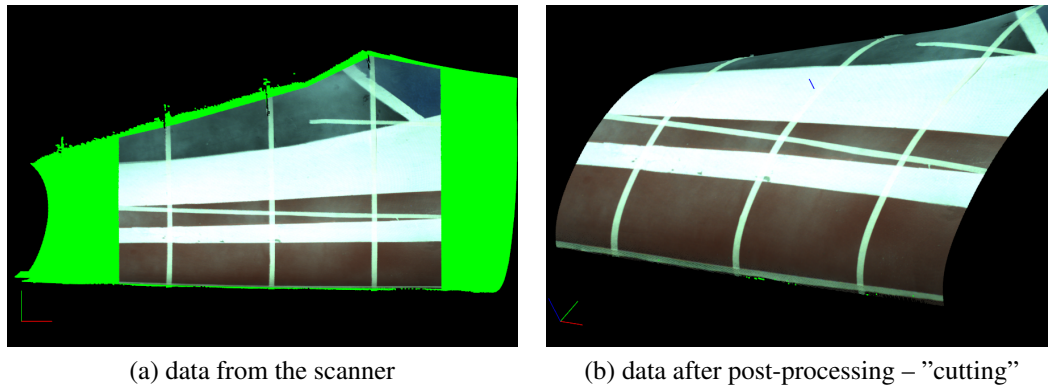


Figure 3.7: Processing data, erasing ("cutting") data from one measurement/scan session [64]

ment sectors after their aggregation (Fig. 3.8). Initially, single clouds were merged by translation and rotation to stationary reference points. Then the exact method of merging clouds was used, consisting of the use of the internal algorithm of the program (interaction algorithm of the nearest points). The algorithm works on the principle of minimizing the root mean square clouding error (RMS - Root Mean Square). In order to obtain the assumed accuracy of reconstruction, it was assumed that the maximum RMS parameter should be about 0.2 mm for simple surfaces, and 0.35 mm for a complex surface. This parameter depends primarily on the correct preparation of the data (pre-processing), the number of combined clouds and their initial (manual) matching.

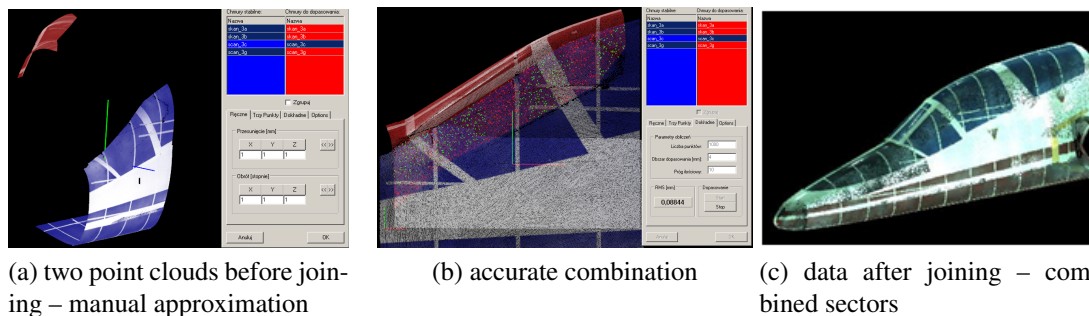
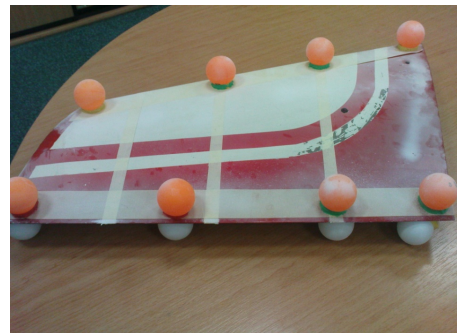
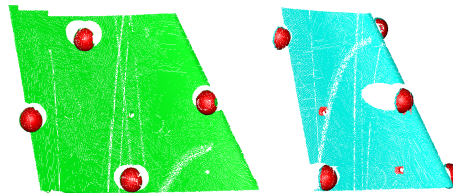


Figure 3.8: The process of overlapping measurement sessions in one sector and subsequent sectors [64]

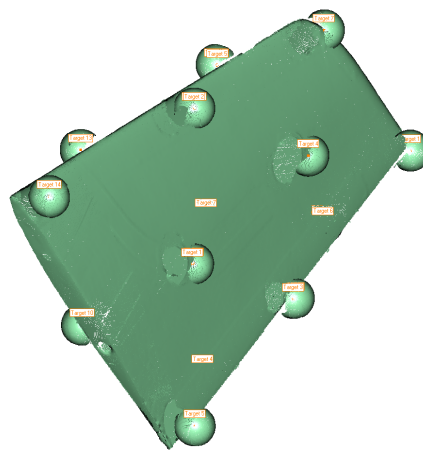
After processing data in the areas of individual measuring sectors, they were combined into one object. In the case of the fuselage, it was assumed that sectors 5 (Fig. 3.5a) and 6 (Fig. 3.5a) will be the core sectors, i.e. the other sectors will be matched to them. During the assembly, there were problems with sectors 7 (Fig. 3.5a) and 8 (Fig. 3.5a) connection - engine nacelle. It was not possible to properly connect them to the neighboring ones. Therefore, it was decided to match each cloud exactly. For this reason, the model was folded from the tail (sector 14 on fig. 3.5a) to the bow (sector 6 on figure 3.5a). Sector 3 was assumed as the base for the wing. At this stage, there were difficulties with placing the sectors on the trailing edge. This problem was explained at the stage of planning the scanning process. The correct algorithm of accurate point cloud combination requires a minimal environment in which merging takes place. The problem of not being able to do this for a given geometry has been solved by using spherical markers. They were positioned such that a minimum of four was visible in one measurement. They were used as markers in the registration process (figure 3.9), which eliminated the effect of shape deformation at the leading and trailing edges that occurred in the case of recording measurements without markers. A similar solution was used for the horizontal stabilizer.



(a)



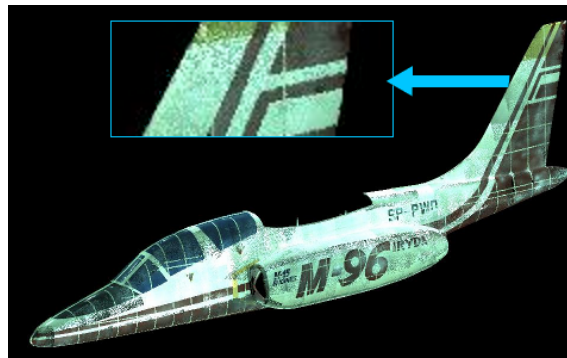
(b)



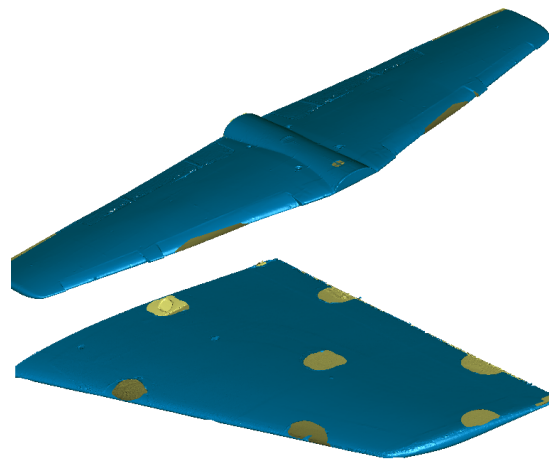
(c)

Figure 3.9: Joining process of point clouds for the horizontal stabilizer; (a) actual object with markers, (b) two point clouds – the second includes three markers corresponding to the same markers in the first one, (c) virtual object with markers - point cloud [78]

As a results three independent parts of the model were obtained form of corrected point clouds for fuselage, wing and horizontal stabilizer (Fig. 3.10).



(a) fuselage



(b) wings and horizontal stabilizer

Figure 3.10: The result of the second stage - three independent parts of the model as a point cloud [78]

Table 3.2: Summary

Goal

- Obtaining the geometry of the plane in the form of point clouds

Completed tasks

- Preparation of the model - matting of the surface, meshing the body, arrangement of markers on the wings and horizontal stabilizer
- Scanning – 96 measurements for the body, 40 measurements for the wing, 24 measurements for the horizontal stabilizer
- Correction of point clouds
- Connecting point clouds

Results

- Three independent point clouds mapping body, wing and horizontal stabilizer

3.4 Creation of the reduced structural model

In order to carry out correct numerical calculations related to analysis the dynamics behavior of the structural models, many degrees of freedom is required. In the case of numerical calculations concerning modal analysis, the smallest calculated eigen values and their corresponding eigenvectors are important. A low-dimensional reduced models based on these eigenvalues and eigenmodes. It guarantees results comparable with numerical analysis using an accurate structural model. Applying the modal numerical simplification preserved the selected mechanical properties with the lowest possible model complexity. Both aspects, model accuracy and model complexity are closely related to the reduction process. It is based on reducing the number of degrees of freedom by neglecting unimportant elements, simplifying complex elements or combining several elements and replacing them while maintaining equilibrium. Considering the model in terms of mechanical properties, which are important for the solution obtained in numerical simulation, the aim is to reproduce its behavior as faithfully as possible. It should be remembered that the accuracy of the real model representation on the virtual model influences the correctness of the calculation results, while the complexity of the object determines the duration of its numerical analysis. The reduced structural model in FEMAP software was based on the 3D solid geometry created in CAD Solid Works software. The solid model (Fig. 3.11) contains all the elements of the structure, accurately reproducing the real flutter model. The properties of all elements of the solid model were collected in a spreadsheet.

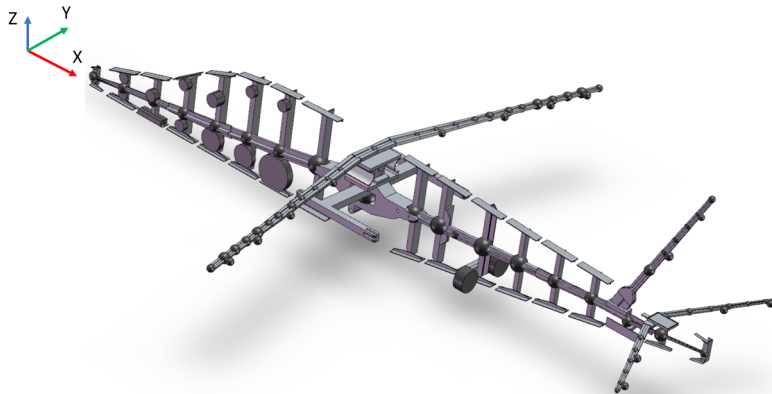


Figure 3.11: 3D CAD geometry based on measurements of the real model at the Institute of Aviation [66].

The model generation process begins with the creation of the main axes (Fig. 3.13) with marked points, determining the position of all sections of the aircraft and the corresponding centers of gravity.

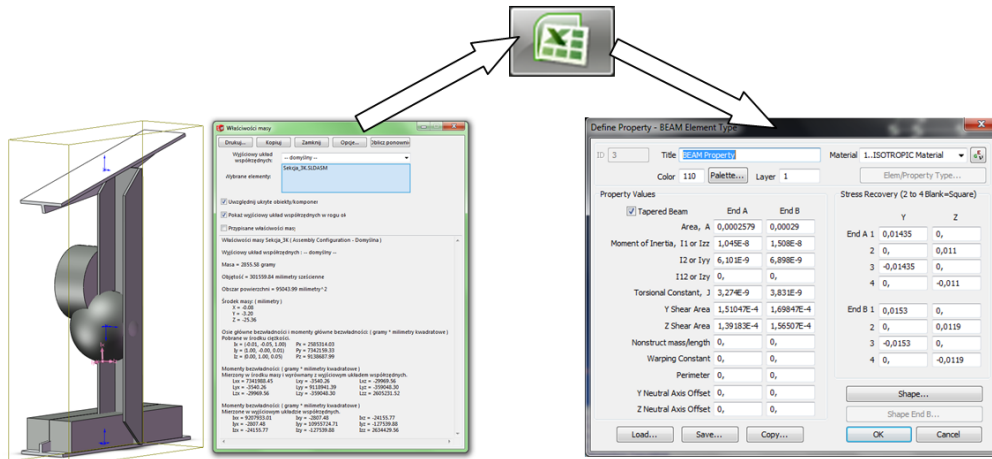


Figure 3.12: Data exchange scheme between SolidWorks and FEMAP [66]

The reduction process is based on the assumption that the model will be built with mass, beam, and rigid body elements only. The first task was to reduce the properties of all elements to parameters describing them as beam or mass elements. Next, the fuselage beams, wings and steering gear were created from beam elements. All the information concerning the geometry of the sections as well as the material properties were taken from the previously prepared spreadsheet. The remaining elements (C-beams, T-beams, masses, etc.). On the basis of Steiner’s statement 3D balance components were reduced to mass element with appropriate moments of inertia and located at the center of gravity of each section. The above step was organized in a spreadsheet and the results were introduced into FEMAP. The idea of exchanging information between SolidWorks software and FEMAP through a spreadsheet, where the necessary calculations were implemented, is shown in Figure 3.12.

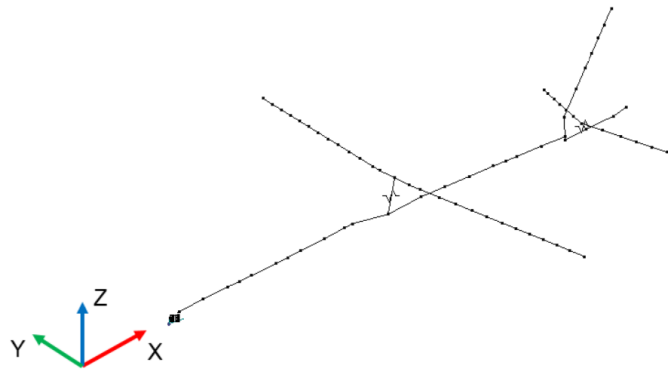


Figure 3.13: Main axes of the reduced structure model [66]

In addition, acceleration sensors located on the real structure were modelled, which were used to determine the form and frequency of natural vibrations during ground resonance tests and were the basis for the verification of the computational model. Therefore, the masses of the acceleration sensors had to be taken into account during the development of the computational model. For this purpose, additional nodes with mass element were introduced in places where the sensors were on the real model. Additionally, at the edges of the aircraft plane, nodes were added, connected to the beams using RBE elements. In order to increase the accuracy of data interpolation between the structure model and the flow calculation grid in the aeroelasticity testing system. The resulting

model consists of 69 beam elements, 96 mass elements and 278 nodes (Fig. 3.14 right).

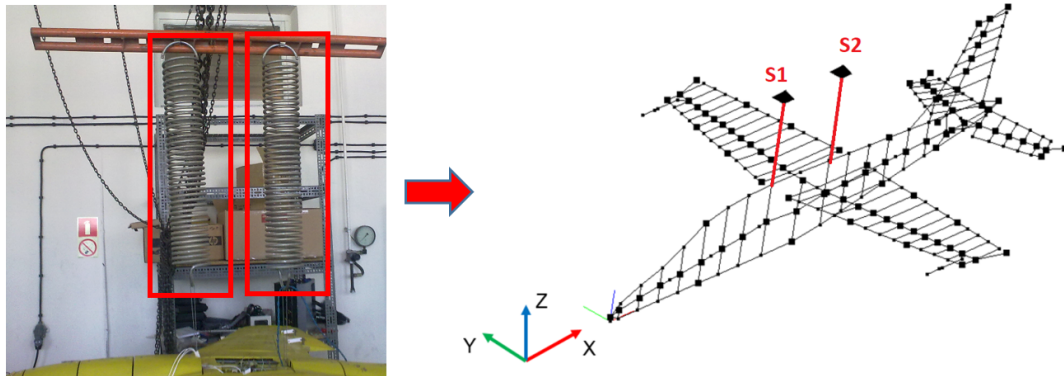


Figure 3.14: Structural model after changing of the boundary condition (S1 and S2 – fixing springs).

The structural model stage has been verified and modified. In parallel with the construction process of the FEA model, ground resonance tests of the flutter model were carried out at the Institute of Aviation in Warsaw. The results obtained for the numerical model were compared with the experimental results. On the basis of ground vibration tests (GVT), the acceleration response were obtained from all accelerometers arranged on the flutter model (Fig. 3.15).



Figure 3.15: Iryda I22 experimental flutter model during GVT tests at the Institute of Aviation in Warsaw.

With these data, the shapes and natural vibrations were determined using dynamic identification methods [29], but the available documentation made it possible to reproduce the frequency values of natural vibrations and the theoretical shape of the appropriate modes. The results for the same shapes were obtained as a result of numerical modal (Fig. 3.14) analysis for the aircraft structural (numerical) model, which allowed an assessment. The initial eigenfrequencies and shapes determined were significantly different from the GVT results [43]. It is necessary to improve the structural model to more accurately determine the eigenmodes according to the experiment. The basis for the modification of the reduced model was modification of boundary conditions the real object during GVT tests. In the numerical model, the fixed point of the structural model is located in the central element of the fuselage, in its center of gravity. This solution was adopted in accordance with the principles used in simulations of flying objects. In the ground vibration tests, the tested model was suspended on two springs attached to the central element of the aircraft fuselage (Fig. 3.15). Boundary conditions defined in this way did not take away all degrees of freedom of the real model, as it was the case in the numerical model. This stiffened the middle fuselage. As a result the fuselage parts (front and rear) behaved independently. After receiving the preliminary results of the modal analysis, the support was introduced in the form of two springs. After the change of configuration numerical modal analysis was performed. Its results are presented in section 3.6.

The next step was a modal numerical analysis using the MSC Nastran solver in order to compute natural frequencies and their shapes. Before starting the calculation, boundary conditions (restraints) were defined in the model. A point in the middle of the central element of the fuselage was chosen as the node which was derived of all degrees of freedom. In the result for modifications were obtained - natural vibrations and shapes presented also in section 3.6. The results from the GVT analysis are compared to the results of the FEMAP modelling strategy in section 3.6. Table 3.3 summarizes of this chapter.

Table 3.3: Summary

Goal
<ul style="list-style-type: none">• Development of a reduced beam model, enabling its use in aeroelastic simulations
Tasks done
<ul style="list-style-type: none">• Reduction of the solid model for beam and mass elements• Construction of a reduced structure model• Carrying out a numerical modal analysis
Results
<ul style="list-style-type: none">• Reduced beam model of the method demonstrator structure• Eigenvalues and shapes corresponding to the resulting model

3.5 Flow grid generation process

Suitable flow grids for the aircraft model have to be generated and the results of modal analysis can be verified for the structural model. The flow grid is a necessary part to perform aeroelastic calculations. By solving the flow equations, the CFD solver determines the pressure distribution, which affects the flow around of the structure. In addition in each aeroelastic iteration analysis, the flow mesh is deformed corresponding to the elastic deformations of the structure model. There are two important factors that determine the correctness of the mesh. First of all, the mesh should be dense enough to accurately reflect the geometry of the improved model, especially in areas such as the leading and trailing edges. The second factor is the geometric correctness of the generated and updated mesh elements to obtain convergence. Consequently, the correct preparation of the mesh becomes a complex process. The software package CentaurSoft software was used to generate a flow grid for the aircraft model. It allows for generating unstructured grids and save them in the format required by CFD solver. As described in section 3.3, a geometry model generated through reverse engineering gave the starting point. The surfaces of the sphere were adopted as the outer surface of the computation domain (farfield). The coordinate system of the aircraft was defined at the beginning of the fuselage. The global coordinate system coincides with the sphere coordinate system. The furthest point of the plane was in the center of the sphere with a diameter of 46 m (source S1 on figure 3.16), with the length of the plane was 3.3 m, and the wingspan 2.4 m (source S2 on figure 3.16). Due to the symmetry in the aircraft geometry, the prepared geometry was divided into two parts. By using the symmetry boundary conditions, it is possible to halve number of nodes, which significantly reduces the computational effort. In relation to the experimental flutter model, it was not possible to use such a solution. In the GVT studies of the symmetric model, anti-symmetrical shapes were also obtained. The symmetry reduced model cannot cover the modes. Therefore, the full geometry has to be discretized. The topological correctness of the prepared geometry had to be checked. The main criteria is continuity, especially on the surfaces. There are tools in the mesh generator, which not only formally check the correctness of the mesh, but also fix the errors found. In the case of the NURBS surface model of the method demonstrator, the geometry was mapped correctly and saved with high accuracy. Before proceeding in creating a flow mesh, the surfaces were divided into two groups corresponding to applied boundary conditions in the flow calculations. The spherical surface was assigned to the group called "farfield" and the surface of the plane to the group "irya". The resulting flow meshes were unstructured meshes, which arose from the choice of the flow calculation solver and the mesh deformation tools. From the point of view of aeroelastic simulations, the most important result of the flow calculations is the pressure distribution on the aircraft surface. This is the input information for subsequent programs in the aeroelastic system. For the flow analysis, the linear Euler equation was chosen in which fluid viscosity was not taken into account. This procedure is used in aeroelastic analysis [4] as a compromise between the accuracy and the duration of calculations [35,45].

Aeroelastic calculations need high computing power and efficient computer equipment. The application of the Euler equation describing the flow without the viscosity component results in a shorter calculation time compared to the calculations according to the RANS/URANS model. The choice of the Euler equation (to describe the flow) determines the type of the grid needed for the calculation. In this solution, a boundary layer in the grid is not required and the entire volume of the grid can be discretized by tetrahedral elements. The CentaurSoft generator allows to create a grid with a boundary layer which is based on an unstructured inviscid grid. In order to analyze the required calculation time such a process was carried out and preliminary calculations were carried out with dense inviscid and viscous meshes. Grid generation started by defining a global parameters for the characteristic length of the elements. Its value was set to 0.512 m. Then, according to the methodology of creating meshes, the source density was distributed inside

the domain. In this way, the areas where the size of the elements were different from the global settings were determined. The distribution of sources of density in the aircraft area is shown in Figure 3.16. The sources allow the user to increase the mesh density in the regions of interest to increase the accuracy of the calculations. In addition, sources density are located on the surfaces of the aircraft and domain are shown in Figure 3.17.

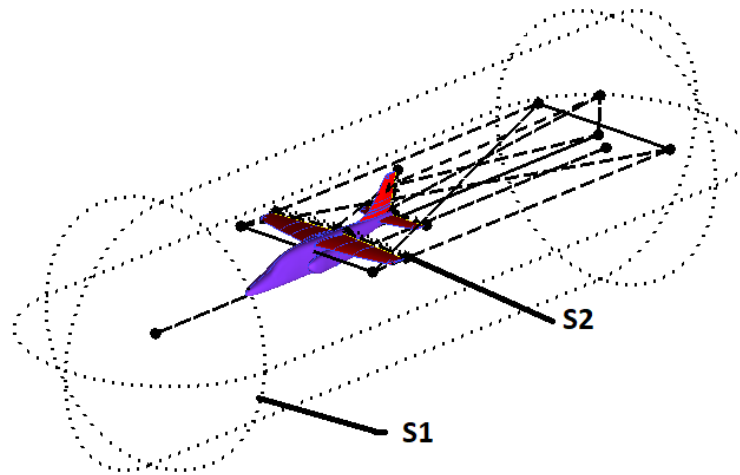


Figure 3.16: Global sources S1, S2 of flow grid density located around the aircraft

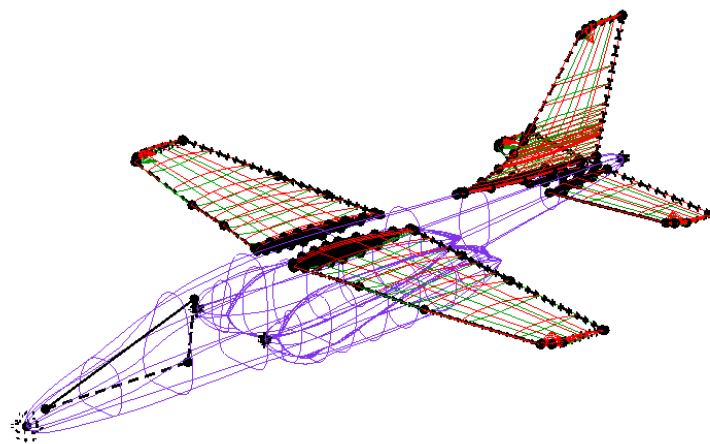


Figure 3.17: Global sources of flow grid density located on the wings and the stabilizer [65]

A detailed arrangement of the sources of flow grid density on individual components is shown in Figures 3.18, 3.19 and 3.20. The position of the sources results from the level of geometry complexity and the location of the expected higher pressure gradients. This is closely related to the expected accuracy of the flow calculations.

Depending on the location of the density source, different values are describing the size of elements and values of their growth coefficient. The values of parameters related to the size and variability of elements at all surfaces were used. The smallest element sizes were located on the leading edges of horizontal stabilizer (0.001 m), wings (0.002 m) and vertical stabilizer (0.004 m). The element size was set at 0.01 m on all trailing edges. The element sizes defined by successive sources gradually increased to 0.25 m around the aircraft. A growth factor of 1.5 was determined

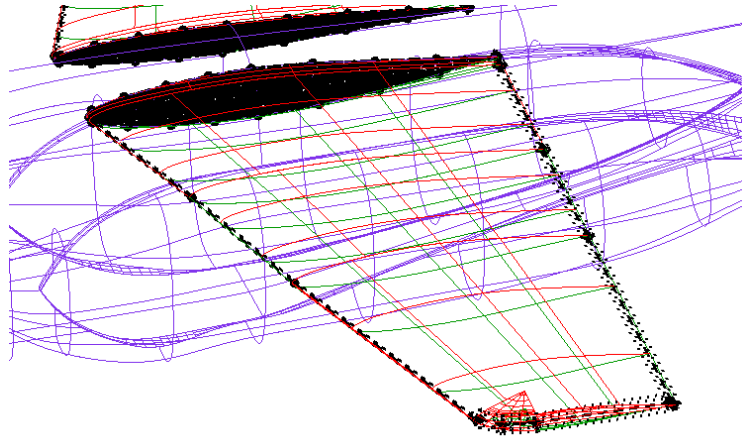


Figure 3.18: Global sources of the flow grid density located on the wings

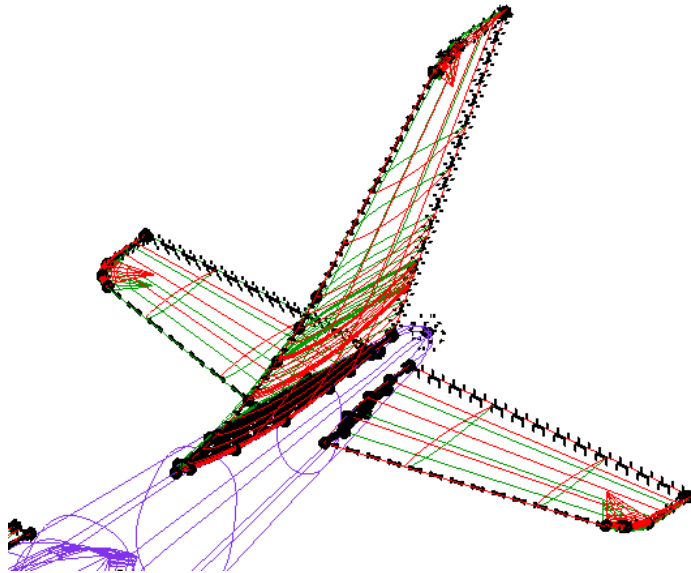


Figure 3.19: Global sources of the flow grid density situated at the ballasts

in all sources for coarsening. At this stage of the work, flow meshes with a different number of elements were generated. The coarse mesh (6 million nodes and 1.1 million elements) was intended for preliminary calculations, and the refined mesh with a larger number of elements (14 million nodes and 2.2 million elements) was used for the final flutter analysis. Both grids were subjected to the error search procedure, taking the following criteria into account:

- duplicated elements - two elements built on the same nodes,
- uncovered surfaces - each wall of a three-dimensional element must be associated with the wall of another three-dimensional element or with a two-dimensional element,
- spatial orientation - the correct order of nodes in the element is checked,
- interpenetrating elements - checking if an element does not penetrate another element.

Figures 3.21 and 3.22 present the distributions of Jacobian quality criterion (CentauroSoft) for both computational grid:

The structure of the meshes did not contain any erroneous elements and the obtained quality of elements was at the level presented in the charts. Further in optimization is achieved by the available repair tools were used, which improved the quality of the worst elements by changing

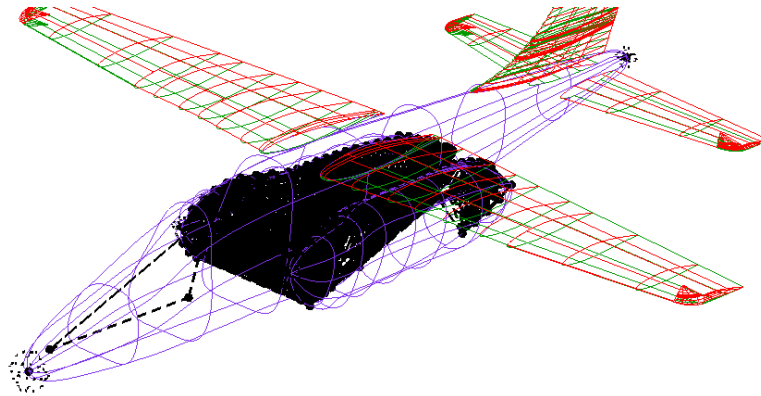


Figure 3.20: Global sources of the flow grid density located on the fuselage

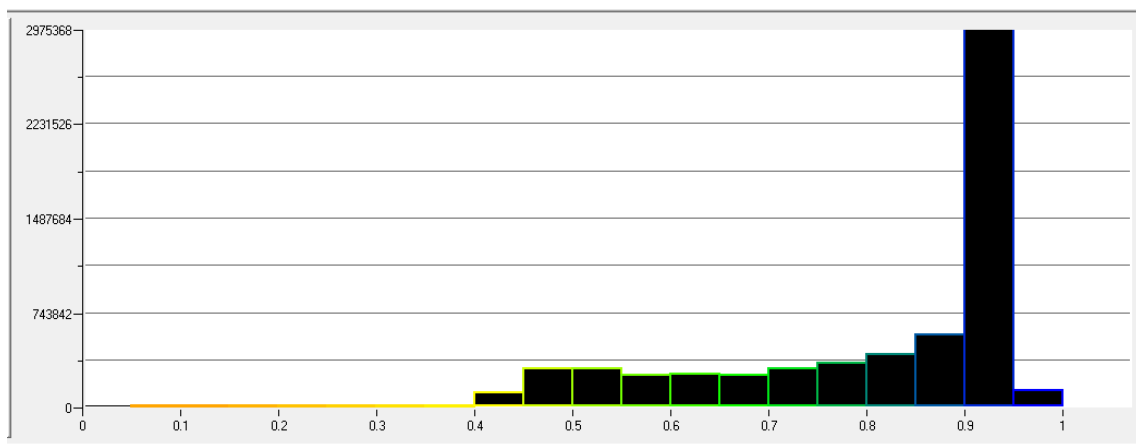


Figure 3.21: The Jacobian quality criterion for elements of the coarse grid for the initial calculations

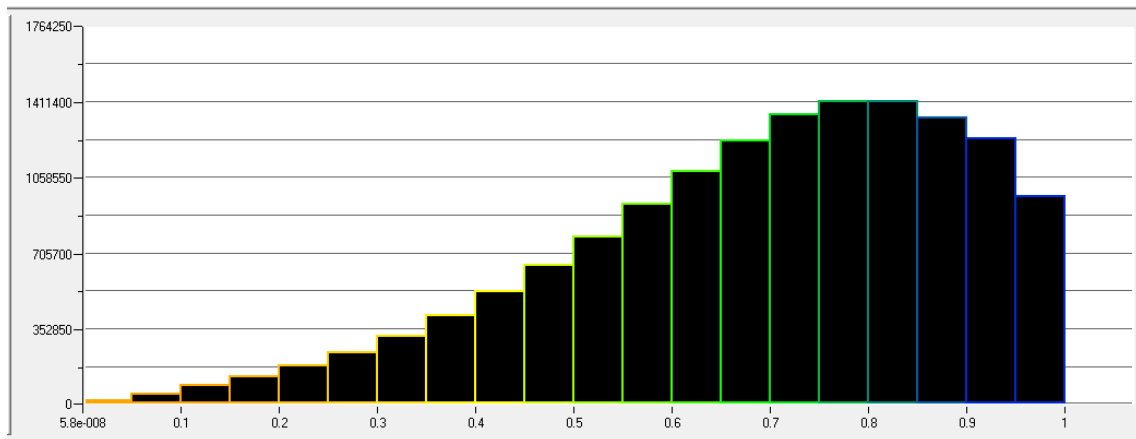


Figure 3.22: The Jacobian quality criterion for elements of the final grid for the flutter analysis

the position of the nodes. Based on the inviscid mesh, a mesh with a boundary layer was generated. The basic parameter determining the thickness of the boundary layer is y^+ , which is defined as the dimensionless distance of the mesh node closest to the surface (edge):

$$y^+ = \frac{u^* \cdot y}{\nu} \quad (3.7)$$

where:

$$u^* - \text{''friction velocity''}, \text{ which is defined as: } u^* = \sqrt{\frac{\tau_w}{\rho}},$$

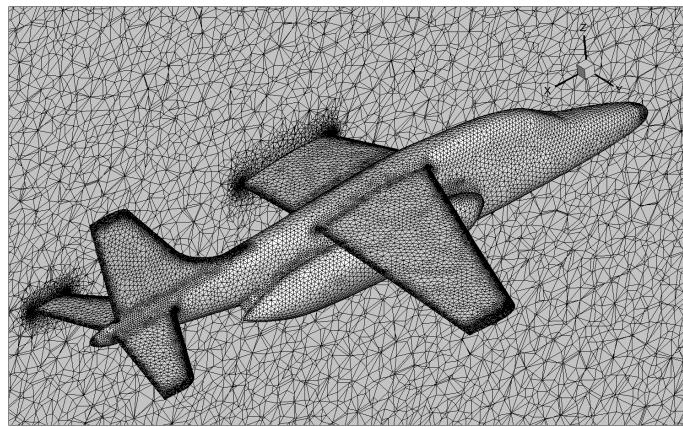
τ_w – shear stress on the wall,

ρ – fluid density on the wall,

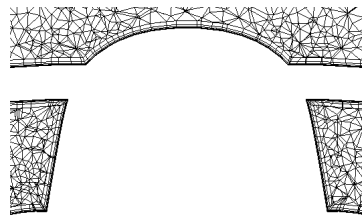
y – first layer thickness,

ν - kinematic viscosity.

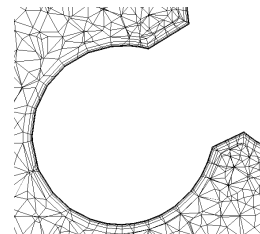
A boundary layer was generated containing nine layers, the first with a thickness of 0.01 mm and a growth factor of 2.05, which provided an average parameter $y^+ = 1.5$. For turbulence model *Wilcox $k - \omega$* a boundary layer with such parameters is sufficient to describe the speed profile distribution at the surface of the object. The generated mesh consisted of 15.5 million nodes and 8 million elements. Figure 3.23 highlights selected locations of the flow grid. Based on inviscid grid and the boundary layer corresponding simulation were performed. They are presented in section 3.7.



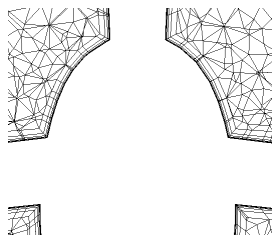
(a) The surface grid and the cross section of the volumetric grid (with a vertical plane)



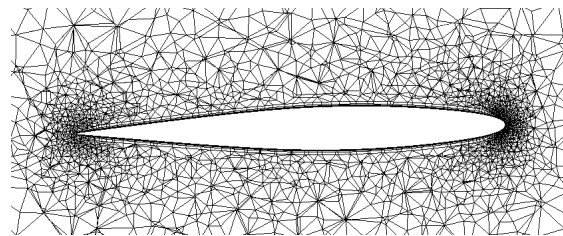
(b) A boundary layer between the wing and the fuselage



(c) A wall boundary layer on the engine nacelle



(d) A boundary layer between the rudders and the fuselage



(e) Boundary layer on the edge of the wing

Figure 3.23: Unstructured mesh with the boundary layer of an aircraft [77]

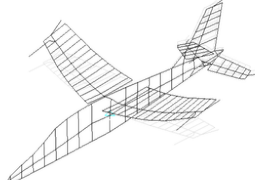
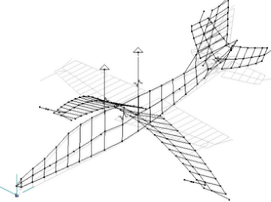
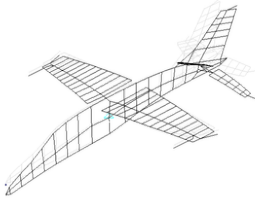
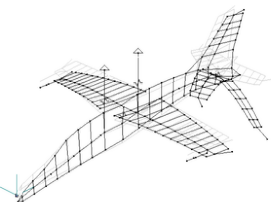
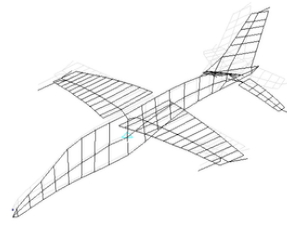
Table 3.4: Summary

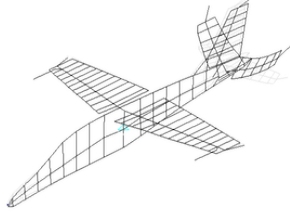
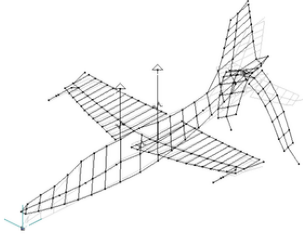
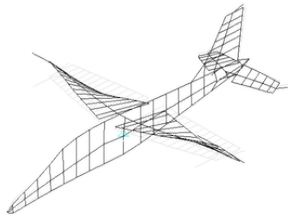
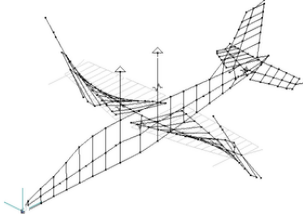
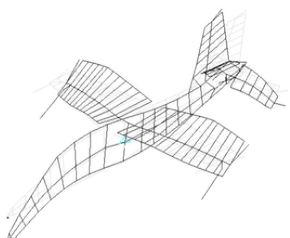
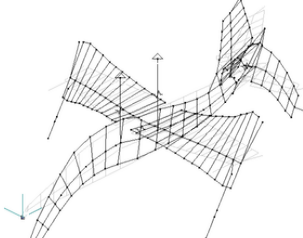
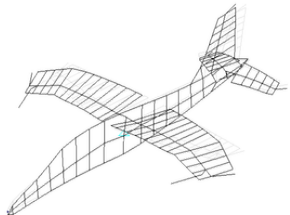
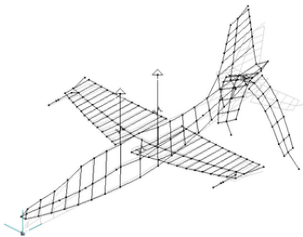
Goal
<ul style="list-style-type: none">• Development of three flow grids:<ul style="list-style-type: none">• coarse for initial CFD calculations grid• high accuracy for final CFD calculations grid• high accuracy with a boundary layer for comparative CFD calculations grid
Tasks performed
<ul style="list-style-type: none">• Checking the correctness of the surface model for the generation of the flow grid• Specifying parameters and generating flow grids• Checking the correctness of the grids for flow calculations and their deformations
Results
<ul style="list-style-type: none">• Three flow grids developed using the CentaurSoft package

3.6 Boundary conditions of the structural model

In section 3.4, the boundary condition of the numerical model was modified and the results of the modal analysis of the new structural model were verified. For each mode of natural vibration obtained by the GVT experimental tests, the same shapes was assigned from the results of the numerical analysis. After the change of boundary condition, the numerical model was more consistent with the real model. Only two shapes could not be identified in the numerical model. Compared to the results before the modifications, where 13 modes were missing, it can be concluded that the new type of boundary condition improved the numerical results. The table below presents a comparison of natural vibrations obtained from the GVT test and numerical analysis. Table 3.5 and Table 3.6 summarizes the results for symmetrical and anti-symmetrical modes respectively.

Table 3.5: Comparison of numerical and experimental results - symmetrical modes

Symmetrical modes	
Experimental results - GVT	Numerical results - NASTRAN
1. 1-wing bending	
	
4,61 Hz	5,02 Hz ($\delta=8,8\%$)
2. 2-node fuselage bending	
	
6,23 Hz	6,80 Hz ($\delta=9,1\%$)
3. 2-node wing and fuselage bending	
	
7,02 Hz	not obtained -

Symmetrical modes	
Experimental results - GVT	Numerical results - NASTRAN
4. 1-bending of the horizontal stabilizer	
	
11,56 Hz	12,10 Hz ($\delta=4,6\%$)
5. 2-wing torsion	
	
14,47 Hz	17,43 Hz ($\delta=20\%$)
6. 3-node fuselage bending	
	
15,58 Hz	18,02 Hz ($\delta=15,58\%$)
7. 1-Horizontal bending of the wing	
	
17,88 Hz	22,89 Hz ($\delta=28\%$)

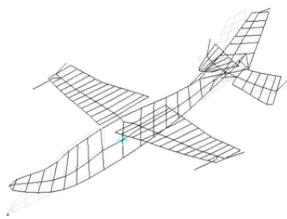
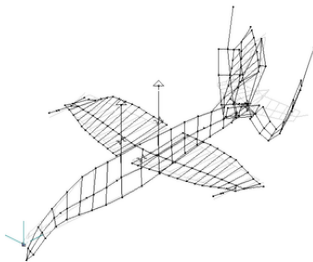
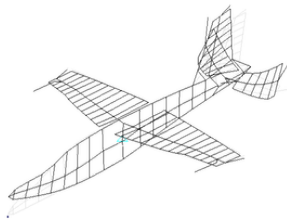
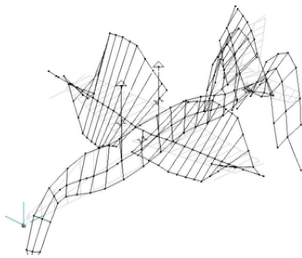
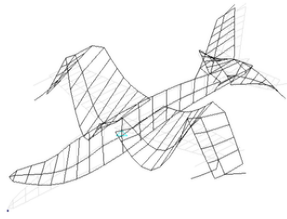
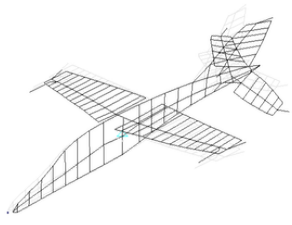
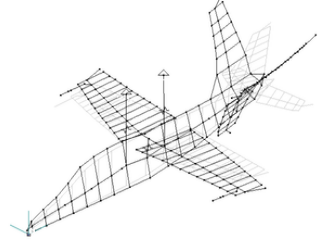
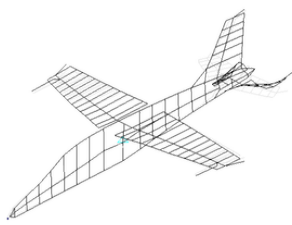
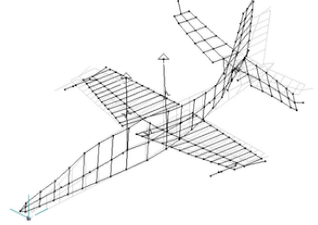
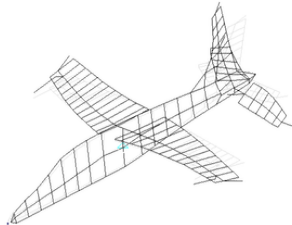
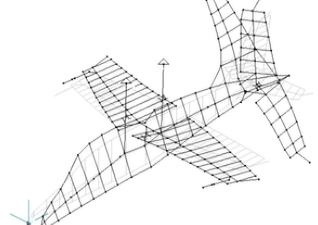
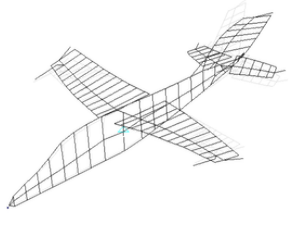
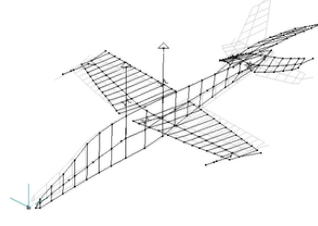
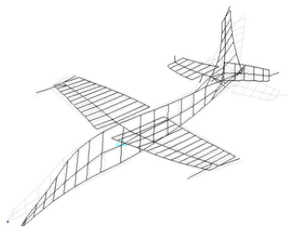
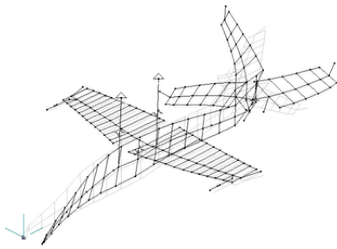
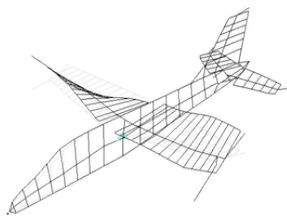
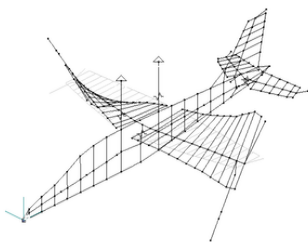
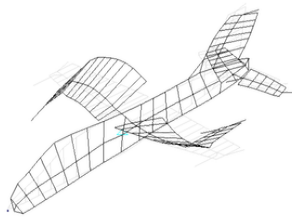
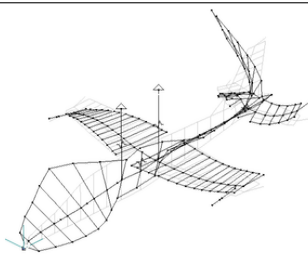
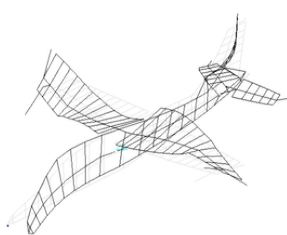
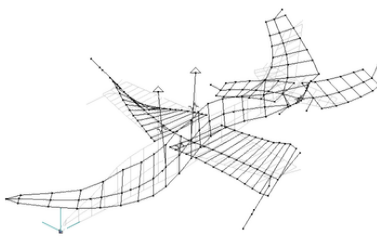
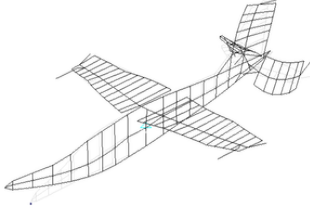
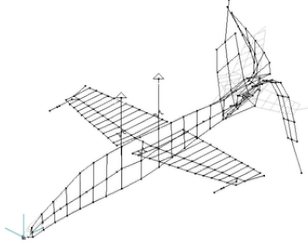
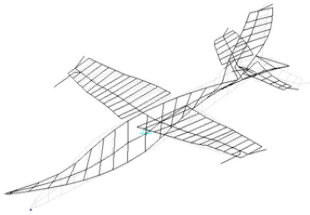
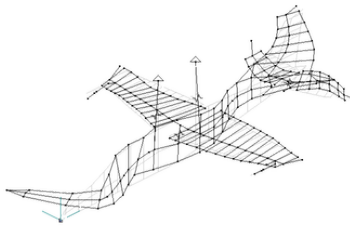
Symmetrical modes	
Experimental results - GVT	Numerical results - NASTRAN
8. II. wing bending	
	
40,10 Hz	39,20 Hz ($\delta f=2,2\%$)
9. I. Horizontal bending of the horizontal stabilizer	
	
44,60 Hz	37,01 Hz ($\delta=17,01\%$)
10. III. wing bending	
	not obtained
48,30 Hz	-

Table 3.6: Comparison of numerical and experimental results - anti-symmetrical modes

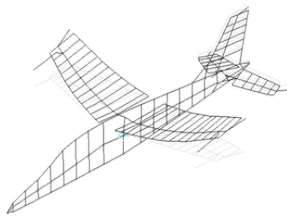
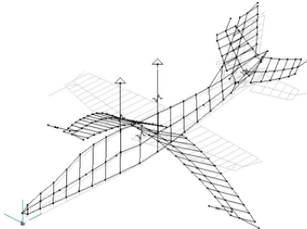
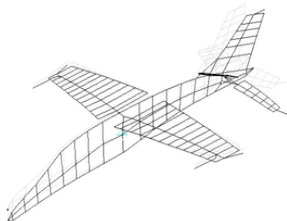
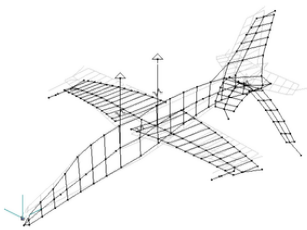
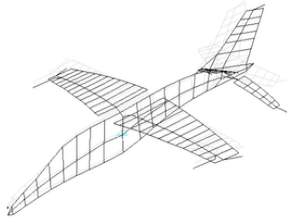
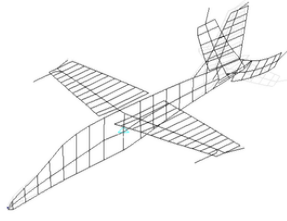
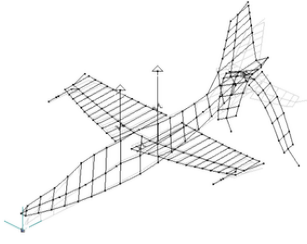
Anti-symmetrical modes	
Experimental Results - GVT	Numerical results - NASTRAN
1. Scissor-type tail-plane oscillation	
	
4,11 Hz	4,43 Hz ($\delta=7,78\%$)
2. 2-node horizontal bending and torsion of the fuselage	
	
4,90 Hz	4,55 Hz ($\delta=7,1\%$)
3. Horizontal scissor swinging of the wings relative to the fuselage	
	
6,70 Hz	4,99 Hz ($\delta=25,5\%$)
4. Fuselage torsion	
	
7,81 Hz	8,94 Hz ($\delta f=14,4\%$)

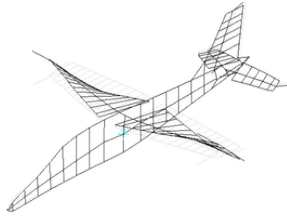
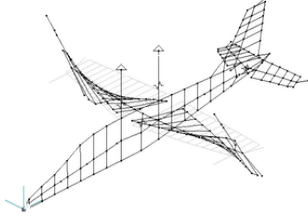
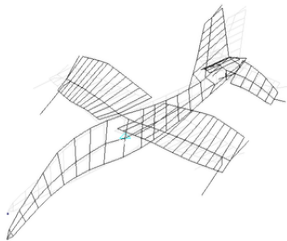
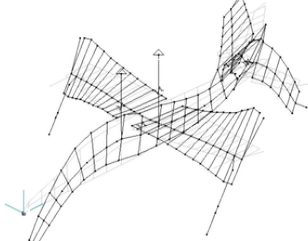
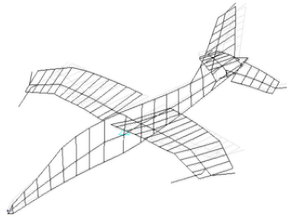
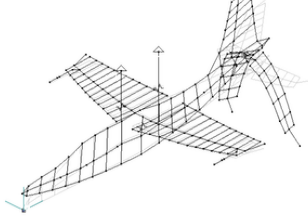
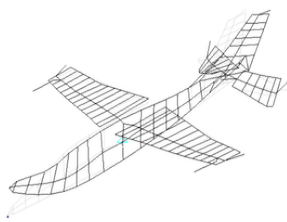
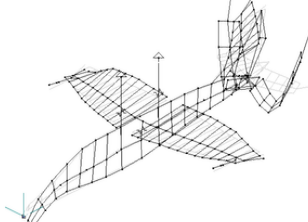
Anti-symmetrical modes	
Experimental Results - GVT	Numerical results - NASTRAN
5. 3-node fuselage bending	
	
10,47 Hz	11,67 Hz ($\delta=11,4\%$)
6. Bending of the vertical stabilizer	
	
14,54 Hz	12,36 Hz ($\delta=14,99\%$)
7. I. wing bending	
	
15,10 Hz	17,42 Hz ($\delta=15,3\%$)
8. I. wing torsion	
	
17,98 Hz	19,81 Hz ($\delta=10,1\%$)

Anti-symmetrical modes	
Experimental results - GVT	Numerical results - NASTRAN
9. I. torsion of the horizontal stabilizer	
	
30,80 Hz	27,20 Hz ($\delta=11,60\%$)
10. Horizontal bending and torsion of the fuselage	
	
39,90 Hz	42,25 Hz ($\delta=5,88\%$)

Analyzing the frequency discrepancies and relative errors, it appears that the numerical model is still not compatible with the experiment. The accuracy of the structural model will have influence on the accuracy of the FSI results. **The next modification, which was introduced in order to improve the compatibility of the model with the real object, consisted in entering the exact material data of the aluminum alloy used.** Commonly used alloys differ in Young's modulus and Poisson's ratio. Tuning of the model was based on changing these parameters compensating the differences resulting from the geometrical simplifications at the stage of the solid model generation. It omitted small connecting elements (bolts, rivets) and simplified geometrical transition in the contact regions between fuselage to wings and fuselage to stabilizers. The process of tuning the mechanical parameters turned out to be very complicated due to the large number of parameters - each component had different material properties independent of the others and one parameter could affect several modes. The change of parameters caused improvements for specific modes and, at the same time, worsened others (modes). So the process of manual adjustment of the model turned out to be complicated and time-consuming. The results of the modifications (material properties) are presented in the tables 3.7 and 3.8.

Table 3.7: Comparison of numerical and experimental results

Symmetrical modes	
Experimental results - GVT	Numerical results - NASTRAN
1. I. wing bending	
	
4,61 Hz	4,65 Hz ($\delta=0,86\%$)
2. 2-node fuselage bending	
	
6,23 Hz	5,91 Hz ($\delta=5,10\%$)
3. 2-node fuselage and wing bending	
	
7,02 Hz	not obtained -
4. I. bending of the horizontal stabilizer	
	
11,56 Hz	9,68 Hz ($\delta=16,20\%$)

Symmetrical modes	
Experimental results - GVT	Numerical results - NASTRAN
5. I. torsion of the wing	
	
14,47 Hz	13,94 Hz ($\delta=3,66\%$)
6. 3-node fuselage bending	
	
15,58 Hz	15,27 Hz ($\delta=1,90\%$)
7. I. Horizontal bending of the wing	
	
17,88 Hz	17,08 Hz ($\delta=4,47\%$)
8. II. wing bending	
	
40,10 Hz	37,33 Hz ($\delta=6,90\%$)

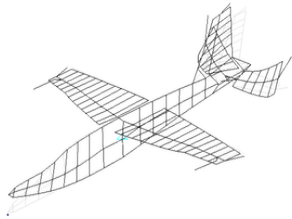
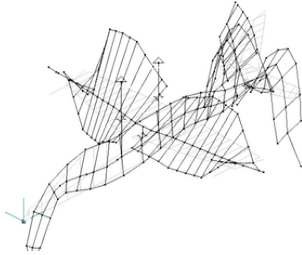
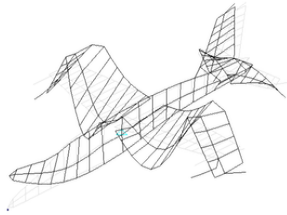
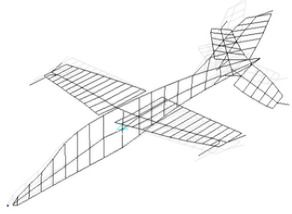
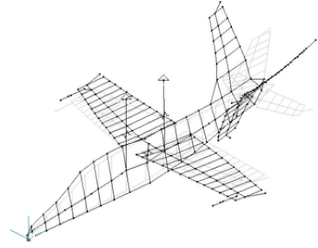
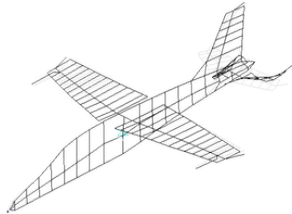
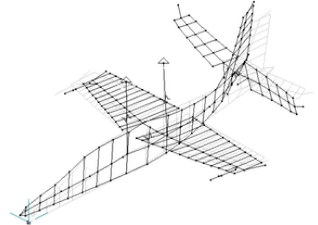
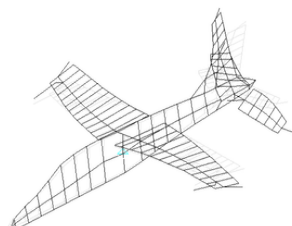
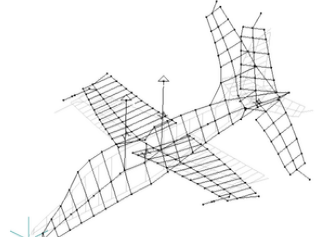
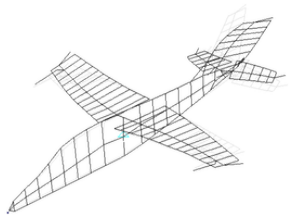
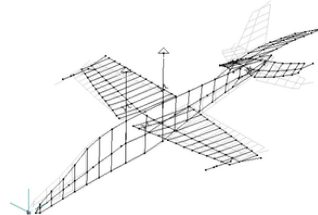
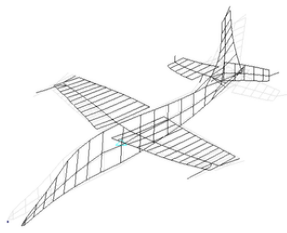
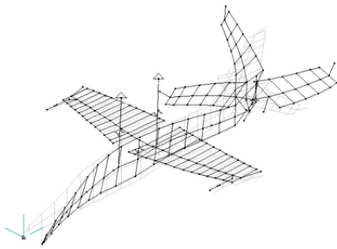
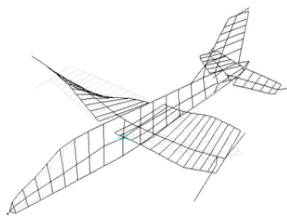
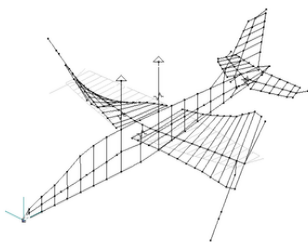
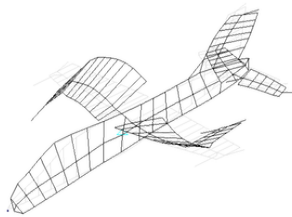
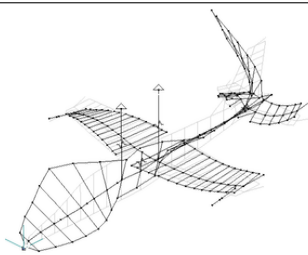
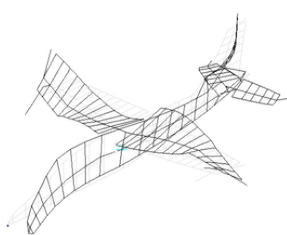
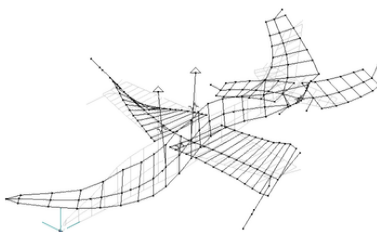
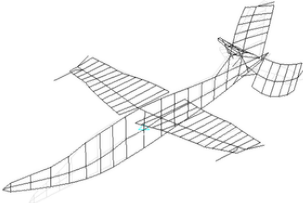
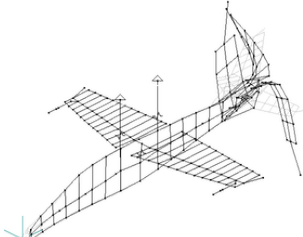
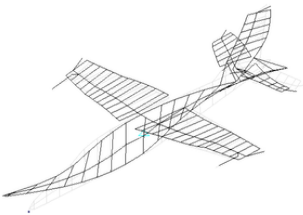
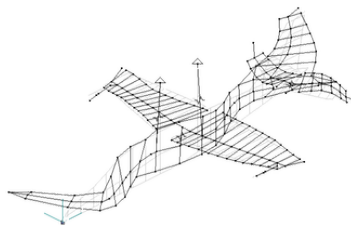
Symmetrical modes	
Experimental results - GVT	Numerical results - NASTRAN
9. I. Horizontal bending of the horizontal stabilizer	
	
44,60 Hz	38,55 Hz ($\delta=13,05\%$)
10. III. wing bending	
	not obtained
48,30 Hz	-

Table 3.8: Comparison of numerical and experimental results

Anti-symmetrical modes	
Experimental results - GVT	Numerical results - NASTRAN
1. Scissor tail swinging	
	
4,11 Hz	3,85 Hz ($\delta=6,30\%$)
2. 2-node horizontal bending and torsion of the fuselage	
	
4,90 Hz	4,06 Hz ($\delta=17,10\%$)
3. Horizontal scissor rocking of the wing in relation to the fuselage	
	
6,70 Hz	6,16 Hz ($\delta=8,05\%$)
4. torsion of the fuselage	
	
7,81 Hz	6,67 Hz ($\delta=14,5\%$)

Anti-symmetrical modes	
Experimental results - GVT	Numerical results - NASTRAN
5. 3-node fuselage bending	
	
10,47 Hz	10,15 Hz ($\delta=3,05\%$)
6. Bending of the vertical stabilizer	
	
14,54 Hz	14,72 Hz ($\delta=1,2\%$)
7. I. wing bending	
	
15,10 Hz	16,28 Hz ($\delta=7,8\%$)
8. I. torsion of the wing	
	
17,98 Hz	15,12 Hz ($\delta=15,9\%$)

Anti-symmetrical modes	
Experimental results - GVT	Numerical results - NASTRAN
9. I. torsion of the horizontal stabilizer	
	
30,80 Hz	29,57 Hz ($\delta=3,99\%$)
10. Horizontal bending and torsion of the fuselage	
	
39,90 Hz	36,74 Hz ($\delta=7,9\%$)

The results obtained are similar with the experimental results for 18 out of 20 natural vibrations. The symmetrical modes 3 and 10 were not identified in the numerical model (this is due to beam simplifications for the wing and fuselage connection - neglect of bolted connections). Analyzing the frequency values for symmetrical modes, discrepancies in modes no. 1, 2, 5, 6 and 7 did not exceed $\delta=5\%$ relative error. For mode 4, the error was $\delta=16,20\%$ for a frequency difference of 1.88 [Hz]. For mode 8 below $\delta=7\%$, while for mode 9 a relative error of $\delta=13,05\%$ was obtained for a frequency difference of 6.05 [Hz] compared to the experimental model. The analysis of anti-symmetrical modes leads to obtained results. An maximum relative error of frequency value obtained for modes 1, 3, 5, 6, 7, 9, 10 was $\delta=7,8\%$. For modes 2, 4 and 8 the relative error of frequency value were $\delta=17,10\%$, $\delta=14,50\%$, $\delta=15,90\%$ respectively. The relative error values obtained are significantly lower for the modified model. Considering in the context of the frequency difference received error below 1 Hz for modes 1, 2, 3, 5, 6 and below 2 Hz for modes 4, 7 and 9. The others were below 3 Hz. In case of the values of frequencies discrepancies for the modes with the lowest value of frequencies, which are the most important in terms of flutter analysis (they represent the highest values of vibration amplitudes), were the smallest. Differences increases for higher modes with significantly higher eigenfrequency. The lack of complete documentation and incomplete information about the structure of the model caused the model reconstruction on the basis of data obtained with the use of reverse engineering and additional measurement on the physical wind tunnel model. In the process of manually tuning the structural model, it was very difficult to obtain results with better accuracy. This was due to a large number of variables which influenced the eigenvalues and correlated effects of dynamic reactions. The lack of the identification of two eigenmodes is most reasonable found by the process of reduction of the solid model, in which some information about the structural representation could have been omitted. Despite the imperfect representation of the complex dynamical behavior, it was decided to proceed with the achieved accuracy [67]. The defined final FEA model of the I22

Iryda aircraft was used in the aeroelastic simulations presented in chapter 4.

Table 3.9: Summary

Goal
<ul style="list-style-type: none">• Verification of the computer structural model and necessary further tuning of its mechanical properties
Tasks performed
<ul style="list-style-type: none">• The model with changed boundary conditions has been validated• Further modifications were made - change of material parameters• Re-verification was carried out
Results
<ul style="list-style-type: none">• Reduced structural model satisfactorily consistent with the results of GVT tests for the aircraft

3.7 Modification of the model

In order to carry out an aeroelastic simulation for the investigation of the flutter phenomenon, several modifications of the model were prepared. Their purpose was to introduce differences in the model sensitivity with respect to this phenomenon. The aircraft flutter model was created during the process of real aircraft design and was used for flutter studies in the wind tunnel. The flutter phenomenon was identified, at a speed of about $v = 32m/s$ [67]. The results were obtained for the demonstrator model with adjustable rudders. The system of the numerical analysis of the flutter phenomenon in the Flutter Research Laboratory at the Poznan University of Technology does not allow to conduct such research (see chapter 3.2). Therefore, modifications were made to the structure of the flutter plane model - all movable elements (flaps, stabilizers and elevator) were fixed with the entire structure and immobilized in a neutral position. Then, preliminary tunnel tests were carried out, which showed that is no flutter phenomenon in the speed range up to $v = 35m/s$, for the modified structure. In order to present the correct operation of the developed method, it was necessary to prepare different versions of the I22-Iryda aircraft model. They had different properties that would cause the flutter phenomenon in different flow conditions. The basic structural model prepared on the basis of the flutter model has been positively verified. Therefore all modifications described below refer to it. One of the reasons for the flutter phenomenon is the incorrect balance of the stabilizers. In a properly designed aircraft, the center of gravity of the moving ailerons should be in front of their rotation axis (measuring in global CS along the X axis of the FEA model). The flutter phenomenon can be excited by introducing additional masses, which change the balance of the aircraft. Therefore, additional masses were added at the trailing edges of wings and stabilizer, which leads to individual mass configurations. The actual additional weights and their distribution are summarized in Table 3.10 and in figure 3.24 [77].

Table 3.10: Configurations of the method demonstrator structural model with the description of the distribution of additional masses

Case	Description of the distribution of masses
0	The basic model described in chapter 3.6 without additional mass/load
1	Version with a load of 50g fixed at the contact between the aileron and the wing tip, approx. 1cm from the trailing edge (symmetrically, on both wings; total weight: 100g)
2	Version with a load of 50g fixed at the contact between the aileron and the wing tip and a load of 50g fixed at the contact between the aileron and the flap, approx. 1cm from the run-off edge (symmetrically, on both wings; total weight: 200g)
3	Version with a load of 50g mounted at the junction of the stabilizer and the end of the model vertical stabilizer and a load of 20g mounted at the height of the upper stabilizer hinge, approx. 1cm from the trailing edge (total weight: 70g).
4	Version with a load of 20g mounted at the outer corner of the stabilizer approx. 1cm high from the stabilizer edge (symmetrically, on both stabilizers, total weight: 40g).
5	Combination of versions 3 and 4 (total weight: 110g)

Five new configurations of the basic structural model have been prepared. Two configurations concern the wing load, the next horizontal and vertical stabilizer additional masses. The last one is a combination of configurations 3 and 4. Configurations have been selected to take into account

the possibility of flutter phenomena both on the wings and on the steering surfaces.



Figure 3.24: Mass configurations of the method demonstrator; colors denote variants according to Table 3.10: 1) red, 2) red + yellow, 3) green, 4) violet, 5) green + violet [65].

After the preparation of the models, modal analyses were carried out for all cases, while the ground vibration tests (GVT) were carried out at the Institute of Aviation. The next task was to verify the prepared modifications of the basic model. This process took place analogously as described in the above chapters. The introduced changes were relatively small and did not reveal any new mode shapes of natural vibrations in the model. Only, the numerical values of eigenfrequencies were changed. The verification consisted of checking whether the received changes in computer simulations corresponded to those from ground vibration tests. Detailed breakdowns are presented in the Table 3.11 and 3.12. The obtained results of simulations for all configuration are listed in the left column, while those obtained from GVT experiments on the right.

Table 3.11: Summary of numerical and GVT results - symmetrical

Symmetrical modal shapes							
No.	Modal shape	Case 0 [Hz]		Case 1 [Hz]		Case 2 [Hz]	
		Num.	GVT	Num.	GVT	Num.	GVT
1	I. Bending of the wings	4,61	4,65	4,47	4,55	4,46	4,50
2	2-Nodal fuselage bending	6,23	5,91	6,25	5,90	6,26	5,90
3	2-Nodal fuselage bending and wings	7,02	-	7,05	-	7,05	-
4	I. Bending of the horizontal stabilizer	11,56	9,68	11,70	9,68	11,72	9,67
5	I. Torsion of the wings	14,47	13,94	14,09	10,82	14,18	10,10
6	3-Nodal fuselage bending	15,58	15,27	15,51	15,22	15,50	15,22
7	I. Horizontal bending of the wings	17,88	17,08	17,42	-	17,64	-
8	II. Bending of the wings	40,10	37,33	39,20	37,32	38,40	37,34
9	I. Horizontal bending of the horizontal stabilizer	44,60	38,55	44,70	38,71	45,60	38,59
10	III. Bending of the wings	48,30	-	47,80	-	48,20	-
No.	Modal shape	Case 3 [Hz]		Case 4 [Hz]		Case 5 [Hz]	
		Num.	GVT	Num.	GVT	Num.	GVT
1	I. Bending of the wings	4,61	4,65	4,61	4,64	4,61	-
2	2-Nodal fuselage bending	6,24	5,90	6,24	5,80	6,21	-
3	2-Nodal fuselage and wings bending	7,01	-	7,00	-	6,95	-
4	I. Bending of the horizontal stabilizer	11,70	9,55	11,23	9,55	11,18	-
5	I. Torsion of the wings	14,45	13,94	14,47	13,94	14,43	-
6	3-Nodal fuselage bending	15,48	15,14	15,57	15,26	15,46	-
7	I. Horizontal bending of the wings	17,87	-	17,89	17,08	17,86	-
8	II. Bending of the wings	40,50	37,00	40,10	36,85	40,00	-
9	I. Horizontal bending of wings	45,40	38,24	45,00	38,47	45,30	-
10	III. Bending of the wings	48,90	-	48,10	-	48,00	-

Table 3.12: Summary of numerical and GVT results - anti-symmetrical

Anti-symmetrical modal shapes							
No.	Modal shape	Case 0		Case 1		Case 2	
		[Hz]	[Hz]	[Hz]	[Hz]	[Hz]	[Hz]
		Num.	GVT	Num.	GVT	Num.	GVT
1	Scissor bending rudders	4,11	3,85	4,06	3,84	4,07	3,83
2	2-Nodes horizontal bending and fuselage torsion	4,90	4,06	4,89	4,05	4,92	4,04
3	Vertical scissors bending wings relative to the fuselage	6,70	6,16	6,68	6,14	6,75	6,13
4	Fuselage torsion	7,81	6,67	7,86	6,63	7,88	6,62
5	3-Nodal fuselage bending	10,47	10,15	10,46	10,15	10,44	10,14
6	I. Torsion of the wings	14,54	14,72	13,74	10,96	13,42	10,29
7	I. Bending of the wings	15,10	16,28	15,10	16,28	14,90	16,27
8	II. Torsion of the wings	17,98	15,12	17,71	15,11	17,80	15,11
9	I. Torsion of the horizontal stabilizer	30,80	29,57	29,30	29,57	29,50	29,57
10	Horizontal bending and torsion of fuselage	39,90	36,74	40,10	36,74	39,70	36,74
No.	Modal shape	Case 3		Case 4		Case 5	
		[Hz]	[Hz]	[Hz]	[Hz]	[Hz]	[Hz]
		Num.	GVT	Num.	GVT	Num.	GVT
1	Scissor bending the fuselage	3,98	3,73	4,04	3,79	3,97	3,69
2	2-Nodal bending and torsion of fuselage	4,94	4,04	4,78	4,00	4,78	3,99
3	Vertical scissors bending wings relative to the fuselage	6,64	5,93	6,76	6,11	6,58	5,87
4	Fuselage torsion	7,48	6,42	7,86	6,66	7,45	6,42
5	3-Nodal fuselage bending	10,42	10,08	9,75	10,04	9,60	9,96
6	I. Torsion of wings	14,48	14,71	14,54	14,71	14,48	14,72
7	I. Bending of wings	15,07	16,07	15,10	16,27	15,08	16,07
8	I. Bending of wings	17,89	15,11	17,91	15,07	17,96	15,14
9	I. Torsion of the horizontal stabilizer	28,60	29,31	28,60	29,04	28,40	28,57
10	Horizontal bending with torsion of fuselage	39,10	36,73	39,10	36,71	39,40	36,70

The results presented in the tables above confirm that, like the basic model, all its modifications are consistent with the respective modifications of the flutter model. Analyzing the results of the frequency values for the symmetrical modes presented in Table 3.11, a decrease in their value was obtained for the mode no.1 - I. Bending of the wings, and the mode no. 5 - I. Torsion of the wings. These values change for cases 0, 1, and 2, where additional masses are added on the wings. In the case of the frequency values for the anti-symmetrical modes presented in 3.12, a small decrease in their value was obtained for the mode no. 2 - 2-Nodal bending and torsion of fuselage and for mode no. Fig. 5 - 3-Nodal of fuselage bending for cases 3, 4, and 5, where additional masses were given on the vertical and horizontal stabilizers. A greater change in the

frequency value was obtained for the mode no. Fig. 6 - I. Torsion of the wings for cases 0, 1, and 2, where additional masses were added on the wings. As the consequence, 5 models of the structure were generated, with different mechanical properties, in which the flutter phenomenon is predicted for different critical velocities. This is essential for the testing and verification regime in the developed method.

Table 3.13: Summary

Goal
<ul style="list-style-type: none"> • Preparation of various mass configurations of the structural model • Verification of prepared models
Tasks performed
<ul style="list-style-type: none"> • The possibility of the flutter phenomenon depending on the balance of the steering surfaces was analyzed • 5 different mass distribution to further investigate the flutter phenomena • All configurations have been verified by of an ground vibration tests (GVT).
Results
<ul style="list-style-type: none"> • 5 revised cases of the structure model

3.8 Preparation of the calculation

The current chapter presents the results of simulations carried out for the real airplane model. The numerical configuration of the aeroelastic environment for studying the flutter phenomenon is presented in chapter 3.2. The adopted solution implies three steps to recalculate each numerical case in this work:

- steady calculations - determining the displacement of each of the components of the aircraft structure (wings, stabilizers, fuselage) due to aerodynamic forces,
- load initialization - deriving the structure from the steady state,
- non-stationary calculations - examination of the structure's response in time to the given load.

The first step of numerical flutter simulation, steady calculations, is to prepare the entire environment for conducting proper non-stationary calculations. The goal of steady state calculation is the stable positioning of the aircraft in a steady. Generally, between five to ten data exchanges are necessary to achieve stationary balance. Then the structure is obtained from the steady state by giving deformation-controlled impulse loading. Following, non-stationary calculations are carried out. At this stage of the flutter simulation, approximately three to four data exchanges are performed in each aeroelastic loop to determine the position of the aircraft structure of the given time step. Figure 3.25 illustrates how much calculation time is consumed by the three different stages. The initiation of flutter simulation, which combines stationary calculations which impact load, takes only small part of the overall calculation time. The computation time of each aeroelastic simulation loop is the sum of wall time of flow calculations, data exchange and structural calculations. Structural calculations and data interpolation tools have been implemented on a single processor. In addition, the use of the modal method provided effective simulations of structural part of the system. The clock time of these two simulation steps is less than a minute. The efficiency of the flow simulation in the DLR TAU-code software is therefore decisive for the simulation. Parallelization is currently the best measure to reduce calculation time. Using an unstructured mesh without and with a boundary layer (section 3.5), calculations were performed to check the performance of the aeroelastic analysis. For the inviscid grid, the wall time was 480 seconds (8 minutes) using 8 computational nodes. However, for calculations on a viscous grid, the clock time was 15540 seconds (about 4.3 hours) using 100 cores. This is due to a more complex type of calculations - the use of the turbulence model requires a large number of iterations in the DLR TAU-code software to obtain the required convergence of the flow part. Aeroelastic calculations using the equation connecting the flow part - RANS - are about 30 times longer than in the case of calculations based on the Euler equation for the same load case.

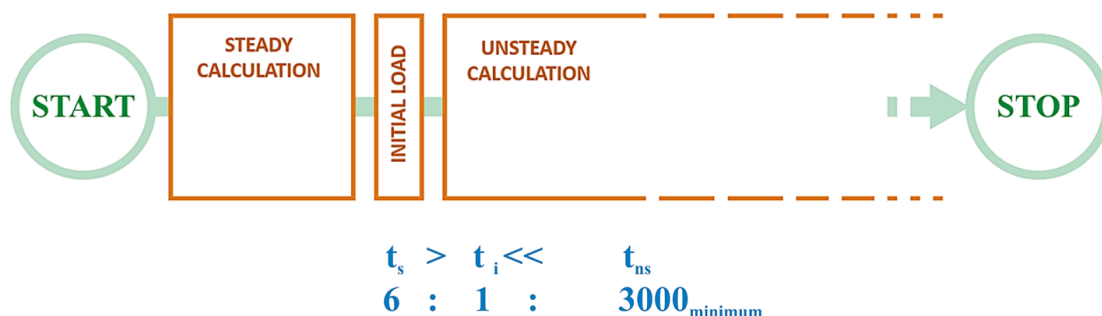


Figure 3.25: Stages of numerical calculations of the aeroelastic problem and the comparison of their times in relation to others [43].

The time for calculations of non-stationary flutter simulations depends on the time step, the total time of the phenomenon studied and the performance of the computer equipment. The time step was defined as $1/512$ [s] and was consistent with value from the sampling of the measuring apparatus at the Institute of Aviation. In the aeroelastic analyses, calculations should last until the occurrence of flutter as until the establishing stable oscillations (which is equivalent to steady state). It is possible to simulate the behavior of the aircraft in the initial phase of the flutter phenomenon, but large displacements of the components in the actual structure cause in general the complete failure of certain aircraft components. **In the numerical analysis, the module responsible for the flow mesh deformation identifies the bad quality of the elements and stops the simulation.** In the event where damping appears in the structure of the method demonstrator, six seconds were used as the maximum time of the aeroelastic phenomenon to be studied. As presented (section 3.6) in the design of the demonstrator, the lowest eigenvalue occurs at a frequency around 4 [Hz]. This is the most dangerous case. The assumed calculation time is sufficient for investigating the flutter phenomenon. Preliminary numerical flutter analyzes of the method demonstrator show that the time to simulate one time step for 8 cores of a computer cluster takes about 480 seconds, while for 40 cores can reduce the time to approx. 340 seconds. The simulations were performed using the Euler governing equation. The adopted parameters of aeroelastic simulation show that more than 3000 time steps have to be calculated. For 40 cores of the cluster, the planned time of one simulation takes two weeks, and for 8 - almost three. In the section 4.1, five variants of structural mass configuration of structures are presented. For each variant, four simulations of measuring points are scheduled for different values of the inflow speed on the structure ($v = 20, 25, 30, 35[m/s]$). Therefore, 20 independent flutter simulations had to be performed to determine the damping coefficients of each variant of the method demonstrator. Using all the resources of the computer cluster and analyzing each of the variants and each of the measurement points sequentially, the predicted time of simulation of all cases is about 9 months. Therefore it was decided to carry out two independent simulations in parallel with 8 nodes computer cluster each. Then the predicted simulation time is three months. For five test cases, preliminary simulations were carried out for one velocity ($v = 35[m/s]$) and with a time step of $1/128$ [s]. For this purpose, a computer cluster was used, allowing parallel computation on eight computational nodes. After the first month, the preliminary results were available and finally presented in section 4.1. The discussed results were necessary to define the cases to be recalculated in the full velocity range to determine the damping ratios of the aircraft design. Table 3.14 summarizes the work and research described in this chapter.

Table 3.14: Summary

Goal
<ul style="list-style-type: none">• Performing initial aeroelastic calculations for unbalanced cases for the aircraft• Beginning of basic numerical analyzes of selected mass configurations of the aircraft
Tasks done
<ul style="list-style-type: none">• Expansion of the aeroelastic system with the possibility of error control and data archiving
Results
<ul style="list-style-type: none">• Completion of initial simulations

Chapter 4

Results

4.1 Numerical analysis - initial calculation

In the current chapter of thesis presented was to perform aircraft analysis for various mass configurations. The simulation does not directly return quantitative results of the flutter. Visualization of the results allows a qualitative assessment of the system structure response and determines whether there is a flutter phenomenon for the tested configuration under specific flow conditions. The direct results of the initial numerical simulations are the displacement and angle rotation values obtained from elements such as wings, vertical and horizontal stabilizers in which the flutter phenomenon occurs [67]. The obtained displacements and angles described the behavior of the aircraft model, whose response consisted of a combination of appropriate eigenmodes. On their basis, both initial load response and the occurrence of the flutter phenomenon were investigated. The Fig. from 4.2 to Fig. 4.16 present the each diagram combines the displacement and the rotation components w.r.t. to the coordinate system indicated in figure 4.1. The results are presented for individual mass configuration cases according to the table 3.10. For five test cases, preliminary simulations were carried out for velocity ($v = 35[m/s]$) and with a time step of $1/128 = 0.0078 [s]$. The time step was defined according to the sampling rate of the wind tunnel measurement systems [69]. It was necessary due to the correct interpretation of the results for the preparation of experimental tests in the wind tunnel as part of cooperation with IoA Warsaw.

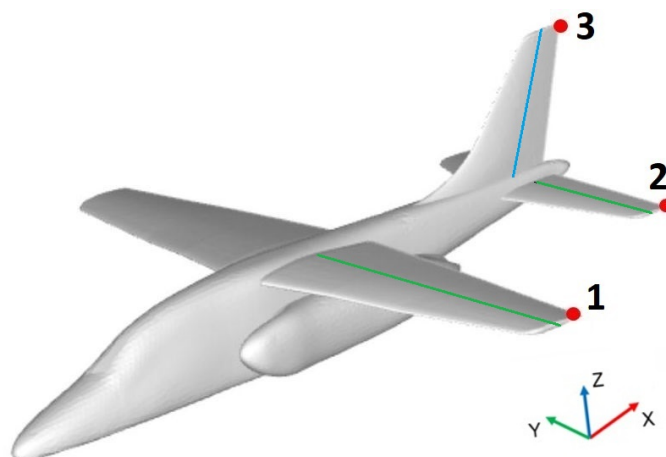


Figure 4.1: Measuring nodes located on aircraft model for initial calculation.

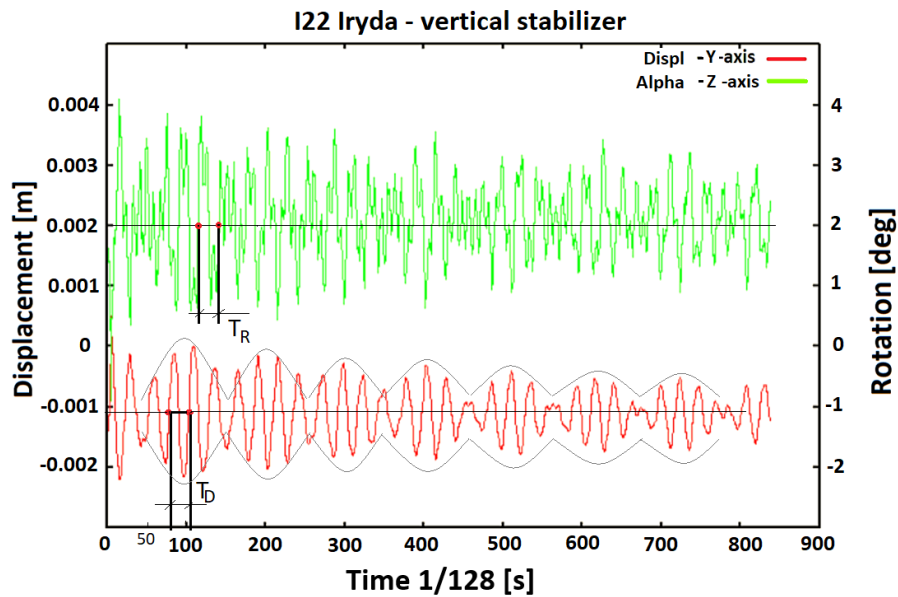


Figure 4.2: Summary of results for configuration No. 1 acc. to table 3.10 - displacements and rotations of the **node 3** on the vertical stabilizer.

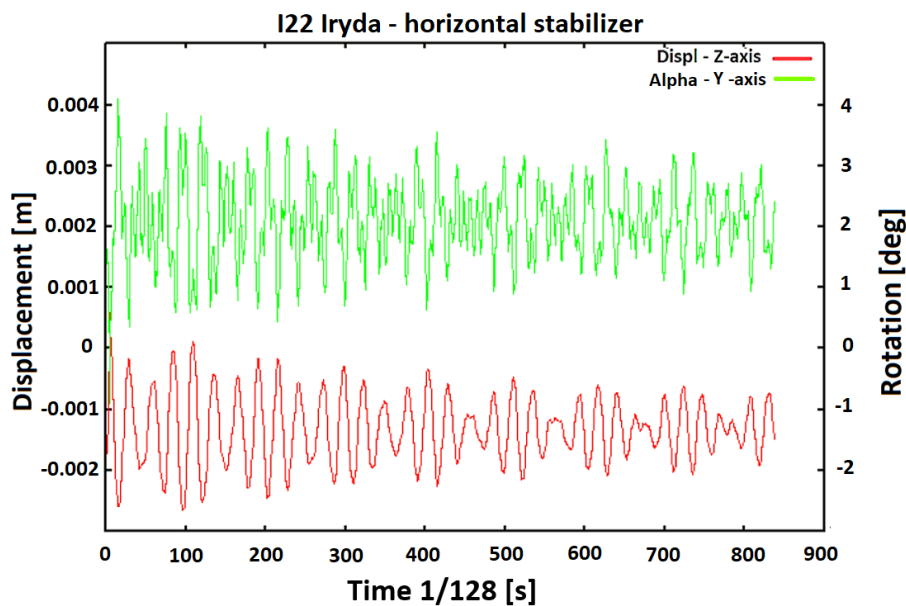


Figure 4.3: Summary of results for configuration No. 1 acc. to table 3.10 - displacements and rotations of the **node 2** on the horizontal stabilizer.

According to the Fig. 4.2 and 4.3 the number of time steps per one period for displacement and rotation angle were determined. Then the analysis of the displacement diagrams, the time period and frequency of the function can be approximated $T_D \approx 28/128 \approx 0.22[s]$. Where T_D and T_R are the periods for displacement and rotation respectively. According to the diagram Fig. 4.2, it was assumed that the period values for T_D displacement and T_R rotation angle are very similar.

$$f \approx \frac{1}{28/128} \approx \frac{1}{0.22} \approx 4.57[Hz] \quad (4.1)$$

For the horizontal and vertical stabilizer, the displacement and rotation angle graphs are very similar. The frequency value $4.57[Hz]$ corresponds to the frequency for mode No. 1 according to table 3.12 (Case 1) - Scissor bending rudders and the frequency for mode No. 2 - 2-Nodal bending and torsion of fuselage. **Although the shapes obtained for the stabilizers and wings contain responses for all modes, the aircraft responds mainly at the lowest stiffness.** The Fig. 4.2 marked a curve of repeated sequences of the displacement course. This can be identified as a beating phenomenon. Beating is a phenomenon resulting from the superimposition of two vibrations with similar amplitudes and slightly different frequencies. The analysis of the periodic changes in displacement and rotation angles shown in the Fig. 4.2, Fig. 4.3 and Fig. 4.4, one can conclude that in this case obtained similar frequencies and amplitudes for the wings and stabilizers.

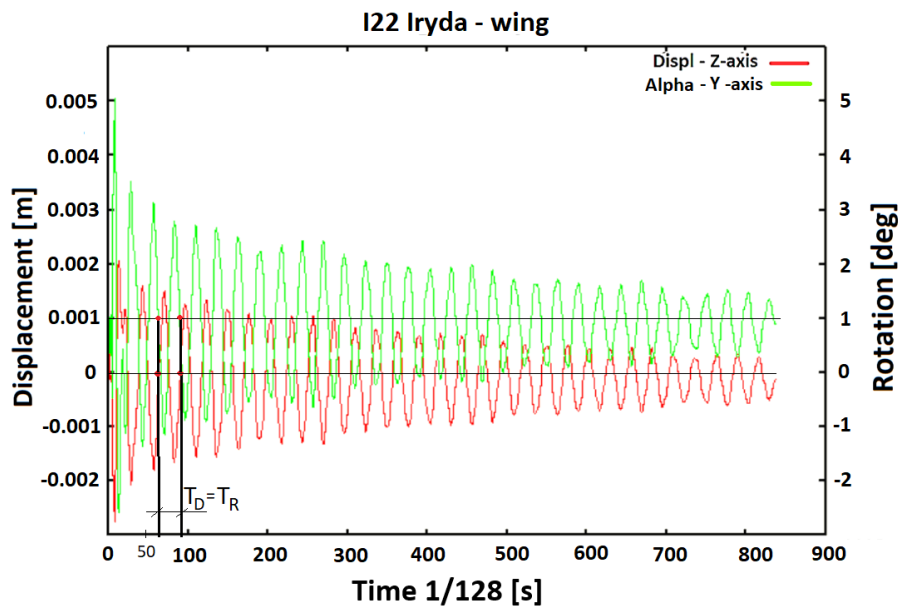


Figure 4.4: Summary of results for configuration No. 1 acc. to table 3.10 - displacements and rotations of the **node 1** on the wing.

Similar to stabilizers for case 1 the analysis of the displacement and rotation diagrams according to Fig. 4.4, the time period and frequency can be approximated $T_D \approx 27/128 \approx 0.21[s]$, where value 27 means time steps. The period values T_D (displacement) and T_R (rotation angle) are very similar in this case as well.

$$f \approx \frac{1}{27/128} \approx \frac{1}{0.21} \approx 4.74[Hz] \quad (4.2)$$

For the wing of I22 Iryda aircraft the frequency value $4.74[Hz]$ corresponds mainly to the frequency for mode No. 1 according to table 3.11 (Case 1) - I bending of the wings. This frequency is consistent with the first lowest frequency response for wing bending. Analyzing the periodic curve for case 1, i.e. the first configuration of the I22 Iryda aircraft, one can see the response of the aircraft in accordance with the determined eigenmodes and their frequencies.

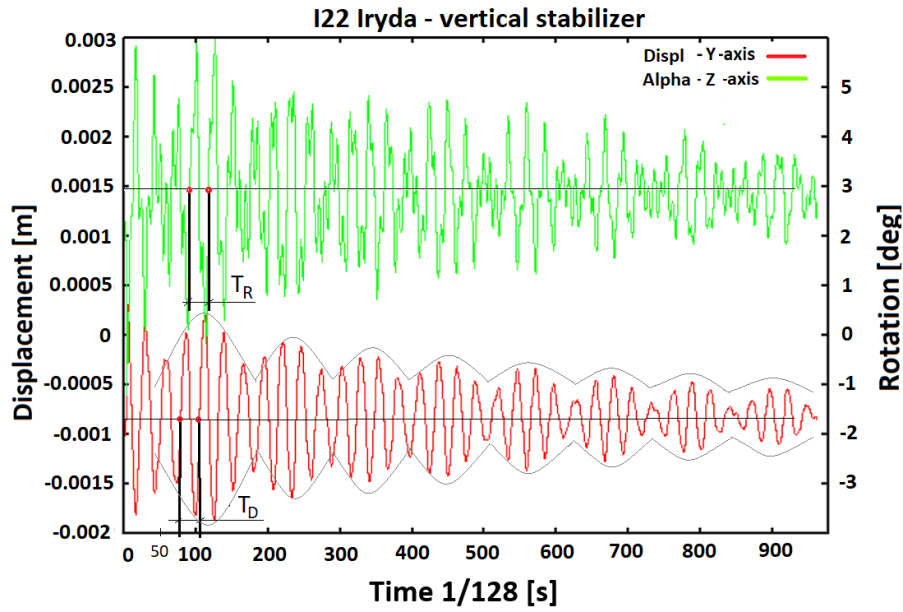


Figure 4.5: Summary of results for configuration No. 2 acc. to table 3.10 - displacements and rotations of the **node 3** on the vertical stabilizer.

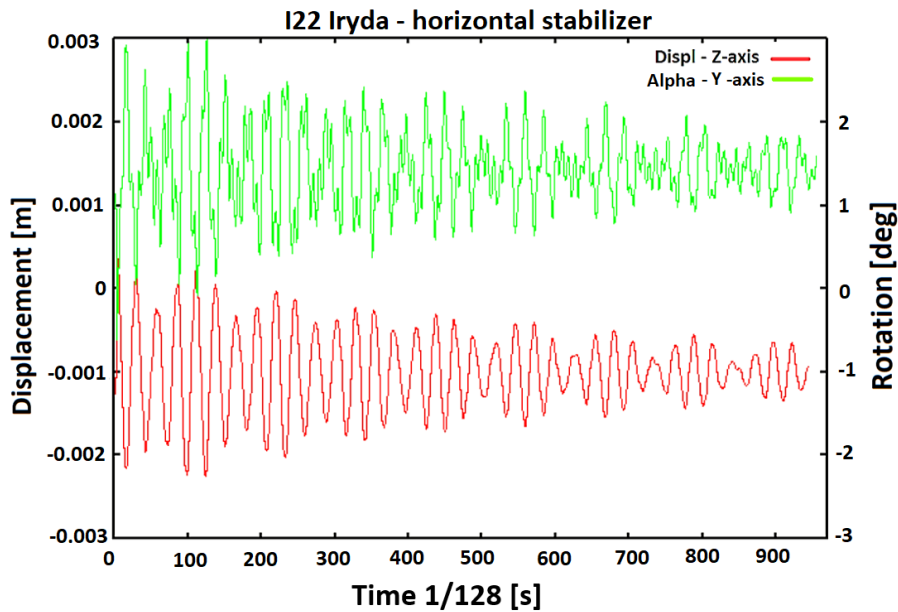


Figure 4.6: Summary of results for configuration No. 2 acc. to table 3.10 - displacements and rotations of the **node 2** on the horizontal stabilizer.

Regarding to the case 2 in Table 3.10 the analyzing of the displacement and rotation angle diagrams according to Fig. 4.5 and Fig. 4.6, the time period and frequency of the function can be approximated $T_D \approx 26/128 \approx 0.20[s]$, where value 26 is obtained from graph and means time steps. For case 2 The period values T_D (displacement) and T_R (rotation angle) are very similar.

$$f \approx \frac{1}{26/128} \approx \frac{1}{0.20} \approx 4.92[Hz] \tag{4.3}$$

For the horizontal and vertical stabilizer, the displacement graphs are very similar in this case as well. The frequency value $4.92[Hz]$ corresponds to the frequency for mode No. 1 according to table 3.11 (Case 2) - Scissor bending rudders and the frequency for mode No. 2 - 2-Nodal bending and torsion of fuselage. The additional masses added on the wings did not significantly affect the rigidity of the aircraft's rear fuselage and their frequency. The change for Case 2 does not significantly affect the stability of the stabilizers and fuselage. In this case, the phenomenon of beating was also obtained.

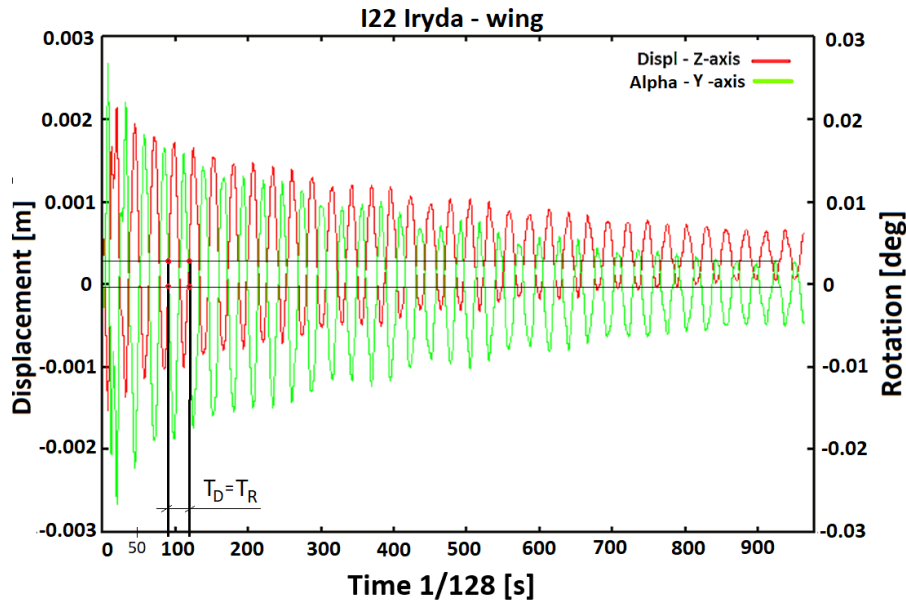


Figure 4.7: Summary of results for configuration No. 2 acc. to table 3.10 - displacements and rotations of the **node 1** on the wing.

The analysis of the displacement and rotation angle diagrams according to Fig. 4.7, the time period and frequency of the function for case 2 can be approximated $T_D \approx 29/128 \approx 0.22[s]$. The value 29 is obtained from graph and means time steps. As shown in the Fig. 4.7, the periods for displacement T_D and rotation angle T_R are the same.

$$f \approx \frac{1}{22/128} \approx \frac{1}{0.22} \approx 4.41[Hz] \quad (4.4)$$

For the wing of I22 Iryda aircraft the frequency value $4.41[Hz]$ corresponds to the frequency for mode No. 2 according to table 3.11 (Case 2) - I. Bending of wings. This frequency is consistent with the first lowest frequency response for wing bending. Comparing the frequency for the configuration No. 2 regards to the reference configuration of the I22 Irida aircraft, it can be seen that adding additional masses resulted in a slight decrease in wing stability which is due to the lower frequency for wing bending. For case 2 it is not observed a significant decrease in value that can cause flutter phenomena.

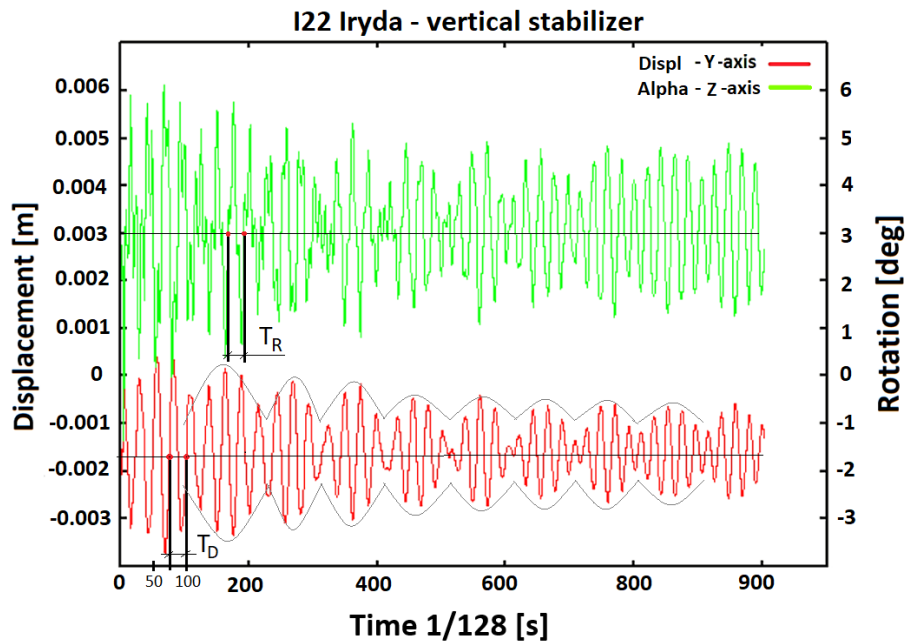


Figure 4.8: Summary of results for configuration No. 3 acc. to table 3.10 - displacements and rotations on the **node 3** on the vertical stabilizer.

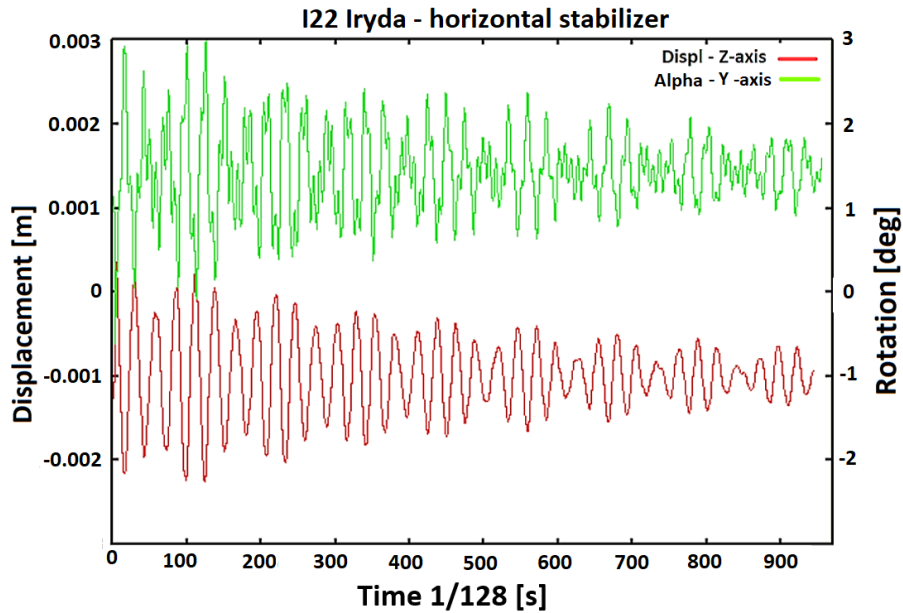


Figure 4.9: Summary of results for configuration No. 3 acc. to table 3.10 - displacements and rotations of the **node 2** on the horizontal stabilizer.

Regarding to the table 3.10 and the analysis the displacement and rotation angle diagrams according to Fig. 4.8 and Fig. 4.9, the time period and frequency of the function for case 3 can be approximated $T_D \approx T_R \approx 27/128 \approx 0.21[s]$. Where value 27 is defined as a time steps.

$$f \approx \frac{1}{27/128} \approx \frac{1}{0.21} \approx 4.74[\text{Hz}] \quad (4.5)$$

For the horizontal and vertical stabilizer, the displacement graphs are very similar. The frequency value $4.74[\text{Hz}]$ corresponds to the frequency for mode No. 1 according to table 3.11 (Case 3) - Scissor bending rudders and the frequency for mode No. 2 - 2-Nodal bending and torsion of fuselage. Adding additional masses to the vertical stabilizer causes a decrease in stability in the tail section of the aircraft's fuselage. The change of the stabilizers frequency for the configuration No. 3 is $0.6[\text{Hz}]$ with regard to the configuration No. 2. However, this is not a significant decrease in value that can cause flutter phenomena on stabilizers. In this case, the phenomenon of beating was also obtained, which has been marked in Fig. 4.8.

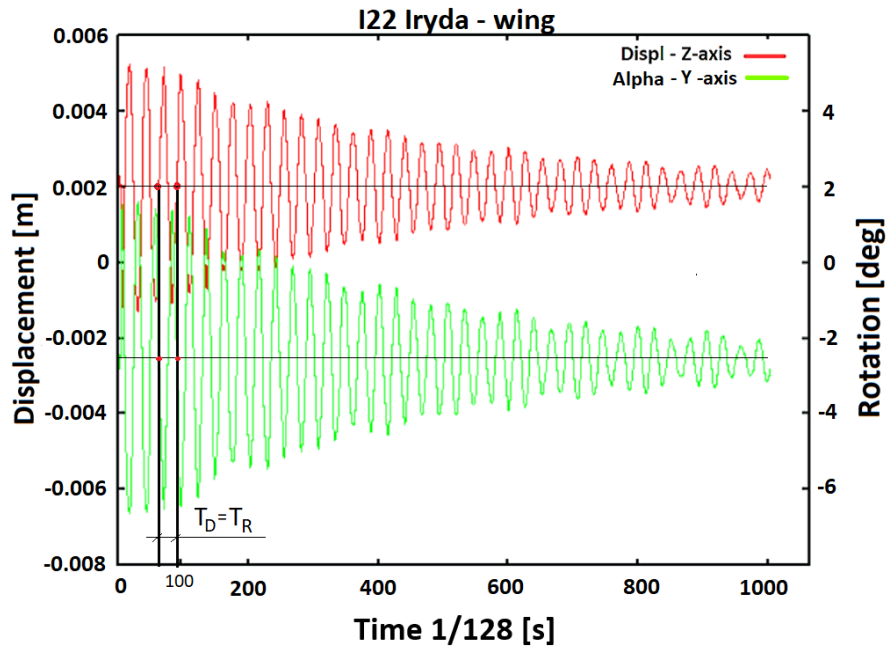


Figure 4.10: Summary of results for configuration No. 3 acc. to table 3.10 - displacements and rotations of the **node 1** on the wing.

The analysis of the displacement and rotation angle diagrams according to Fig. 4.7, the time period and frequency of the function for case 2 can be approximated $T_D \approx 29/128 \approx 0.22[\text{s}]$. The value 29 is obtained from graph and means time steps. For case 3 the periods for displacement T_D and rotation angle T_R are very similar.

$$f \approx \frac{1}{22/128} \approx \frac{1}{0.22} \approx 4.41[\text{Hz}] \quad (4.6)$$

For the wing of I22 Iryda aircraft the frequency value $4.41[\text{Hz}]$ corresponds to the frequency No. 2 according to table 3.11 (Case 3) - I. Bending of wings. This frequency is consistent with the first lowest frequency response for wing bending. Adding additional masses located on vertical stabilizers resulted in a slight decrease in wing stability which is due to the lower frequency for wing bending. However, this is not observed a significant decrease in value that can cause flutter phenomena.

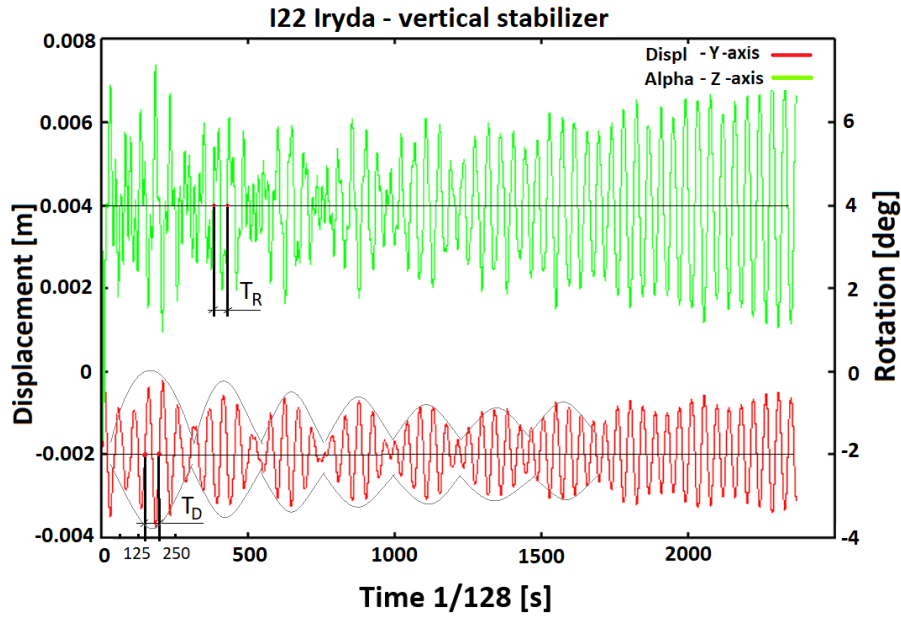


Figure 4.11: Summary of results for configuration No. 4 acc. to table 3.10 - displacements and rotations of the **node 3** on the vertical stabilizer.

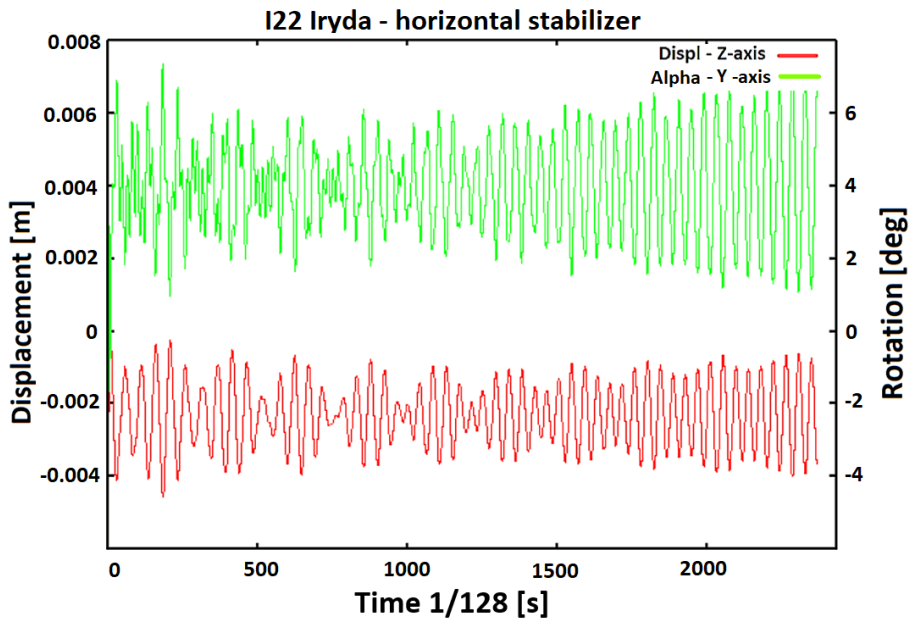


Figure 4.12: Summary of results for configuration No. 4 acc. to table 3.10 - displacements and rotations of the **node 2** on the horizontal stabilizer.

In configuration No. 4 the additional masses were located on the horizontal stabilizers (Fig. 3.24), an increase in the oscillation amplitude can be observed for the rear part of the fuselage. The analysis of the displacement and rotation angle diagrams according to Fig. 4.11 and Fig. 4.12, the time period and frequency of the function can be approximated $T_D \approx T_R \approx 35/128 \approx 0.27[s]$, where value 35 denote time steps.

$$f \approx \frac{1}{35/128} \approx \frac{1}{0.27} \approx 3.70[Hz] \quad (4.7)$$

For the horizontal and vertical stabilizer, the displacement and rotation angle diagrams are very similar. The frequency value $3.70[Hz]$ corresponds mainly to the frequency for mode No. 2 according to table 3.11 (Case 4) - 2-Nodal fuselage bending and to the frequency for mode No. 1 according to table 3.12 (Case 4) - scissors bending the fuselage. In this case, other function components of the displacement and rotation angle can be observed. These are higher frequencies, which required Fourier transformation to determine. However, this is not relevant to this analysis. In the Fig. 4.11 and Fig. 4.12 one can observe an increase in the amplitude. The oscillation value for the displacement is in the range of 2 [mm] and for the angle of rotation 4 [deg]. For the examined period for case 4, the increase in the amplitude did not increase rapidly. The frequency decrease associated with the rear fuselage, where the horizontal and vertical stabilizers are located, may affect the possibility of flutter. This will be the subject of further analysis. The additional masses placed to change the stability of the aircraft resulted in lower frequencies for the rear part of the fuselage. The change for Case 4 is more visible $\approx 1.0[Hz]$ and may affect the stability of the aircraft's stabilizers and rear part of fuselage. In case 4, the phenomenon of beating was also obtained and is more visible, which has been marked in Fig. 4.11.

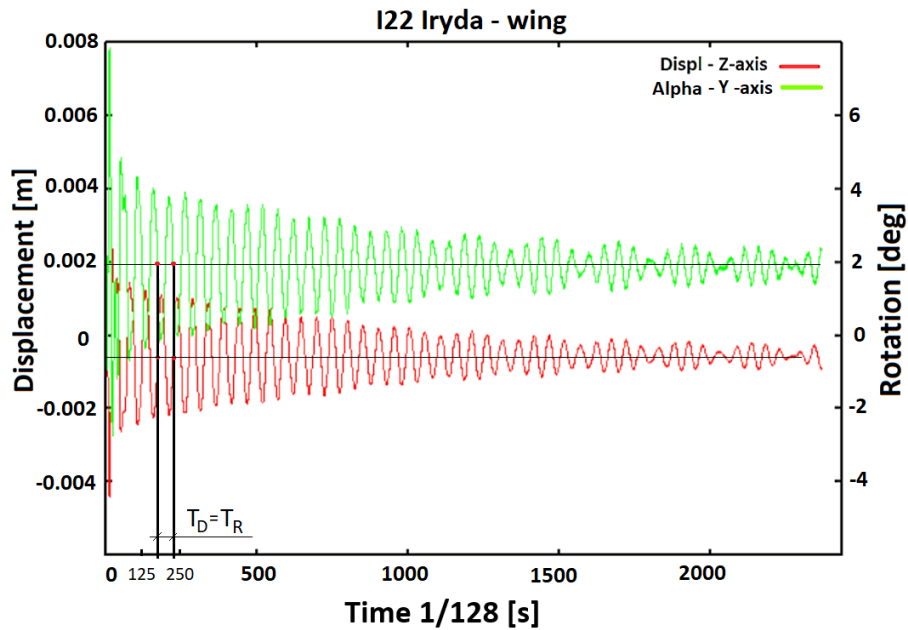


Figure 4.13: Summary of results for configuration No. 4 acc. to table 3.10 - displacements and rotations of the **node 1** on the wing.

The analysis of the displacement and rotation angle diagrams according to Fig. 4.13, the time period and frequency of the function for case 2 can be approximated $T_D \approx 45/128 \approx 0.35[s]$. Where value 45 means time steps. For case 4 the periods for displacement T_D and rotation angle T_R are the same.

$$f \approx \frac{1}{45/128} \approx \frac{1}{0.35} \approx 2.85[Hz] \quad (4.8)$$

For the wing of I22 Iryda aircraft the frequency value $2.85[Hz]$ corresponds to the frequency for mode No. 2 according to table 3.11 (Case 4) - I. Bending of wings. This frequency is consistent with the first lowest frequency response for wing bending. Analyzing the graphs for case 0, the basic configuration of the I22 Irida aircraft, one can also see a decrease in frequency as a result of the FSI analysis. Adding additional masses to the horizontal stabilizers resulted in a further

decrease of wing stability. The periodic curve is damped in this case (Case 4), which can be seen in figure 4.13. Flutter wings in this case will not occur.

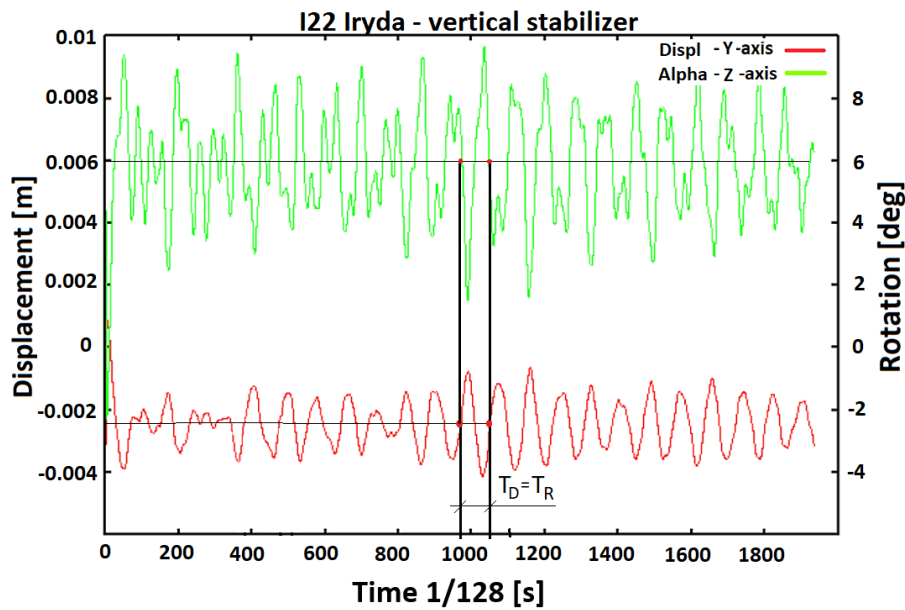


Figure 4.14: Summary of results for configuration No. 5 acc. to table 3.10 - displacements and rotations of the **node 3** on the vertical stabilizer.

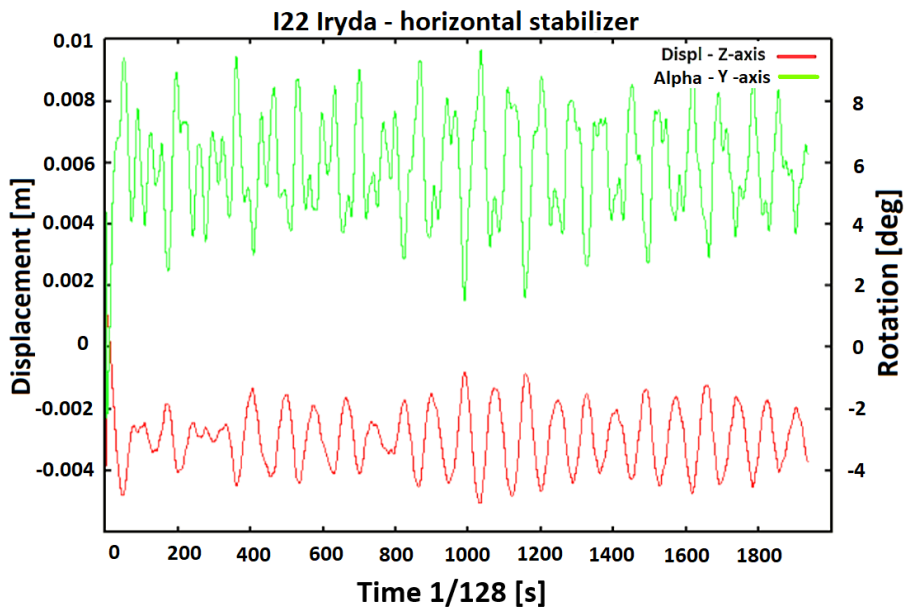


Figure 4.15: Summary of results for configuration No. 5 acc. to table 3.10 - displacements and rotations of the **node 2** on the horizontal stabilizer.

For Case 5, which is a combination of configurations 3 and 4, additional masses were added on both stabilizers - vertical and horizontal. The analyzing of the displacement diagrams according to Fig. 4.14 and Fig. 4.15, the time period can be determined. The displacement and angle rotation over time for configuration 5 contains many components, the determination of which requires decomposing the signals into individual eigenvalues. The primary frequency of the function can be approximated $T_D = T_R \approx 45/128 \approx 0.35[s]$

$$f \approx \frac{1}{45/128} \approx \frac{1}{0.35} \approx 2.84[Hz] \quad (4.9)$$

For the horizontal and vertical stabilizer, the displacement graphs are very similar. The frequency value $2.84[Hz]$ corresponds mainly to the frequency No. 2 according to table 3.11 (Case 5) - 2-Nodal fuselage bending and to the frequency No. 1 according to table 3.12 (Case 5) - scissors bending the fuselage. In this case, other signal components can be observed. These are higher frequencies, which required Fourier transformation to determine. However, this is not relevant to this analysis. The frequency decrease associated with the rear fuselage, where the horizontal and vertical stabilizers are located, may affect the possibility of flutter. This will be the subject of further analysis. The additional masses placed to change the stability of the aircraft resulted in lower frequencies for the rear part of the fuselage. The change for Case 5 is more visible $\approx 2.0[Hz]$ and may affect the stability of the aircraft's stabilizers. For case 5, the beating phenomenon is not visible, it is caused by a greater frequency difference due to the additional masses and the change in the balance of the aircraft components.

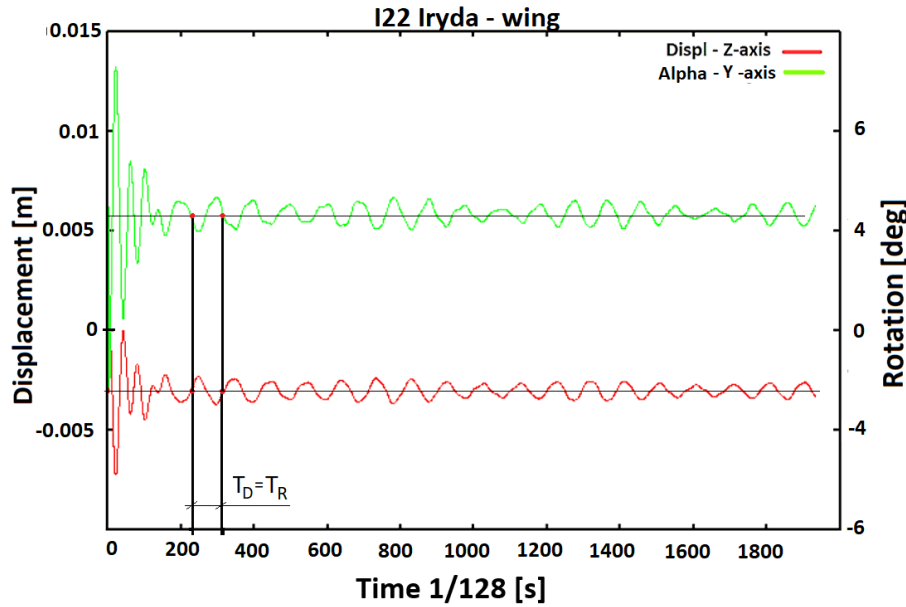


Figure 4.16: Summary of results for configuration No. 5 acc. to table 3.10 - displacements and rotations of the **node 1** on the wing.

For case 5 the analysis of the displacement and rotation angle diagrams according to Fig. 4.16, allow the time period and frequency of the function for case 5 can be approximated $T_D = T_R \approx 52/128 \approx 0.40[s]$. The value 52 means time steps.

$$f \approx \frac{1}{52/128} \approx \frac{1}{0.40} \approx 2.46[Hz] \quad (4.10)$$

For the wing of I22 Iryda aircraft the frequency value $2.28[Hz]$ corresponds to the frequency No. 2 according to table 3.11 (Case 5) - I. Bending of wings. In case 5, the decrease in oscillation frequency estimated from the displacement analysis read from the aircraft wing is due to the additional masses located on the aircraft. For configuration 5, the wing displacement maintains a constant amplitude, as shown in the Fig. 4.16. This case will also be further analyzed for flutter investigation in FSI and wind tunnel analysis.

The presented figures 4.2-4.16 of displacement and rotation angle for the horizontal and vertical stabilizers and wings for a particular mass configuration indicate the aerodynamic damping

of individual components of the airplane for particular mass configurations. By adding additional masses, no flutter effect was obtained. The main goal of the initial calculations was to indicate which configuration will be analyzed more thoroughly using DMD (Dynamic Mode Decomposition) analysis in order to determine the damping ratio for selected shapes of eigenmodes [75, 76].

The purpose of the aeroelastic simulations was to prepare experimental tests in the wind tunnel and appropriate numerical tests. From the presented results, options 4 and 5 were selected for further experimental and numerical analysis. This was dictated by the increase in the amplitude in real time on the horizontal stabilizer surfaces, which may indicate the occurrence of the flutter phenomenon - particularly noticeable in configuration No. 4 (Fig. 4.11, 4.12, 4.13). For configuration 3, a tendency to increase the amplitude over time (Fig. 4.8, 4.9, 4.10) can be observed. Configuration 5, which is a combination of configurations of masses No. 3 and 4, was selected for further analysis of the flutter phenomenon (experimental and numerical) due to the displacement amplitude and angle values shown in Figures: 4.14, 4.15 and 4.16.

Decomposition into dynamic modes decomposition (DMD - Dynamic Modes Decomposition) is one of the methods to obtain global modes based on empirical data without referring to governing equations. This method is similar to the decomposition into principal components (POD - Proper Orthogonal Decomposition; PCA - Principal Component Analysis), which, however, lacks dynamic information about the data. The dynamic mode decomposition does not contain any averaging operation, which means that information on the course of the process under investigation in space and time is preserved. The real parts of the matrix's eigenvalues represent the growth or attenuation rates and the imaginary parts the eigenvalues of the related DMD modes. At this stage, the initial calculations were completed. The numerical analysis for the final configuration are presented in section 4.2.

Table 4.1: Summary

Goal
<ul style="list-style-type: none"> • Carrying out initial aeroelastic calculations
Task done
<ul style="list-style-type: none"> • Selection of configuration for further research - analysis of initial results • Completion of numerical simulations
Results
<ul style="list-style-type: none"> • Results of initial calculation for masses configuration

4.2 Numerical analysis - final calculation

The main goal of the previous tasks was to analyze the results of the initial calculations; on this basis the parameters were set and the configurations were selected for calculation. Based on the analysis of mass configurations for the maximum assumed velocity (section 4.1), it was found that the loads in configuration 1 (Case 1 - table 3.10) and 2 (Case 2 - table 3.10) cause slightly smaller changes in the dynamic response of the aircraft when compared to reference configuration (Case 0 - 3.10). The biggest changes were caused by the load used in configuration 4 (Case 4 - 3.10) and 5 (Case 5 - 3.10). Therefore, three configurations were selected for the purposes of further calculations and tests in the wind tunnel: the reference model and configurations 4 and 5. As a preliminary result for configuration 3 and 4 can lead to the occurrence of flutter. The flutter phenomenon will be assessed on the basis of the α (Eq. 4.25) decay rates determined from the Dynamic Mode Decomposition (DMD) analysis depending on the flow velocity. The sign of the α_j decay rate explains the stability of the system; negative sign means damping [76]. If modal damping ratios fall below 0.015 – 0.02 [67], there is a danger of the flutter phenomenon. The velocity, at which this occurs considered as critical flutter velocity. The goal of analyzing of the aerodynamic damping ratios for eigenmodes of fluttering shapes (wings and stabilizers of the aircraft) of the model is:

- determination of the character of the aerodynamic damping of the basic shapes near the critical flutter velocity (whether the flutter is preceded by a slight or rapid decrease in damping),
- determination of the range of velocities in which the aerodynamic damping ratios for selected eigenmodes decreases,
- investigation of the influence of some design parameters on the aerodynamic damping for specific eigenmodes.

The decrease in the damping ratios causes an increase in the amplitude of the displacement and rotation for stabilizers and wings. It is related to the service of life of the structure or its elements, the safety, the flight comfort and the pilot properties. In aircraft flutter tests according to regulations (e.g. JAR, CS) it is assumed as dangerous, the drop of the attenuation of damping ratio about 0.03 – 0.04 is considered decisive for the acceptance of the aircraft for flight [67].

During the aeroelastic simulations, damping ratios are not calculated. As a result of the simulation, information such as the displacement or the acceleration at individual nodes of the structural model is obtained. These data are the result of the displacement for all shapes of natural vibrations that the model covers in the simulated flow. It is necessary to process the signals of points to identify the eigenmodes. In real wind tunnel tests, the signals from the measuring points of the numerical model correspond to acceleration signals from accelerometers [69]. Currently, accelerometers were attached to the physical model of the aircraft to obtain the information necessary to determine the current value of the damping ratios during wind tunnel tests.

In order to analyze numerical results for carrying out experimental tests in a wind tunnel, points were selected corresponding to the location of the named sensors on experimental flutter model (Fig. 4.17). The data (obtained in each test) were used to determine the α coefficients from equation 4.25 for given velocities and to collect them on the structure damping charts. The definition of the measurement points of the numerical model is based on the location of accelerometers on the real model of the aircraft and has to be accounted for the geometrical model in the first stage. Next, the time step of the numerical aeroelastic analysis was determined. The measuring equipment consists of accelerometers wired to an analog-to-digital converter and an amplifier connected to the computer with software. The software allowed for real-time tracking of displacements at measurement points [68], [69].

The equipment at the Institute of Aviation in Warsaw made it possible to record the acceleration up to a frequency 512[Hz], which corresponded to a time step of 0,0039s [69]. The final

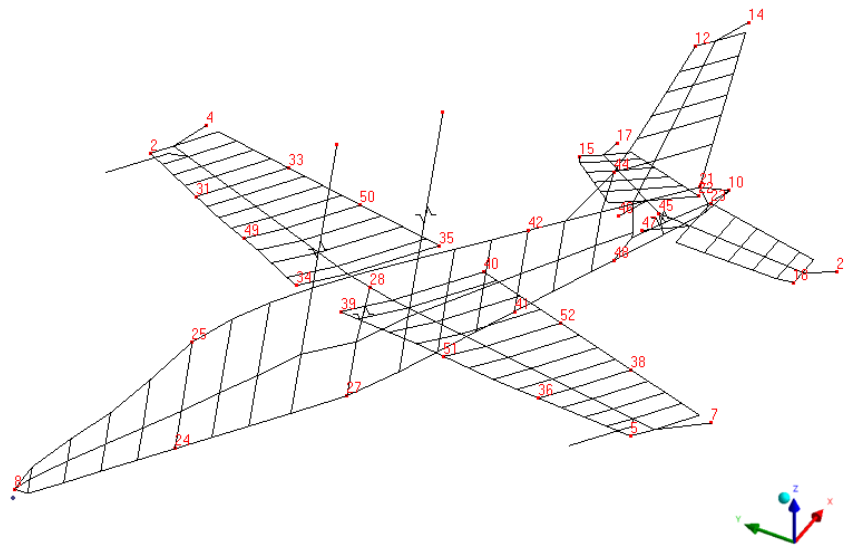


Figure 4.17: Distribution of the sensors on the aircraft structural model

calculation results were presented as the distribution of damping ratios for individual shapes of eigenmodes depending on the flow velocity (Fig. 4.22 and 4.30). Furthermore, tests for different velocities had to be carried out for each selected mass configuration. Preliminary studies conducted by the Institute of Aviation during the design of the aircraft showed that the phenomenon of flutter for wind tunnel velocities can be obtained from $V_X = 20[m/s]$ to $V_X = 35[m/s]$. The simulation was carried from velocities $V_X = 20[m/s]$ to $V_X = 35[m/s]$ by an increment $V_X = 5[m/s]$.

For signals that consist of several sinusoidal signals, it is not possible to determine the amplitudes of two consecutive maxima. In this case, it is necessary to use dynamic identification methods. They allow the signal to be split into components that correspond to individual shapes and to determine their attenuation coefficients. Computational tools have been developed at the Institute of Aviation in Warsaw to solve this problem in the experimental part. The input signal is the shapes of displacement or acceleration from individual sensors, therefore it is possible to use it both for signals from the wind tunnel experiment and for signals derived from numerical calculations. As an output, the application determines the shapes and frequencies of eigenmodes and their damping ratios [68].

Tests in the wind tunnel have shown a flutter phenomenon, on the tail section under the condition of the released (moving) ailerons. Due to the lack of simulations reflecting the moving parts of the aircraft, such as stabilizers and flaps, these elements were fixed in the numerical model. Adding the masses at the ends of blocked stabilizers was to force the occurrence of the flutter phenomenon. Based on numerical calculation using of the structural model shown in Fig. 4.17, the distribution (Fig. 4.19, 4.20 and 4.21) of decay rates α and frequencies f for individual modes were determined. These results were obtained based on the Dynamic Mode Decomposition (DMD) method described below. The method determines modes of the structural response in FSI analysis.

For the analysis of numerical results of the aeroelastic simulations, the DMD method was used to determine the α decay rate (explains the stability of the system) of particular mode shapes. DMD can be characterized as a statistical method, based on experimental data – a set of snapshots (Fig. 4.18). It is the time domain analysis, where snapshots are acquired in constant time steps.

One of the advantages of this solution is no recurrence to the governing equation. It means, any structure can be analyzed, because the state matrix does not contain information about the structure topology or connections. On the other hand, the state matrix includes dynamical information about the data, hence the eigenvalues of the state matrix characterize the frequencies and the decay rates of the system. DMD can be viewed as Laplace analysis [75].

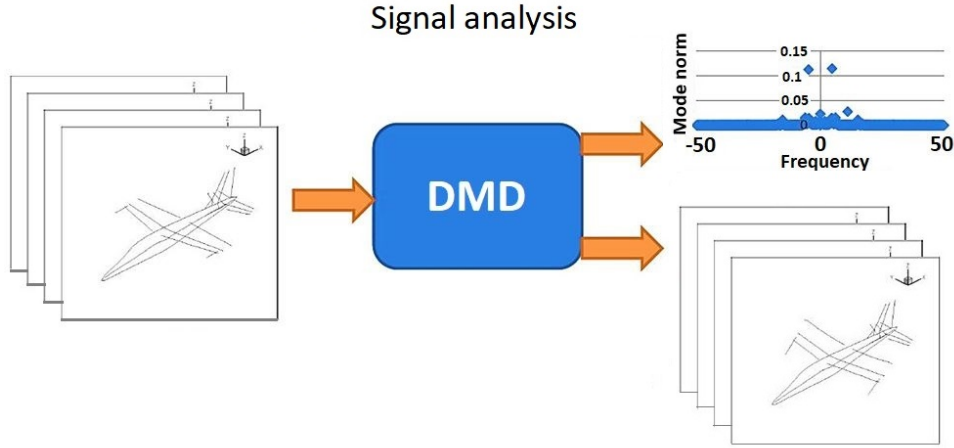


Figure 4.18: Diagram of the DMD analysis - set of snapshots from the numerical simulation as input, shapes with frequencies and growth rates as output

This section provides a brief explanation of DMD as described below. The details can be found in [75] and [76]. Consider a sequential set of data arranged in a $n \times m + 1$ matrix

$$Z = [u_0, \dots, u_m] \quad (4.11)$$

where u are the displacements and n is the number of state variables and $m + 1$ is the number of observations (snapshots). The data x_i are from simulations collected at the time t_i from a given dynamical system and assume that the data are acquiesced in time, with a time step Δt . We assume that the data Z are generated by linear dynamics, i.e., assume that there exists a linear operator A such that

$$\mathbf{u}_{(k+1)} = A\mathbf{u}_k, \quad (4.12)$$

for

$$k = 0, \dots, m - 1 \quad (4.13)$$

The goal of the DMD method is to find an eigendecomposition of the (unknown) operator A . To proceed, we use an arrangement of the data set into two large data matrices.

$$X = \begin{bmatrix} u^{(1)}(x_1) & u^{(2)}(x_1) & \dots & u^{(m-1)}(x_1) \\ u^{(1)}(x_2) & u^{(2)}(x_2) & \dots & u^{(m-1)}(x_2) \\ u^{(1)}(x_3) & u^{(2)}(x_3) & \dots & u^{(m-1)}(x_3) \\ \vdots & \vdots & \ddots & \vdots \\ u^{(1)}(x_n) & u^{(2)}(x_n) & \dots & u^{(m-1)}(x_n) \end{bmatrix}, \quad (4.14)$$

$$X^\dagger = \begin{bmatrix} u^{(2)}(x_1) & u^{(3)}(x_1) & \dots & u^{(m)}(x_1) \\ u^{(2)}(x_2) & u^{(3)}(x_2) & \dots & u^{(m)}(x_2) \\ u^{(2)}(x_3) & u^{(3)}(x_3) & \dots & u^{(m)}(x_3) \\ \vdots & \vdots & \ddots & \vdots \\ u^{(2)}(x_n) & u^{(3)}(x_n) & \dots & u^{(m)}(x_n) \end{bmatrix}, \quad (4.15)$$

Equation 4.12 can be reformulated in matrix notation,

$$X^\dagger = AX, \quad (4.16)$$

Then the DMD of the data matrix Z is given by the eigendecomposition of A . We can approximate operator A by using singular value decomposition (SVD) of data matrix. Now, by applying SVD to X ($X = U\Sigma V^*$) and the pseudo-inverse matrix, it can be transformed as:

$$A = X^\dagger X^\dagger = X^\dagger V \Sigma^{-1} U^* \quad (4.17)$$

It is noted that \dagger and $*$ mean the pseudo-inverse matrix and adjoint matrix, respectively. The SVD outputs, U , Σ , and V , are the contains the temporal structures (referred to as chronos), a diagonal matrix consisting of singular values, and the spatial structures (referred to as topos), respectively. It should be noted that calculating the eigendecomposition of the $n \times m$ matrix A can be prohibitively expensive if n is large, i.e., if $n \gg m$. As a result, the goal is to compute eigenvectors and eigenvalues without explicitly representing or manipulating A . A low-rank approximation matrix \tilde{A} is constructed for this purpose, and its eigendecomposition is calculated to obtained the DMD modes and eigenvalues. The DMD *modes* and DMD *eigenvalues* are intended to approximate the eigenvectors and eigenvalues of A . A reduced SVD of $X = U_r \Sigma_r V_r^*$ can be used to obtained the low-rank approximation matrix \tilde{A} , where U_r is $n \times r$, Σ_r is $r \times r$ diagonal, V_r is $m \times r$, and r is the rank of X , ($r \leq m$). Then, using 4.17, we obtained the low-dimensional representation

$$\tilde{A} \equiv U_r^* A U_r = U_r^* X^\dagger V \Sigma_r^{-1}. \quad (4.18)$$

The reduced matrix \tilde{A} is the projection of the matrix A on the space linearly generated by the columns of U_r . Then, eigenvalue modes of \tilde{A} can be derived by computing the following eigendecomposition:

$$\tilde{A}W = W\Lambda, \quad (4.19)$$

where W and Λ are the eigenvectors and eigenvalues of \tilde{A} , respectively. Finally, the DMD mode vectors Λ can be obtained by reconstructing the eigendecomposition of A from W and Λ because the eigenvalues for A are equivalent to Λ ,

$$A\Phi = \Phi\Lambda \quad (4.20)$$

$$\Phi = X^\dagger V \Sigma_r^{-1} W. \quad (4.21)$$

The following algorithm (Table 4.2) provides a robust method for computing DMD modes and eigenvalues. The DMD modes given by the columns of Φ describe the spatial structure that contributes the most to the overall evolution captured in the measurement sequence [71], and the DMD eigenvalues in Λ describe the dynamics and frequencies of the corresponding DMD modes.

Table 4.2: Algorithm - DMD

Algorithm - DMD**Input:** Data matrices X' and X , and rank r .**Output:** DMD modes Φ and eigenvalues Λ

- 1: **Procedure** DMD(X' , X , r .)
- 2: $[U, \Sigma, V] = SVD(X, r)$ (Reduced r -rank SVD of X)
- 3: $\tilde{A} = U^* X' V \Sigma^{-1}$ (Low-rank approximation of A)
- 4: $[W, \Lambda] = EIG(\tilde{A})$ (Eigen-decomposition of \tilde{A})
- 5: $\Phi = X' V \Sigma^{-1} W$ (DMD modes of A)
- 6: **End Procedure**

Finally, knowing the DMD modes Φ and eigenvalues $\Lambda = \text{diag}\{\lambda_i\}$ it is possible to reconstruct the time series of data set Z in Eq. 4.11 by expression

$$\Psi = \Lambda^{t/\Delta t} \Phi^\dagger a \quad (4.22)$$

$$\Psi = \{\Psi_1 \Psi_2 \dots \Psi_{n-1}\} \quad (4.23)$$

where Δt is the sampling rate and a represents the amplitudes determined by an optimal problem explained in Ref. [76]. In addition, by multiplying Φ and Ψ , one is able to reconstruct an approximation to the original data matrix,

$$X \simeq \Phi \Psi, \quad (4.24)$$

The growth rate α and the frequency f of the j -th mode, respectively, can be calculated by the following equations:

$$\alpha_j = \frac{\text{Re}\{\ln(\lambda_j)\}}{\Delta t} \quad (4.25)$$

and the frequency is described by:

$$f_j = \frac{\text{Im}\{\ln(\lambda_j)\}}{2\pi\Delta t} \quad (4.26)$$

where λ_j is the eigenvalue of j th mode in Λ . Moreover, by using α_j and f_j , a continuous time eigenvalue [73] can be expressed as $e^{(\alpha_j + i2\pi f_j)t}$, where i is the imaginary unit [76]. Since α_j is the ratio of the exponential function, the sign of the α_j ratio explains the stability of the system; a positive sign, negative sign, and zero mean amplification, damping, and oscillation, respectively.

The results of the DMD analysis are presented as the distribution of the decay rates for individual modes of their frequencies (Fig. 4.19, Fig. 4.20 and Fig. 4.21). Each point represents a single mode. From the point of view of flutter analysis, the modes that have the lowest frequencies and relate to the wings and stabilizers are of particular interest. These are modes with the lower frequencies. At the same time we get the low α growth rate. The weakly damped eigenmodes at lower frequency are less stable and, therefore, more probable to be observed in a real flutter experiment. Only for these modes, the amplitude of the excited vibration is increasing at the critical flutter velocity. **The analysis of the graphs is not sufficient to evaluate the aerodynamic damping for individual modes (wings and stabilizers).** It is necessary to identify the mode by checking its form (e.g. twisting the wings). Checking how its the α coefficient changes for successive

simulations (in this case, for increasing velocities) may give an answer about the critical flutter velocity.

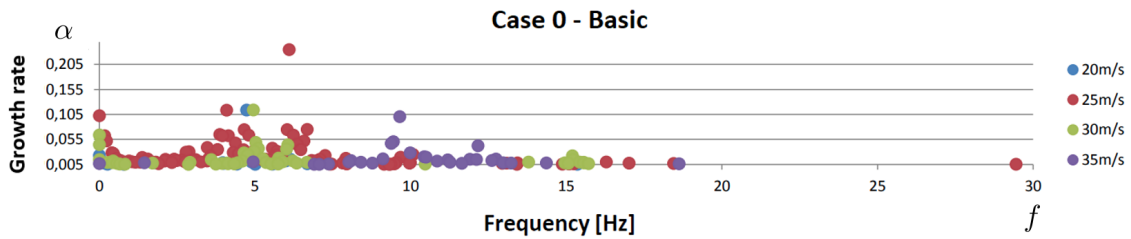


Figure 4.19: Distribution of the α decay rates for individual modes or their frequencies for the configuration of case 0 – basic

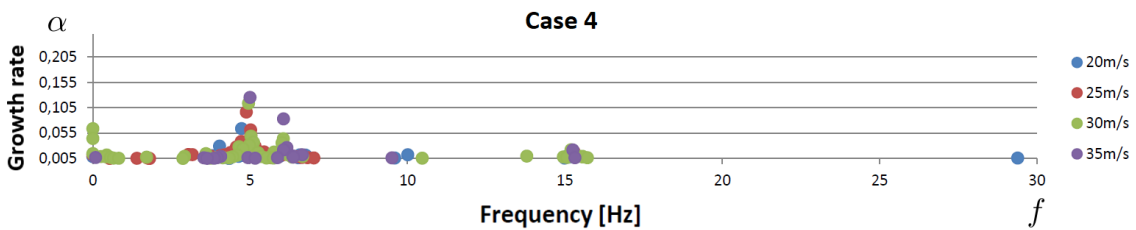


Figure 4.20: Distribution of the α decay rates for individual modes or their frequencies for the configuration of the case 4

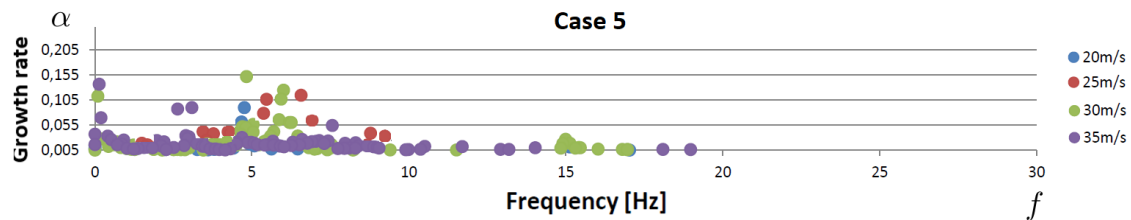


Figure 4.21: Distribution of the α decay rates for individual modes or their frequencies for configuration of the case 5

Fig. 4.22, 4.23 and 4.24 show the results of α rates for three selected sensors (Fig. 4.17). Sensor No. 5 is located at the end of the wing’s leading edge, sensor No. 14 is located on the trailing edge of the vertical stabilizer (at its maximum height), while sensor No. 20 is located at the trailing edge of the horizontal stabilizer. The selection of the above sensors is justified by to obtained the largest displacement in these positions - enabling the identification of modes of natural vibrations. On the figures is shown that higher decay rate values are for the low frequency range. These values corresponding to the modes for the wing and stabilizers of the aircraft, which is the subject of the study to related of the flutter phenomena.

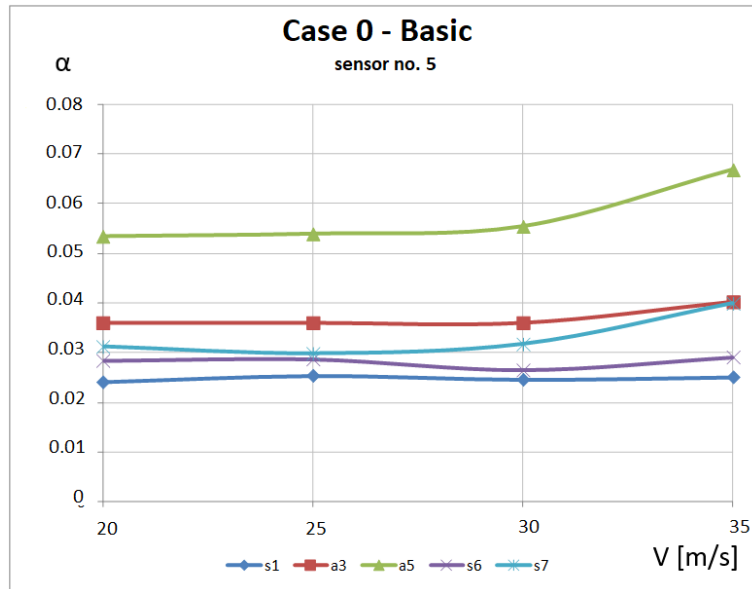


Figure 4.22: The α decay rates for sensor No. 5 in the basic configuration. Designation: s_1, s_6, s_7 - first, sixth and seventh symmetrical mode, according to table 3.7, a_3, a_5 - third and fifth anti-symmetrical mode, according to table 3.8

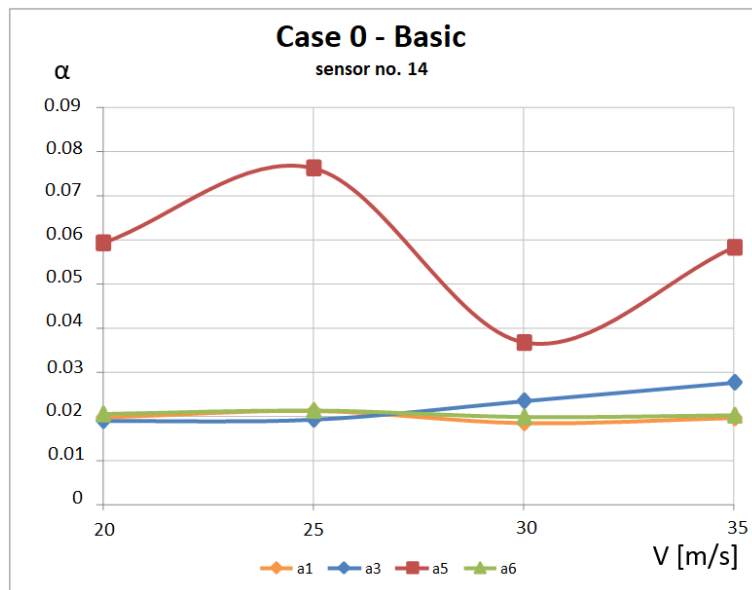


Figure 4.23: The α decay rates for sensor No. 14 in the basic configuration. Designation: a_1, a_3, a_5, a_6 - first, third, fifth and sixth anti-symmetrical mode, according to table 3.8

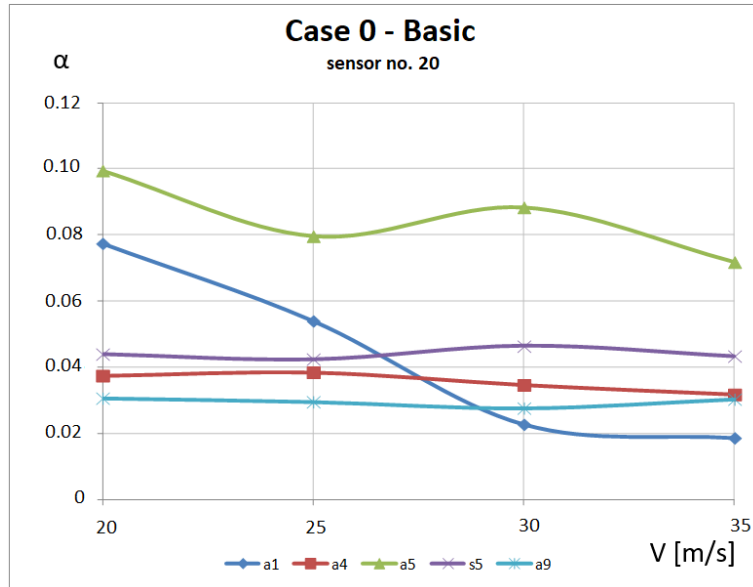


Figure 4.24: The α decay rates for sensor No. 20 in the basic configuration. s_5 - fifth symmetrical mode, according to table 3.7, a_1 , a_4 , a_5 , a_9 , - first, fourth, fifth and ninth anti-symmetrical mode, according to table 3.8

Fig. 4.22 shows the α decay rate of sensor No. 5 (basic configuration) fixed at the wing. The damping of the structure for symmetrical modes increases with increasing velocity. The exception is symmetrical mode s_6 shown on Fig. 4.22, which decreases in the range of $V_X = 25 - 30[m/s]$. None of the values also falls below 0.02. Analyzing the data from sensor No.14 (Fig. 4.23), which was located on the vertical stabilizer for anti-symmetrical modes a_1 , s_3 and a_6 , the values of α decay rates remain constant, equal to 0.02. The anti-symmetrical decay rates (α) of mode No. 5 exhibit relatively large discrepancies, however, they are much greater than the 0.015 limit. The diagram for sensor No. 20 (Fig. 4.24) located on a horizontal stabilizer shows five eigenmodes. Three of them behave stable and their values do not change in quality. In the case of anti-symmetrical mode No. 5 this holds true for each velocity in the specified range the α rates are relatively high and the modes are quickly suppressed. The first anti-symmetrical mode exhibits the most dangerous characteristics (Fig. 4.24). The value of decay rate (α) decreases with an increasing velocity to the level of 0.02 at $V_X = 30[m/s]$ (Fig. 4.25), which is permissible for the structure of the aircraft. A further increase in velocity does not cause a decrease in the α rate.

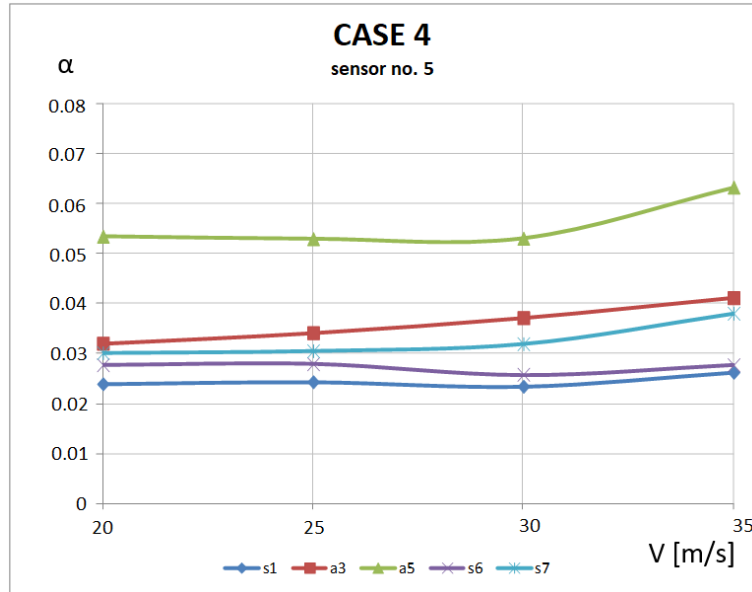


Figure 4.25: The α decay rates for sensor No. 5 in the fourth model configuration. Designation: s_1 , s_6 , s_7 - first, sixth and seventh symmetrical mode, according to table 3.7, a_3 , a_5 - third and fifth anti-symmetrical mode, according to table 3.8

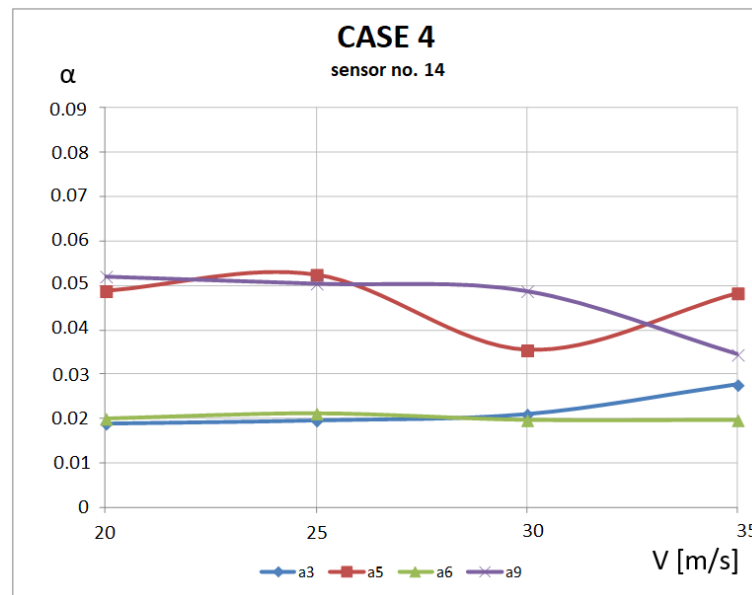


Figure 4.26: The α decay rates for sensor No. 14 in the fourth model configuration. Designation: a_3 , a_5 , a_6 , a_9 - third, fifth, sixth and ninth anti-symmetrical mode, according to table 3.8

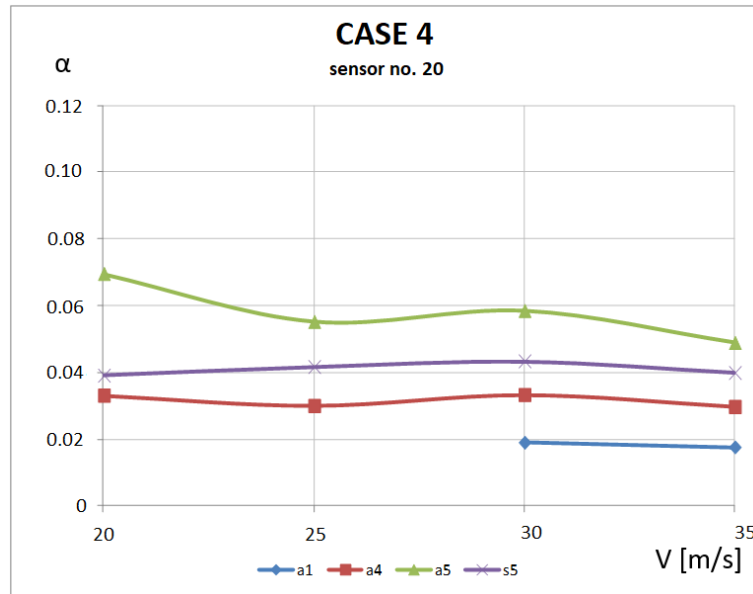


Figure 4.27: The α decay rates for sensor No. 20 in the fourth model configuration. Designation: $a1$, $a4$, $a5$ - first, fourth and fifth anti-symmetrical mode, according to the table 3.8, $s5$ - fifth symmetrical mode, according to table 3.7

Fig. 4.25, shows the α decay rates chart from the amplitudes on the wing for fourth configuration, does not show significant changes compared to the basic configuration. Decay rate (α) for all eigenmodes increase as velocity increases or amplitudes remain constant. In subsequent α charts for sensor No. 14 (Fig. 4.26), compared to the setup configuration, no anti-symmetrical mode No. 1 was identified, while anti-symmetrical mode No. 9 was revealed. Its minimum decay rate drops to 0.035 for a velocity of $V_X = 35[m/s]$. Anti-symmetrical mode No. 5 maintains the similar mode characteristics, however, its values for individual velocities are lower compared to the basic configuration (flutter phenomenon was not observed). However, they do not fall below the critical value 0.015 [67]. The α charts of the other modes are maintained at the level as in the setup configuration. On the basis of amplitudes from sensor No. 20 (horizontal stabilizer - Figure 4.30), for velocity $V_X = 20[m/s]$ and $V_X = 25[m/s]$ no anti-symmetrical mode No. 1 was identified. This mode is only revealed for velocities from $V_X = 30[m/s]$ and the α rate is about 0.019. All other α rates, despite the fact that in comparison with the setup configuration they decreased. Their values remained at a safe level.

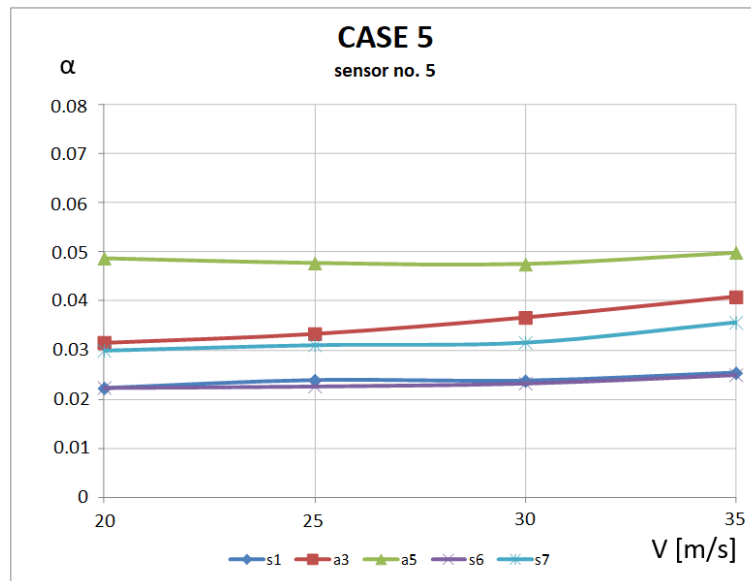


Figure 4.28: The α decay rate for sensor No. 5 in the fifth mass configuration. Designation: s_1 , s_6 , s_7 - first, sixth and seventh symmetrical mode, according to table 3.7, a_3 , a_5 - third and fifth anti-symmetrical mode, according to table 3.8

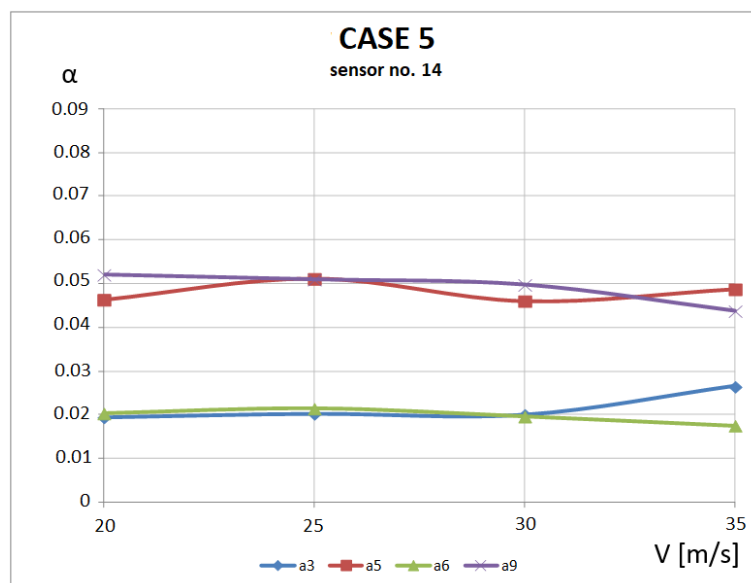


Figure 4.29: The α decay rate for sensor No. 14 in the fifth mass configuration. a_3 , a_5 , a_6 , a_9 - third, fifth, sixth and ninth anti-symmetrical mode, according to table 3.8

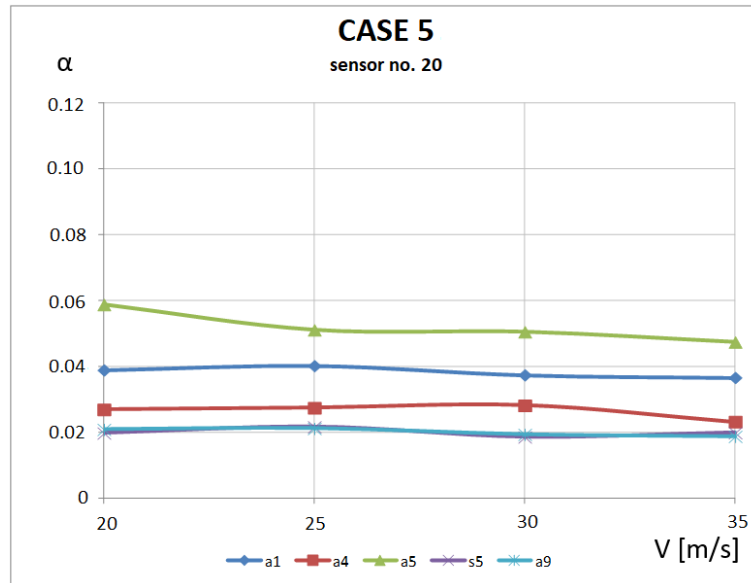


Figure 4.30: The α decay rates for sensor No. 20 in the fourth model configuration. Designation: s_5 - fifth symmetrical mode, according to table 3.7, a_1 , a_4 , a_5 , a_9 - first, fourth, fifth and ninth anti-symmetrical mode, according to table 3.8

The α decay rate obtained on the basis of three sensors in mass configuration No. 5 (Fig. 4.28), shows a gradual downward tendency compared to the setup and fourth configuration. The lowest values reach 0.02. Based on the above charts, it is possible to extrapolate curves and estimate for which velocity the rate will reach a critical value of 0.015. Figure 4.31 shows the courses of the mode No. 5 symmetrical α rates for all calculated mass configurations. The value of the α decay rate, with the increase in velocity for the analyzed variants, changes slightly and fluctuates around one value for the given configurations. For the fifth variant, this rate is half the size than for the basic variant and mass configuration No. 4 - it is 0.02. However, it is still greater than the value considered critical for the safety of the structure. [67].

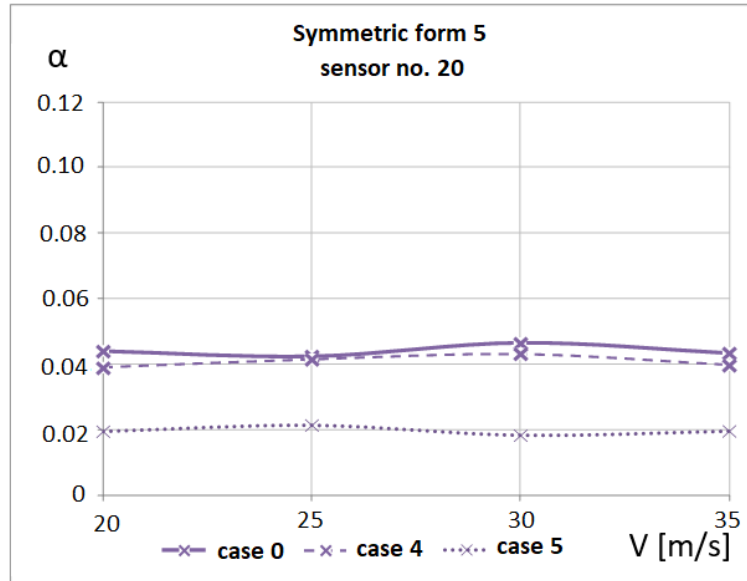


Figure 4.31: List of symmetrical the α decay rates of mode No. 5 for various mass configurations. Data obtained from sensor No. 20 - horizontal stabilizer [43]

Also in the case of experimental tests carried out in the wind tunnel at the Institute of Aviation in Warsaw, no flutter phenomenon was observed for the defined configurations. The process of experimental research in the wind tunnel and the results of observing the behavior of the I22-Iryda aircraft were presented in the papers [68], [69].

The developed methodology for testing the aeroelastic properties of the aircraft structure allows the system response to be analyzed only in the range of linear properties. This is a simplification as it does not include the exact description of the material which impacts the structural model. Comparing the curves obtained from the calculations for the selected modes of natural vibrations, the increasing load on the trailing edge of the wing or horizontal stabilizer causes a decrease in the decay rate. The changes introduced in the presented mass configurations caused noticeable differences in the obtained results. This allows checking how modifications to the model structure in areas susceptible to high vibration amplitudes cause changes in the obtained decay rates. This allows you to define the system's sensitivity to modifications of the examined structure. The preparation and the performance of numerical simulations require significantly less financial investment than experimental research in a wind tunnel. The difference increases even more when measuring for multiple mass configurations and a specific velocity range. The analysis presented in this chapter deals with the structure of the Irida I22 aircraft. As part of the work, a complex tool on FSI analyses was developed. This analysis assumes linear material behavior for the aircraft model. This is a limitation that allows the FSI analysis for structures made from the classical materials. In order to extend the possibility of using other materials with non-linear properties, it is necessary to develop algorithms that have been proven for linear configurations. A deeper analysis of the interaction between fluid and structure in relation to the nonlinear material properties was conducted in terms of non-linear elastic behavior of the structure and is presented in the subsection 5.5.6.

Chapter 5

Non-linear aeroelasticity

5.1 Introduction

The chapter 4 presented the results of calculations carried out for the aircraft flutter model. As part of this work developed algorithms and a method of the FSI analysis. The main goal of the research was to create numerical tools for FSI analysis to investigate flutter phenomena. The phenomenon may cause damages of the structure of the aircraft and is one of the main objectives in the safety of the structure. The presented results are acceptable for the linear behavior of the structure. The approach presented in this chapter prevents a deeper material analysis of the structural model. The expansion of computer technologies allows an increasing use of numerical simulations in the early stages of aircraft design more and more often. The role of wind tunnel experiments and initial test flights used to verify the validity of design solutions seems to be diminishing. Large systems for three-dimensional simulations of Fluid Structure Interactions (FSI) constitute highly-specialized and costly software. Most of the codes are based on a variety of simplifications. One of them is the assumption of linearity of the structural model being in contradiction with real-life situations. The approach presented in this chapter allows a non-linear material analysis of the structural model. In general, the typical formulation used for non-linear analysis depends on the nonlinear effects involved, with three different sources being identified:

- **Geometric non-linearities** describe the following issues:
 - large displacements, large rotation but small strain – displacements and rotation of fibers are large, but fiber extension and angle changes between fibers are small; the stress-strain relation may be linear or non-linear.
 - large displacements, large rotation, and large strains – fiber extension and angle changes between fibers are large, fiber displacements and rotation may also be large; the stress-strain relation may be linear or non-linear.
- **Material non-linearities** describe a non-linear relation between stresses and strains.
- **Non-linear boundary conditions**, where either the forces vary due to the structure's displacement, which is called follower force problem, or the boundary conditions change due to motion and contact to another structural component.

For the investigation two cases of structural non-linearity were considered in the thesis. Geometric non-linearity defined as: large displacements, large rotation but small strain. Material non-linearities defined by a non-linear elastic hyperelastic model. What is crucial for carrying out the assumed analyses is to extend a numerical tool [52] comprising a flow and a structural program

and a space grid deformation model for a system to consider the non-linearity of the structure. This chapter presents the results of simulations for non-linear structural models. This stage of the work is an extension of the FSI research towards the behavior of the structure in response to aerodynamic loading. The goal of the work is therefore to analyze the structure up load levels, which are the source of a non-linear response.

5.2 Computational aeroelasticity

The Computational Aeroelasticity combines methods used in Computational Fluid Dynamics and Computational Structural Mechanics [55]. The non-linearity of the structure is often neglect in aircraft design in FSI simulation e.g. [53, 55–57]. This limits the possibility of simulating such cases as flight maneuvers, in which considerable deformation of structure occurs, and cases with a non-linearity in constitutive equations. The non-linearity is also of particular importance for biological flows as for example the blood flow in the blood vessels [57]. Computational methods for different aspects of aeroelastic responses are an ongoing subject of scientific examination. To illustrate the point, many aspects [53] in FSI are related to searching interdependence between aerodynamics and structural dynamic in a flow and the dynamics of structure. This approach is connected with many complications resulting from two independent numerical codes interacting which each other.

Another problem to be solved is the way of exchanging information between programs for fluids and structure, with a different level of the discretization and a use of different methods (finite elements, finite volumes). One significant problem in the analyses of FSI is a description of particular states in relation to two different coordinate systems. Quite often is [53] used of Lagrange's description - a movable coordinate system (Computational Structure Mechanics - CSM) or Euler's description - a stationary coordinate system (Computational Fluid Dynamics - CFD). Thus, it is necessary to devise appropriate techniques of data exchange between these two systems. This procedure was explained in chapter 2.4. In the dynamic analysis it is necessary to define the correct time step. The tools used for the simulation require the same time steps for the CSM and CFD code to be set in order to obtain proper couplings in the movement of the structure and fluid meshes.

5.3 The non-linear structural problem

The numerical algorithm for aeroelastic calculations consists of fluid and structural domain. This section presents the algorithm of aeroelastic calculations using non-linear structural models. To outline the question of a non-linear structural problem, let us consider the governing equations for the structural motion:

$$M\ddot{\mathbf{q}}(t) + C\dot{\mathbf{q}}(t) + K\mathbf{q}(t) = \mathbf{F}(t) \quad (5.1)$$

where M, C, K - mass, damping and stiffness matrices, respectively. $\ddot{\mathbf{q}}(t), \dot{\mathbf{q}}(t), \mathbf{q}(t)$ describe, respectively, the vectors of acceleration, velocity and generalized displacements and $\mathbf{F}(t)$ defines the external load. In case of linear problems relationships between load and displacement are proportional. In case of structural non-linearity (covering the scope of work), the last matrix of the left side of the equation 5.1 K is defined by function representing the stiffness matrix of the structure. The equation 5.2 for non-linear structural problems used in the case of work is as follows:

$$M\ddot{\mathbf{q}}(t) + C\dot{\mathbf{q}}(t) + K(\mathbf{q})\mathbf{q}(t) = \mathbf{F}(t), \quad (5.2)$$

Where the stiffness matrix K is a function considering the non-linear properties of the structural model. C represents the damping matrix which can be deformation-dependent, too. Non-linear damping phenomena in relation with FSI algorithm can be applied in the flow control methods. This is not the scope of this thesis. Structural damping is not included in the FSI analysis presented in this chapter. Its effect on flutter phenomena is small and does not depend on the flow velocity. The main objective was to investigate the response of the structural model for defined flow velocities.

5.3.1 Non-linear elastic material models used in simulations

In structural calculations with a constitutive material non-linearity, a hyperelastic material for elastomers is a typical example. A hyperelastic material is a type of constitutive model for ideally elastic material for which the stress strain relationship is derived from a strain energy density function. The hyperelastic material is a special case of a Cauchy elastic material. For many materials, linear elastic models do not accurately describe the observed material behaviour. The most common example of this kind of material is rubber, whose stress strain relationship can be defined as non linearly elastic, isotropic and incompressible. Hyperelasticity provides a means of modeling the stress strain behavior of such materials. The behavior of elastomers often conforms closely to the hyperelastic ideal. Filled elastomers and biological tissues are also often modeled via the hyperelastic idealization. To define a hyperelastic material, constitutive models based on the so-called polynomial describing the strain energy density W , accumulated in the volume of the material. The amount of this energy describes the area under the stress-strain curve. The stress-strain relationship is derived from the equation:

$$\sigma_{ij} = \frac{\partial W}{\partial \epsilon_{ij}} \quad (5.3)$$

The polynomial describing the strain energy density for a hyperplastic material is based on strain invariants Eq. 5.4 or tensile coefficients Eq. 5.5.

$$W = (\bar{I}_1, \bar{I}_2, \bar{I}_3) \quad (5.4)$$

$$W = (\lambda_1, \lambda_2, \lambda_3) \quad (5.5)$$

Where:

$I_1 = \lambda_1^2 + \lambda_2^2 + \lambda_3^2$ – first strain invariant,

$I_2 = \lambda_1^2 \lambda_2^2 + \lambda_2^2 \lambda_3^2$ – second strain invariant,

$I_3 = \lambda_1^2 \lambda_2^2 \lambda_3^2$ – third strain invariant,

$\lambda_1, \lambda_2, \lambda_3$ – tensile coefficients for three directions axes of the Cartesian coordinate system.

The phenomenological model of the strain energy of hyperelastic incompressible materials usually takes the form of an N-order polynomial:

$$W = \sum_{i+j}^N C_{ij} (\bar{I}_1 - 3)^i (\bar{I}_2 - 3)^j \quad (5.6)$$

where C_{ij} is the material constant. The commonly used non-linear elastic material models in structural analyses are Arruda-Boyce, Mooney-Rivlin, Neo-Hooke, Odgen, Polynomial or Yeoh. This chapter outlines the approach towards non-linear elastic material models formulated by Mooney-Rivlin to analyze the FSI simulation. Mooney-Rivlin's material model is described by the function of strain energy density as follows [60]:

$$W = C_{10}(\bar{I}_1 - 3) + C_{01}(\bar{I}_2 - 3) \quad (5.7)$$

where:

W - the energy strain density; \bar{I}_1, \bar{I}_2 - the combination of invariants I_1, I_2, I_3 of the Cauchy Green strain tensor; C_{10}, C_{01} - material constants describing the behavior of the material [60].

The Mooney-Rivlin material model used in the work is based on two invariants. In practice, it means the possibility of describing more kind of non-linear elastic materials.

5.4 The Fluid Structure Interaction Algorithm

There are many methods to perform fluid-structure interaction computations. For a material with a linear relationship between stress and strain, equations describing all the coupled physical phenomena are coupled in one code. As each of the components of the coupled problem has different mathematical and numerical properties (linear/non-linear equations, symmetric/anti-symmetric matrices, etc.), this approach is computationally challenging. The alternative approach, used in this work, is based on the code coupling, where fluid flow computations and structural analyses are performed by separate packages. Depending on the particular problem, different numerical strategies might be employed. An overview of these strategies is found in pioneering studies by Farhat and others [59].

For aeroelastic calculations, a control script was programmed, which combines the individual numeric codes into one integrated program. The designed control scripts allow efficient calculations. The program starts with the static analysis, proceeds with the perturbed solution and, finally, continues with the dynamic analysis. Individual modules used in the presented calculations are discussed in the section 5.4.1.

5.4.1 The description of the FSI algorithm for structures with non-linear behavior

Figure 5.1 shows the FSI calculation algorithm for structures with non-linear behavior. The static computations are performed to introduce initial conditions for a dynamic FSI analysis.

In FSI calculations, an aircraft is loaded with forces determined from the aerodynamic pressure distribution calculated using the CFD code. The analysis is initiated with CFD computation (DLR TAU-Code). The complete process consists of three stages. The first stage generates the consistent CFD grid (Fig. 5.1) and checks the results for negative volumes and other grid pathologies. Then, the grid is partitioned. The division depends on the number of used computational nodes. This number is dependent on the size of the task and the amount of time for the MPI (Message Passing Interface) packet to pass on messages. The next stage constitutes a significant part of the flow analysis. After defining the boundary conditions and preparing the numerical tools, the calculations are performed. It follows the parameter specifications, such as units, the coupling surface, object files, to conduct the data exchange between the two codes. Then the CFD data, in the form of the pressure distribution on the coupling surfaces, are translated into forces and interpolated from the CFD grid to the structural grid. The exchange occurs through the coupling surface, specified on the basis of the structural model and the flow model. **The next step consists of structural calculations by means of the structural code. Depending on settings, it is possible to perform a traditional linear analysis or to take non-linearities of structural model into account. Additionally, the simulation scheme can be expanded with relevant dynamic analyses which is necessary in analyzing dynamic response of the tested object depending on the types of the input function. In the case of dynamic simulations, the algorithm has been extended with an additional iterative loop (figure 5.2).**

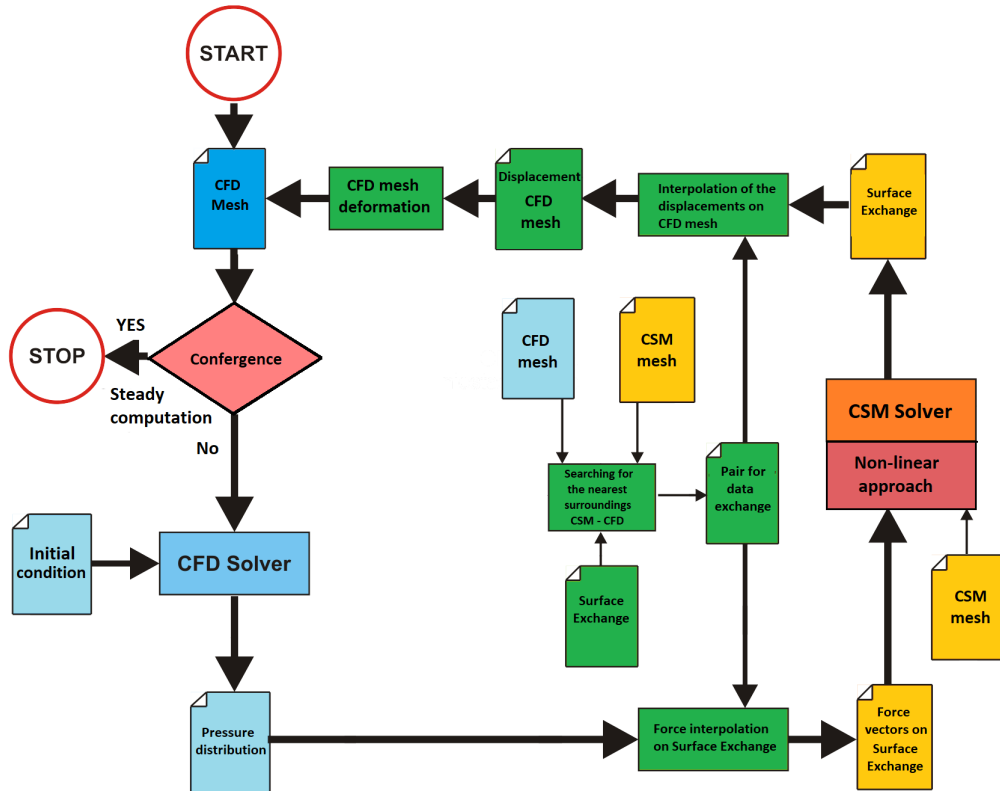


Figure 5.1: The scheme of FSI steady state analysis included a non-linear approach in CSM code

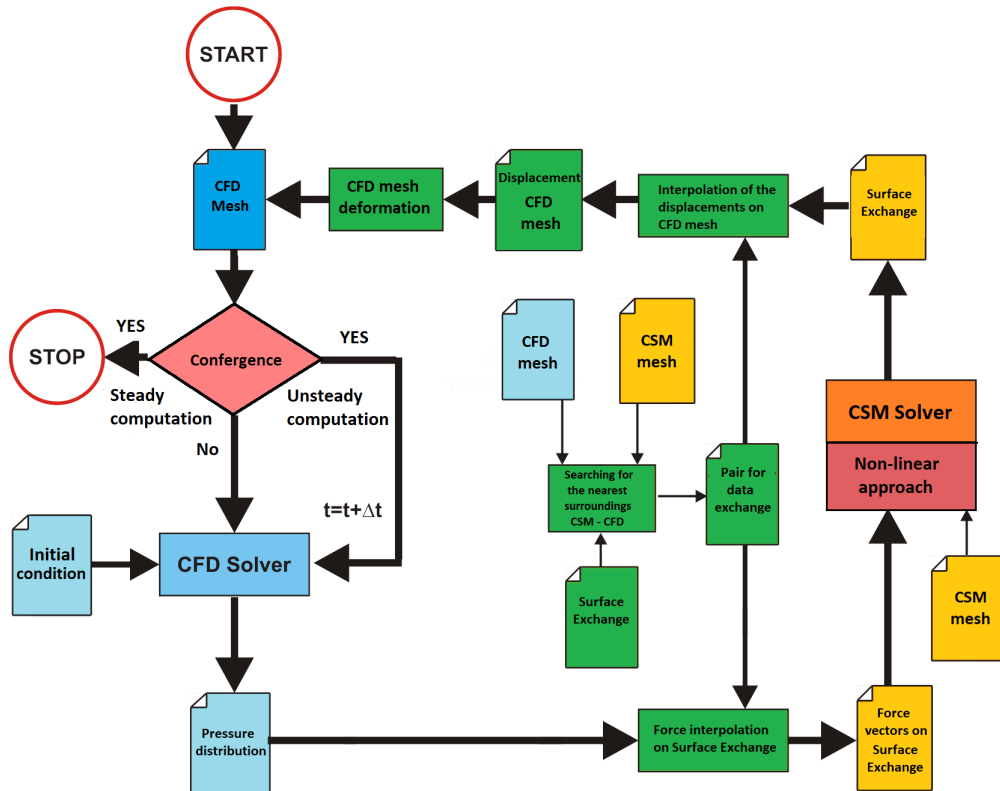


Figure 5.2: The scheme of FSI dynamic analysis included a non-linear approach in CSM code

In this case, after introducing the initial condition (the input function) the dynamic response of the system to the initial perturbation in a given period of time is investigated. Dynamic aeroelastics also takes the acceleration of the structural grid (the grid's dynamics) and its impact on the flow into account. Information on the dynamics of the grid is obtained on the basis of current displacement increment and on the basis of the previous flow solution. Typical time coupling procedures used for aeroelastic simulations are described in [59]. Here, the partitioned time stepping is used. This technique has the advantage of being easy to implement, since the independent fluid and structure solvers can be freely chosen. In a partitioned coupling, the fluid and structure computations are resolved consecutively. It is therefore necessary to predict the displacement of the structure between times t^n and t^{n+1} so that the fluid code can be run on an updated domain at each iteration. The prediction of fluid loadings must be chosen such that the structural solver provides an evaluation of the motion of the consistent interface with respect to the generated loads. The time step is separately set for each program and the transition to the next time step takes place after obtaining the convergence of individual codes: CSM and CFD. The time coupling is solved explicitly as boundary conditions imposed by one system onto the other. To prevent numerical instability the time step is decreased and sub-iterations are performed. By sub-iterating, the fully coupled solution is obtained. The size of the time step for all the used modules is managed by the CFD solver DLR TAU-code. The interface for this aeroelastic computations was developed in TAURUS project [81]. The description of a similar management of aeroelastic time coupling can be found in [93].

5.5 FSI analysis for a chosen non-linear problem

5.5.1 The validity of the algorithm for the experiment of the Naca0012 airfoil [70]

The first test case to validate the developed FSI algorithm for linear and non-linear approaches was the Naca0012 wing. The experiment was carried out at the Institute of Aviation (IoA) in Warsaw in a wind tunnel. The algorithm of experimental research has been based on a state-of-the-art research scheme known [63]. It is a standard experimental research scheme used to determine the critical flutter velocity for the studied profile. **The first task was numerical modeling of the real system in such a way as to obtained the most accurate eigenfrequencies and shapes regards to the experiments.** The structural model is based on two degrees of freedom - displacement and rotation of the wing profile. (Fig. 5.5). Determined modes are shown in the Figure 5.3.

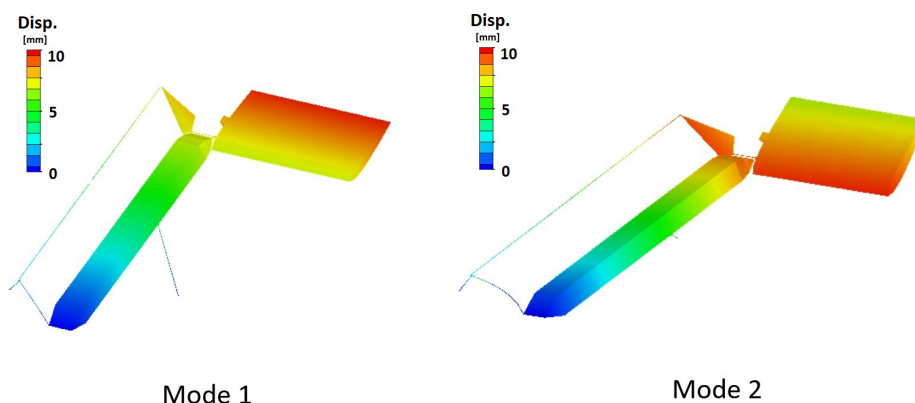


Figure 5.3: Modal shapes obtained from the modal analysis: 1 - mode of wing movement; 2 - the mode of rotation of the wing.

The frequency values obtained from the modal analysis and their comparison with the experimental data are presented in the Table 5.1.

Table 5.1: Experimental and numerical eigenfrequencies of the model provided by IoA

No.	Experiment [Hz]	Numerical [Hz]
1.	4,53	4,51
2.	5,57	5,56

Detailed data was published in [63]. The studies on flutter (structure response) proved that in models with linear characteristics an infinite rise in the amplitude can occur and the structure is damaged in a short period of time. Contrary, in systems where non-linear springs were used in the suspension system, the oscillations with a constant amplitude (LCO - Limit-Cycle Oscillations) were observed after reaching the critical velocity.

5.5.2 Experiment data

The experiment setup (Fig. 5.4) has been conducted in two stages at the Institute of Aviation (IoA):

- stage 1 - examining the behavior of the wing profile under the influence of flow where the springs characterized by the linear properties have been used,
- stage 2 - in the place of springs characterized by the linear properties, springs elements with the non-linear properties have been used.



Figure 5.4: View of the testing setup in the wind tunnel of the Naca0012 profile

In the experiment [63], a wind tunnel has been used with the height of $500[mm]$ and the width of $200[mm]$. In the wind tunnel, the examined profile (Fig. 5.4) has been placed, whereas the mechanical system of damping together with a measuring apparatus has been outside the area of flow. Below the sequence of the research and its results in the form of displacement (along the Y axis) and the rotation about the (about the Z axis) axis (the measurement point - Fig. 5.5) are shown.

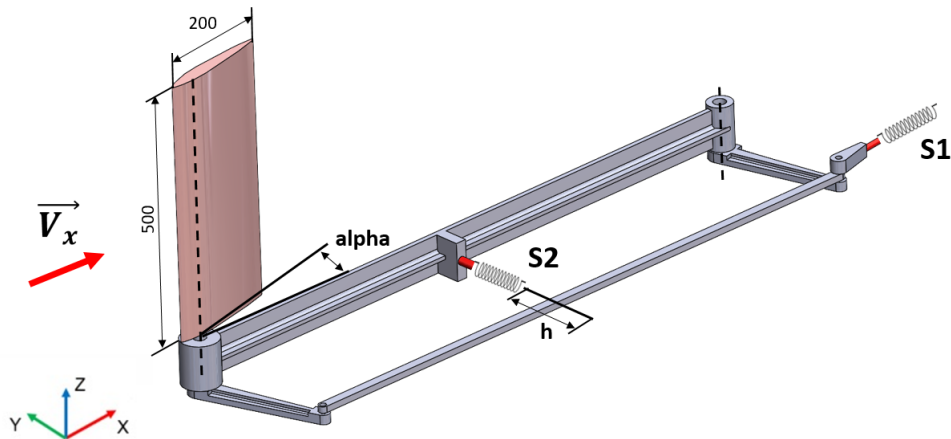


Figure 5.5: Naca0012 setup used in the experiment

The linear approach In the first stage of the wind tunnel test in the damping system of the Naca0012 profile under examination, springs characterized by linear approach (Fig. 5.6) have been used. The studies have been carried out for the following flow conditions:

- the angle of attack $\alpha = 0.1^\circ$ along X axis
- the velocities of inflow $V_X = 19.4; 20.8[m/s]$

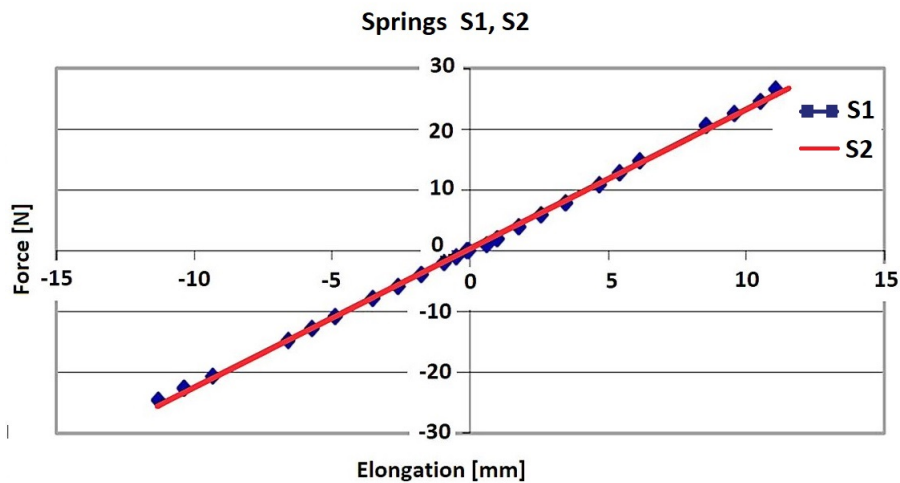


Figure 5.6: Springs S1 and S2 characteristic in a linear approach

As a result of measurements, the displacement (along the Y-axis) and the angle of rotation (about the Z-axis) have been obtained as a function of time (Fig. 5.7, 5.8 and 5.9) for specified velocities of inflow. To study the response of the system, it was necessary to create the initial condition so that the system was not in equilibrium. The time t_n on the presented figures (Fig. 5.7, 5.8 and 5.9) is defined as the time of this condition. The duration of the initial condition had no effect on the response and behavior of the system. For the initial velocity of flow $V_X = 19.4[m/s]$ (Fig. 5.7), the oscillations of the examined wing profile are decay.

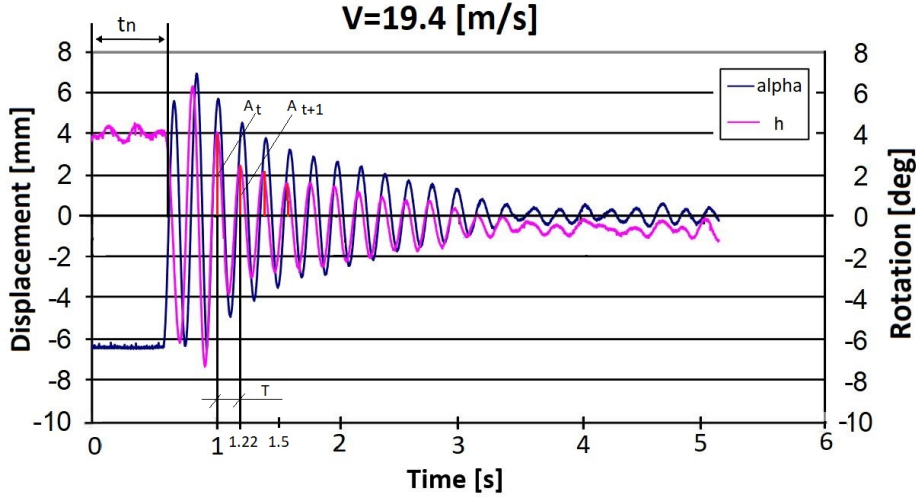


Figure 5.7: The displacement and the angle of rotation (Fig. 5.4) as a function of time for the linear case, at the inflow velocity of $V_X = 19.4[m/s]$,

Figure 5.7 shows the displacement and angle of rotation over time. Based on the obtained periodic functions, the frequency and damping ratio can be determined. The value of the damping ratio determines the behavior of the system. By defining D as the damping ratio and analyzing the values [103], we can determine the stability of the system if:

- Strongly damped ($D > 1$) – the system does not oscillate, but follows (exponential decay) to stability. The greater the value of D , the slower the system returns to equilibrium.
- Poor damping ($0 < D < 1$) – the system oscillates with an exponentially decreasing amplitude and a frequency lower than that of the undamped system. An increase in damping causes a faster decay of the amplitude and a decrease in the frequency of vibrations of the system.
- Undamped ($D = 0$) – the system oscillates with a constant amplitude at its natural frequency.
- Undamped, unstable system ($-1 < D < 0$) – the system oscillates with increasing amplitude. Flutter may occur in this case.

Given the periodic data of the displacement h and the angle α , the logarithmic decrement of the Λ damping was determined from:

$$\Lambda = \ln \left(\frac{A_t}{A_{t+1}} \right) = \ln \left(\frac{A_0 e^{-\beta t}}{A_0 e^{-\beta(t+T)}} \right) = \beta T \quad (5.8)$$

The D damping ratio is defined as:

$$D = \frac{\beta}{\omega_0} = \frac{\beta}{2\pi f_0} = \frac{\Lambda}{2\pi} \quad (5.9)$$

where β where beta is the damping coefficient defined as $\frac{b}{2m}$, b : damping constant.

Using the equation 5.9 and finding the logarithmic damping decrement Λ , we can determine the stability of the system.

The analysis of the displacement diagrams according to Fig. 5.7, the time period and frequency of the function for the $V_X = 19.4[m/s]$ can be approximated $T = 0.22[s]$.

$$f = \frac{1}{0.22} = 4.54[Hz] \quad (5.10)$$

The frequency $4.54[Hz]$ corresponds to the frequency no. 1 table 5.1 - moving of the Naca0012 wing. Obtaining the amplitude values in subsequent time steps for a periodic harmonic function, we can determine the value of the damping ratio D from the equation:

$$D = \frac{\ln\left(\frac{A_t}{A_{t+1}}\right)}{2\pi} = \frac{1}{A_t - A_{t+n}} \ln\left(\frac{A_t}{A_{t+n}}\right) = 0.1 \quad (5.11)$$

With respect to the above description, the value of D is in the range $0 < D < 1$. This means that the system is damped.

In the next stage of the wind tunnel test, the inflow velocity has been increased to $V_X = 20.8[m/s]$. The displacement as a function of time (Fig. 5.8) shows that the amplitude of displacement of the profile at the initial stage of the research is greater than for the lower flow velocity. The amplitude of oscillations is decaying in a longer period of time and more slowly.

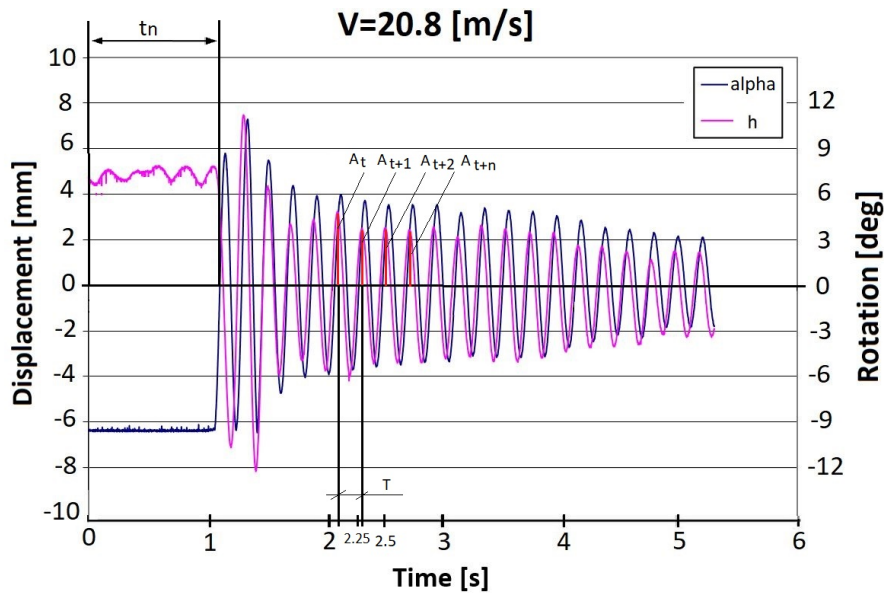


Figure 5.8: The displacement and the angle of rotation (Fig. 5.4) as a function of time for the linear case, at the inflow velocity of $V_X = 20.8[m/s]$.

The analysis of the displacement diagrams according to Fig. 5.8, the time period and frequency for case 2 can be determined $T = 0.22[s]$.

$$f = \frac{1}{0.22} = 4.54[Hz] \quad (5.12)$$

The frequency $4.54[Hz]$ corresponds to the frequency no. 1 table 5.1 - moving of the Naca0012 wing. Obtaining the amplitude values in subsequent time steps for a periodic function, we can determine the value of the damping ratio D from Eq. 5.11. The value for velocity $V_X = 20.8[m/s]$ is $D = 0.028$. With respect to the above description, the value of D is in the range $0 < D < 1$. This means that the system is damped. The damping ratio is lower for the speed $V_X = 20.8[m/s]$ which means that the system has slower damping. The final result of the experiment for a linear spring was to determine the critical flutter velocity $V_F = 21.3[m/s]$. The displacement and the angle of rotation as a function of time at the critical flutter velocity is shown in Figure 5.9.

The analysis of the displacement diagrams according to Fig. 5.9 based on the equation 5.12 the frequency obtained is $4.54[Hz]$. This value is the same as in the previous cases. The frequency $4.54[Hz]$ corresponds to the frequency no. 1 table 5.1 - moving of the Naca0012 wing.

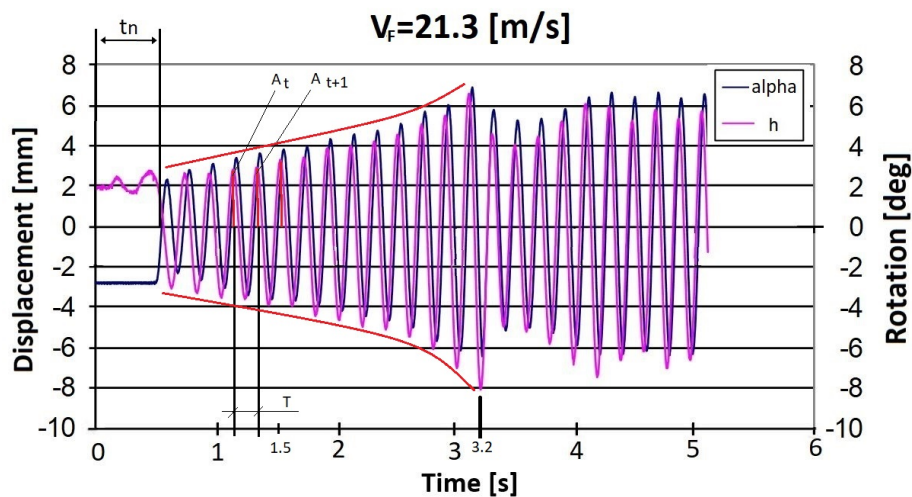


Figure 5.9: The function of the profile displacement and rotation (Fig. 5.4) with the flutter critical velocity of $V_F = 21.3[m/s]$,

The analysis the sequence, the displacement and the angle of rotation as a function of time for the velocity of $V_X = 21.3[m/s]$ one can assume that the critical velocity has been gradually attained. Obtaining the amplitude values in subsequent time steps for a periodic function, we can determine the value of the damping ratio D from the equation 5.11. The damping ratio for velocity $V_X = 21.3[m/s]$ is $D = -0.012$. With respect to the above description, the value of D is in the range $-1 < D < 0$. This means that the system is unstable with increasing oscillation amplitude. A rapid growing of the amplitude for the critical flutter velocity activated the secure system at $t = 3.2[s]$, so the signal analysis was carried out for $t < 3.2[s]$ (Fig. 5.9). For the velocity $V_X = 21.3[m/s]$, the damping effects are over resonance and the amplitude is enlarging significantly (Fig. 5.9). The experiment was abandoned to preserve the fixing system of the wing profile. The critical velocity of the flutter has been attained. It leads the complete failure of the wing.

The non-linear approach In the second stage of the experiment, in the damping system for the examined Naca0012 profile, springs characterized by non-linear stiffness have been used (Fig. 5.10). The studies have been carried out for the following conditions:

- the angle of attack $\alpha = 0.1^\circ$
- the velocities of inflow $V_X = 17.6; 25.5; 28.2[m/s]$

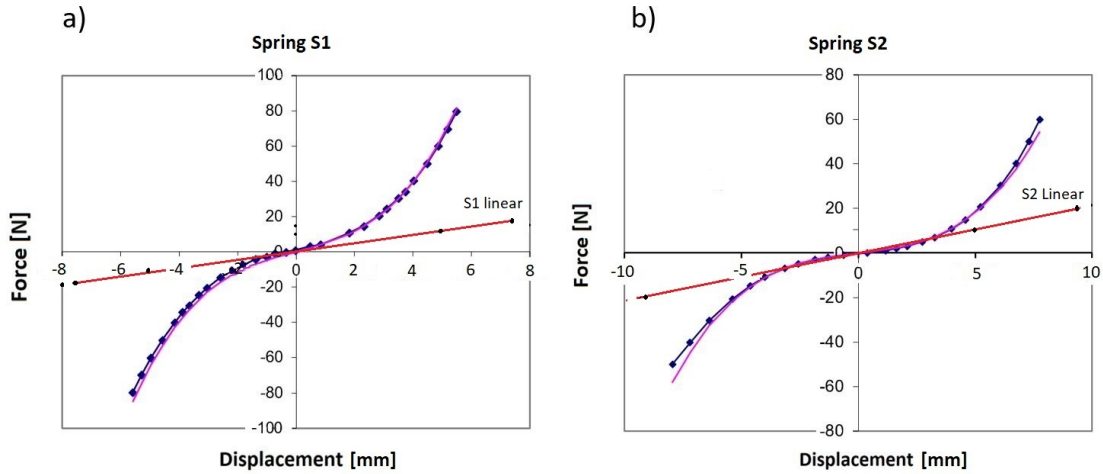


Figure 5.10: Spring characteristics used in experimental studies of the Naca0012 profile: a) associated with the rotation of the system, b) associated with the displacement (Fig. 5.4)

The objective of the experiment was to investigate the system response using elements with non-linear characteristics. In addition, the characteristics of linear springs have been added to the Fig. 5.10 to compare the ranges of forces in relation to elongation. The results of the experiments in the form of the displacement and the angle of rotation of the profile as a function of time, employing the assigned inflow velocities are shown in Fig. 5.11, 5.12 and 5.13.

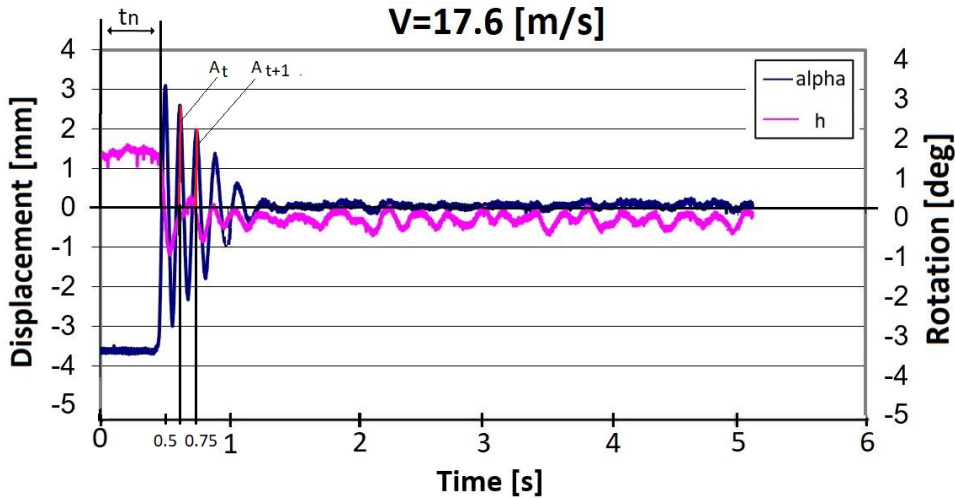


Figure 5.11: The displacement and the angle of rotation of the profile (Fig. 5.4) as a function of time for a non-linear case at the inflow velocity of $V_{\infty} = 17.6[m/s]$

The analysis of the displacement diagrams according to Fig. 5.11, the time period and frequency of the function for case 2 can be approximated $T = 0.19[s]$. The response frequency of the system for non-linear cases are close to those determined from the modal analysis.

$$f = \frac{1}{0.19} = 5.26[Hz] \tag{5.13}$$

The frequency $5.26[Hz]$ corresponds to the frequency no. 2 table 5.1 - rotation of the Naca0012 wing. Analyzing the periodicity of the displacement value h and the angle of rotation α , a greater

damping of the displacement can be seen. This is due to the difference in spring stiffness S_1 compared to S_2 . Obtaining the amplitude values in subsequent time steps for a periodic function, we can determine from the Eq.5.11 the value of the damping ratio $D = 0.05$.

Based on the above definition, the value of D is in the range $0 < D < 1$. This means that the system for the velocity $V_X = 17.6[m/s]$ is damped.

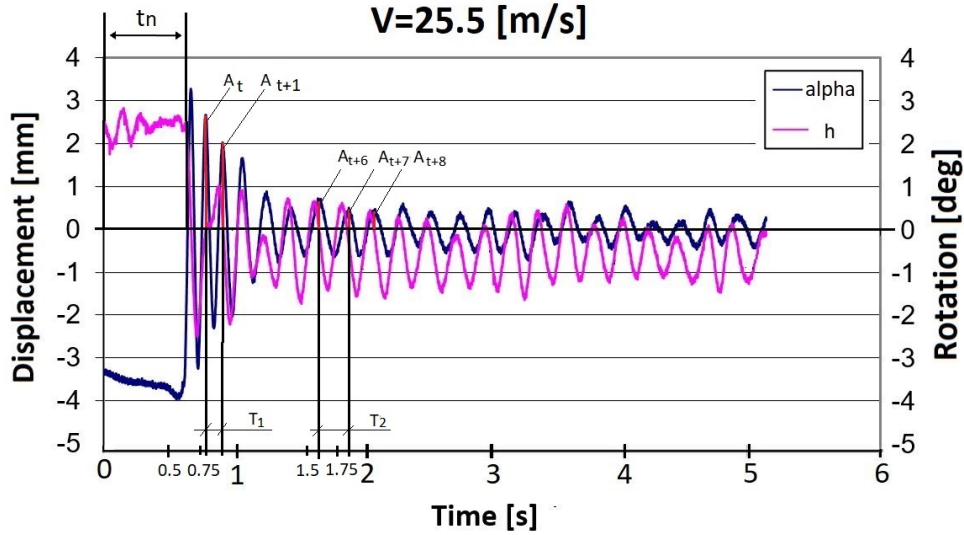


Figure 5.12: The displacement and the angle of rotation of the profile (Fig. 5.4) as a function of time for a non-linear case at the inflow velocity of $V_x = 25.5[m/s]$

In the next stage of the wind tunnel test, the inflow velocity has been increased to $V_X = 25.5[m/s]$.

The analysis of the displacement diagrams according to Fig. 5.12, the time periods of frequencies changes was determined at the beginning and next part of the experiment. This is due to the non-linear load curve of the springs. At the beginning of the experiment the period can be estimated to $T_1 = 0.13[s]$ and $T_2 = 0.22[s]$. The response frequencies of the system for non-linear cases can be approximated:

$$f_1 = \frac{1}{0.13} = 7.69[Hz]; f_2 = \frac{1}{0.22} = 4.54[Hz] \quad (5.14)$$

The Analysis the periodicity of the displacement value h and the angle of rotation α , you can observe the damping at the beginning of the experiment. The values of the damping ratios $D_1 = 0.035$ and $D_2 = 0.0047$ were determined from the Eq.5.11. The obtained values of the damping ratio D at the beginning and in the further part of the experiment fall within the range $0 < D < 1$. It can be seen that in the next part its value is close to ($D = 0$). This means that the system is not damped and the oscillations are of constant amplitude.

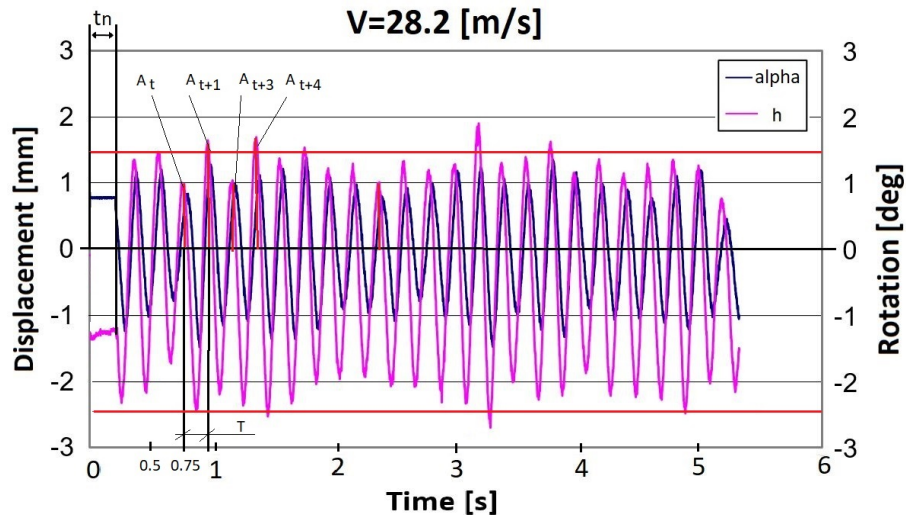


Figure 5.13: The displacement and the angle of rotation of the profile (Fig. 5.4) as a function of time for non-linear case at the inflow velocity of $V_X = 28.2[m/s]$

n the final stage of the experiment, the velocity has been increased to $V_X = 25.5[m/s]$. The analysis of the displacement diagrams according to Fig. 5.13, the time period of the function for velocity $V_X = 25.5[m/s]$ can be approximated with $T = 0.23[s]$. The response frequency based on the equation 5.14 is $f = 4.34[Hz]$. The obtained values of the damping ratio D for this case is ($D = 0$).

For the velocity $V_x = 28.2[m/s]$ (5.13) the profile oscillations behavior similar to that attained in the linear case - but with a constant amplitude. The flutter phenomenon has not been observed.

The wind tunnel test has been carried out in exactly the same way as in the case of linear elements. For the inflow velocity of $V_x = 17.6[m/s]$, the displacement has been recorded, and the angle of rotation of the examined profile as a function of time. The amplitude of oscillations has been decay in a short period of time. A similar result has been attained compare Figures 5.7, 5.8 and 5.9). Then, the critical flutter velocity for the linear setup was investigated. No increase in the amplitude has been observed. For the inflow velocity of $V_x = 25.5[m/s]$, i.e. above the critical value for the linear case there have been oscillations of a small and stable amplitude (Fig. 5.13). The amplitude of oscillations, as opposed to studies carried out in the first stage of the experiment, has remained stable. In this approach, the presence of oscillations at the limit cycle oscillations (LCO) phenomenon has been observed.

5.5.3 Numerical simulation of the Naca0012 profile

Aeroelastic simulations of non-linear structures are very complex perform with most of the standard FSI codes. The results of the experiments presented above were used for numerical validation of the FSI code for both the linear and the non-linear approach. To simulate the experiment for the system having two degrees of freedom with non-linear restoring force, it was necessary to adapt the structural code and to rebuild the algorithm of fluid and structure interacting with each other. A structural model has been created for the examined profile (Fig. 5.14) and a CFD grid has been generated (Fig. 5.15).

On the basis of the experimental setup, a structural numerical model was developed (Fig. 5.14), containing the wing structure and assembly system, which was then implemented in the FSI code.

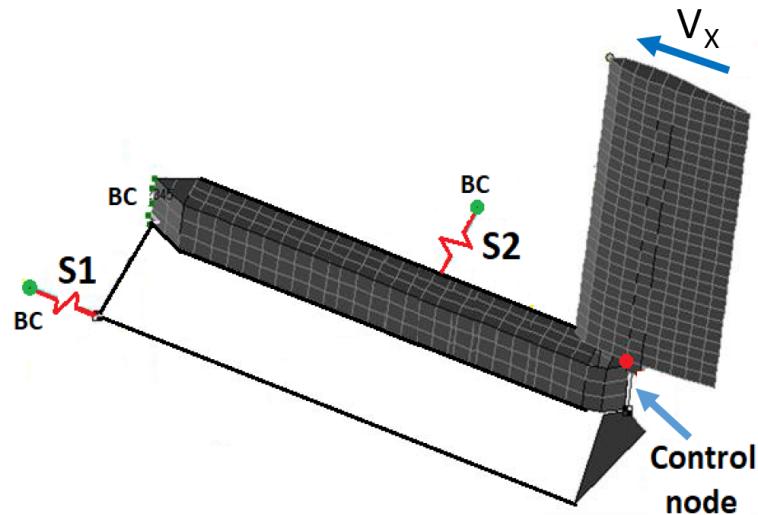


Figure 5.14: The FEA model of the Naca0012 profile with non-linear springs used (S1, S2). The model reflects the experiment at the IoA. BC – boundary condition [63]

The geometrical model and derived FE model mesh for the profile was generated by the give data and a flow mesh for flow calculations was created. The CFD mesh consisted of 20 mill. tetrahedral elements and 11,5 mill. nodes (Fig. 5.15). To achieve the most accurate results, the structural model has been checked by comparing the eigenfrequencies calculated by the numerical modal analysis with the ones determined experimentally (Table 5.1). For the numerical model shown on the Fig. 5.14, the stiffness of structural elements and springs was defined according with the data from the wind tunnel.

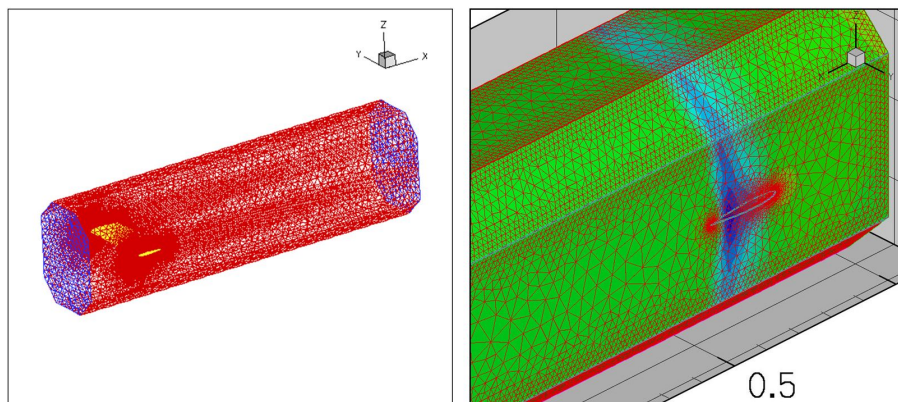


Figure 5.15: A CFD grid for the Naca0012 profile. Geometry of the domain reflects the experimental setup of the wind tunnel.

Figure 5.16 shows the velocity field $V_x = 28.2[m/s]$ in the inflow direction of the flow domain for the selected time steps. The time step was set to $t = 0.01[s]$.

The linear approach Calculations have been made for the same configuration as in the experimental studies. In the first stage, standard linear elements have been used. As a result, the displacement and the angle of rotation as a function of time for the specified boundary conditions have been obtained. Figures 5.17 and 5.18 show sequences of displacement and the angle of rotation (the control node) as a function of time, obtained as a result of calculations using the linear

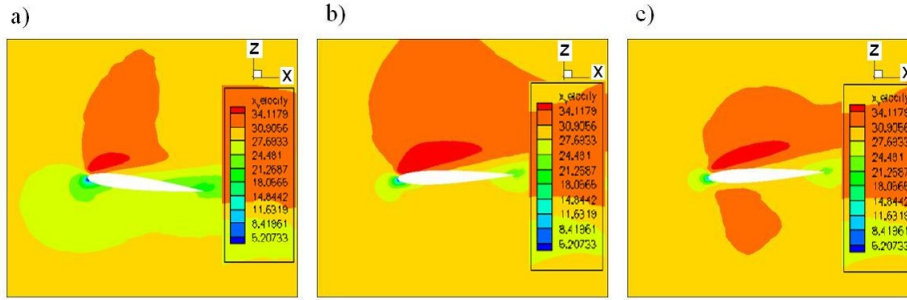


Figure 5.16: The velocity field $V_x = 28.2[m/s]$ for: a) 1 time step; b) 10 time steps; c) 20 time steps

elements.

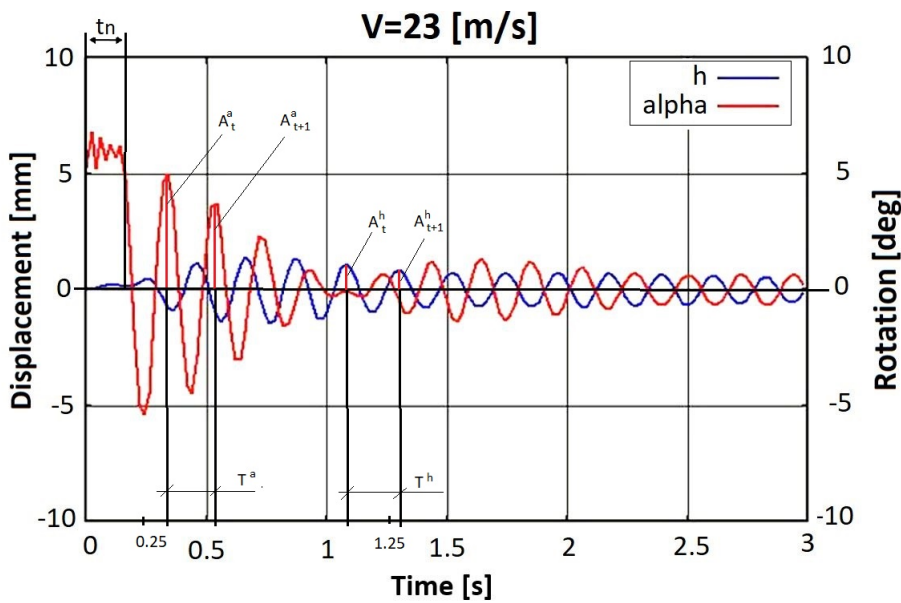


Figure 5.17: The displacement and the angle of rotation (the control node) as a function of time for the linear case at the inflow velocity of $V_x = 23[m/s]$

Figure 5.17 shows the sequence of displacement and the angle of rotation of the control node as a function of time for an approximate inflow velocity of $V_X = 23[m/s]$. Analyzing the time history of displacement h and wing rotation angle α using equation 5.14 and 5.11 the frequencies have values $f^a = 5.56[Hz]$, $f^h = 4.56[Hz]$ respectively. The time periods $T^a = 0.18[s]$, $T^h = 0.21[s]$ and the damping rates $D^a = 0.08$, $D^h = 0.035$ can be determined. The frequency values are consistent with the eigenfrequencies determined numerically. The values of D are in the range $0 < D < 1$. For inflow velocity $V_X = 23[m/s]$ the system is damped. The flutter phenomenon was not observed.

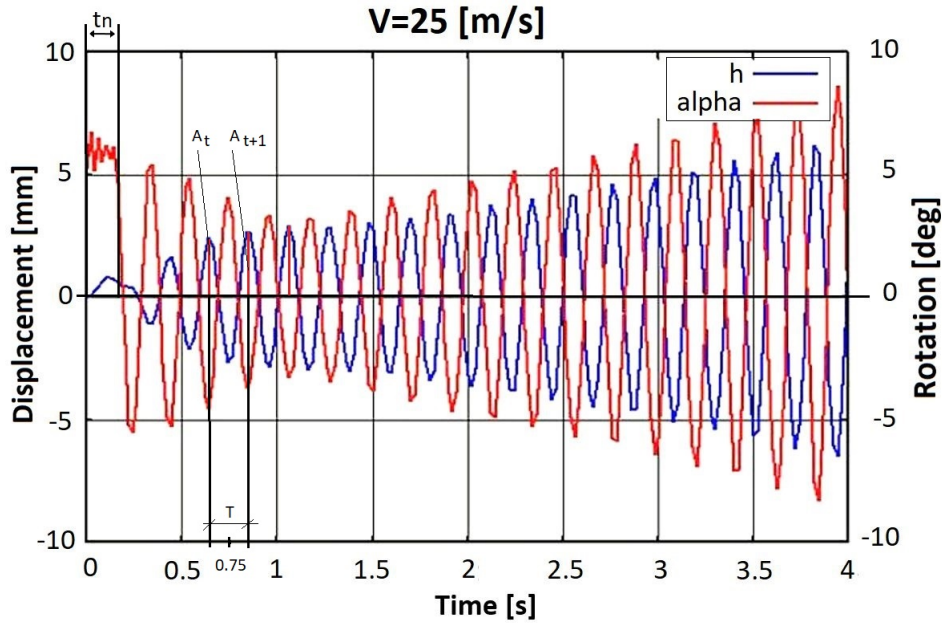


Figure 5.18: The displacement and the angle of rotation (the control node) of the profile as a function of time - the critical flutter velocity - $V_X = 25[m/s]$

After increasing the velocity to $V_X = 25[m/s]$ (Fig. 5.18), one can observe that the amplitude of the profile's oscillation is growing rapidly in time. The frequencies obtained are the same as for the inflow velocity $V_X = 23[m/s]$, while the damping ratio based on the Figure 5.18 was estimated at $D = -0.04$. The value of the damping coefficient D is < 0 and is in the range where the system is unstable with increasing oscillation amplitude. The critical flutter velocity has been reached at $25[m/s]$ for the numerical model, which is similar with the results of the experimental studies.

The non-linear approach In the second stage of the simulation, the standard linear elements have been replaced with non-linear elements to simulate the non-linear restoring force. As in the case of the previous simulation, the in-house MF3 code has been used to carry out a structural analysis. The properties of the non-linear springs used in the experimental damping system with the Naca0012 profile have been implemented in the FSI code.

Figure 5.19 shows the sequence of the displacement and the control node rotation angle as a function of time for the inflow velocity of $26[m/s]$.

The analysis the time history of displacement h and wing rotation angle α using equations 5.14 and 5.9 the frequencies $f^a = 5.26[Hz]$, $f^h = 4.54[Hz]$ and the damping ratios $D^a = 0.027$, $D^h = 0.06$ can be determined, where α and h are the angle and the displacement respectively. The frequency values are similar with the eigenfrequencies determined numerically. The values of D are in the range $0 < D < 1$. For the case of the inflow velocity $V_X = 26[m/s]$, for which the system was unstable in the linear case, the system is damped in the non-linear case, which means that no flutter occurs.

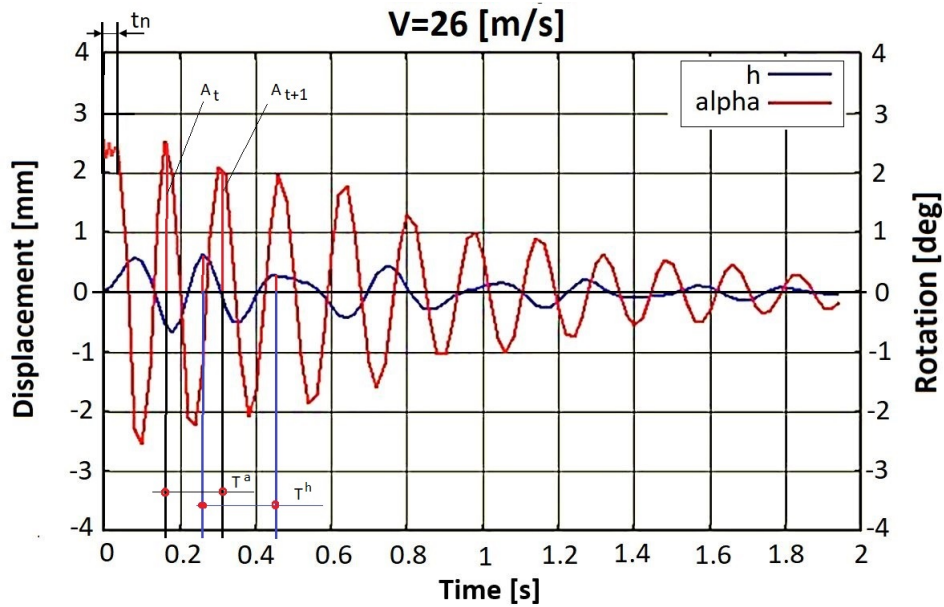


Figure 5.19: The displacement and the profile's rotation angle (the control node) as a function of time for the non-linear case at the inflow velocity of $V_X = 26[m/s]$

After increasing the velocity to $V_X = 29[m/s]$, one could observe (Fig. 5.20) the profile's oscillations with a similar amplitude as in the linear case. The frequencies obtained are the same as for the inflow velocity $V_X = 26[m/s]$.

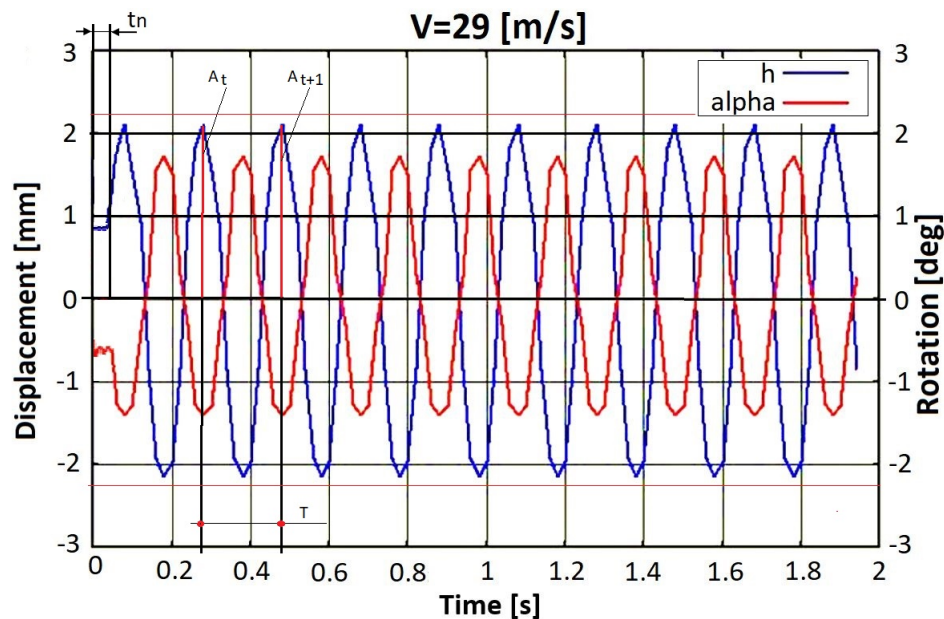


Figure 5.20: The displacement and the profile's rotation angle (the control node) as a function of time for a non-linear case at the inflow velocity of $V_X = 29[m/s]$

The obtained value of the damping ratio D in this case is ($D = 0$). For the velocity $V_x = 29[m/s]$ (Fig. 5.20) the profile oscillations with a constant amplitude, which means that LCO phenomena occurs.

5.5.4 Summary

Validation of the numerical analysis with the experiment show similarities for the investigated phenomena. In both cases, the same structure response was obtained - Flutter for linear approach and LCO for non-linear approach. Both experimental and numerical analyses research and computer simulation confirm that the use of elements with non-linear load characteristics significantly changes the nature of the phenomena occurring for the tested profile. In the linear case, a dangerous and catastrophic flutter phenomenon occurred. In the case of the non-linear approach, the oscillation phenomenon of constant amplitude (LCO) occurred. The differences in the results between the linear and non-linear approaches show that it would be impossible to conduct such analysis using one scheme. Therefore, it was necessary to extend the computational system with the possibility of analyzing non-linear cases. The extensive tool allows to analyze a number of other cases in which elements with non-linear load characteristics were used. The algorithm is still developing in order to obtain the highest accuracy of calculations in relation to experimental tests. The LCO can be present in any sort of non-linear system, in the context of aeroelasticity, LCO typically is exhibited as an oscillatory torsional response of the wing, the amplitude of which is limited, but dependent on the nature of the non-linearity as well as flow properties, such as speed, altitude, and Mach number. The LCO motion is often dominated by antisymmetric modes. LCO are not described by standard linear aeroelastic analysis, and they may occur at flight conditions below, were linear instabilities such as flutter are predicted. Although the amplitude of the LCO may be above structural failure limits, more typically the presence of LCOs results in a reduction in vehicle performance, leads to airframe-limiting structural fatigue, and compromises the ability of pilots to perform critical mission-related tasks. When LCOs are unacceptable for flight performance, extensive and costly flight tests for aircraft/store certification are required. The algorithm developed and validated with tests in the wind tunnel allows to take into account the phenomena described above, such as LCO.

5.5.5 A numerical simulation for non-linear material model exemplified by the flexible delta profile

As part of the FSI analysis for a geometric non-linearity and non-linear elastic material model of Mooney-Rivlin. [61], an example of a geometry is selected - a flexible delta wing [57] (Fig. 5.21 and 5.22). This object has been subjected to the load for linear-elastic and non-linear elastic material. The main objective was to investigate how taking into account non-linear properties in the structural analysis affects the response of the structural model in the FSI analysis.

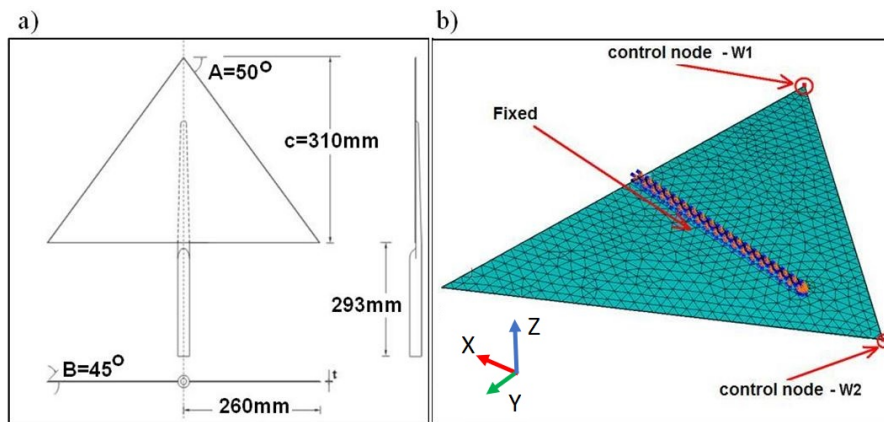


Figure 5.21: A flexible delta wing: a) geometry [57]; b) a structural grid with applied boundary conditions

The structural model has been created in Nastran FEA system (Fig. 5.21). It consists of approx. 3500 6-nodes shell elements having the following properties:

- thickness: $T = 10[mm]$
- Young's module $E = 60[MPa]$
- Poisson ratio $\nu = 0.3$
- Density: $\rho = 1100[kg/m^3]$

The materials were defined to obtain similar stiffness for linear-elastic and non-linear-elastic material (Fig. 5.25). The flexible Delta wing is a common example in flow analysis as a profile that achieves large displacements under aerodynamic forces [60]. The boundary conditions have been specified in the form of restraints in line with the experimental data [60]. The next step in preparing the FSI calculations was to generate a three-dimensional CFD grid for the URANS analysis (Fig. 5.22). The grid consists of 3 mill. tetrahedral elements, approx. 45000 prismatic elements and 152 regular tetrahedron-like elements.

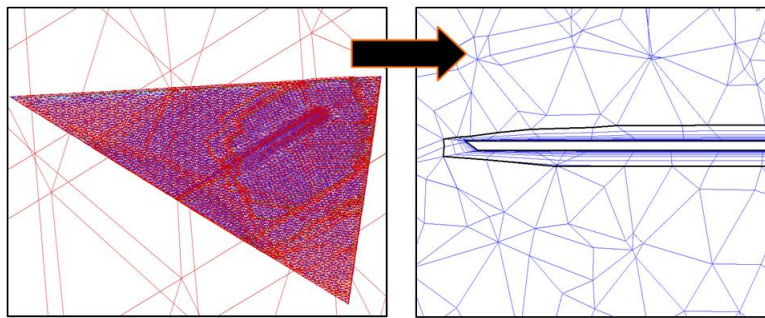


Figure 5.22: A flexible delta wing - a CFD grid for the URANS analysis

The grid was generated and has been tested to check for grid connectivity and the quality of particular elements. An analysis of the FSI has been performed for the following boundary conditions and parameters:

- Velocity $V_X = 5, 10, 15, 20[m/s]$
- Atmospheric pressure $P = 0.1[MPa]$
- Reynolds number $Re = 620,000$ [60]
- Angle of attack $\alpha = 10^\circ$
- Time step $t = 0.01[s]$
- Turbulence model: LEA $k - \omega$ - (Linearized Explicit Algebraic Stress Model)

A flexible delta wing with the linear approach In the first stage of the numerical simulation, linear-elastic material has been used for the flexible delta wing in line with the assumptions specified above. Figure 5.23 shows the results of the calculations of displacement for the control nodes W1 and W2 of the structural model as a function of time for the inflow velocity of $V_X = 20[m/s]$. For this case a rapid increase in amplitude of displacement has been observed in the function of time. Further details and the evolution of other state variables can be found in [59]. As a result of the calculations made for the first inflow velocity $V_X = 5[m/s]$ [59], the amplitude of the displacements specified in the W1 and W2 control nodes increase slightly. The calculations have been repeated to verify the results obtained for this and other cases.

As the inflow velocity is increased to $V_X = 20[m/s]$, the amplitude of the displacement (Fig. 5.23) show that the critical velocity has been obtained. The amplitude of the displacement has been grown rapidly in line with the value at which a real model would be heavily deformed or even destroyed.

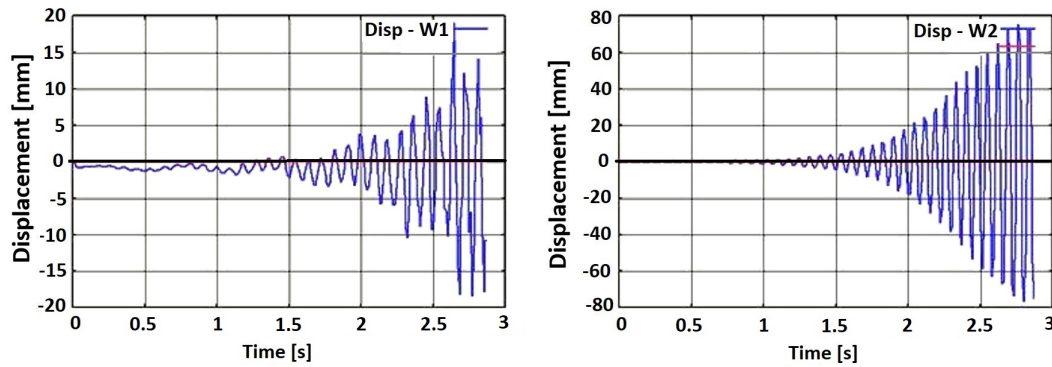


Figure 5.23: The displacements measured at control points as a function of time in the linear case at the inflow velocity $V_X = 20[m/s]$: left W1 node, right W2 node.

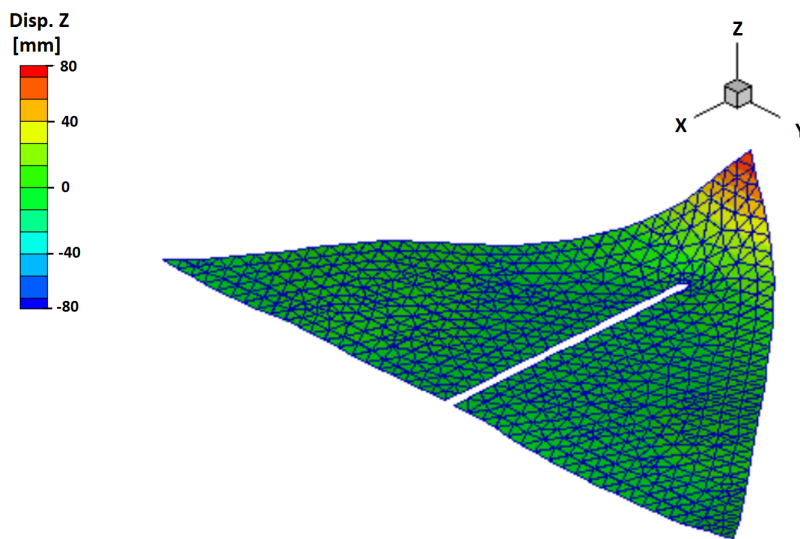


Figure 5.24: Displacement of the delta wing structural model for a calculation time $t = 2.5[s]$ - linear case

The Figure 5.24 show plotted of the delta wing displacement for the time step of $t = 2.5[s]$ - large displacements are visible in the front part of the profile. The calculations due to the large deformation of the flow mesh were stopped due to difficulties with the convergence of the DLR TAU-Code solver.

A flexible delta wing with the Mooney-Rivlin non-linear model The next stage of the numerical simulation implemented the Mooney-Rivlin non-linear elastic material model for a flexible delta wing. In order to compare linear and non-linear models in the elastic domain, the initial parameters have been specified according to the stress-strain curve shown in the Figure 5.25.

- Thickness: $T = 2[mm]$
- Constants: $C_{10} = 60, C_{01} = -54[MPa]$
- Density: $\rho = 1100[kg/m^3]$

The curve in Figure 5.25 shows the non-linear relationship between stress and strain for a hyperelastic material. Simulations for specific velocities V_X (5, 10, 15 and $20[m/s]$) have been made in an analogous way.

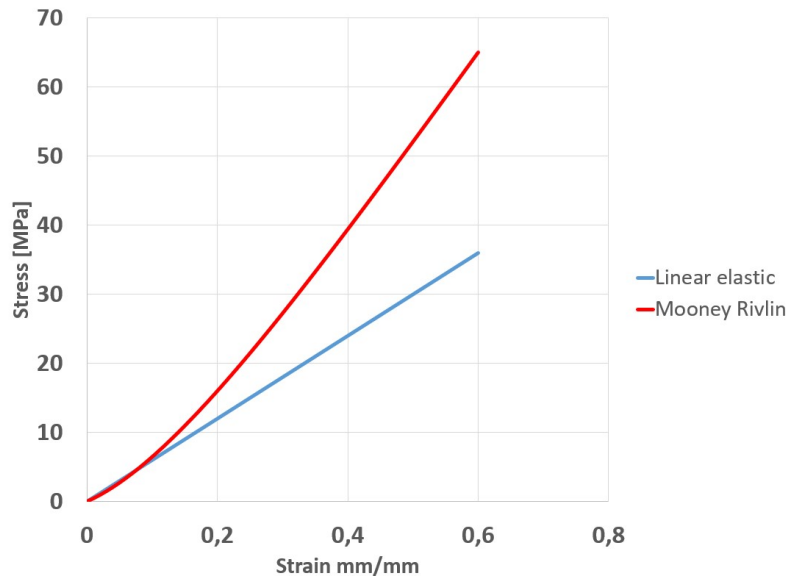


Figure 5.25: Stress-strain curve for linear-elastic and hyperelastic material

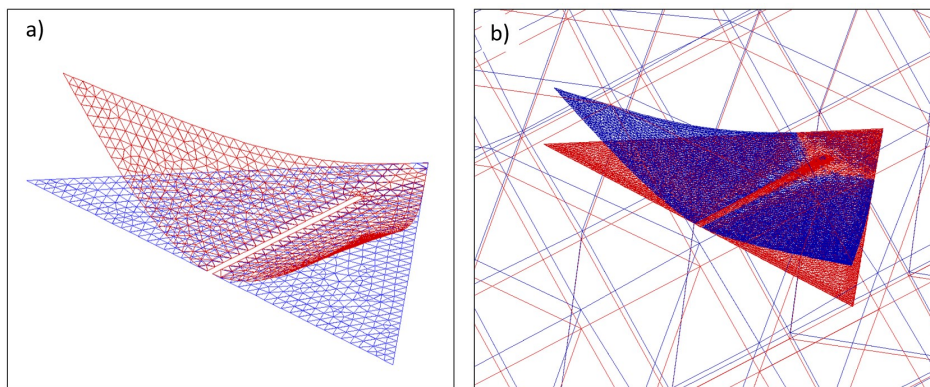


Figure 5.26: A flexible delta wing: a) deformation of the CSM mesh: b) deformation of the CDF mesh

Figure 5.26 shows the deformation of the structural mesh (Fig. 5.26a) and the deformation of the flow mesh (Fig.5.26b) **for the chosen period of analysis for the linear material.**

Below, the results for the W1 and W2 nodes displacements for the structural model (Fig. 5.27) as a function of time with the inflow velocity of $V_X = 20[m/s]$ are duplicated.

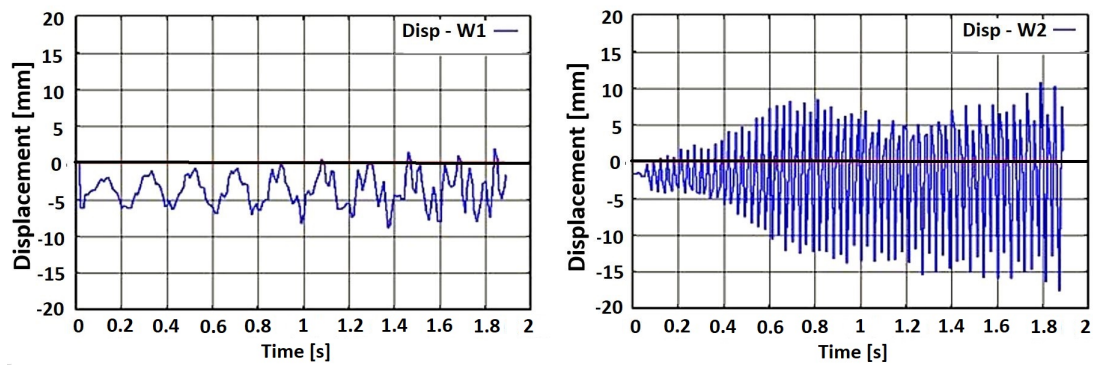


Figure 5.27: The displacements measured at control points as a function of time in the non-linear case of Mooney-Rivlin material model at the inflow velocity of $V_X = 20[m/s]$: left W1 node, right W2 node.

As a result of the simulations carried out for the speed of $V_X = 20[m/s]$ (Fig. 5.27), when flutter has occurred for the linear case, for non-linear elastic material obtained oscillations with steady amplitudes.

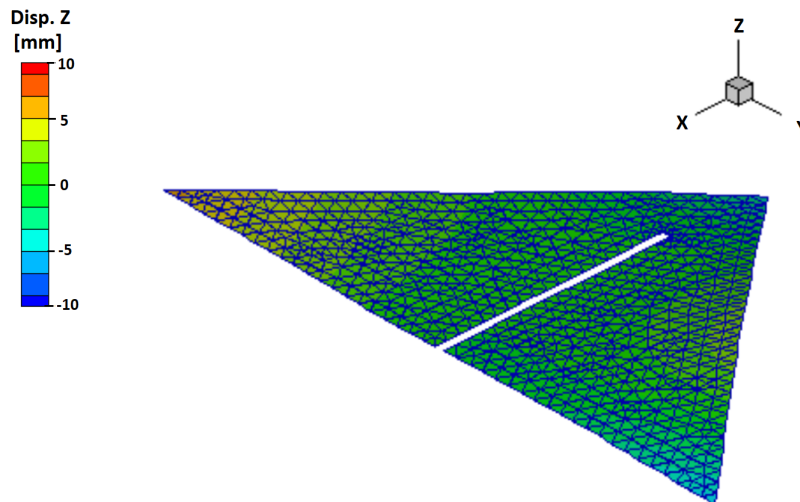


Figure 5.28: Displacement of the delta wing structural model for a calculation time $t = 1.8[s]$ - non-linear case

The Figure 5.28 shows plotted of the delta wing displacement for the time step of $t = 1.8[s]$ - the resulting maximum displacement varies periodically within a limit of $10[mm]$ which is about eight times less than the limit found by employing the linear approach

For the same conditions the non-linear model exhibits different behavior. The delta wing behaves stable for defined flow conditions. This behavior results from the stress-strain curve analysis for a nonlinear-elastic material. In the linear case, an increase in force causes a linear increase in displacement. For the hyperelastic (non-linear elastic) case, the increase in force causes a non-linear increase in displacement - lower than in the linear case.

5.5.6 Conclusions

In this chapter, the system for large scale aeroelastic simulation with material non-linearity has been implemented. The results of the computational analysis prove that the use of non-linear

material models in the structural model also significantly change the response of the structural model in the FSI analysis. In the case of using a linear-elastic material model, the displacement amplitude increases rapidly. In the case of using hyperelastic non-linear material models, the displacement amplitude reached a constant value and did not increase rapidly. Flutter occurred only in the linear case. The results were also obtained for large deflections of the structure. This confirms that the algorithm allows of the FSI analysis not only for the non-linear material, but also with large displacements.

Introducing the non-linear damping matrix to the system will be a natural direction of development. It will extend the scope of the practical usability to the modeling of active control of aeroelastic phenomena. The performed analysis showed that the change of the material model of the structure changes the dynamic response of the system under the influence of aerodynamic load. Although this does not mean that damage will not occur. The use springs with non-linear stiffness in the suspension system for the Naca0012 profile causes smaller displacements of the system with the increasing aerodynamic force. Hence, the oscillation is constant in the non-linear case, while we observe flutter for springs with the linear load characteristics. The results for the Naca0012 wing presented in section 5.5.3 show the change damping, if non-linear springs are used in the wing suspension system. A change in the oscillation amplitude was also observed for the delta profile.

Recently, materials produced by the additive manufacturing (AM) technique are increasingly used in the aerospace industry, for which it is necessary to use non-linear models describing their behavior.

The last chapter is a description of the research on the mechanical behavior of the material structure and was carried out in a research group at BTU Cottbus- Senftenberg. This is important from the point of view of damage modeling of structures made of unconventional materials, for which the use of a linear approach is insufficient.

Chapter 6

Material behavior analysis

6.1 Introduction

Calculations considering both for the actual configuration of the aircraft and the non-linearity of the material do not provide a complete description of the structural behavior. The basic approach to testing the structure in terms of safety is limited to the analysis of the system response to aerodynamic loads only in the elastic range. Currently, the development of the aviation industry is observed in the direction of the development of unmanned aerial vehicles (UAV) and the use of new materials for their construction. UAV operation conditions require to reduce weight even further for an increased operating range. One possibility is to use new production techniques and materials. New materials, especially those used in 3D printing, lack a complete experimental assessment (in terms of cyclic behavior, damage) and a suitable, exact and numerically efficient material model. Chapter 6 describes an experimental and numerical investigation of the behavior of the printed material under the influence of various load cases and temperature. The modern development of 3D printing technology and the use of new materials make this technique more and more often used in small-scale UAV production (Fig. 6.1).

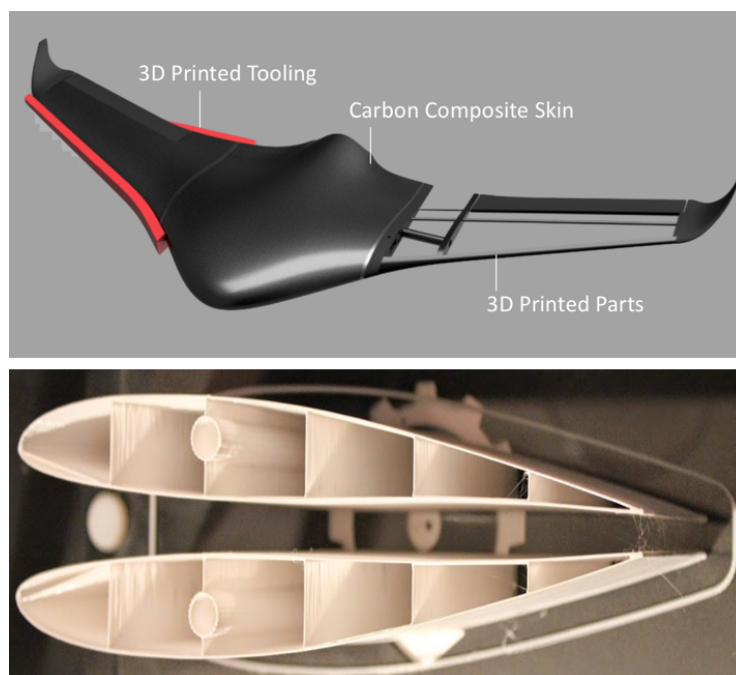


Figure 6.1: 3D printed UAV [6]

A good example of the development of new technologies in the construction of UAVs is the example of the wing shown in the Figure 6.2. The wings, created by NASA and Massachusetts Institute of Technology (MIT) engineers, comprise thousands of tiny triangles of matchstick-like struts bolted together to form an open, lightweight lattice framework, which is covered with a thin polymer layer. According to the developers, this forms a mechanical metamaterial with the stiffness of a rubber-like polymer and the lightness and low density of an aerogel. The lattice has a density of $5.6[kg/mm^3]$, compared to rubber with a density of $1500[kg/m^3]$. The material's mix of stiff and flexible components means instead of requiring separate movable parts such as ailerons to control the roll and pitch of a plane, parts of the wing - or the whole wing - can deform to achieve the same effect as for moving components [133].

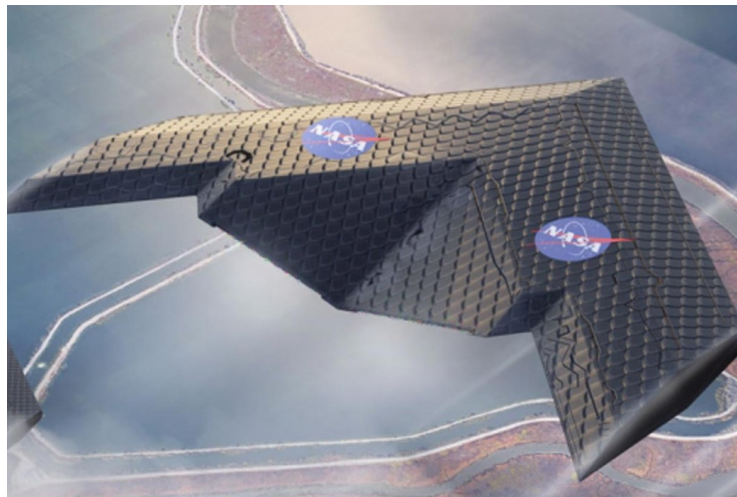


Figure 6.2: 3D printed UAV [133]

The presented example shows the growing use of parts made from materials by AM techniques in construction. New materials require a research process that is much broader than for commonly known and used materials. The new approach also requires changes in numerical calculations and requires a more thorough analysis of the structure model in terms of material behavior. A major issue is the description of new materials in terms of applicability and most importantly the process of damage under the influence of various loads. The current research at BTU Cottbus-Senftenberg is being conducted towards new materials in different aspects. This chapter presents one of the processes of testing 3D printed polyamide PA12. The following description contains only a selected scope of research relevant for studied loading regime. Investigation carried out provides more information on the mechanical properties of AM materials. The research is based on experiments and numerical modeling of material and damage behavior. The papers [105–107] describe the mechanical properties of PA12 printed material include the micro-structural evolution in uniaxial tensile test. The purpose of the study was to determine parameters for the numerical models used to characterize the behavior of the material and the failure process. Schob et al. [106] describe an experimental study with numerical validation of printed polyamide 12 for cyclic loading. The paper [107] presents the influence of temperature on the change of strain and stress in the process of quasi-static loading.

As has already been shown in paper [105], the coupling of the Chaboche material model and the Gurson-Tvergaard-Needleman (GTN) damage model enabled the numerical simulation of 3D printed polyamide 12 (PA12) under quasi-static loading. In the current study, these investigations for dynamic loads are continued. In order to represent the material behavior of the additive PA12 for dynamic loading numerically, the previously used Chaboche model was extended. Also the

GTN model was extended and further damage mechanisms, which became evident in the micro-analysis, were considered. Due to the influence of temperature on stress and strain of polymers, the temperature was measured during the experiments and the self-heating effect was taken into account when determining the parameters. The current state of the art shows that additive manufacturing has become more and more important. At the beginning, additive manufacturing process was primarily used for prototyping, but now the field of application has expanded. This also applies to aviation techniques. In order to satisfy the new requirements, it is essential to introduce new test methods for additively manufactured materials. Currently, the number of testing standards for AM materials is very limited. In 2015, Forster [118] reported that 47 standards exist, but 27 of them cannot be applied and 20 are only partially applicable. In addition to this challenge, the manufacturing processes are not yet optimized, as proven by investigations of the material structure [104]. Since no test standards are available, it is not possible to obtain material parameters from data sheets. Having such standards would allow future qualification and standardization of AM parts. It is also important for the process of design and analysis of structures also used in the aerospace industry. In recent years, Technical Committee for Road Transport and Traffic Telematics (CEN/TC 438) has collaborated with ISO/TC 44/SC 14 Welding and brazing in aerospace and ISO/TC 61/SC Thermoplastic materials, forming joint working groups (JWGs). The work resulted in the following published in 2020. ISO/ASTM 52941 standards for the additive manufacturing of Laser Beam Powder Bed Fusion (LB-PBF) for aerospace applications. The standards these are as follows:

- ISO/ASTM 52941-20. Additive manufacturing - Performance and reliability System - Acceptance testing of machines operating using Laser Beam Powder Bed Fusion technology for metallic materials for aerospace applications,
- ISO/ASTM 52942-20. additive manufacturing - Qualification principles. - Qualification of operators of machines and equipment operating Powder Bed Fusion technology for metals and components manufactured additively for aerospace applications.

The International Organization for Standardization is constantly working on more standards related to 3D printing. Thus, it can be assumed that the industry will receive clear and transparent rules in the coming years, which will be applied across the entire value chain. The presented and published results are part of the research carried out in the process of standardization of materials produced with the AM technique. In order to carry out the investigation, the samples preparing was necessary. The samples were prepared by selective laser sintering (SLS) 3D printing technique. A PA2200 powder, specifically developed for SLS, was used. A sPro 230 printer from 3D Systems was used with a power of 70 W. It was run with a laser scanning speed of 10 [m/s] for the filling and 5 [m/s] for the contour in order to obtain a homogeneous sinter structure. The layer thickness was 0.08-0.15 mm. The temperature of the printing chamber and the process was 170 °C and 200 °C. The powder particles had a size in the range of 20-80 μm and were spherical in shape.

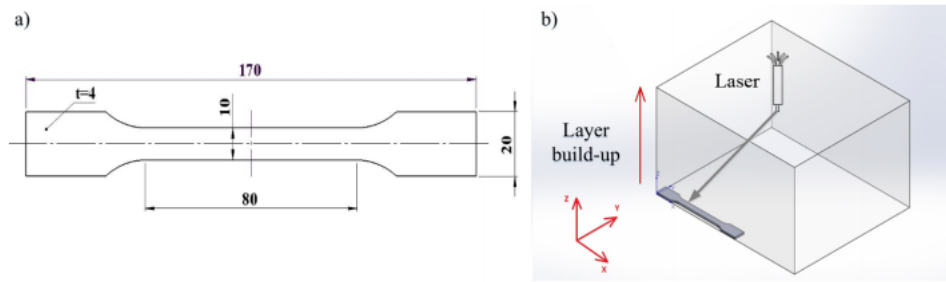


Figure 6.3: a) Shape and dimensions of the specimen, b) Sketch of the built job: single printed layers are in the xy -plane, the build-up direction of the layers is the z direction [106]

Due to the fact that no test standards exist for AM polymers under cyclic and temperature loading [118], the test geometry was selected according to DIN EN ISO 527 [119], as sketched in Fig. 6.3. In previous investigations, it was observed that the material properties depend only marginally on the printing direction [120]. For this reason, all tests were performed on samples oriented as sketched in Fig. 6.3b, namely x -direction. The same geometry was used in the studies described by Schob et al. in [106, 107].

6.2 Experiments

From the point of view of understanding the new 3D printed material, experiments were carried out with cyclic and quasi-static loading for different temperature levels in the chamber. In order to accurately describe the mechanical behavior of the material, it was also necessary to know its microstructure. For this purpose, cyclic tests were carried out at different load levels, and the temperature variation of the sample was simultaneously measured. Subsequently, the microstructure was investigated by scanning electron microscopy (SEM), X-ray refraction radiography and computer tomography (CT). With the experimental results, the numerical model of Chaboche and GTN could be calibrated and extended. With the extension and coupling of the Chaboche and GTN model to achieve a good agreement between experiment and numerical simulation. The approach presented in this chapter shows the procedure for testing new materials to define optimal parameters. Additionally, the specimens isothermal and non-isothermal tensile tests were carried out. To minimize the self-heating effect due to high testing speed, a displacement rate of 0.5 mm/min was chosen. The described temperature dependency investigation is based on results found in the paper [107].

6.2.1 Cyclic tests

The cyclic tests were performed at 23 °C (room temperature) on a servo-hydraulic test machine from ZwickRoell, with a 25 kN load cell. Fifteen force controlled tests were done at different force amplitude F_a levels with a stress ratio of $R = -1$ and a frequency of $f = 3$ Hz. The resulting stress amplitudes σ_a , depending on the width a and thickness b of the samples (Fig. 6.4a), are presented in the Table 6.1. An anti-buckling device was used. This consisting of two plates (dimension 50 mm x 70 mm x 4 mm), which are connected by screws. The test specimen is placed between these plates. The plates were coated with a polytetrafluoroethylene (PTFE) tape to minimize friction between the sample and the anti-buckling device, Fig. 6.4b.

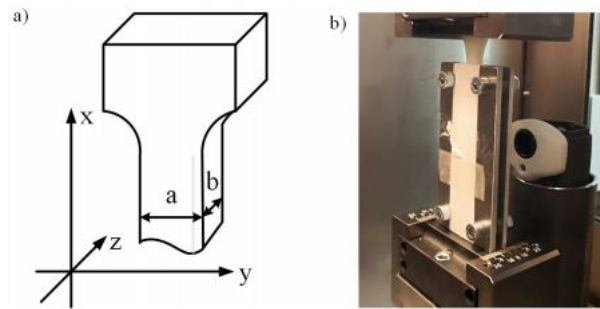


Figure 6.4: a) Dimensions of the sample, b) Test set up with anti-buckling device and infrared camera [106]

Table 6.1: Stress levels of cyclic tests [106]

F_a/N	Name	a/mm	b/mm	σ_a/MPa
1300	T6	10.00	4.00	32.50
	T5	9.85	4.10	32.19
	T7	10.00	4.15	31.33
1100	T4	9.95	4.10	26.96
	T2	9.90	4.15	26.77
	T3	10.00	4.15	26.51
900	T8	9.90	4.00	22.73
	T10	9.90	4.00	22.73
	T9	9.85	4.15	22.02
800	T13	9.90	3.95	20.46
	T12	9.95	4.00	20.10
	T11	9.90	4.05	19.95
700	T15	9.95	4.00	17.59
	T17	9.95	4.00	17.59
	T16	9.98	4.00	17.54

6.2.2 Temperature measurements

In the cyclic tests, the temperature of the sample was measured to study the observation of the self-heating phenomenon. A small inspection window was cut into one of the plates of the anti-buckling device. The temperature of the specimen was measured during loading by a Voltcraft infrared camera IR-550A, Fig.6.4b. The distance to spot size ratio was 8:1 and the degree of emission was permanently 0.95. Emissivity is the measure of an object's ability to emit infrared energy. Emitted energy indicates the temperature of the object. For this reason, the gauge length was marked with a matt black color [106].

6.2.3 Isothermal and non-isothermal tensile tests

Another important phenomenon was the analysis of the influence of ambient temperature on the values of strains and stresses. For the isothermal tensile tests four levels of chamber temperature, 10 °C, 20 °C, 30 °C and 40 °C were selected. Five tests were conducted for every temperature level. In order to reach a thermal equilibrium, the samples were stored under test temperature in the temperature chamber for one hour before the test started. Three non-isothermal tensile tests

(T_1, T_2, T_5), where $T_1 = 10\text{ }^\circ\text{C}$ with different temperature curves and same displacement rate of 0.5 mm/min were performed, Fig. 6.5. The temperature was changed cyclically between $10 - 45\text{ }^\circ\text{C}$ with different temperature rates. The temperature during the isothermal and non-isothermal tests was measured in the temperature chamber.

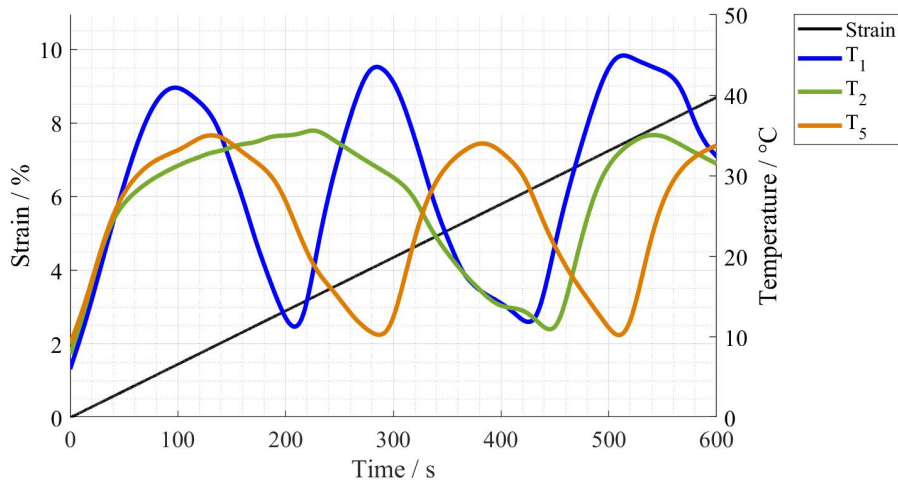


Figure 6.5: Conditions for non-isothermal tensile tests. Left y-axis: strain-time curve, right y-axis: temperature-time curve

The results of the conducted experiments are presented in the results section 6.4.2.

6.3 Microstructure of material

In order to properly model the mechanics of the material, and to determine the appropriate parameters for the material models, it was necessary to know the microstructure of the material before and after the tests. From the point of view of the material description used and the GTN damage model, porosity was an important feature. For this purpose, Scanning electron microscopy (SEM), X-ray refraction and computed tomography tests were carried out. These tests were performed for the cyclic load tests. The details of the methods are described in [106]. The results of the microstructure observations are presented below.

6.3.1 Scanning electron microscopy

The results of the SEM analysis reveal an inhomogeneous microstructure of the specimens and the presence of pores. Fig. 6.6a illustrates the fracture surface of one of the specimens. A fatigue crack propagation with characteristic striations to the left of the bold red dotted line can be observed. The left framed box shows a magnification of the area of fatigue crack propagation, Fig. 6.6b. To the right of the bold red dotted line, a ductile fracture is formed, which can be recognized by the typical flakes. A magnification of the fractured area is represented in Fig. 6.6c.

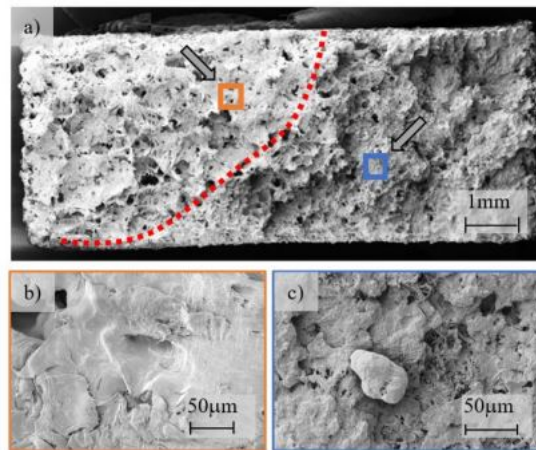


Figure 6.6: Scanning electron micrographs, a) crack surface, $40\times$ magnification, b) detail of area with characteristic striations, $1000\times$ magnification, c) detail of ductile forced fracture, $1000\times$ magnification, taken from [120].

6.3.2 X-ray refraction

For the X-ray refraction measurements, an approximately 20 mm long piece was cut from the measure length of both a cyclic loaded (T2 in Tab. 6.1) and a virgin specimen. The two samples were scanned in steps $\Delta x_R = 1$ mm, $\Delta y_R = 0.1$ mm (building up the so-called X-ray refraction topogram) and examined with the following experimental set-up: a standard fine structure X-ray tube (operated at $U = 40$ kV, $I = 0.8$ mA) providing nearly monochromatic radiation (Mo-K α), a beam-defining slit, identifying an incident beam cross section is $500 \times 40 \mu\text{m}^2$, two scintillation detectors (Fig. 6.8, right), allowing the simultaneous detection of the X-ray refraction and transmission intensity behind the sample (I_R and I_T).

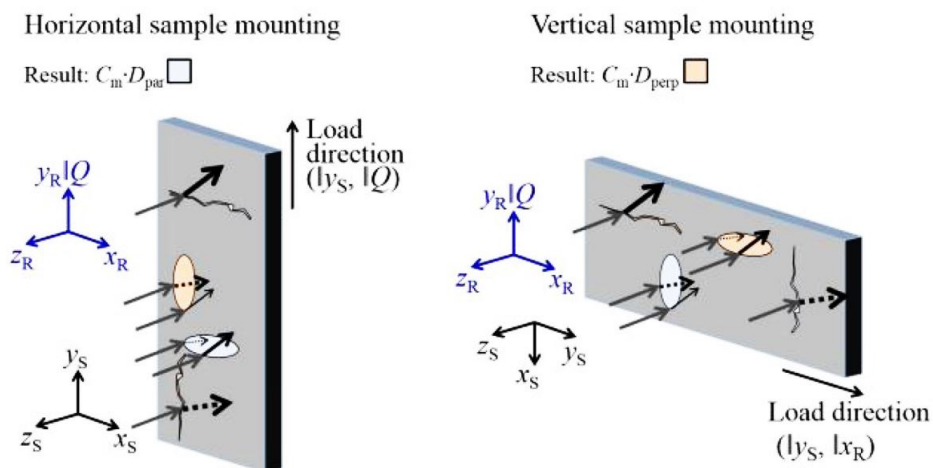


Figure 6.7: Sensitivity of the measured X-ray refraction intensity to different sample orientation [106].

The set-up consisted in practice in a modified small-angle scattering X-ray camera of the Kratky type. By measuring the two intensities with and without (index 0) a specimen in the beam, one obtains the so-called refraction value $C_m \cdot D$:

$$C_m \cdot D = \frac{I_R/I_{R0}}{I_T/I_{T0}} - 1 \quad (6.1)$$

where D is the sample thickness, I_R is a X-ray refraction and I_T is a transmission intensity behind the sample (Fig. 6.8). The derivation of Eq. 6.1 is given in [127]. It indicates that there is no (measured) refraction if the relative change I_R/I_{R0} is exclusively caused by absorption: if $I_R/I_{R0} = I_T/I_{T0}$, then $C_m = 0$. While, with the participation of I_R refraction, this increases as well has $I_R/I_{R0} > I_T/I_{T0}$, so that $C_m > 0$. C_m represents a relative measure of the volumetric specific surface Σ (surface per unit volume). It is a relative value to the calibration constant. To obtain absolute values of the specific surface a calibration sample of the same material with priorly known specific surface (*e.g.*, a monodisperse powder) is needed. Usually, I_T and I_{T0} are used to calculate the absorption properties, since $\mu \cdot D = -\ln(I_T/I_{T0})$ (Beer Lambert law), μ being the linear attenuation coefficient. With priorly known μ_0 (tabulated or reference data of the dense material) the porosity p is estimated as:

$$p = 1 + \ln\left(\frac{I_T}{I_{T0}}\right)/(\mu_0 \cdot D) \quad (6.2)$$

since the porosity lowers the macroscopically measured thickness D to an effective thickness $(1 - p)D$.

Fig. 6.9a depicts the refraction topographs of $(C_m \cdot D)_{par}$ (left) and $(C_m \cdot D)_{perp}$ (right), whereas Fig. 6.9b shows the cumulative $C_m \cdot D$ profiles obtained from the two orientations for direct comparison. The samples show very distinct refraction signals. In the virgin state (V), the refraction values are $(C_m \cdot D)_{par} = 0.23$ and $(C_m \cdot D)_{perp} = 0.27$. Such values indicate internal surfaces, which are attributed to pores. They show a small degree of anisotropy (elongation in axial direction). The cyclic loaded (C) specimen exhibits refraction values of 0.61 and 0.44, respectively, more than twice as large as the sample from virgin specimen. Since the porosity does not change substantially (as obtained from the CT results), the additional internal surface is supposed to be due to deformed (elongated) pores. $(C_m \cdot D)_{par} > (C_m \cdot D)_{perp}$ indicates that those pores are preferentially oriented perpendicular to the tensile direction (*i.e.*, extended along the transverse direction, x_S in Fig. 6.7).

The measurements were performed with two different sample orientations: with the load direction parallel (Fig. 6.7, left) and perpendicular (Fig. 6.7, right) to the scattering vector Q of the camera system (respectively vertical and horizontal orientations in the following).

This tendency was already observed in a statically loaded specimen [105]. The changes were lower in that case: $(C_m \cdot D)_{par} = 0.54$ and $(C_m \cdot D)_{perp} = 0.47$. This implies, that the deformed pores are likely to grow continuously with increasing number of load cycles. The transmission measurement in horizontal orientation of the samples is shown as topograph in Fig. 6.10a and as cumulative profiles in Fig. 6.10b. Comparing to bulk material, the 3D printed samples show less attenuation. According to Eq. 6.2, this is attributed to an estimated porosity of about 5%.

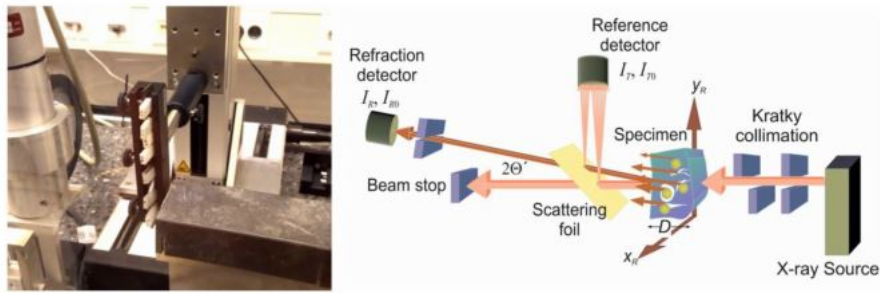


Figure 6.8: Left: detail of the experimental set-up with samples mounted vertically ($Q \parallel x_S$, sensitive for axial surfaces see Fig. 6.7, right), showing the Kratky collimation (covered by lead), the sample manipulation and the reference detector. Right: schematic laboratory set-up of the scanning X-ray refraction topography technique. [106]

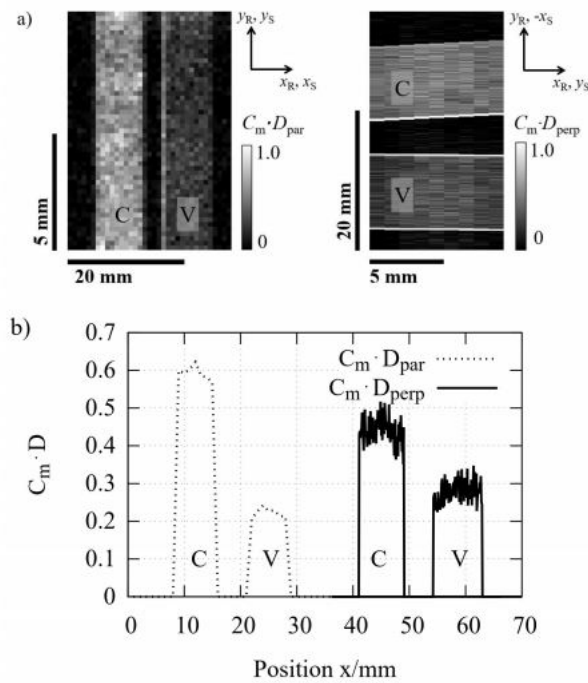


Figure 6.9: a) $C_m \cdot D$ topographs obtained from horizontally (left) and vertically (right) mounted cyclic loaded (C) and virgin samples (V). The different pixel size (scan increments) is due to the beam cross-section (see above). The directions of scattering Q ($\parallel y_R$) and load ($\parallel y_S$) are indicated. b) Cumulative $C_m \cdot D$ profiles of the cyclic loaded (C) and virgin (V) sample in horizontal and vertical orientation, revealing the significantly higher specific surface in the cyclic loaded sample.

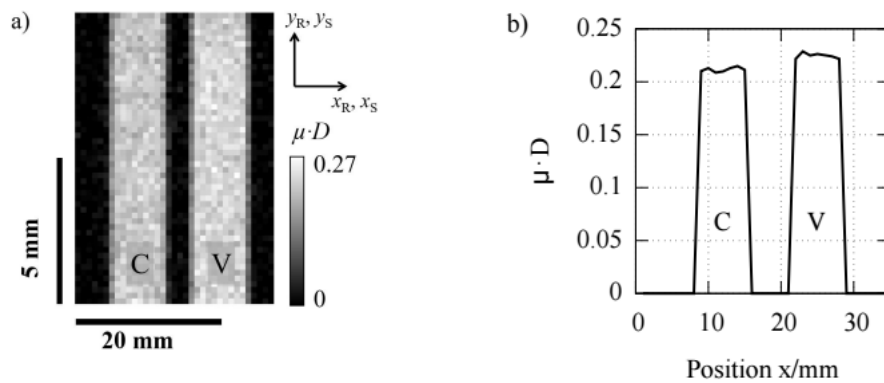


Figure 6.10: a) $\mu \cdot D$ topographs of cyclic loaded (C) and virgin (V) sample, b) $\mu \cdot D$ cumulative profile of cyclically loaded (C) and virgin (V) sample

The entire procedure is fully explained in [106].

6.3.3 Computed tomography

In the virgin sample, a bimodal pore size distribution occurs with a gap at about $100 \mu\text{m}$ equivalent pore diameter with 91% of the number of identified pores being smaller but contributing just 4% to the integral porosity. For the cyclically loaded sample the gap is less pronounced and located at about $70 \mu\text{m}$. The percentage of pores with diameters smaller than $70 \mu\text{m}$ amounts to 81%, which also contributes 4% to the integral porosity. As to be seen from Fig. 6.11, the center of gravity of large pore size shifts from $222 \mu\text{m}$ (virgin) to $180 \mu\text{m}$ for the cyclic loaded sample. The integral porosity increases from 3.9% (virgin) to 4.2% (cyclic loaded).

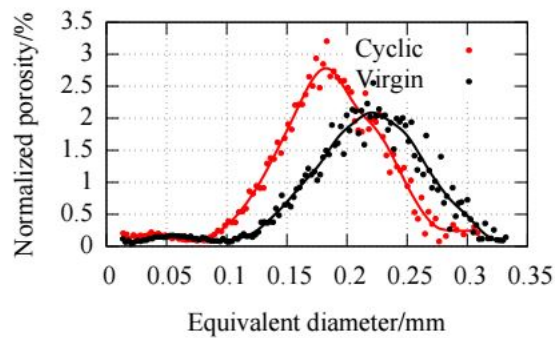


Figure 6.11: Normalized porosity as a function of the equivalent pore diameter of the virgin and the cyclic loaded sample. Note the different gap and peak positions.

Fig. 6.12a shows a representative reconstruction slice of both samples. It exhibits sections of large pores, which tend to have a more complex shape in the virgin sample. The distribution of pores illustrated by a 3D rendering in Fig. 6.12b. Pores with diameters smaller than $80 \mu\text{m}$ are colored in red, while pores above $80 \mu\text{m}$ diameter are shown in blue (see Fig. 6.12b).

The physical shape of small pores is hard to assess due to the very limited number of voxels (e.g., 8 voxels for an equivalent diameter of $20 \mu\text{m}$). For larger pore sizes the evaluation of the actual pore shape is much more accurate. It turns out that the shape of larger pores tends to be more spherical after cyclic load. Fitting the actual pore surface A vs. equivalent diameter D (see Fig. 6.13) results in functions $A = 2.64 \pi D^2$ for the virgin and $A = 2.05 \pi D^2$ for the cyclic loaded

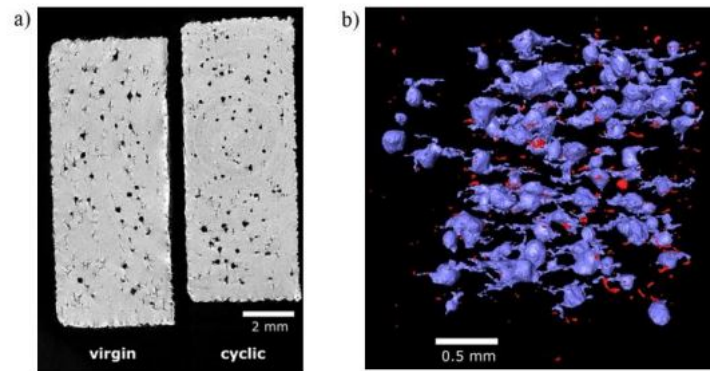


Figure 6.12: a) 2D reconstruction slice of the virgin and cyclic loaded sample (showing a $4 \times 10 \text{ mm}^2$ cross section perpendicular to the load direction), b) 3D rendering of pores below $80 \text{ }\mu\text{m}$ (red) and above $80 \text{ }\mu\text{m}$ (blue) equivalent diameter of a $2 \times 2 \times 2 \text{ mm}^3$ detail of the cyclic loaded sample.

sample (for spheres holds $A = \pi D^2$). While these fits represent the average shape of large pores very well, smaller pores deviate towards smaller surface.

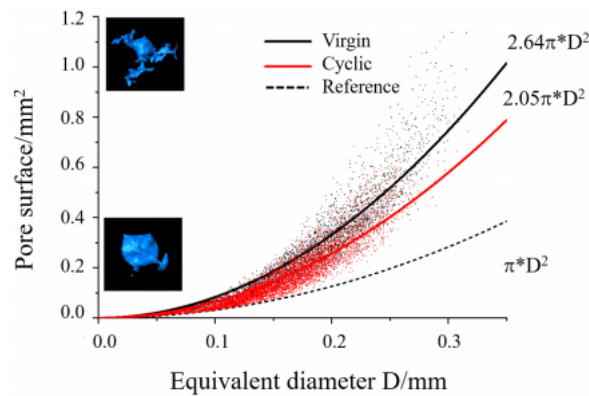


Figure 6.13: Actual pore surface as a function of the equivalent pore diameter as obtained from 34700 individual pores in the virgin and from 57800 individual pores in the cyclic sample within equal volumes of 351 mm^3 . The reference line indicates the geometrical minimum of spheres. Comparison of the fit curves indicates a higher deviation from sphericity for the pores inside the virgin sample. The insets visualize that a large pore surface (at given diameter) corresponds to complex shapes and vice versa [106].

6.4 Results

6.4.1 Material behavior

Cyclic tests

While the static behavior of PA12 has been well investigated in previous work [105], cyclic tests allow for revealing cyclic softening. Fig. 6.14 shows the stress-strain diagram of the test with the highest (test 6) and lowest (test 16) load amplitude. As shown in section 5.3, the structure response in FSI analyzes is periodically variable, hence the study is of great cognitive importance for modeling new materials in aviation applications. Due to the higher load, the hysteresis increases as a function of time. This is reflected in Fig. 6.14, left, which is evident from the increase of the

viscoplastic elongation.

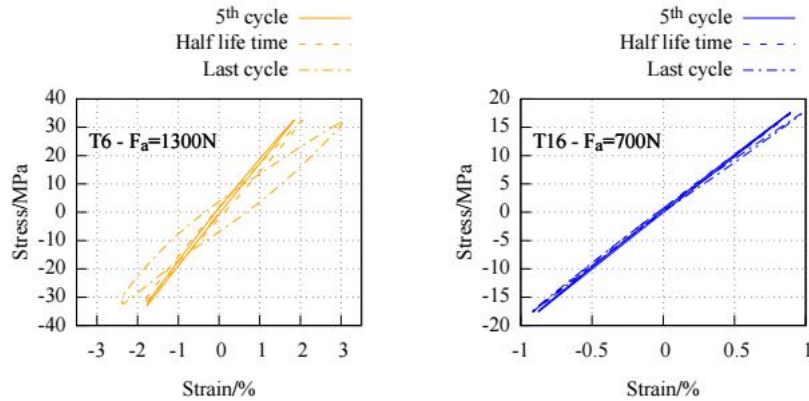


Figure 6.14: Cycle softening, left: test 6 ($F_a=1300N$) with a high pronounced cyclic softening and right: test 16 ($F_a=700N$) with less pronounced cyclic softening. Last cycle $\approx 522^{th}$ cycles

Observing the strain-time response of the maximum and minimum values of the strain amplitudes, we notice that an expansion of the envelope curve occurs, Fig. 6.15. This phenomenon is typically denoted as cyclic softening. Moreover, cyclic softening is more pronounced with larger load amplitudes.

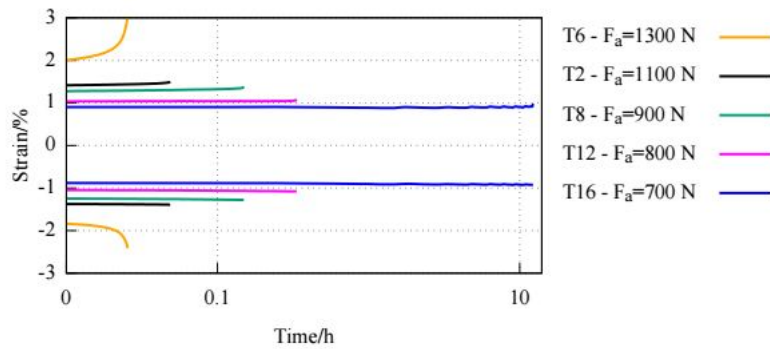


Figure 6.15: Cyclic softening, envelope curve of all load levels

For the evaluation of the specimen lifetime, the number of cycles N in the range $N > 10^3$ is the most significant figure. All tests with breakage below 1000 cycles were not considered for the estimation of the SN-curve. The results of the cyclic tests are listed in Table 6.2.

Table 6.2: Results of cyclic tests [106]

σ_a/MPa	32.5	32.19	31.33	26.96	26.77	26.51	22.73	22.73
N/-	277	1	142	339	529	721	483	1614
Name	T6	T5	T7	T4	T2	T3	T8	T10
Considerd	no	no	no	no	no	no	no	yes
σ_a/MPa	22.73	20.46	20.10	19.95	17.59	17.59	17.54	
N/-	1876	1255	3602	3881	33361	103585	132284	
Name	T9	T13	T12	T11	T15	T17	T16	
Considerd	yes	yes	yes	yes	yes	yes	yes	

Thus, the equation of the SN-curve was estimated by a linear regression to $lg(N) = 26.00 - 17.07 * lg(\sigma_a)$ based on data of eight remaining test. The correlation coefficient was $r^2 = 0.8281$ and the standard deviation was $s = 0.13$. Fig. 6.16 shows the SN-diagram with the experimental data and the fitted curve.

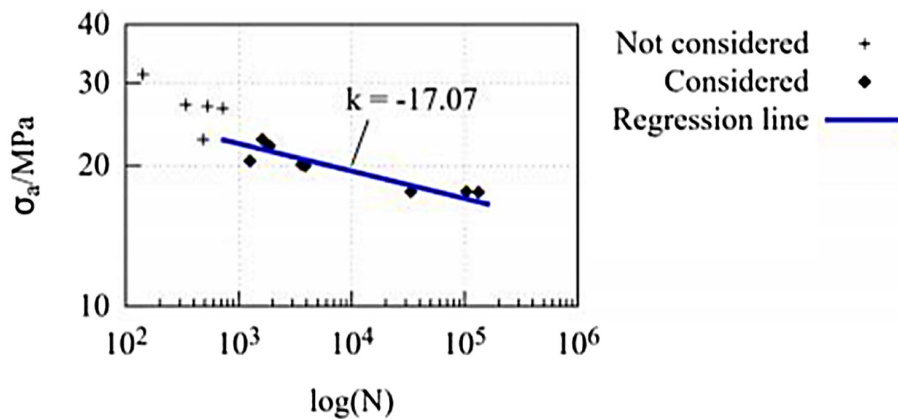


Figure 6.16: SN curve of 3D printed PA12 at a stress ratio of $R = -1$ and a frequency of $f = 3$ Hz. Diamond symbols indicate values considered for the determination of the regression (blue line) with a slope of $k = -17.07$

Self-heating

During cyclic loading, the specimens exhibit self-heating at all loading levels. As can be seen in Fig. 6.17, this effect depends on the loading amplitude. With an amplitude of 1300 N, the temperature increased by 4.5 K. An increase by 1.5 K is identified at the lowest loading level of 700 N.

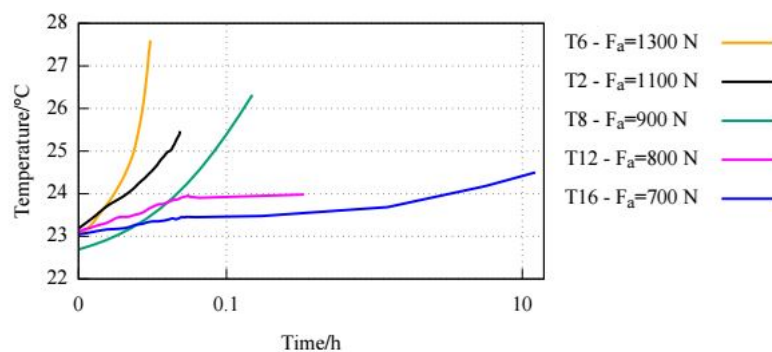


Figure 6.17: Temperature increasing during the cyclic loading. Load levels are reported in Tab. 6.1

6.4.2 Isothermal tensile test

Whereas in previous investigations [106] the material behavior under room temperature was investigated, the material and damage behavior as a function of temperature is presented in the following.

A representative technical stress-strain curve was selected for each temperature level of isothermal test, Fig. 6.18.

The statistical evaluation of all isothermal tests is shown in Table 6.3 with the mean values \bar{x}_i and standard deviations s_i .

A significant temperature dependency is visible. As the temperature rises, the Young's modulus E and ultimate tensile strength UTS decrease whereas the elongation at break increases ε_b .

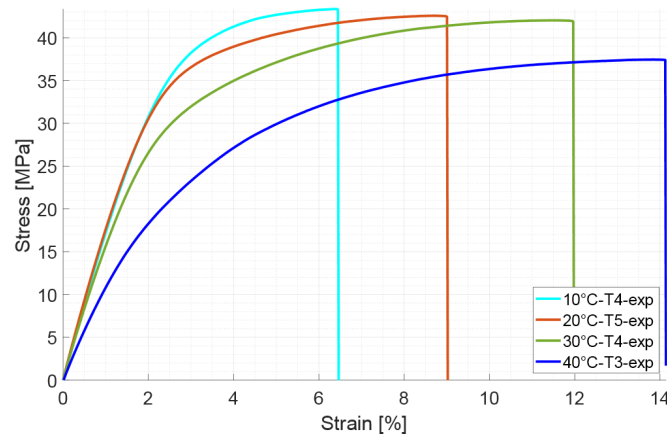


Figure 6.18: Technical stress over strain chart for sample tensile test at different temperature levels.

Table 6.3: Mean values and standard deviation of the material properties for isothermal tensile test

	Unit	10 °C	20 °C	30 °C	40 °C
\bar{x}_E	[MPa]	1776.03	1771.2	1561.7	1068
s_E	[MPa]	0.45	0.73	0.33	0.38
\bar{x}_{UTS}	[MPa]	43.44	42.15	42.25	37.88
s_{UTS}	[MPa]	0.48	0.32	0.48	1.12
\bar{x}_{ε_b}	[%]	6.63	8.34	11.68	14.82
s_{ε_b}	[%]	0.25	0.45	0.22	0.92

6.4.3 Non-isothermal tensile test

The results of the non-isothermal tests are shown in Figure 6.19. The upper diagram shows the strain and temperature loads. The lower diagram illustrates the stress-time stress. Based on the isothermal tests, the material becomes more viscous as the test temperature increases. This effect is also visible in the non-isothermal tests. It should be considered, that the temperature measurement took place in the temperature chamber and not on the specimen. This has led to a phase shift ϕ . At the beginning of the non-isothermal tests, the stress increases linearly with increasing temperature and increasing strain.

This part of the curve ($t = 40$ [s]) should be understood as a running-in process. In the further course of the stress-time curves, a stress increase (hardening) with phase shift occurs as the temperature decreases. Conversely, when the temperature rises, a decrease in stress (softening) with time delay can be seen. Moreover, a stress decrease with phase shift can be seen when the temperature increases. The phase shift (Fig. 6.19) occurs most significantly at T_1 with faster temperature cycles.

6.5 Numerical simulations

6.5.1 Material model by Chaboche

Investigations published in the paper [105] have shown that additively manufactured PA12 behaves viscoplastically. New phenomena were identified in this work under cyclic loading. This is a completely different behavior of the material, which has so far been analyzed in the FSI (linear-elastic) approach. They include cyclic softening and self-heating. We also observed that pores

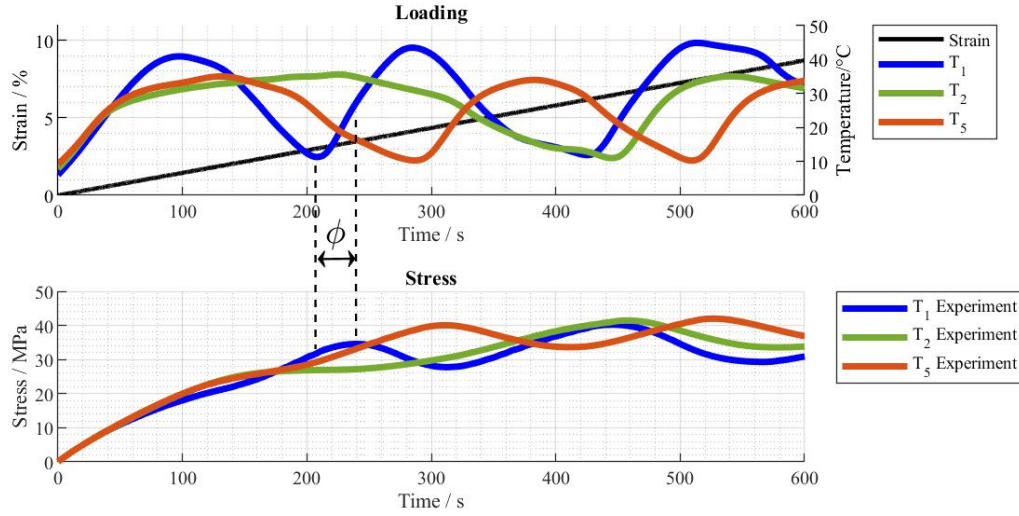


Figure 6.19: Results of non-isothermal tests

do not really close, unless they are actually penny-shaped cracks (with virtually zero thickness). The latter were not observed, see sections 6.4.1 and 6.3.3. Using a classic Chaboche model [109], as was implemented for the static load conditions, it was not possible to simulate the material behavior neither cyclic loading, even accounting for damage. For this reason, the Chaboche model was further modified [110]. The Chaboche model is composed of a differential equation system. The origin of this model is the additive decomposition of the total strain rate $\dot{\epsilon}^{tot}$ (measured strain) into an elastic $\dot{\epsilon}^{el}$ and a viscoplastic $\dot{\epsilon}^{vp}$ part,

$$\dot{\sigma} = E(\dot{\epsilon}^{tot} - \dot{\epsilon}^{vp}) \quad (6.3)$$

with the stress σ and the Young's Modulus E . Here, the definition of the viscoplastic strain rate is decisive. The main focus was to insert the viscoplastic strain rate $\dot{\epsilon}^{vp}$:

$$\dot{\epsilon}_{ij}^{vp} = \lambda \frac{\partial \phi}{\partial \sigma_{ij}}, \text{ with } \lambda = \left(\sigma_{ij} \frac{\partial \phi}{\partial \sigma_{ij}} \right)^{-1} (1 - f) \sigma_M \dot{\epsilon}_M^{vp} \quad (6.4)$$

with the rate of equivalent viscoplastic strain $\dot{\epsilon}_M^{vp}$ and the damage parameter f . The damage parameter f is described in more detail in section 6.5.2 in the light of the phenomena under consideration. The isotropic hardening σ_M describes the extension of the flow surface and is defined by the yield stress σ_y , the viscosity factor K and the viscosity exponent n .

$$\sigma_M = \sigma_y + K(\epsilon_M^{vp})^{1/n} \quad (6.5)$$

$$\epsilon_M^{vp} = \sqrt{\frac{2}{3} \epsilon_{ij}^{vp} \epsilon_{ij}^{vp}} \quad (6.6)$$

The following equation defines the flow function of viscoplastic behavior:

$$\phi = \left(\frac{\sigma_{eq}^{eff}}{\sigma_M} \right)^2 + 2q_1 f^* \cosh \left(\frac{3q_2}{2} \frac{\sigma_m^{eff}}{\sigma_M} \right) - 1 - (q_1 f^*)^2 \geq 0 \quad (6.7)$$

where q_1 , q_2 and f^* are damage parameters which are described in section 6.5.2. Furthermore, the flow function is defined by the effective stress σ_m^{eff} and the von Mises equivalent stress σ_{eq}^{eff} ,

$$\sigma_{eq}^{eff} = \sqrt{\left[\frac{(\sigma_{xx}^r - \sigma_{yy}^r)^2 + (\sigma_{yy}^r - \sigma_{zz}^r)^2 + (\sigma_{zz}^r - \sigma_{xx}^r)^2 + 6((\sigma_{xy}^r)^2 + (\sigma_{yz}^r)^2 + (\sigma_{xz}^r)^2)}{2} \right]} \quad (6.8)$$

$$\sigma_m^{eff} = \left(\frac{\sigma_{xx}^r + \sigma_{yy}^r + \sigma_{zz}^r}{3} \right) \quad (6.9)$$

$$\sigma_{ij}^r = \sigma_{ij} - \alpha_{ij}^* \quad (6.10)$$

$$\alpha_{ij}^* = (1 - f) \sum_{k=1}^2 \alpha_{ij}^{(k)} \quad (6.11)$$

where σ_{ij}^r is the relative stress. Compared to the previous investigation [105], the kinematic hardening α_{ij} was extended. The GTN damage model presented in Section 6.5.2 cannot simulate cyclic softening. An extension of kinematic hardening with the term $-\gamma^{(k)} \varphi^{(k)} \alpha_{ij}^{(k)} \dot{\varepsilon}_M^{vp}$ was used [111, 112]. Hence the kinematic hardening is defined:

$$\dot{\alpha}_{ij}^{(k)} = \frac{2}{3} C^{(k)} \dot{\varepsilon}_{ij}^{vp} - \gamma^{(k)} \varphi^{(k)} \alpha_{ij}^{(k)} \dot{\varepsilon}_M^{vp} - R_{kin}^{(k)} \alpha_{ij}^{(k)} \quad (6.12)$$

$$\varphi^{(k)} = \varphi_{\infty}^{(k)} + (1 - \varphi_{\infty}^{(k)}) \exp(-\omega^{(k)} \varepsilon_M^{vp}) \quad (6.13)$$

$$\dot{\varepsilon}_M^{vp} = \frac{\sigma_{ij}^a \dot{\varepsilon}_{ij}^{vp}}{(1 - f) \sigma_M} \quad (6.14)$$

where C and γ are hardening parameters, R_{kin} denote the static recovery and $\omega^{(k)}$ is a decay constant.

The advanced Chaboche model contains 11 parameters. On the one hand, these were directly adapted to the results of the experiments and, on the other hand, fitted by using an internal optimisation tool, which is described in detail in the papers [107, 108]. It was not possible to simulate the material and damage behavior over the complete number of cycles without using sampling points. The measured temperature development of the test specimens was taken into account. Therefore, parameters were adjusted for three temperature levels based on the measured temperature curve (Fig. 6.17). In the subsequent numerical simulation, the value for the respective parameter is interpolated between the sampling points depending on the actual temperature.

The parameters determined for cyclic test are shown representatively in Table 6.4.

Table 6.4: Temperature-dependent parameters of Chaboche model for cyclic test

Parameter	Unit	$T_1 = 22.59 \text{ }^\circ\text{C}$	$T_2 = 24.506 \text{ }^\circ$	$T_3 = 25.644 \text{ }^\circ\text{C}$	
Young's modulus	E	MPa	1960	1913	1879
Yield stress	σ_y	MPa	2.9185	1.8823	1.8423
Viscosity parameter	K	MPa	8470	49189	49189
Viscosity exponent	n		0.7012	0.65	0.72
Hardening parameter	C_1	MPa	3983.1	3618.3	3611.3
Hardening parameter	C_2	MPa	1545.4	1370.2	1370.2
Hardening parameter	γ_1		309.67	1324.3	1324.3
Hardening parameter	γ_2		1.4312	1.4391	1.4391
Decay constant	ω_1		45.057	45.952	45.952
Decay constant	ω_2		0.98612	0.98612	0.98612
Saturation factor	$\phi_{\infty,1}$		0.38772	0.38619	0.38619
Saturation factor	$\phi_{\infty,2}$		0.99869	0.99869	0.99869
Static recovery	R_{kin}	s^{-1}	0.012256	0.10262	0.10262

Table 6.5 shows the optimized Chaboche material parameters for the isothermal (iso) and non-isothermal (niso) tensile tests. The detailed procedure for determining the parameters for this test has been published in [107].

Table 6.5: Optimized values of the Chaboche model for isothermal (iso) and non-isothermal (niso) tensile tests and constant values of Johnson-Cook approach

	Unit	iso				niso
		10 °C	20 °C	30 °C	40 °C	T_5
E	[MPa]	1674.7	1614	1440.1	1113.9	1561.6
σ_y	[MPa]	21.178	17.579	15.865	5.4149	11.305
C_1	[MPa]	124.36	126.24	137.36	137.263	135.14
C_2	[MPa]	135.48	100.06	163.6	54.217	134.59
γ_1		402	402	402	402	402
γ_2		75.158	75.158	75.158	75.158	75.158
K	[MPa]	2156	6928.3	5116.1	47176	3892.2
n		1.56	1.2818	1.2231	1.0351	1.3726

In this case it is evident that the Young's modulus E and yield point σ_y decrease with increasing temperature. No clear tendency can be seen for parameters C_1 and C_2 . The hardening parameters γ_1 and γ_2 remain constant and are independent of temperature. The viscosity parameter K generally increases with increasing temperature. In comparison, the viscosity parameter n behaves contrary, it decreases with increasing temperature.

6.5.2 Damage model by Gurson-Tvergaard-Needleman (GTN)

As published in paper [105], the virgin samples have a large portion of spherical pores. Due to the cyclic loading, pore growth occurs. The spaces between the voids are also reduced to an extent such that coalescence arises. This coalescence needs to be embedded in the GTN model [115]. So that it takes into account pore growth, nucleation and coalescence, Fig. 6.20.

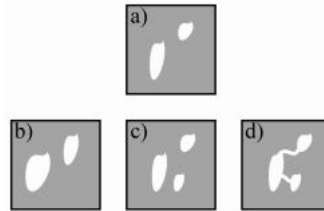


Figure 6.20: Phenomena of void evolution, a) virgin material with voids, b) growth, c) nucleation and d) coalescence of voids

In Eq. 6.7 f^* is the modified void volume fraction, which is applied to model the relationship between loss of material carrying capacity and coalescence.

$$f^* = \begin{cases} f_0 & \text{if } t=0 \\ f & \text{if } f \leq f_c \\ f_c + \frac{\frac{1}{q_1} - f_c}{f_F - f_c} (f - f_c) & \text{if } f_c < f \leq f_F \end{cases} \quad (6.15)$$

The initial porosity f_0 is determined at time $t = 0$. When a critical void volume limit f_c is reached, coalescence occurs. This process continues until a failure value f_F is reached and the material fails. The void volume fraction f is described by the growth f_{growth} and nucleation $f_{nucleation}$ of voids.

$$\dot{f} = \dot{f}_{growth} + \dot{f}_{nucleation} \quad (6.16)$$

$$\dot{f}_{growth} = (1 - f) \dot{\varepsilon}_{ij}^{vp} \delta e_i e_j \quad (6.17)$$

$$\dot{f}_{nucleation} = \frac{f_N (\dot{\sigma}_M + \dot{P})}{S_N^\sigma \sqrt{2\pi}} e^{-\frac{1}{2} \left(\frac{\sigma_M + P - \sigma_N}{S_N^\sigma} \right)^2} \quad (6.18)$$

$$P = \frac{1}{3} \sigma_{ij} \delta e_i e_j \quad (6.19)$$

where f_N is the nucleation porosity, S_N^σ the stress standard deviation, P the hydrostatic stress, $\delta e_i e_j$ unit tensor and σ_N the mean stress. The model considers kinematic hardening. Table 6.6 shows the parameters used for numerical simulation. The initial porosity f_0 was assumed from the previous investigation, [105]. The numerical simulation of the material and damage

Table 6.6: Temperature-dependent parameter of GTN model for test 2

Parameter	Unit	$T_1 = 22.5^\circ\text{C}$	$T_2 = 24.5^\circ\text{C}$	$T_3 = 25.6^\circ\text{C}$
1. Tvergaard-Needleman constant	q_1	1.1378	1.0229	1
2. Tvergaard-Needleman constant	q_2	0.9006	0.75419	0.5
Initial porosity	f_0	0.047	0.047	0.047
Nucleation porosity	f_N	0.03	0.03	0.03
Critical porosity	f_c	0.15	0.15	0.15
Failure porosity	f_F	0.8	0.8	0.8
Mean stress	σ_N MPa	0	0	0
Stress standard deviation	S_N^σ	0.09997	0.09997	0.09997

behavior was carried out by implementing the Chaboche and GTN model in Matlab.

Table 6.7 shows the optimized GTN damage parameters for the isothermal (iso) and non-isothermal (niso) tensile tests. The detailed procedure for determining the parameters for this test has been published in [107].

Table 6.7: Optimized values of the GTN model for isothermal (iso) and non-isothermal (niso) tensile tests and constant values of Johnson-Cook approach

Unit	iso				niso
	10 °C	20 °C	30 °C	40 °C	T_5
q_1	2.014	0.9875	1.7575	0.621	1.6692
q_2	1.0907	1.999	0.59146	0.5478	1.414
f_0	0.047	0.047	0.047	0.047	0.047
f_f	0.25	0.4740	0.25844	0.295	0.3352
f_c	0.160	0.1146	0.16383	0.170	0.1593
S_N	0.06	0.0002	0.0497	0.0019	0.0241
f_N	0.233	0.0019	0.13219	0.162	0.22
d					0.4267
T_m [°C]					135
T_0 [°C]					9.05

Figure 6.21 shows the temperature dependence of the damage parameters. A normalized diagram was chosen in order to compare the influence of temperature more effectively. It can be seen that all three damage parameters decrease with increasing temperature.

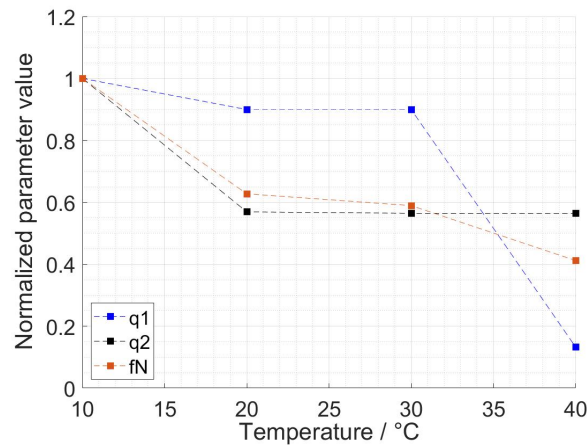


Figure 6.21: Temperature dependence of damage parameters q_1 , q_2 , and f_N

If the temperature increases from 10 °C to 20 °C, the temperature influence of q_2 and f_N is highest. Between 20 °C and 30 °C, all parameters are constant. If the temperature is increased further to 40 °C, the temperature dependence of q_1 is very significant. Thus it can be clearly shown that the damage parameters are temperature-dependent and are decisive for the simulation of the damage behavior.

6.6 Application of models

6.6.1 Cyclic test

As already described in Section 6.5, an internal optimization tool was used to fit the parameters of the material and damage model. Fig. 6.22 shows the result of the numerical simulation compared to experimental results. The envelope curves of the simulated and measured maximum and minimum stress match well. This implies that the Chaboche model can be used to describe cyclic softening.

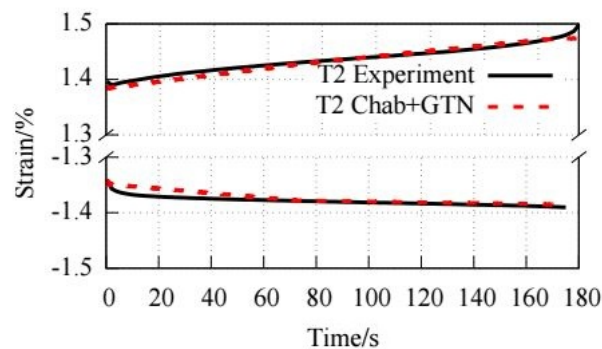


Figure 6.22: Cyclic softening, minimum and maximum strain values over time [106]

In addition, three separate cycles were selected to test whether the material behavior can be mapped using the Chaboche model. Fig. 6.23 shows an excellent agreement for all three time ranges.

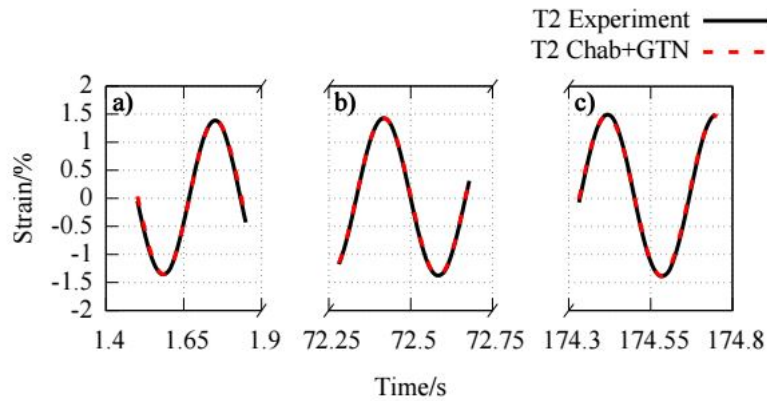


Figure 6.23: Validation of test 2 of different cycles, a) 5th cycle, b) 217th cycle (half lifetime) and c) 522th cycle (when fracture occurs) [106].

By coupling the material model of Chaboche with the GTN damage model, it is possible to cover the time of rupture correctly, Fig. 6.23 (right, last cycle).

6.6.2 Isothermal tests

The determined parameters of Section 6.5 constituted the basis for the numerical simulation. In this section the results of the isothermal tensile tests are shown first. The influence of the damage parameters f_N , q_1 , and q_2 is discussed in more detail in [107]. Finally the results of the non-isothermal tests are presented. For all numerical tests, $f = f_F$ is the failure criterion.

Figure 6.24 shows the results of the numerical simulations compared to experimental results for the isothermal tensile tests. The analysis the stress-strain curves obtained for different temperatures, a decrease in stiffness and yield strength for the printed polyamide PA12 can be observed for the temperature of 40 °C in relation to the temperature of 10 °C. Analyzing the elongation of the sample for the temperature of 40 °C is more than twice as high as for the temperature of 10 °C. With the change of mechanical properties of PA12 for different temperatures, it was necessary to determine new parameters of material models. The numerical stress-strain curves match well for all temperature levels with the experimental results.

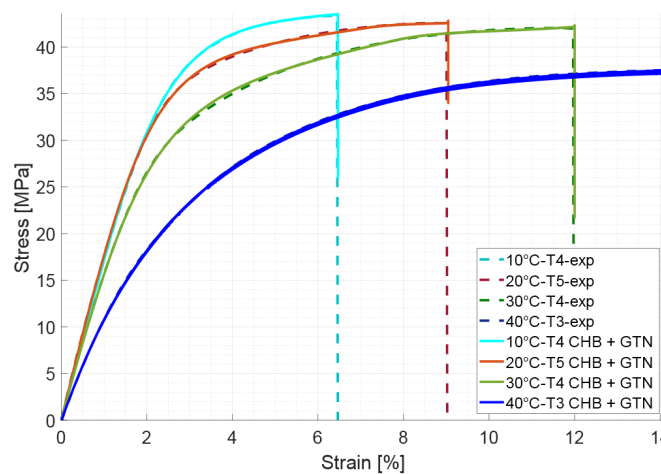


Figure 6.24: Comparison of numerical and experimental results of isothermal tensile tests

With the selected material model of Chaboche and the GTN damage model it is possible to re-

produce the material and damage behavior of additively manufactured PA12 at different isothermal temperature levels. Further simulations were carried out to investigate the influence of the damage parameters in more detail. One of the three parameters was selected and doubled or halved and compared with the optimized curve. As reference the stress-strain curve from the isothermal tests at 10 °C was chosen.

6.6.3 Non-isothermal tests

Considering the Johnson-Cook approach it is possible to model the material and damage behavior under non-isothermal test conditions, Fig. 6.25 . The parameters were adapted to test T_5 . The maximum deviation between experimental and numerically calculated stress is 0.38 MPa. The numerical stress-time curves of tests T_1 and T_2 also match excellently with the experimental results. For the tests T_1 and T_2 the deviations are 2.76 MPa and 3.83 MPa. This represents a relative deviation x of the maximum experimental stress of $x_{T_1} = 9.52 \%$ and $x_{T_2} = 6.8 \%$

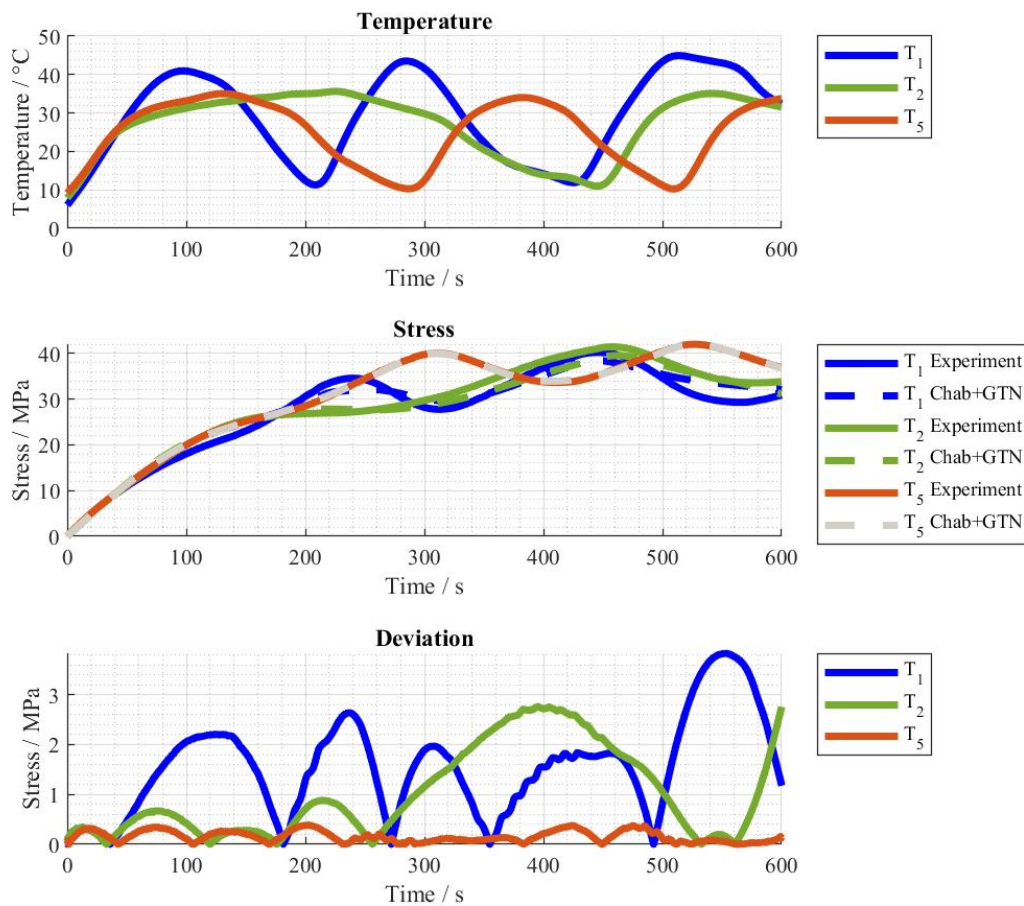


Figure 6.25: Influence of temperature change on stress during tensile test

6.7 Concluding remarks

This chapter describes both the numerical modelling and experimental investigation of additively manufactured polyamide PA12:

- under isothermal and non-isothermal quasi-static tensile loads
- under cyclic loading based on experimental investigations of the microstructure

The main goal of this research was to understand the mechanics of the new printed materials and to develop numerical models describing their behavior and damage process. This process required many complex experiments and tests. It was also necessary to develop a new numerical modeling approach. As described above, the tested 3D printed material has viscoelastic and viscoplastic properties. In addition, the results of microstructure studies show porosity. Therefore, the Chaboche and GTN models were chosen for the description. For cyclic test has shown that by extending the Chaboche- and GTN-model also the material and damage behavior under cyclic loading can be modelled.

New phenomena were observed due to cyclic loading. One effect is cyclic softening. This was considered numerically by the extension of the Chaboche model and led to excellent agreement between experiment and simulation. Furthermore, the self-heating of the samples was considered in the numerical simulation by temperature support points. The determined parameters are interdependent. This means that it is possible to obtain similar results with a modified parameter set. In order to exclude this variability in the future, the parameter set has to be validated by further tests and changes in the test conditions. An investigation of the material and damage behavior under shear load would be beneficial and contributes to the validation of the parameters.

Microstructural investigations have shown that spherical and non-spherical pores occur inside of the material and that the surface has a high roughness due to the manufacturing process. Despite the fact that the GTN model does not take into account any non-spherical pores, a good agreement has been shown with experiments. These parameters are necessary for the simulation process of real geometries used in the construction of aircraft structures. These tests will serve to expand the FEA structural code taking into account the non-flexible behavior of the structure with damage.

For the isothermal tensile tests at different temperature levels a definite temperature dependence of both material and damage parameters could be analyzed and the necessity of parameter optimisation for each temperature level could be shown. In the non-isothermal tensile tests, the challenge was to be able to map the material and damage behavior with one set of parameters. This was successfully achieved by extending the Chaboche model by the Johnson-Cook approach. A good correlation between the numerical simulation and the experimental results was achieved. In summary, it can be stated that the material model of Chaboche including the Johnson-Cook extension and the GTN damage model can be used for PA12 under isothermal and non-isothermal tensile loads and that it represents all occurring phenomena. The presented model does not yet consider exclusive splitting of the thermal strain. For this purpose, the coefficient of thermal expansion will be determined in the future. Due to the large number of parameters, it is recommended to carry out a sensitivity analysis in the future.

Chapter 7

Summary

The presented postdoctoral dissertation is devoted to research on the impact of FSI for selected cases of structural models and development of suitable simulations algorithms. Despite the simple formulation of the phenomena of interaction, numerical simulations of the structural-flow coupling is a complex issue. Even if a number of simplifications concerning both the flow domain (e.g. inviscid flow) and the structural domain (e.g. linear model) have been adopted, modeling this type of phenomena involves solving a number of physical and numerical problems. The growing sector of air transport, in combinations with increasing requirements on engineering design solutions and higher degree of complexity involves phenomena of interaction playing a more important role in future developments. An example of such phenomena are the structure-flow interactions.

With the development of new computer techniques, modeled discrete systems can more and more reflect continuous systems close to reality. One of the assumptions bringing the physical model closer to the numerical one is taking the nonlinear properties of the structure into account. The main purpose of the work was to analyze the behavior of the structural model under the influence of aerodynamic load. Initially, an approach was used in which the material of the structure model exhibits linear properties. The actual configuration of an aircraft obtained in cooperation with the Institute of Aviation in Warsaw was selected as a demonstrator for the research.

The Iryda I-22 aircraft was used as a test case to check the possibility and correctness of the operation of individual numerical tools. The calculations were carried out for various variants of the mass distribution of the aircraft. The results were presented in the form of diagrams of displacement and angle of rotation for the wings, vertical and horizontal stabilizers of the aircraft. Additionally, an analysis of the damping coefficients of individual vibration modes was carried out in order to investigate the flutter phenomenon. As part of the work, the existing aeroelastic system was expanded with the possibility of calculations taking the nonlinear properties of the structural model into account. It should be emphasized that the developed calculation algorithm is fully three-dimensional and designed for computational parallelization systems. It is based on numerical tools that are standard in modern CFD technology and, therefore can find direct application in the analysis of real objects. The use of the possibilities of such a system, along with the possibility of a full analysis of the non-linear structure developed in this work is of significant practical importance. The accuracy of the calculations for the structural-flow coupling system was checked by comparing the obtained results with the experimental data.

The results were checked for linear and non-linear configurations by analyzing the NACA 0012 profile. A fully non-linear formulation was also used in the research of the flexible delta wing. In the case of the existing experimental studies, good agreement of the computational model and the results of the experiment was obtained. This confirmed the usefulness of the algorithm for further research and practical applications. As a result of the simulations, differences between the linear and non-linear approach were found. The nature of the aeroelastic phenomena of the body

exposed to the fluid is fundamentally changing by the applied modeling approach. Damage to take into account the nonlinear properties of structural models results in other responses and phenomena. This fact is more and more often reflected in additional experimental research and works on the development of aeroelastics. Alternative materials are playing an increasingly important role in currently applied design concepts for aircraft structures. Especially in the construction of the more and more commonly used unmanned aerial vehicles (UAV), 3D printed materials are a key element that affects the basic parameters. Until the 2010s, the research was typically conducted and the aeroelastic calculation algorithm for commonly used materials mainly in the linear range was developed. A deeper analysis of the interaction between fluid and structure in relation to the non-linear properties of the material was conducted in terms of the hyperelastic behavior of the structure. The current development of light weight materials, and the increasing widespread use of 3D printing technology is causing the increasing use of new materials in the aviation industry. This applies particularly to the design and construction of unmanned aerial vehicles, where the basic requirements are lightweight design and maximum range.

Unfortunately, meeting the above criteria means that the materials are often used not only in a elastic range. In case of FSI investigated above the elastic limit, damage mechanics to be considered in the material modeling as well. The damage process in view of such dangerous phenomena as flutter (aircraft construction) requires a separate material modeling process and the analysis of the damage process. The author began cooperation with BTU Cottbus-Senftenberg in a team, which different modeling approaches for manufacturing materials based on an experimental testing regime to develop the new numerical tools to describe mechanical properties. An important point of the research is the development and use of advanced material models (Chaboche, Bodner-Partom) and damage models (Gurson Tvergaard Needleman). The conducted tests of material behavior were carried out in particular for cyclic loading of the structure, which is most often occurring in FSI calculations. The results of the research where the author participated were published in joint papers [105–107] and [108] included in the bibliography.

Bibliography

- [1] Albano E., Rodden W. P., "A doublet-lattice method for calculating the lift distribution on oscillating surfaces in subsonic flow," AIAA Journal, Vol. 7, No. 2 DOI = <https://doi.org/10.2514/3.5086> 1969.
- [2] Arnoldi W. E., "The principle of minimized iterations in the solution of the matrix eigenvalue problem", Quarterly of Applied Mathematics, volume 9, pages 1729, 1951.
- [3] Ashley H., Zartarian G., "Piston theory - a new aerodynamic tool for aeroelastician" J. Aero Sciences, Vol. 23, No. 12, 1956.
- [4] Attorni A., Cavagna L., Quaranta G., "Aircraft T-tail flutter predictions using computational fluid dynamics", Journal of Fluids and Structures, 27, p. 161-174, 2011.
- [5] Batina J., "Unsteady Euler spring method for three-dimensional unstructured dynamic meshes", AIAA Paper 89-0150, 1989.
- [6] "3dprintingindustry", <https://3dprintingindustry.com/>
- [7] Bourke P., "Polygonising a scalar field" <http://paulbourke.net/geometry/polygonise/> May, 1994.
- [8] Beckley D.A., Evans M.W., Raman, V.K., "Multikey Retrieval from K-d Trees and Quad-Trees", ACM, 1985.
- [9] Cozac I., "Shepard method - from approximation to interpolation", Studia Univ. "Babes-Bolyai", Mathematica, Vol. XLVIII, no. 2, June 2003.
- [10] Cullum J., Willoughby R., "Lanczos algorithms for large symmetric eigenvalue computations", Vol. 1, ISBN 0-8176-3058-9(v.1)
- [11] Dat R, Meurzec JL., "Sur les calculs de flottement par la method dite du "balayage" en frequence reduite", La Recherche Aerospaciale 133, 1969.
- [12] "Description of DLR TAU-code", 2006.
- [13] Donea J., Huerta A., Ponthot J.-Ph., Rodriguez-Ferran A., "Arbitrary Lagrangian-Eulerian methods", Encyclopedia of Computational Mechanics, John Wiley & Sons Ltd., 2004.
- [14] DLR, "Tau-Code user guide", revision 1.24, Stuttgart, 2004.
- [15] DLR, "Tau-Code technical documentation", Stuttgart, 2004.
- [16] "EDGE theoretical formulation", FOI, Swedish Defence Research Agency, 2007.
- [17] Eick S. G., "Graphically displaying text", Journal of Computational and Graphical Statistics, Vol. 3 1994.

- [18] Eilasson P., "EDGE A Navier-Stokes solver for unstructured grids", FOI, Swedish Defence Research Agency, 2001.
- [19] Ekstrom S.-E., Berggren M., "Agglomeration Multigrid for the vertex-centered dual discontinuous Galerkin method", ADIGMA, NNFM 113, pp 301-308, 2010.
- [20] Farhat C., Geuzaine P., Brown G., "Application of a three-field Non-linear Fluid-Structure formulation to the prediction of the aeroelastic parameters Of An F-16 Fighter", Elsevier Science Ltd., 2002.
- [21] Farhat C., Geuzaine P., Grandmont C., "The discrete geometric conservation law and the nonlinear stability of ALE schemes for the solution of flow problems on moving grids", Journal of Comput. Phys. 174 pp 669-694 2001.
- [22] Franhofer SCAI, "MpCCI 4.0.0-0 documentation", Sankt Augustin, 17 September 2009.
- [23] Franhofer SCAI, "Specification of MpCCI version 2.0", Sankt Augustin, 2003.
- [24] Friedman J.H., Bentley J.L. and Finkel R.A., "An Algorithm for finding best matches in logarithmic expected time", Transactions on Mathematical Software, 3, 209-226, ACM, 1977.
- [25] Friendly M., "Milestones in the history of thematic cartography, statistical graphics, and data visualization", Report of Grant OGP0138748 July 5, 2006.
- [26] Fung, Y.C., "An introduction to the theory of aeroelasticity", Dover, ISBN 978-0486678719, 1994.
- [27] Hodges D.H., Pierce G. A., "Introduction to structural dynamics and aeroelasticity", Cambridge University Press, 2011.
- [28] Gerhold T., Friedrich O., Evans J., Galle M., "Calculation of complex three-dimensional configuration employing the DLR-TAU Code", AIAA.
- [29] Giergiel J., Uhl T., "Identification of mechanical systems", PWN, Warsaw 1990.
- [30] Hamming R. W., "Numerical methods for scientists and engineers", ISBN 0-486-65241-6 Dover Publications Inc., New York, 1986.
- [31] Hassig HJ, "An approximate true damping solution of the flutter equation by determinant iteration", J Aircraft, 1971.
- [32] Kamakoti R., Shyy W., "Fluid-structure interaction for aeroelastic applications", Elsevier Ltd., 2005.
- [33] Kovalev K., "Unstructured hexahedral non-conformal mesh generation", PhD Thesis, Vrije Universiteit Brussel, 2005.
- [34] Kruszewskiego J., "Metody elementów skończonych w dynamice konstrukcji", Wydawnictwo Arkady, Warszawa, 1984.
- [35] Lee-Rausch M. E., Batina J. T., "Wing flutter boundary prediction using an unsteady Euler aerodynamic method", NASA Technical Memorandum 107732, Langley Research Center, March 1993.
- [36] Lesoinne M, Farhat C., "Stability analysis of dynamic meshes for transient aeroelastic computations", AIAA Paper no. 93-3325, 11th AIAA Computational Fluid Dynamics Conference, 1993.

- [37] Li Z., "Parallel computations of 3d unsteady compressible Euler equations with structural coupling", Indianapolis, 2002.
- [38] Lorenson W. E., Cline H. E., "Marching Cubes: A high resolution 3D surface construction algorithm", Computer Graphics Proceedings of SIGGRAPH '87, Tom 21, Nr 4, ACM, New York, 1987.
- [39] Löhner R., "Applied computational fluid dynamics techniques: an introduction based on finite element methods", ISBN 978-0-470-51907-3, West Sussex, John Wiley & Sons Ltd., 2008.
- [40] Lynch D., O'Neill K., "Elastic grid deformation for moving boundary problems in two space dimensions", Finite Elements in Water Resources, University of Mississippi, 1980.
- [41] Posadzy P., "Modelowanie i analiza zjawisk aeroelastycznych w zastosowaniu do praktycznych zagadnień przepływowych", PhD-thesis, Poznan University of Technology 2007.
- [42] Posadzy P., Morzynski M., "Deliverable D5.2-24 - final report on functionality of the implemented generic CSM code (Milestone M8)", Poznan, August 2004.
- [43] Morzynski M., Nowak M., red. "Contemporary calculation methods in aeroelasticity for the complete configuration of the aircraft", Book Poznan University of Technology Poznan, 2016.
- [44] Press W., Teukolsky S., Vetterling W., Flannery B., "Numerical recipes. The art of scientific computing", 3rd Edition, ISBN 0-521-88068-8 2007.
- [45] Robinson B. A., Batina J. T., Yang H. T. Y., "Aeroelastic analysis of wings using the Euler Equations with a deforming mesh", NASA Technical Memorandum 102733, Langley Research Center, November 1990.
- [46] Rossow C.-C., Kroll N., Schwamborn D., "The MEGAFLOW project - numerical flow simulation for aircraft", 2006.
- [47] Roszak R., "Modelowanie sprzeżenia strukturalno-przepływowego z uwzględnieniem wybranych zagadnień nieliniowych", Poznań, 2006.
- [48] Roszak R., Posadzy P., Stankiewicz W., Morzyński M., "Fluid-structure interaction for large scale complex geometry and non-linear properties of structure", Arch. Mech., 61, 1, pp. 3-27, Warszawa, 2009.
- [49] Smith J., "Aeroelastic functionality in edge. Initial implementation and validation", FOI, Swedish Defence Research Agency, 2005.
- [50] Tor-Magne Stien Hagen, "Interactive visualization on high-resolution tiled display walls with network accessible compute- and display-resource", Rozprawa Doktorska, Maj 2011.
- [51] Zienkiewicz O.C., Taylor R.L. "The finite element method, vol. 1: The basis", Fifth edition, Barcelona, Butterworth-Heinemann, ISBN 0-7506-5049-4, 2000.
- [52] Posadzy P., Morzynski M. "Deliverable D5.2-24 - final report on functionality of the implemented generic CSM code (Milestone M8)", Poznan University of Technology, 2004.
- [53] Kamakoti R., "Computational aeroelasticity using a pressure-based solver", University of Florida, 2004.

- [54] Posadzy P., "The modelling and analysis of aeroelasticity phenomena in practical flow applications", Poznan University of Technology, 2007.
- [55] Bisplinghoff R.L., Ashley H., Halfman R.L., "Aeroelasticity", Addison Wesley, Reading, MA, 1955.
- [56] Atluri S.N., Shen S., "The Meshless local Petrov-Galerkin (MLPG) method: a simple less-costly alternative to the finite element boundary element Method", *Computer Modeling in Engineering Sciences*, 3, 1, 11-52, 2002.
- [57] Guruswamy G. P., Byun C., "Fluid-structure interactions using Navier-Stokes flow equations coupled with shell finite element structures", 24th Fluid Dynamics Conference, Orlando, FL, AIAA-93-3087 1993.
- [58] Atluri S.N., Shen S., "The meshless local Petrov-Galerkin (MLPG) method", *Computer Modeling in Engineering and Sciences* 3, 11-52, 2002.
- [59] Farhat C., Lesoinne M., "Two efficient staggered algorithms for the serial and parallel solution of three-dimensional nonlinear transient aeroelastic problems", *Comput. Methods Appl. Mech. Engrg.*, 182, pp. 499–515, 2000.
- [60] Roszak R., "Fluid-structure interaction for nonlinear property of structural models", Poznan University of Technology, PhD Thesis, 2006.
- [61] Bjornsson P., Danielsson H., "Strength and creep analysis of glued rubber foil timber joints", Lund University, Sweden, 2005.
- [62] Steger J.L., Bailey E., "Calculation of transonic aileron buzz", *AIAA Journal*, 18, 3, 249-255, 1980.
- [63] Szelag D., Lorenc Z., Fornasier L., Posadzy P., "A digitally controlled suspension system for the real time generation of the structural nonlinearities in the flutter wind tunnel validation testing ", *Proceedings of the International Forum on Aeroelasticity and Structural Dynamics*, Munich, Germany, 2004.
- [64] Rychlik M., Niezgodka M., Hausa H., Kotecki K. "Development of a computer CAD geometry of an aircraft model for flutter tests using reverse engineering techniques", *Works of the Aviation Institute 220*, 125-134, ISSN 0509-6669, Warsaw, 2011.
- [65] Roszak R., Rychlik M., Stankiewicz W., Kotecki K., Hausa H., Morzynski M., Nowak M. "Aeroelastic computations for aircraft model for flutter analysis based on GVT model", *Works of the Aviation Institute 220*, 148-160, ISSN 0509-6669, Warsaw, 2011.
- [66] Kotecki K., Hausa H., Goluchowski B., Niezgodka M., Roszak R., Stankiewicz W., Rychlik M., Morzynski M., Nowak M. "The design of numerical structural model for aeroelastic computations of aircraft's flutter model", *Works of the Aviation Institute 220*, 135-147, ISSN 0509-6669, Warsaw, 2011.
- [67] Krzymien W. "Dynamically similar models of airplanes and their role in aeroelastic properties tests", *Works of the Aviation Institute 220*, 59-69, ISSN 0509-6669, Warsaw, 2011.
- [68] Krolkowski R., Lenort F., Niepokolczycki A. "The demonstration of the method for quick estimation of the aircraft wind tunnel tests", *Works of the Aviation Institute 220*, 161-185, ISSN 0509-6669 Warsaw, 2011.

- [69] Krolikowski R., Lenort F., Niepokolczycki A. "Demonstration of a quick estimation of the aero-elastic properties of an airplane during tests in a wind tunnel", Works of the Aviation Institute 220, 84-124, ISSN 0509-6669 Warsaw, 2011.
- [70] Hansen J. R. "A History of the langley aeronautical laboratory", NASA SP-4305, 1917- 1958
- [71] Rowley C., Mezić I., Bagheri S., Schlatter P., and Henningson D. "Spectral analysis of non-linear flows", *J. Fluid Mech.* 641, 115-127 2009.
- [72] Jovanovic R., Schmid P. J., Joseph, and Nichols W. "Sparsity-promoting dynamic mode decomposition", *Phys. Fluids* 26, 2014.
- [73] Gorniewicz L., Ingarden R. L. "Analiza matematyczna dla fizyków", Wydawnictwo Naukowe Uniwersytetu Mikołaja Kopernika Book ISBN: 978-83-231-2924-0 Torun, 2012.
- [74] Bazilevs Y, Calo V. M., Zhang Y., Hughes T.J.R., "Isogeometric fluid-structure interaction analysis with applications to arterial blood flow", *Computational Mechanics* 1432-0924 2006, doi = 10.1007/s00466-006-0084-3.
- [75] Noack B., Stankiewicz W., Morzynski M., Schmid P. "Recursive dynamic mode decomposition of transient and post-transient wake flows", *Journal of Fluid Mechanics*, 809, 843-872, 2016, doi = 10.1017/jfm.2016.678
- [76] Stankiewicz, W., Morzynski, M., Kotecki K., Roszak R., Nowak M., "Modal decomposition based global stability analysis for reduced order modeling of 2D and 3D wake flows", *Numerical Methods in Fluids*, 81, 178-191, 2015, doi = 10.1002/flid.4181
- [77] Roszak R., Stankiewicz W., Morzynski M., Nowak M., Rychlik M., Hausa H., Kotecki K. "Computational and experimental investigation of aeroelasticity for the flutter aircraft model", *World Academy of Science, Engineering and Technology* 67, 7-14, 2012,
- [78] Rychlik M., Roszak R., Morzynski M., Nowak M., Hausa H., Kotecki K. "Preparation of computer model of the aircraft for numerical aeroelasticity tests flutter", *World Academy of Science, Engineering and Technology*, 67, 1-7, 2012, doi = doi.org/10.5281/zenodo.1056330
- [79] Appa K., "Finite-surface spline", *Journal of Aircraft*, 26, 495-496, 1989.
- [80] Wisniowski W., "Resonance tests of flying objects - method and analysis of results", Works Institute of Aviation, 7 2010 ISSN 0509-6669
- [81] "Technology development for aeroelastic simulations on unstructured grids, Fifth E.U. Framework Programme", G4RD-CT-2001-00403, <http://cordis.europa.eu>.
- [82] Harder R.L., Desmaris R.N., "Interpolation using surface splines", *Journal of Aircraft*, 9, 2, 189-191, 1972.
- [83] Farhat C., Lesoinne M., "Two efficient staggered algorithms for the serial and parallel solution of three-dimensional nonlinear transient aeroelastic problems", *Comput. Methods Appl. Mech. Eng.*, 182, 499-515, 2000.
- [84] Benson D.J., Hallquist J.O., "A single surface contact algorithm for the post-buckling analysis of shell structures", *Comput. Methods Appl. Mech. Eng.*, 78, 141-163, 1990.
- [85] Maman N., Farhat C., "Matching fluid and structure meshes for aeroelastic computations", *Computers and Structures*, 54, 4, 779-785, 1995.

- [86] Löhner R., "Some useful data structures for the generation of unstructured grids", *Applied Numerical. Math*, 4, 123-135, 1988.
- [87] Kuo Y., Hwang S.-Y., Hu H., "A data structure for fast region searches", *IEEE design and test of computers*, 6, 5, 20-28, 1989.
- [88] Knuth D., "Sorting and searching. The art of computer programming, vol. 3", Addison-Wesley, Massachusetts, 1973.
- [89] "Mesh-based parallel Code Coupling interface". MpCCI 2.0 User Guide Fraunhofer Institut Algorithmen und Wissenschaftliches Rechnen October 23, 2003
- [90] Asano T., Edahiro M., Imai H., Iri M., Murota K., "Practical use of bucketing techniques in computational geometry", 1985, 153-195, *Computational Geometry, Vol. 2: Machine Intelligence and Pattern Recognition*, North-Holland, Amsterdam, ed. Toussaint G.T.
- [91] Farhat C., Degand C., Koobus B., Lesoinne M., "Torsional springs for two-dimensional dynamic unstructured fluid mesh", *Comput. Methods Appl. Mech. Engg.*, 163.
- [92] Farhat C., Pierson K., Degand C., "CFD based simulation of the unsteady aeroelastic response of a maneuvering vehicle", *AIAA Journal*, 2000-0899, 2000.
- [93] Fornasier L., Rieger H., Tremel U., van der Weide E., "Time-dependent aeroelastic simulation of rapid manoeuvring aircraft", *AIAA Paper*, 949, 2002.
- [94] "Reduced-order-model approach for aeroelastic analysis involving aerodynamic and structural nonlinearities", Munteanu S., Rajadas J., Nam C., Chattopadhyay A., *AIAA Journal*, 43, 3, 560-571, 2005.
- [95] "Aeroelastic model reduction for affordable computational fluid dynamics-based flutter analysis" Kim T., Hong M., Bhatia K.G., SenGupta G., *AIAA Journal*, 43, 12, 2487, 2005,
- [96] "A high dimensional harmonic balance approach for an aeroelastic airfoil with cubic restoring forces", Liu L., Dowell E.H., Thomas J.P., *Journal of Fluids and Structures*, 23, 3, 351-363, 2007,
- [97] "A hierarchy of low-dimensional models for the transient and post-transient cylinder wake", Noack B.R., Afanasiev K., Morzynski M., Tadmor G., Thiele F., *Journal of Fluid Mech.*, 497, 335-363, 2003.
- [98] "Structural non-linearities and the nature of the classic flutter instability", Coller B.D., Chamara P.A., *Journal of Sound and Vibration*, 277, 4-5, 711-739, 2004.
- [99] "Supercritical as well as subcritical Hopf bifurcation in nonlinear flutter systems", Chen Y., Liu J., *Applied Mathematics and Mechanics*, 29, 2, 199-206, 2008.
- [100] "Aeroelastic analysis of transonic wings using Navier-Stokes equations and a nonlinear beam finite element model", Garica J. A., Gurusway G. P., *AIAA Journal*, 99 1215 1999
- [101] "Fluid-structure interactions using Navier-Stokes flow equations coupled with shell finite element structures", Guruswamy, G. P., Byun, C., *AIAA Journal*, 93 3087 1993
- [102] Heinze S. "Aeroelastic concepts for flexible wing structures", KTH PhD Thesis ISBN 978-91-7178-706-4 KTH Sweden 2005

- [103] "Automatic control systems", Benjamin C. Kuo, M. F. Golnaraghi, John Wiley & Sons, New York, 2003
- [104] Ziółkowski, G., Chlebus, E., Szymczyk, P., Kurzac, J., "Application of X-ray CT method for discontinuity and porosity detection in 316L stainless steel parts produced with SLM technology", *Archives of Civil and Mechanical Engineering* 14, 4, 608–614, 2014.
- [105] D. Schob, R. Roszak, I. Sagradov, H. Sparr, M. Ziegenhorn, A. Kupsch, F. Léonard, B.R. Müller, G. Bruno, "Experimental and numerical simulation of material and damage behaviour of 3D printed polyamide 12 under quasi-static loading", *Archives of Mechanics*, 71, 4-5, 507-526, 2019, doi = 10.24423/aom.3162.
- [106] D. Schob, R. Roszak, I. Sagradov, H. Sparr, M. Ziegenhorn, A. Kupsch, F. Léonard, B.R. Müller, G. Bruno, "Experimental determination and numerical simulation of material and damage behaviour of 3D printed polyamide 12 under cyclic loading", *Engineering Fracture Mechanics*, 229, 4-5, 507-526, 2020, doi = 10.1016/j.engfracmech.2019.106841
- [107] R. Roszak, D. Schob, I. Sagradov, K. Kotecki, H. Sparr, P. Maasch, R. Franke, M. Ziegenhorn. "Experimental determination and numerical simulation of temperature dependent material and damage behaviour of additively manufactured polyamide 12", *Mechanics of Materials*, 159, 103893-1 - 103893-8 2021, doi = 10.1016/j.mechmat.2021.103893
- [108] G. Ziolkowski, K. Gruber, E. Tokarczuk, R. Roszak, M. Ziegenhorn. "X-ray Computed Tomography for the ex-situ mechanical testing and simulation of additively manufactured IN718 samples", *Additive Manufacturing*, 45, 102070-1 - 102070-21 2021, doi = 10.1016/j.addma.2021.102070
- [109] Chaboche, J.-L., "Constitutive equations for cyclic plasticity and cyclic viscoplasticity", *International Journal of Plasticity* 5, 3, 247-302, doi = 10.1016/0749-6419(89)90015-6.
- [110] Chaboche, J. L., "A review of some plasticity and viscoplasticity constitutive theories", *A review of some plasticity and viscoplasticity constitutive theories*, 24, 10, 1642-1693, doi = 10.1016/j.ijplas.2008.03.009.
- [111] Kuna, M., "Numerische Beanspruchungsanalyse von Rissen", *Finite Elemente in der Bruchmechanik Springer Book* 2008, doi = 10.1007/978-3-8348-9285-0.
- [112] Lemaitre, J., Chaboche, J. L., "Mechanics of solid materials", Cambridge University Press, 1990, doi = 10.1017/CBO9781139167970.
- [113] M. Gologanu and J.-B. Leblond and J. Devaux, "Approximation models for ductile metals containing non-spherical voids - case axisymmetric prolate ellipsoidal cavities", *Journal Mech. Phys. Solids*, 41, 11, 1723-1754, 1993, doi = 10.1016/0022-5096(93)90029-F.
- [114] V. Monchiet, G. Bonnet, "Gurson-type model accounting for void size", *International Journal of Solids and Structure* 50, 320-327, 2013, doi = 10.1016/j.ijsolstr.2012.09.005
- [115] "Analysis of the cup cone fracture in a round tensile bar" V. Tvergaard, A. Needleman, *Acta Metallurgica* 32, 1, 1984, doi = 10.1016/0001-6160(84)90213-X.
- [116] A.K. Asraff, S. Sheela, R. Jacob, K. Jayamani, S. Sarath, C. Nair, J. Cycric. "Structural integrity assessment - modelling of low cycle fatigue failure through damage mechanics" *Proceedings of ICONS 2018*, 2020, doi = 10.1007/978-981-13-8767-8-6.

- [117] J. Besson, C. Guillemer-Neel, "An extension of the Green and Gurson models to kinematic hardening" *Mechanics of Materials*, 35, 1-18, 2003, doi = 10.1016/S0167-6636(02)00169-2.
- [118] A. M. Forster, "Materials testing standards for additive manufacturing of polymer materials" *Additive Manufacturing*, 2015, doi = 10.6028/NIST.IR.8059.
- [119] DIN Deutsches Institut für Normung e.V. "DIN EN ISO 527-2: Kunststoffe - Bestimmung der Zugeigenschaften: Teil 2: Prüfbedingungen für Form- und Extrusionsmassen", 2012.
- [120] R. Franke and D. Schob and M. Ziegenhorn, "Test method and numerical simulation mechanical properties of 3D-printed thermoplastics", *Additive Fertigung von Bauteilen und Strukturen* 137-158, 2017, doi = 10.1007/978-3-658-17780-5-9.
- [121] M.P. Hentschel, K.-W. Harbich, D. Ekenhorst, J. Schors, "Röntgentopographie der Faser- und Polymerorientierung", *Materialprüfung*, 39, 121-123, 1997.
- [122] A. Kupsch, A. Lange, M.P. Hentschel, Y. Onel, T. Wolk, A. Staude, K. Ehrig, B.R. Müller, G. Bruno, "Evaluating porosity in cordierite-based diesel particulate filter materials. Part 1- X-ray refraction", *Journal of Ceramic Science and Technology* 4, 169-176, 2013, doi = 10.4416/JCST2013-00021.
- [123] A. Kupsch, B.R. Müller, A. Lange, G. Bruno, "Microstructure characterization of ceramics via 2D and 3D X-Ray refraction techniques", *Journal of the European Ceramic Society*, 37, 5, 1879-1889, 2017, doi = 10.1016/j.jeurceramsoc.2016.12.031.
- [124] B.R. Müller, R.C. Cooper, A. Lange, A. Kupsch, M. Wheeler, M.P. Hentschel, A. Staude, A. Pandey, A. Shyam, G. Bruno, "Stress-induced microcrack density evolution in β -eucryptite ceramics: experimental observations and possible route to strain hardening" *Acta Materialia*, 144, 627-641, 2017, doi = 10.1016/j.actamat.2017.10.030.
- [125] R. Laquai, B.R. Müller, G. Kasperovich, J. Haubrich, G. Requena, G. Bruno, "X-ray refraction distinguishes unprocessed powder from empty pores in selective laser melting Ti-6Al-4V ", *Materials Research Letters*, 6, 2, 130-135, doi = 10.1080/21663831.2017.1409288
- [126] A. Jameson and L. Martinelli N. A. Pierce, "Optimum aerodynamic design using the Navier-Stokes equations, *Theoretical and Computational Fluid Dynamics*, 10, 213-237, 1998, doi = 10.1007/S001620050060.
- [127] F.E. Fensch-Kleemann and K.-W. Harbich and M.P. Hentschel "Microstructural characterisation of porous ceramics by X-ray refraction topography", *Ceram. Forum Int.*, 79, 11, E35-E38, 2002.
- [128] Thermo Fisher Scientific, "Thermo Fisher scientific Avizo software (version 9.4)".
- [129] R. M. Kolonay "Computational aeroelasticity", Presentation at RTA-NATO 1-5 2001.
- [130] J.F. Gerbeau, M. Vidrascu, P. Frey "Fluid Structure Interaction in blood flows on geometries based on medical imaging, *Computers and Structures* 83, 155-165, 2005, doi = 10.1016/j.compstruc.2004.03.083.
- [131] P. Crosetto, P. Reymond, S. Deparis, D. Kontaxakis, N. Stergiopoulos, A. Quarteroni, "Fluid?structure interaction simulation of aortic blood flow, *Computers and Fluids* 43, 1, 46-57, 2010, doi = 10.1016/j.compfluid.2010.11.032.

- [132] M. Schafer "Numerical simulation of coupled fluid - solid problems, *Computer Methods in Applied Mechanics and Engineering* 190, 28, 3645-3667, 2001, doi = 10.1016/S0045-7825(00)00290-5
- [133] "Flexible airplane wings are made from thousands of tiny 3D-printed pieces, <https://createdigital.org.au/flexible-airplane-wings-thousands-3d-printed-pieces/>, 2019